MICROFLUIDIC BIOMATERIALS FOR *IN VITRO* 3-D CULTURE

A Dissertation

Presented to the Faculty of the Graduate School

of Cornell University

In Partial Fulfillment of the Requirements for the Degree of

Doctor of Philosophy

by

Nakwon Choi

February 2010

MICROFLUIDIC BIOMATERIALS FOR *IN VITRO* 3-D CULTURE

Nakwon Choi, Ph. D.

Cornell University 2010

Clinicians have made practical efforts for over 100 years in replacing damaged tissues and organs.   However, organ shortage and rejection still remain major challenges.   Rapidly emerging tissue engineering, which is interdisciplinary medical science and technology, has gained attention to resolve the challenges.   The grand aim of tissue engineering is to develop implantable tissue constructs via *in vitro* culture of cells seeded in three-dimensional (3-D) scaffolds formed in biomaterials. Microengineering and microfluidic techniques have demonstrated promising proof-of-concept in developing potentially valuable *in vitro* culture systems.   However, in conventional microfluidic systems, the culture environment is confined to channels. Moreover, most of currently existing cell culture systems do not allow for the creation of fully functional tissues.   This limitation is also due to a lack of understanding principles of tissue function and growth.   Tissue-scale biology, combined with molecular and cell biology, would allow for better understandings of the principles, and can be complementarily interconnected to tissue engineering.   Therefore, we must develop *in vitro* tools to overcome the challenges and to enable tissue engineering and tissue-scale biology.   The development of the enabling tools could lead to exploitation of detailed principles and mechanisms in the study of physiological and pathological processes in a quantitative manner.

First, we present the development of microfluidic scaffolds that are formed by

embedding microfluidic networks directly within biomaterials. Experiments with chondrocytes in calcium alginate demonstrated that these embedded microchannels enable the maintenance of a uniform metabolic environment within the bulk of the scaffold and the creation of distinct soluble environments experienced by cells in their 3-D environment. The generalization of the process into type I collagen allows for the embedded microchannels to serve as a template for microvascular endothelialization within a matrix that can support cellular remodeling.

In the new experimental context offered by these microfluidic scaffolds, we present detailed mass transport considerations in microfluidic biomaterials. Such considerations include quantitative measurements of 1) diffusion of non-reactive solutes and 2) metabolic activity of reactive solutes such as oxygen, which should be also used in designing and operating microfluidic biomaterials.

Finally, we present the development of oxygen-sensing particles that are dispersible in aqueous environment and biocompatible. Experiments show that the oxygen-sensing particles also allow monitoring oxygen concentration in a both spatially and temporally resolved manner. We can use this tool for the direct visualization and optical measurement of oxygen-depletion lengths within cell-seeded 3-D scaffolds *in vitro*, and the measurement of oxygen levels in animal blood streams *in vivo*.

BIOGRAPHICAL SKETCH

Nakwon Choi was born November 3rd, 1978 in Seoul, Korea, the first child of Dong Ho Choi and Jeong Soon Kwak.   While Nakwon spent playful childhood with good friends, he met Mr. Gil Hyun Ryu who was a teacher in his class at Bongeun middle school and had great influence on Nakwon's attitude of mind.   At Yongdong high school, Nakwon's extracurricular activity in Yongdong Broadcasting Station (YBS) also made him become more outgoing.   Nakwon's favorite subjects were mathematics and chemistry; this preference led to his entrance to School of Chemical and Biological Engineering of Seoul National University in 1997.   Then, very fortunately, Nakwon was selected as Korean Augmentation to the United States Army (KATUSA) for the military service and assigned to Headquarters, 20th Support Group, Busan in Camp Hialeah.   For the 26-month service Nakwon had great opportunities to work in various sections (dining facility, logistics support office, information management office, and ROKA service office) where he was able to learn not only English but also American culture via team work with U.S. soldiers.   This experience led to Nakwon's decision to study in the states for his Ph. D..   Before Nakwon came to Cornell University, he had another great chance to perform research on electrokinetics and microfluidics at Dr. Myung-Suk Chun's laboratory in Korean Institute of Science and Technology (KIST) from December, 2003 to August, 2004. It was the place where Nak Won got interested in the field of microfluidics. Nakwon's fortune did not end there; he found "Stroock group" at School of Chemical and Biomolecular Engineering of Cornell University and enjoyed working on "converging" projects, related to microfluidics and tissue engineering, with excellent collaborators over the fields of Biomedical Engineering, Mechanical Engineering, and Materials Science and Engineering.

To my parents, Dong Ho Choi and Jeong Soon Kwak,

and to my wife, Yung Kyung Park

ACKNOWLEDGMENTS

Professor Abraham D. Stroock, thank you for giving me the opportunities to work on the interdisciplinary projects from which I was able to learn significant amount of knowledge and to extend my academic horizon from Chemical Engineering towards various other fields.   I really appreciate your support, encouragements, and valuable advice for the past 5 years.   I am and will be very proud of being one of early members in the Stroock group.

Professor Lawrence J. Bonassar, thank you for inviting me as a semi-permanent group member, providing insightful advice, and being my committee member.   In your laboratory, I was able to learn all the experimental fundamentals of the harvest of primary chondrocytes from bovine joints, cell cultures, and core techniques for tissue engineering.

Professor Donald K. Koch, thank you for being my committee member and providing thoughtful advice on theoretical aspects of mass transport.   I was also able to learn advanced mathematics, which served as an important backbone for my dissertation, from your class.

Professor Claudia Fischbach, thank you for your extraordinary support and collaboration in extending my work to cancer research.   Collaboration with your group allowed me to gain significant insight on the emerging field and to develop my own ambition.

Professor Lara A. Estroff and Jason Dorvee, thank you for inviting me to the field of biomineralization.   With your support and advice, and the collaboration with your group, I was able to enhance my expertise on the theoretical part of biomineralization and mass transport in general as well.

Mr. Glenn Swan, I greatly appreciate your efforts to make all the jig parts that

TABLE OF CONTENTS

LIST OF FIGURES

LIST OF TABLE

CHAPTER 1

INTRODUCTION

Some have probably dreamed that tissues or organs in our body, when they no longer function properly due to physical damage or diseases, could be healed or replaced with replacements that would be virtually the same as one's original tissues or organs in the future. Although this idea may be still a naive dream, humankind has been continuously seeking ways towards realizing it. Since Watson and Crick discovered the double-helix structure of DNA in 1953, biologists have done extensive molecular biology, leading to the completion of the U.S. human genome project (HGP) in 2003 with the hope that all the identified genes in human DNA could help diagnose, treat, and even prevent diseases and disorders. In parallel with the genetic perspective, clinicians have also made practical efforts for over 100 years in replacing damaged tissues and organs. Clinically successful examples include transplantations of skin, cornea, kidney, liver, pancreas, and heart[1-5]. Although the transplantation is a key life-saving therapeutic strategy, there is a significant shortage of tissues and organs available for transplantation largely due to the difficulty to find immunologically matching tissues and organs between a donor and recipient. The shortage also seems to be attributed to aging societies now in many countries. In addition, almost all transplantations are performed with suppression of the immune system, an unavoidable complication that threatens the transplanted patients with serious side effects, including fatal kidney failure and increased risks of cancer and sepsis. This organ shortage and rejection still remain major challenges.

Regenerative medicine is a rapidly emerging field that can provide alternative solutions to overcome the challenges described above and improve human health. It covers primarily the creation of functional living tissues or organs to repair or replace

damaged ones (also see Fig. 1.1A). A core sub-field is tissue engineering which aims at *in vivo* implantation of grown engineered tissues, obtained by culturing three-dimensional (3-D) scaffold biomaterials seeded with cells of interest, *in vitro*[6] (Fig. 1.1B). Until recently, the term "tissue engineering" has been used interchangeably with regenerative medicine. Another sub-field is cell therapy which refers to therapeutic approaches of the use of cells, including stem cells for helping damaged tissues and organs regenerate *in vivo*. Tissue engineering / regenerative medicine is multidisciplinary medical science and technology that include molecular and cell biology, materials science and engineering, chemical engineering, and bio/biomedical engineering. Specifically, tissue engineering requires 1) the appropriate choice of scaffold biomaterials that serve as structural support and allow for cell proliferation, permeation of oxygen and other nutrients, and extracellular matrix (ECM) synthesis, and 2) *in vitro* culture of the scaffolds towards formation of functional tissues.
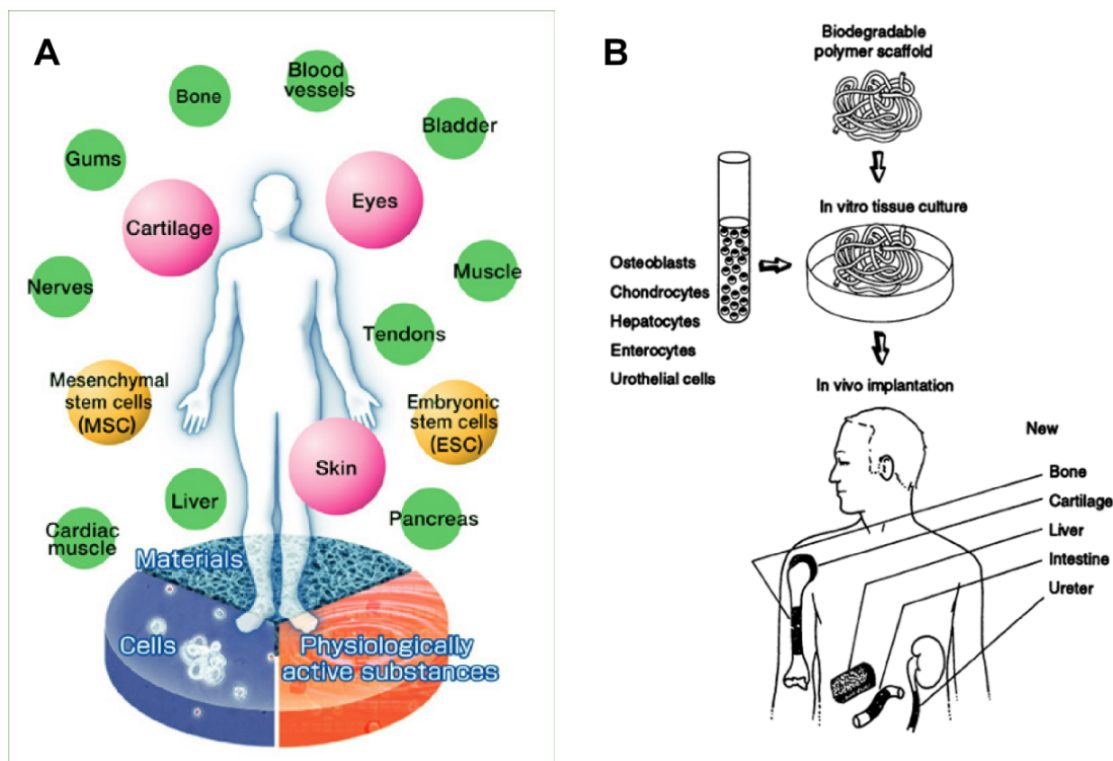
Figure 1.1 Regenerative medicine and tissue engineering. A. Schematic illustration showing tissues and organs to create, and required components for regenerative medicine. Image was obtained from http://www.jpte.co.jp/english/technologies/index.html. **B.** Schematic diagram showing general approaches in tissue engineering. Image was obtained from Langer, R. & Vacanti, J.P., Tissue Engineering. *Science* **260** (5110), 920-926 (1993).

What is tissue?

A tissue, an intermediate level between a cell and an organ (Fig. 1.2A), is composed of a large number of cells (e.g., $\sim 4 \times 10^{10}$ cell/adipose tissue[7]) of a single or more often multiple cell types. In other words, a tissue does not consist of mixture of cells differentiated from endoderm (internal layer), mesoderm (middle layer), and ectoderm (external layer) in a germ layer. This is the formal definition, but in the context of tissue engineering, we sometimes (more often in the future) aim at developing composite tissues (e.g., liver with endothelia). Tissues have their specific functions; for example, articular cartilage between knee joints allows smooth movement of the joints by absorbing load. Tissue size can vary from ~10 micrometers to a few centimeters. Tissues are categorized into 4 groups; 1) connective tissues holding other tissues together, 2) muscle tissues producing force and motion, 3) nervous tissues, and 4) epithelial tissues covering organ surfaces. As we can expect, tissues are spatially heterogeneous in 3-D; for example, the articular cartilage can be divided into superficial, middle, deep, and calcified zones in each of which cell shape and the organization of ECM are different (also see Fig. 1.2B-E). These complexity and characteristics of tissues are reflected in engineering functional ones as excellent challenges. Therefore, strategic approaches from various fields of medicine, science, and engineering are required.
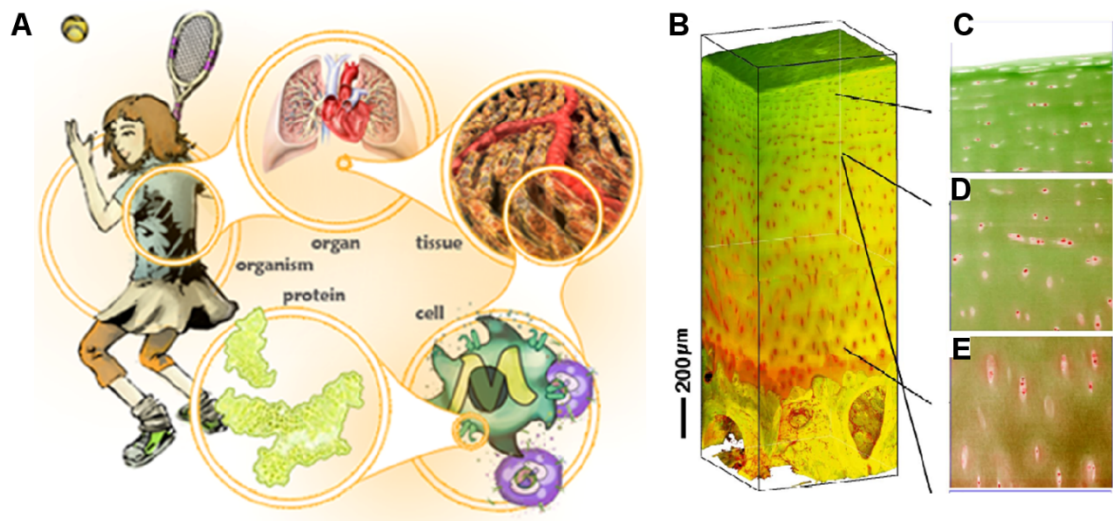
Figure 1.2 Various levels consisting of the body and human articular cartilage. A. Illustration showing various levels of an organism: protein-cell-tissue-organ-organism. Image was obtained from http://www.sites.duq.edu/sepa/regmed/regmedbasics/CellsTissuesandOrgans.shtml. **B.** 3-D view of human articular cartialge. **C-E.** 2-D virtual sections from image in B. Images were obtained from Sah, *et al.*, 48th Annual Meeting of the Orthopaedic Research Society Transactions **27**, 0363 (2002).

Scaffold biomaterials

Researchers have been using a variety of biomaterials as tissue scaffolds, typically synthetic polymers, naturally derived hydrogels, or composite materials of the two. Widely used biodegradable synthetic polymers include poly(glycolic acid) (PGA), poly(lactic acid) (PLA), and poly(lactic-co-glycolic acid) (PLGA). These polymers can be extruded and molded into 3-D fibrous meshes to host cells, and cultured *in vitro* and *in vivo*[8-10]. Although the biodegradable polymers allow for relatively precise control over scaffold properties (e.g., surface to volume ratio, degrade rate), high concentrations of degradation products, when they are not removed efficiently, show toxicity in some cases[11].

Most commonly used naturally derived hydrogels are alginate and collagen. Alginate is a poly(saccharide) polymer, extracted from algae and composed of D-mannuronate and L-guluronate subunits. It is easy to seed cells uniformly in its pre-gel form (i.e., viscous liquid), and divalent ions such as calcium can solidify the gel via cross-linking between guluronate subunits with the calcium ions. This aspect allows for the creation of desired 3-D structural shapes via injection molding[12-13] or computer-aided direct deposit[14]. Alginate can be also chemically modified relatively easily to induce integrin-mediated interactions, involved during cell attachment and migration, by covalently attaching oligopeptide adhesion ligands (i.e., RGD motif)[15]. Collagen is a fibrous triple-helix protein and the most abundant ECM component in our body, implying that it could provide better biological recognition as a scaffold material. While commercially available collagen is still very expensive, relatively large quantities for experiments in a laboratory can be obtained by harvesting animal tissues (e.g., rat tendons) and purifying collagen via ultracentrifugation. It can be gelled simply by increasing pH and temperature to form 3-D structure despite its

substantially lower stiffness (i.e., Young's modulus) compared with alginate. Both alginate and collagen are permeable to small and macromolecules.

In vitro tissue culture systems

Appropriately chosen scaffold biomaterials seeded with cells in bulk need to be cultured *in vitro* to allow for tissue development, which could take weeks and months. The most important aspect is to nourish cell-seeded scaffolds well enough throughout culture periods such that undesired heterogeneity (i.e., distribution of viable cells and deposition of ECM) within the scaffolds, caused by oxygen and nutrient depletion or accumulation of waste products, does not arise. Designing *in vitro* tissue culture systems is, in fact, an excellent chemical engineering problem associated with mass transport to and within the cell-seeded scaffolds. More specifically, oxygen supply in engineered tissue constructs is a key to successful development of functional tissues, because viable cells should maintain their metabolic activity and phenotypic behavior for ECM synthesis. This issue was considered even before the field of tissue engineering was born. In 1919, Krogh first conceptualized and modeled oxygen transport from a cylindrical capillary to a muscle tissue with a Danish mathematician, Erlang's help[16] (Fig. 1.3). For simplicity, the Krogh model is based on a couple of major assumptions; convectively delivered oxygen from the vascular capillary only diffuses and is consumed by cells in the tissue with zeroth order kinetics (i.e., constant consumption rate). The Krogh length can be then defined as a characteristic length over which oxygen is depleted. Therefore, another vascular capillary should be located within a Krogh length of its neighbor. Despite the assumptions used to simplify the mathematical model, the Krogh cylinder still has broad relevance to the fields of physiology, biomedical engineering, and clinical practice as a core consideration. Colton is also one of early pioneers who was concerned about oxygen

supply to implantable artificial organs and stated that oxygen transport should be taken into account in designing devices[17-18].

Generally speaking, static culture of engineered tissue constructs can cause cell death and less deposition of ECM towards the middle of the constructs[19-20] (also see Fig. 1.5A). Note that Ballyns *et al.* have recently observed that static culture of relatively large engineered meniscus constructs resulted in more deposition of ECM within the constructs, with maintaining cellularity for 8 weeks[12]. They have been further investigating to characterize the heterogeneous ECM deposition. In the case of cartilage-meniscus engineering, it seems controversial whether depletion of oxygen is detrimental. Others have also argued that low oxygen increased ECM synthesis for articular cartilage[21]. This may indicate that oxygen concentration has to be more finely controlled in a physiologically relevant way through *in vitro* culture periods rather than maintained at 17 ~ 18 % O_2 in an incubator.
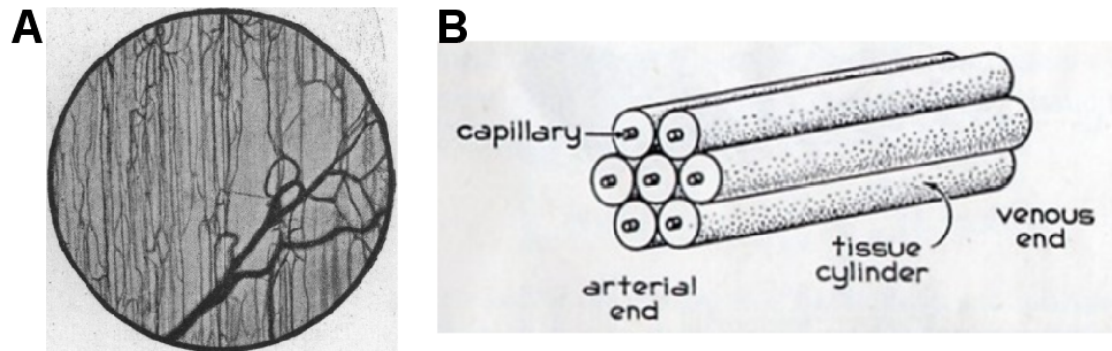
Figure 1.3 The Krogh model. A. Optical micrograph showing vascular capillaries on abdominal muscle wall of the guinea pig. Image was obtained from Krogh, A., The number and distribution of capillaries in muscles with calculations of the oxygen pressure head necessary for supplying the tissue. J. Physiol.-London 52 (6), 409-415 (1919). B. Schematic representation of the Krogh cylinder model. Image was obtained from

http://www.owlnet.rice.edu/~chbe402/proj04/seli/CENG402_Project_Files/Blank%20 Page%202.htm.

Researchers have utilized bioreactors to enhance mass transport both outside and inside cell-seeded scaffolds. Such bioreactors include stirred flasks, rotating wall vessel bioreactors, hollow fiber bioreactors, and direct perfusion bioreactors[22] (Fig. 1.4). The stirred bioreactor allows for continuous agitation of culture media such that concentration boundary layers of oxygen and other growth factors are negligibly thin on surfaces of tissue constructs. Enhanced mass transfer has resulted in slightly more deposition of glycosaminoglycan (GAG), an extracellular component in cartilage, towards central zones within bovine chondrocyte-seeded scaffolds[22-23] (also see Fig. 1.5B). However, it may be practically difficult to precisely control the extent of the enhanced mass transport in the stirred bioreactor because increase of mass transfer could also cause the extraction of synthesized ECM components from cell-seeded scaffolds to well-agitated media. The rotating wall vessel bioreactor could serve as an alternative method to resolve this issue. Enhanced interfacial mass transfer and tolerable ECM extraction, probably attributed to relatively low shear, have demonstrated that ECM was uniformly deposited within scaffolds (Fig. 1.5C). The hollow fiber and direct perfusion bioreactors have been also used to enhance mass transport through permeable cell-seeded fibers and cell-seeded scaffolds respectively. These bioreactors could be slightly more useful for high metabolic cells (e.g., liver and muscle cells), but other cell types can be cultured as well. The hollow fiber reactor has a limitation of growing tissue size because cells or cell-seeded scaffolds are confined within small permeable fibers. The direct perfusion bioreactor has a similar issue that can be caused in the stirred bioreactor; perfusion rate through cell-seeded scaffolds, if it is too high or the scaffolds are not mechanically stiff enough to sustain the direct perfusion, can lead to loss of synthesized ECM and possibly cells as well.
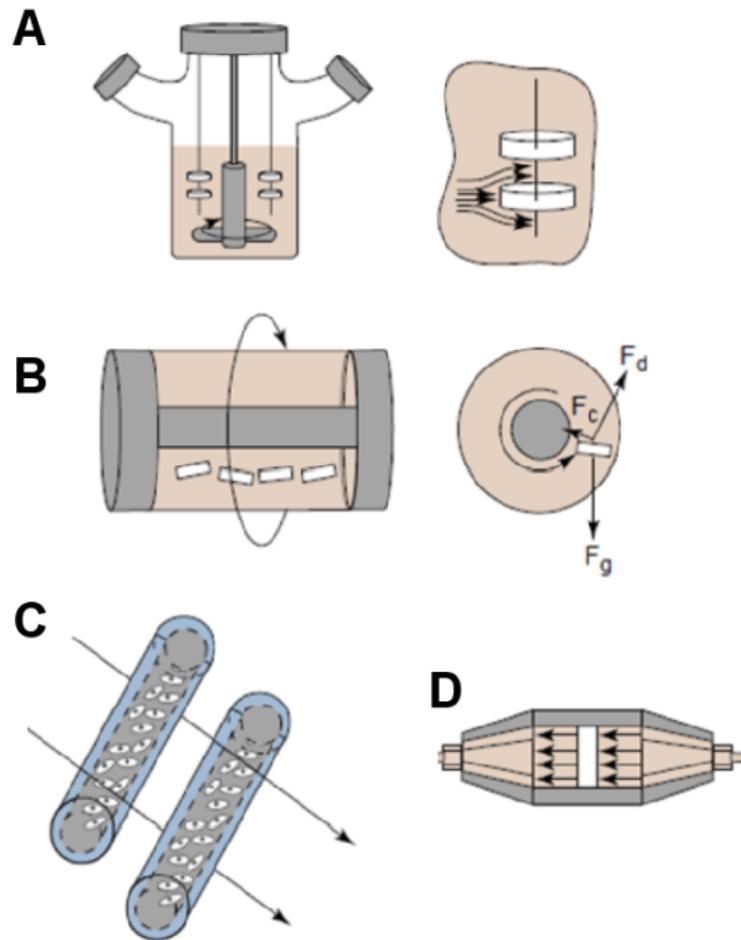
Figure 1.4 Schematic representations of bioreactors used to enhance mass transport for tissue engineering applications. A. Stirred flask. **B.** Rotating wall vessel bioreactor. **C.** Hollow fiber bioreactor. **D.** Direct perfusion bioreactor. Image was obtained from Martin, I. *et al.*, The role of bioreactors in tissue engineering. *Trends Biotechnol.* 22 (2), 80-86 (2004).
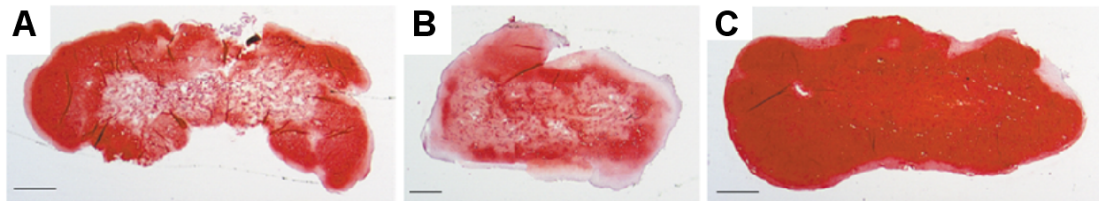
Figure 1.5 Histological cross-sections of engineered cartilage tissues after six weeks of culture in different bioreactors. Red is Safranin-O-stained glycosaminoglycan (GAG). Engineered tissue constructs cultured statically (A), in stirred flask (B), and in rotating wall vessel bioreactor (C). Scale bars, 1 mm. Image was obtained from Martin, I. *et al.*, The role of bioreactors in tissue engineering. *Trends Biotechnol.* **22** (2), 80-86 (2004).

Atala *et al.* have recently reported that they were able to implant tissue engineered bladders in human patients, obtained by culturing collagen or collagen-PGA scaffolds seeded with urothelial and muscle cells for 7-8 weeks *in vitro*[24]. Both this achievement, seen as the first clinically implanted engineered organ in human, and the significant advances in developing bioreactors have enlightened the field of tissue engineering and regenerative medicine with the hope that much more complex tissues could be also engineered and translated to the clinic in the near future. Nevertheless, mass transport limitations are still the biggest challenge towards growing clinically relevant size of engineered tissues because most tissues, with the exception of mature cartilage, are vascularized. The centrally networked vasculature is responsible for delivering oxygen, nutrients, and signaling molecules to the tissues in our body. As Krogh observed in muscle tissues, spacing between vascular capillaries is 50 ~ 200 µm (also see Fig. 1.3A), indicating that oxygen reaches up to the length scale due to metabolism (i.e., diffusion-reaction)[16,25]. Therefore, vascularization of engineered tissue constructs has been considered as a necessary approach in not only overcoming the mass transport limitations but also ultimately better integrating the constructs into the body after *in vivo* implantation. Strategies to vascularize tissue constructs include scaffold functionalization, cell-based techniques, and microengineering techniques[26]. Incorporation of angiogenic factors such as vascular endothelial growth factor (VEGF), basic fibroblast growth factor (bFGF), and platelet-derived growth factor (PDGF) within scaffold biomaterials can allow promoting vascularization by the host release of the factors over culture periods[27-28]. The functionalization of scaffold biomaterials such as PGA, alginate, and collagen can be done by either simple loading of the soluble factors or chemical modification of a scaffold. For instance, collagen decorated with heparin which enhances VEGF binding has shown increase of endothelial tube formation[29]. Co-cultures with endothelial cells[30] and incorporation of

VEGF-transfected cells (i.e., VEGF-producing cells)[31] have also shown enhanced vascularization. As Micro-Electro-Mechanical Systems (MEMS) techniques have been advancing and merging into biological applications, they can also allow the development of promising microfluidic tools in pre-vascularizing scaffolds. The creation of fluidic networks on a biodegradable polymer, poly(glycerol sebacate) (PGS)[32] or silk fibroin[33] has demonstrated proof-of-concept that cells could be cultured within microfluidic channels. Other research groups have also demonstrated that cells can be seeded within microfluidic hydrogels such as agarose[34] (Fig. 1.6A), collagen, and fibrin[35] (Fig. 1.6B). Similarly, we have shown the development of microfluidic biomaterials with calcium alginate seeded with cells[36-37]. Our work represents one of the leading efforts in this direction.

An underlying challenge is micrometer-scale control of the soluble chemical environment in the bulk of 3-D cell cultures; such control is necessary not only to maintain metabolic activity – which is also achievable with simple perfusion – but to deliver metabolites and signals with spatial and temporal control. Another excellent challenge is to develop *in vitro* systems allowing for both the micrometer scale control and cellular remodeling of ECM; such remodeling is always occurring in our body and also essential towards building *in vivo*-like tissues.
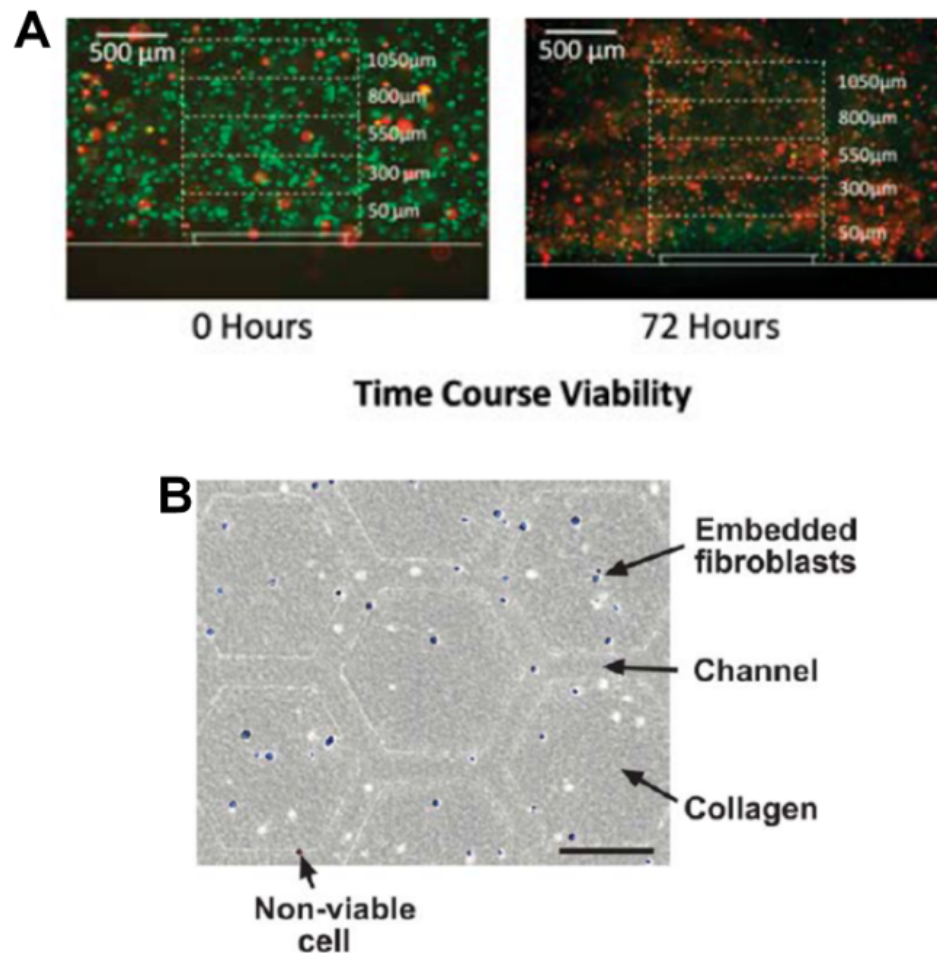
Figure 1.6 Pre-vascularized scaffolds using microfluidics / microengineering techniques. A. Fluorescence micrographs showing live (green) and dead (red) AML-12 murine hepatocytes in agarose with a pre-defined microchannel, at 0 (left) and 72 (right) hr. Image was obtained from Ling, Y. *et al.*, A cell-laden microfluidic hydrogel. *Lab Chip* **7** (6), 756-762 (2007). **B.** Optical micrograph showing fibroblasts in collagen with pre-defined microchannels. Image was obtained from Golden, A.P. & Tien, J., Fabrication of microfluidic hydrogels using molded gelatin as a sacrificial element. *Lab Chip* **7** (6), 720-725 (2007).

Tissue-scale biology

      As stated in the previous section, the current bottle neck point in the field of tissue engineering is to develop functional tissues *in vitro* for clinical use. The approaches described above are mainly focused on developing methodology towards growing engineered tissue constructs better, for example by enhancing mass transport and promoting vascularization within the constructs. However, a seemingly missing aspect from a slightly different perspective is to better understand principles of tissue function and growth. Note that living tissues present a 3-D complexity where cells, ECM, and signaling molecules interplay both biochemically and mechanically. Although molecular biology, which overlaps with genetics and biochemistry, and cell biology have provided with tremendous amount of fundamental knowledge and mechanisms about how living systems are regulated, there is still a relatively big gap in the understanding of biological processes and the recapitulation of physiology on tissue scale for the creation of functional tissues. Therefore, tissue-scale biology can serve as a complementary field that would be interconnected to tissue engineering applications in an iterative manner (also see Fig. 1.7). Tissue-scale biology inevitably demands new tools, "enabling tools" that can be also used for tissue engineering.
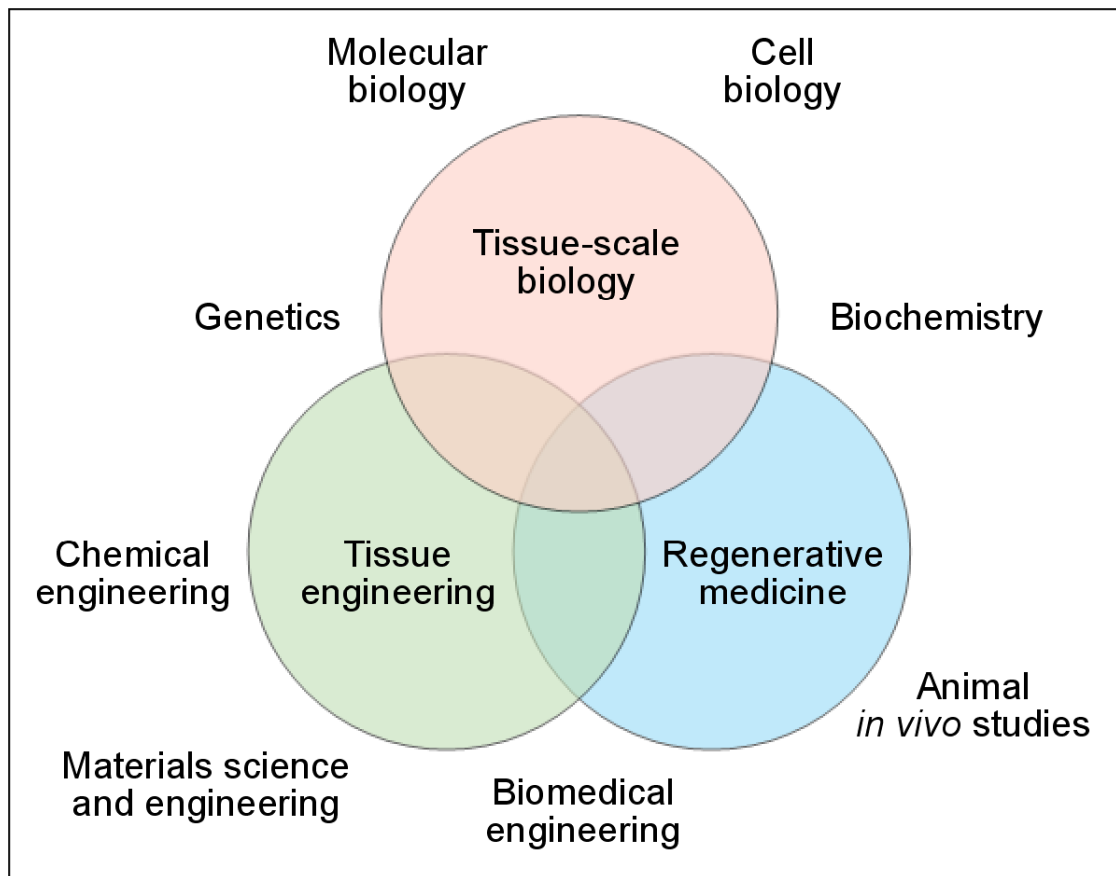
Figure 1.7 Schematic illustration of tissue-scale biology interconnected with tissue engineering and regenerative medicine.

Tissue-scale tumor biology

One may argue that studies of tumor may have nothing to do with tissue engineering. However, elucidating how tumor grows and metastasizes can help develop functional tissues *in vitro* because a key process in tumor progression is angiogenesis (i.e., the formation of new blood vessels from existing ones), which is also a main process in wound healing. Note that both tumor progression and wound healing occur in the body (i.e., a host), but the main distinction between the two is that tumor grows in an uncontrolled manner that does not produce functional tissues. Improved understandings of tumor angiogenesis on tissue scale (or pathologically relevant scale) may also be potentially more useful in improving current anti-angiogenic treatment and cancer therapies more generally.

In order for avascular solid tumor to grow and metastasize, it secrets angiogenic factors such as VEGF and recruits new blood vessels to become vascularized tumor[38]. Oxygen concentration within tumor tissues is a driving factor; specifically, depletion of oxygen or hypoxia created deep in tumor tissues is known to cause angiogenic signaling between tumor tissues and blood vessels[39-41] (also see Fig. 1.8). Although hypoxia-driven up-regulation of VEGF has been considered as the major player to initiate and promote tumor angiogesis, other microenvironmental cues may also play an important role[42]. Fischbach *et al.* have recently shown that cell-cell and cell-ECM interactions in 3-D environment regulate the expression of other angiogenic factors such as bFGF and interleukin-8 (IL-8)[43-44]. IL-8 is generally known as a chemoattractant recruiting neutrophils to inflammation sites, but it has also shown angiogenic effects[45]. One of its receptors, CXCR2 (or IL8RB) mediates both the inflammatory response and angiogenic effects[46-47].

Traditionally, tumor cell response to hypoxia has been studied in either 2-D cell culture or animal *in vivo* models. As briefly stated in the previous section, petri-

18

dish culture is a poor mimic of the *in vivo* microenvironment[48], and can promote

fundamentally different cellular behavior[42-43], particularly related to spatiotemporally

varing oxygen levels. In animal *in vivo* models, it is practically difficult to control

experimental parameters. In addition, the animal models often do not recapitulate

human tumor behavior. A third category of experimental system, 3-D tumor models,

has recently emerged to provide both precise control over experimental conditions and

in-vivo-like microenvironments to recapitulate human tumor behavior[43-44,49-50]. Yet, it

remains a general challenge to separate out oxygen-related effects from other

microenvironmental cues in elucidating angiogenic signaling and direct angiogenesis

in 3-D. Our work described in this dissertation represents the development of

technologies towards addressing the challenge.
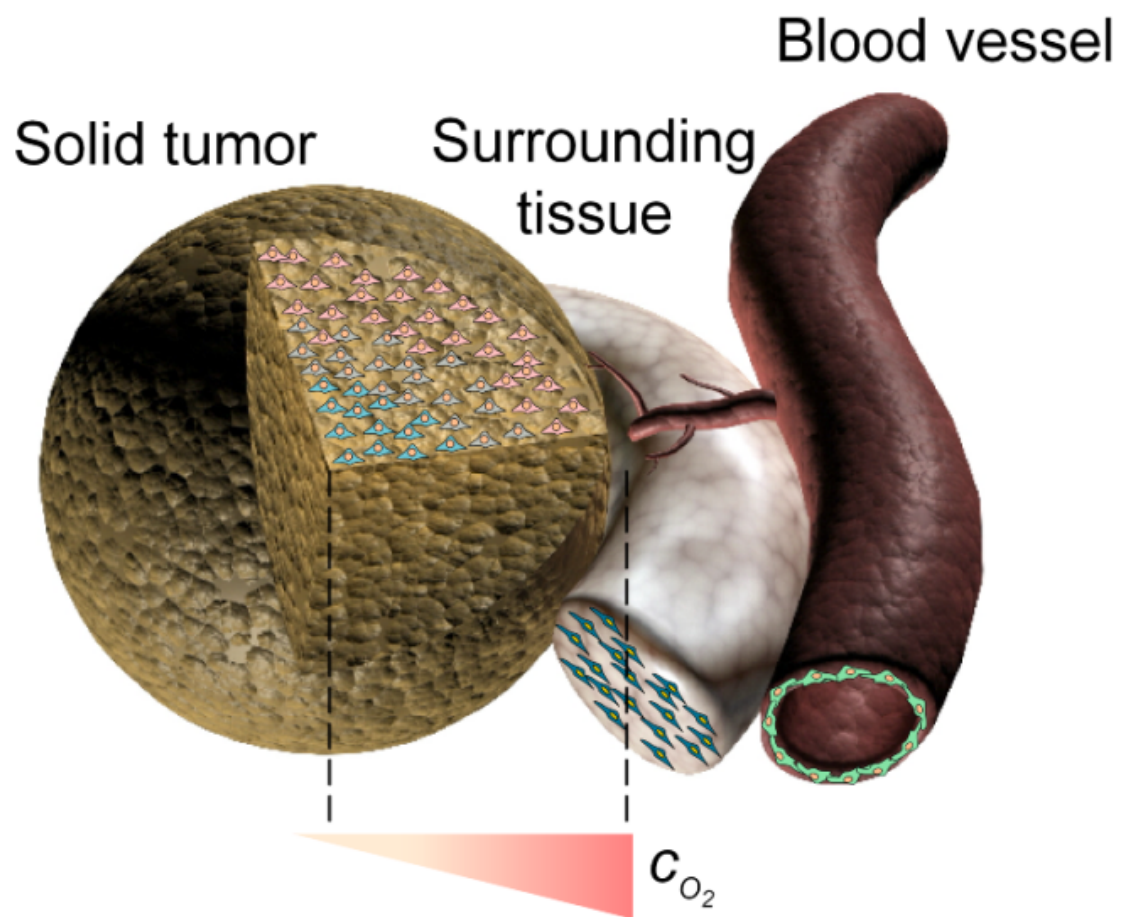
Figure 1.8 Schematic illustration of tumor angiogenesis.

Conclusions and motivations of research

Despite some clinically successful transplantation of tissues and organs, practical challenges remain due to organ shortage and rejection. Rapidly emerging regenerative medicine, which is interdisciplinary medical science and technology, has gained attention to resolve the challenges. The grand aim of a core sub-field, tissue engineering is to 1) choose appropriate scaffold biomaterials, 2) culture cell-seeded 3-D tissue scaffolds *in vitro*, and 3) implant engineered tissues to the body. Researchers have made significant advances towards overcoming mass transport limitations of oxygen and nutrients, and ultimately growing functional tissues *in vitro*. Bioreactors and vacularization of engineered tissue constructs are useful in resolving the limitations. Specifically, microengineering and microfluidic techniques have demonstrated promising proof-of-concept in developing potentially more valuable *in vitro* culture systems. Nevertheless, most of currently existing such systems do not allow for the creation of fully functional tissues. Tissue-scale biology would allow better understanding principles of tissue function and growth, and can be complementarily interconnected to tissue engineering and regenerative medicine. Tissue-scale tumor biology, where angiogenesis is involved, would allow not only for better understandings of the process, which could help develop vascularized functional tissues in the context of tissue engineering, but also for improvement of current anti-angiogenic treatment. Therefore, we must develop *in vitro* tools to enable tissue engineering and tissue-scale biology. These tools should allow for both micrometer scale control of 3-D cellular microenvironment and cellular remodeling of ECM. Quantitative mass transport (e.g., metabolic activity) should be considered in designing such tools. The development of the enabling tools could lead to exploitation of detailed principles and mechanisms in the study of physiological and pathological processes in a quantitative manner.

Summary of dissertation

In Chapter 2, we present the technology development of microfluidic biomaterials based on the embedding of fluidic networks directly within alginate and collagen. Successful microfluidic biomaterials should meet the following conditions: 1) fabrication processes are cell-friendly, and the materials are 2) appropriate for the replication of microstructure, 3) formable into sealed fluidic structures, and 4) diffusively permeable to small and large solutes. We describe considerations related to the choice of biomaterials, fabrication, and qualitative characterization of microfluidic alginate scaffolds that can be utilized for tissue engineering and tissue-scale biology. Then, we characterize microfluidic collagen scaffolds as a structural template for endothelialization.

In Chapter 3, we present details about mass transport considerations in the microfluidic biomaterials. The mass transport considerations are essential in designing microfluidic biomaterials. The details include 1) desirable mode of operation, 2) the development of a technique to measure diffusion of solutes, 3) temporal and spatial control, and 4) quantitative measurements of metabolic activity using a model metabolite and oxygen.

In Chapter 4, we present the development of oxygen-sensing particles as an additional tool. Combining with microfluidic biomaterials, oxygen concentration must not only be controlled but also monitored in a spatiotemporally resolved manner. We describe 1) synthesis of oxygen-sensing micro- and nanoparticles, 2) characterization and calibration of the particles, and 3) biocompatibility. Then, we demonstrate 1) visualization and optical measurement of oxygen-depletion lengths within microfluidic biomaterials, and 2) *in vivo* oxygen imaging.

In Chapter 5, we conclude this dissertation with ideas of future directions that could aid towards developing functional tissues *in vitro* and allow further investigating detailed mechanisms of angiogenic signaling and direct angiogenesis.

REFERENCES

1.   Broelsch, C.E. *et al.*, Liver-transplantation in children from living related donors - surgical techniques and results. *Ann. Surg.* **214**, 428-439 (1991).

2.   Eastlund, T., The histo-blood group ABO system and tissue transplantation. *Transfusion* **38** (10), 975-988 (1998).

3.   Pellegrini, G. *et al.*, The control of epidermal stem cells (holoclones) in the treatment of massive full-thickness burns with autologous keratinocytes cultured on fibrin. *Transplantation* **68** (6), 868-879 (1999).

4.   Sutherland, D.E.R. *et al.*, Lessons learned from more than 1,000 pancreas transplants at a single institution. *Ann. Surg.* **233**, 463-501 (2001).

5.   Young, J.B. *et al.*, Matching the heart-donor and heart-transplantation recipient - clues for successful expansion of the donor pool - a multivariable, multiinstitutional report. *J. Heart Lung Transplant.* **13**, 353-365 (1994).

6.   Langer, R. & Vacanti, J.P., Tissue Engineering. *Science* **260** (5110), 920-926 (1993).

7.   Salans, L.B. *et al.*, Studies of human adipose tissue - adipose cell size and number in non-obese and obese patients. *J. Clin. Invest.* **52** (4), 929-941 (1973).

8.   Freed, L.E. *et al.*, Neocartilage formation *in vitro* and *in vivo* using cells cultured on synthetic biodegradable polymers. *J. Biomed. Mater. Res.* **27** (1), 11-23 (1993).

9.   Freed, L.E. *et al.*, Biodegradable polymer scaffolds for tissue engineering. *Bio-Technology* **12** (7), 689-693 (1994).

10.   Mooney, D.T. *et al.*, Stabilized polyglycolic acid fibre based tubes for tissue engineering. *Biomaterials* **17** (2), 115-124 (1996).

11.   Ignatius, A.A. & Claes, L.E., In vitro biocompatibility of bioresorbable polymers: Poly(L,DL-lactide) and poly(L-lactide-co-glycolide). *Biomaterials* **17** (8), 831-839 (1996).

12.   Ballyns, J.J. *et al.*, Image-guided tissue engineering of anatomically shaped implants via MRI and micro-CT using injection molding. *Tissue Eng. Part A* **14** (7), 1195-1202 (2008).

13.   Chang, S.C.N. *et al.*, Injection molding of chondrocyte/alginate constructs in the shape of facial implants. *J. Biomed. Mater. Res.* **55** (4), 503-511 (2001).

14.   Cohen, D.L. *et al.*, Direct freeform fabrication of seeded hydrogels in arbitrary geometries. *Tissue Eng.* **12** (5), 1325-1335 (2006).

15.   Rowley, J.A. *et al.*, Alginate hydrogels as synthetic extracellular matrix materials. *Biomaterials* **20** (1), 45-53 (1999).

16.   Krogh, A., The number and distribution of capillaries in muscles with calculations of the oxygen pressure head necessary for supplying the tissue. *J. Physiol.-London* **52** (6), 409-415 (1919).

17.   Colton, C.K., Implantable biohybrid artificial organs. *Cell Transplant.* **4**, 415-436 (1995).

18.   Colton, C.K., Engineering challenges in cell-encapsulation technology. *Trends Biotechnol.* **14** (5), 158-162 (1996).

19.   Sutherland, R.M. *et al.*, Oxygenation and differentiation in multicellular spheroids of human-colon carcinoma. *Cancer Res.* **46** (10), 5320-5329 (1986).

20.   Martin, I. *et al.*, Method for quantitative analysis of glycosaminoglycan distribution in cultured natural and engineered cartilage. *Ann. Biomed. Eng.* **27** (5), 656-662 (1999).

21.   Malda, J. *et al.*, Effect of oxygen tension on adult articular chondrocytes in microcarrier bioreactor culture. *Tissue Eng.* **10** (7-8), 987-994 (2004).

22. Martin, I. *et al.*, The role of bioreactors in tissue engineering. *Trends Biotechnol.* **22** (2), 80-86 (2004).

23. Martin, I. *et al.*, Modulation of the mechanical properties of tissue engineered cartilage. *Biorheology* **37**, 141-147 (2000).

24. Atala, A. *et al.*, Tissue-engineered autologous bladders for patients needing cystoplasty. *Lancet* **367** (9518), 1241-1246 (2006).

25. Jain, R.K. *et al.*, Engineering vascularized tissue. *Nat. Biotechnol.* **23** (7), 821-823 (2005).

26. Lovett, M. *et al.*, Vascularization Strategies for Tissue Engineering. *Tissue Eng. Part B-Rev.* **15** (3), 353-370 (2009).

27. Zisch, A.H. *et al.*, Biopolymeric delivery matrices for angiogenic growth factors. *Cardiovasc. Pathol.* **12** (6), 295-310 (2003).

28. Andrae, J. *et al.*, Role of platelet-derived growth factors in physiology and medicine. *Genes Dev.* **22** (10), 1276-1312 (2008).

29. Steffens, G.C.M. *et al.*, Modulation of angiogenic potential of collagen matrices by covalent incorporation of heparin and loading with vascular endothelial growth factor. *Tissue Eng.* **10** (9-10), 1502-1509 (2004).

30. Levenberg, S. *et al.*, Engineering vascularized skeletal muscle tissue. *Nat. Biotechnol.* **23** (7), 879-884 (2005).

31. Geiger, F. *et al.*, VEGF producing bone marrow stromal cells (BMSC) enhance vascularization and resorption of a natural coral bone substitute. *Bone* **41** (4), 516-522 (2007).

32. Bettinger, C.J. *et al.*, Three-dimensional microfluidic tissue-engineering scaffolds using a flexible biodegradable polymer. *Adv. Mater.* **18** (2), 165-+ (2006).

33.   Bettinger, C.J. *et al.*, Silk fibroin microfluidic devices. *Adv. Mater.* **19** (19), 2847-+ (2007).

34.   Ling, Y. *et al.*, A cell-laden microfluidic hydrogel. *Lab Chip* **7** (6), 756-762 (2007).

35.   Golden, A.P. & Tien, J., Fabrication of microfluidic hydrogels using molded gelatin as a sacrificial element. *Lab Chip* **7** (6), 720-725 (2007).

36.   Cabodi, M. *et al.*, A microfluidic biomaterial. *J. Am. Chem. Soc.* **127** (40), 13788-13789 (2005).

37.   Choi, N.W. *et al.*, Microfluidic scaffolds for tissue engineering. *Nat. Mater.* **6** (11), 908-915 (2007).

38.   Carmeliet, P. & Jain, R.K., Angiogenesis in cancer and other diseases. *Nature* **407** (6801), 249-257 (2000).

39.   Hanahan, D. & Weinberg, R.A., The hallmarks of cancer. *Cell* **100** (1), 57-70 (2000).

40.   Harris, A.L., Hypoxia - A key regulatory factor in tumour growth. *Nat. Rev. Cancer* **2** (1), 38-47 (2002).

41.   Bergers, G. & Benjamin, L.E., Tumorigenesis and the angiogenic switch. *Nat. Rev. Cancer* **3** (6), 401-410 (2003).

42.   Bissell, M.J. & Radisky, D., Putting tumours in context. *Nat. Rev. Cancer* **1** (1), 46-54 (2001).

43.   Fischbach, C. *et al.*, Engineering tumors with 3D scaffolds. *Nat. Methods* **4** (10), 855-860 (2007).

44.   Fischbach, C. *et al.*, Cancer cell angiogenic capability is regulated by 3D culture and integrin engagement. *Proc. Natl. Acad. Sci. U. S. A.* **106** (2), 399-404 (2009).

45. Wysoczynski, M. & Ratajczak, M.Z., Lung cancer secreted microvesicles: Underappreciated modulators of microenvironment in expanding tumors. *Int. J. Cancer* **125** (7), 1595-1603 (2009).

46. Benbaruch, A. *et al.*, Signals and receptors involved in recruitment of inflammatory cells. *J. Biol. Chem.* **270** (20), 11703-11706 (1995).

47. Yoshida, S. *et al.*, Involvement of interleukin-8, vascular endothelial growth factor, and basic fibroblast growth factor in tumor necrosis factor alpha-dependent angiogenesis. *Mol. Cell. Biol.* **17** (7), 4015-4023 (1997).

48. Pampaloni, F. *et al.*, The third dimension bridges the gap between cell culture and live tissue. *Nature Rev. Mol. Cell Biol.* **8** (10), 839-845 (2007).

49. Albrecht, D.R. *et al.*, Probing the role of multicellular organization in three-dimensional microenvironments. *Nat. Methods* **3** (5), 369-375 (2006).

50. Lee, G.Y. *et al.*, Three-dimensional culture models of normal and malignant breast epithelial cells. *Nat. Methods* **4** (4), 359-365 (2007).

CHAPTER 2

MICROFLUIDIC BIOMATERIALS AS ENABLING TOOLS FOR TISSUE

ENGINEERING AND TISSUE-SCALE BIOLOGY, *IN VITRO*

I. Introduction

Living tissues in our body - composed of cells and their extracellular matrix (ECM) - are three-dimensional (3-D) and allowed to maintain their functions by the vascular system that provides the tissues with oxygen and nutrients. Although conventional two-dimensional (2-D) cultures, such as monolayer cultures on solid or porous substrates, have provided enormous information in understanding cellular functions within the tissues, the 2-D cultures lack the capability of creating physiologically relevant 3-D microenvironments, including cell-cell and cell-extra cellular matrix (ECM) interactions, and gradients of soluble factors. Recent studies have reported that 3-D cultures show significantly different patterns of cell shape, gene expression, growth, morphogenesis, motility, and differentiation[1-3]. The dearth of *in vitro* tools, biomaterials, and techniques to process the materials has limited our ability to mimic physiological and pathological processes. In addition to *in vivo* animal models, *in vitro* 3-D culture systems to create of realistic tissues *in vitro* are desirable for their potential use as replacements for full animal models in basic biological studies[4-5] and pharmacological and toxicological screens[6], and as replacement tissues for clinical applications[7]. The generation of such tissues, where sophisticated interactions between living cells and host materials, requires tools to control the biological, chemical, and mechanical environment experienced by cells in culture. Significant advances have been made towards this goal: scaffold biomaterials have been developed to host cells in well-defined, 3-D geometries[8-9] and present biospecific extracellular ligands[10-11]; bioreactors have been designed to control global

mass transfer to the surface of cell-seeded scaffolds[12] and to perfuse their bulk[13-14];

and microengineering techniques have been used to tailor extracellular chemistry[15-16],

co-cultures[17], templates for endothelialization[18-19], and to create microfluidic networks

in hydrogels[20] and cell-seeded hydrogels[21-22]. An underlying challenge is micrometer-

scale control of the soluble chemical environment in the bulk of 3-D cell cultures;

such control is necessary not only to maintain metabolic activity – which is also

achievable with simple perfusion – but also to deliver metabolites and signals with

spatial and temporal control. Another important challenge is to develop *in vitro*

systems allowing for both the micrometer scale control and cellular remodeling of

ECM; such remodeling is always occurring in our body and also essential towards

building *in vivo*-like tissues. We address these challenges by embedding microfluidic

networks directly within biomaterials - microfluidic biomaterials - to use convective

mass transfer for control of the distributions and fluxes of solutes in the bulk of the 3-

D culture. Successful microfluidic biomaterials should meet the following conditions:

1) fabrication processes are cell-friendly, and the materials are 2) appropriate for the

replication of microstructure, 3) formable into sealed fluidic structures, and 4)

diffusively permeable to small and large solutes.

Microfluidic biomaterials define microchannels through which externally

controlled, pressure-driven flows deliver solutes to the bulk of the material. We

consider two classes of solutes: reactive solutes such as metabolites and waste

products and non-reactive solutes such as signaling molecules and buffers. Figure

2.1A schematically shows a steady-state distribution of a reactive solute delivered via

the channels (the pink square) and consumed by cells in the bulk to a certain length

scale (the pink shading). For non-reactive solutes, the embedded microchannels can

serve as sources and sinks to generate controlled gradients at steady-state (Fig. 2.1B).

Persistent gradients are useful for the study of basic biological phenomena such as

chemotaxis[23], morphogenesis[24], axonogenesis[25], and angiogenesis[4]. The use of patterns of channels acting as sources and sinks within microfluidic biomaterials could extend these studies into 3-D cultures. In addition, such gradients could be used as a tool to direct development of spatially heterogeneous tissues in the context of regenerative medicine[26-27] and tissue-scale tumor biology[28-29]. Figure 2.1C shows our strategy towards developing remodelable microfluidic biomaterials by endothelial cells: lithographically pre-defined microchannels in biomaterials are used as an endothelialization template. As briefly mentioned above, multi-cellular dynamics in 3-D, specifically by endothelial cells, are key steps in the development of vasculature at embryonic stages[30], wound healing[31], and tumor angiogenesis and metastasis[4,31]. Such remodelable microfluidic biomaterials could aid to find detailed mechanistic clues of these phenomena. Figure 2.1D shows the three architectures of single-level microfluidic networks that we used. In this chapter, we present considerations related to the choice of material, fabrication, and qualitative characterization of microfluidic biomaterials. Details of mass transport in the microfluidic biomaterials are presented in Chapter 2.
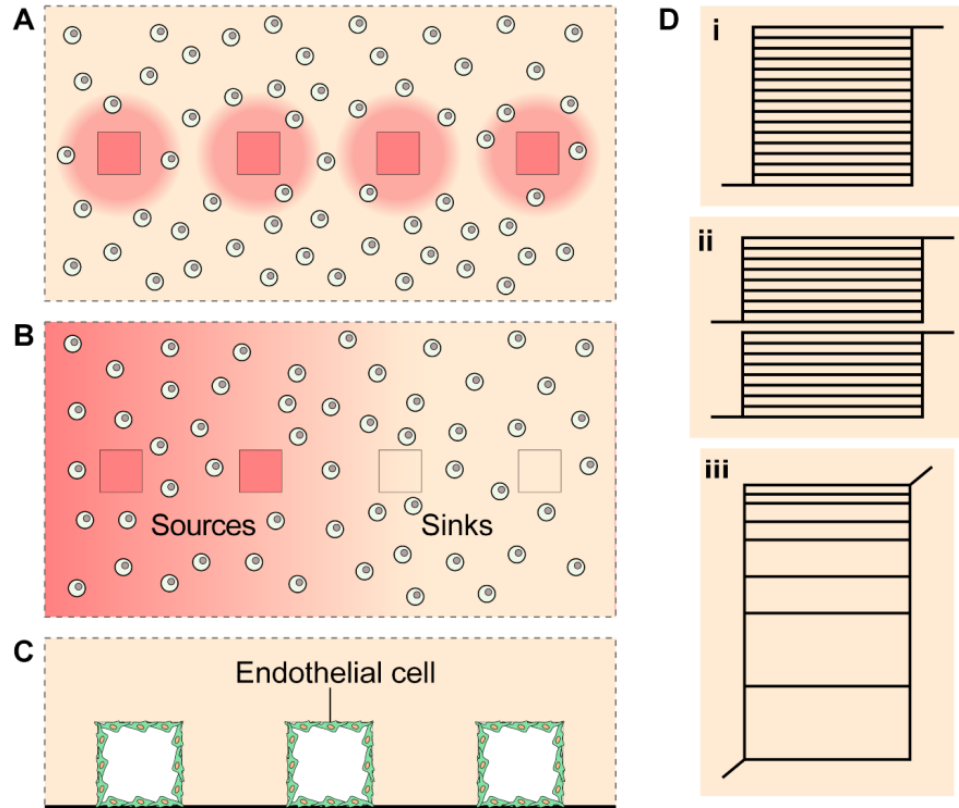
Figure 2.1 Schematic representations of microfluidic biomaterials. A and B.
Cross-sectional views of microfluidic biomaterials. Dispersed cells are shown as
double circles. Microchannels are shown as squares. The pink shading represents
steady-state distributions of solutes: in A, reactive solute is delivered via the channels
and is consumed by cells as it diffuses into the matrix; in B, non-reactive solute is
delivered via the two channels on the left and extracted by the channels on the right.
C. Cross-sectional view of endothelialized microfluidic biomaterial. Green objects
represent endothelial cells on pre-defined microchannel walls. **D**. Architectures of
single-layer microfluidic networks used here: a single network (i), two independent
networks (ii), a single network with variably spaced microchannels (iii).

Materials and methods

 A. Primary chondrocyte isolation and seeding

  Bovine articular cartilage was sterilely harvested from the stifle joints of 1-3-day-old calves (Gold Medal Packing, Syracuse, NY) and digested for 19 h in a 0.3 % [w/v] collagenase solution at 37 °C and 5 % CO_2. Following digestion, cells were isolated following standard protocols[32] and suspended in 4 % [w/v] of charcoal-filtered Protanal LF 10/60 (FMC Biopolymer, Drammen, Norway), a low- viscosity, high-guluronate-content alginate in a pH- and osmotically adjusted buffer solution (pH ~ 7 and 300 mOsm) containing 15 mM N-(2-hydroxyethyl)-piperazine-N'-2-ethanesulfonic acid (HEPES) and 42 mM NaCl at a desired seeding density.

 B. HepG2/C3A and L2 cell isolation and seeding

  HepG2/C3A (human hepatocytes) cells were purchased from the American Type Culture Collection (ATCC). HepG2/C3A cell lines were cultured in Eagle's Modified Essential Medium (MEM) (Invitrogen Co., Carlsbad, California) supplemented with 10 % fetal bovine serum (FBS) (Invitrogen) and 1 mM sodium pyruvate (Sigma-Aldrich), at 37 °C and 5 % CO_2.

  L2 (rat lung epithelial) cells were purchased from the ATCC. L2 cell lines were cultured in 50 % [v/v] Dulbecco's Modified Eagle's Medium and 50 % [v/v] Ham's F-12 medium (DMEM/F-12) (Invitrogen) supplemented with 10 % FBS, at 37 °C and 5 % CO_2.

  Cells were harvested using 0.25 % trypsin / ethylenediaminetetraacetic acid (EDTA) (Invitrogen) and quenched with MEM to re-suspend the cells. Cells were fed every 3-4 days and passed every 6-7 days.

  MEM with a 2 mM GlutaMAX-I supplement (Sigma-Aldrich) or DMEM/F-12 was added to charcoal-filtered Protanal LF 10/60, a low viscosity alginate with a mean

G/M ratio of 70 %, to yield a 4 % [w/v] solution. The alginate solution was allowed to incubate at 37 °C for 12-24 h. The alginate solution was then added to a HepG2/C3A or L2 cell pellet to achieve a desired seeding density. Cells were re-suspended in the alginate by slow stirring with a sterile spatula.

C. Fabrication of microfluidic alginate scaffold

Two jigs were assembled (Fig. 2.3A and Fig. A1.1): one for forming a microstructured slab of calcium alginate (top layer) and one for forming an unstructured slab of gel (bottom layer, with fluidic connections). The acrylic glass slide with tubing provided support to the assembled alginate structure and facilitated fluidic connections between the embedded microfluidic network and the external tubing. The aluminum stencils and acrylic glass slide with tubing were pre-coated with 0.1 % [v/v] poly(ethylenimine) (PEI). The aluminum stencils defined the thickness, size and shape of molded microfluidic scaffold. Each mold had an exit port that allowed evacuation of air from the closed mold during injection.

Once the molding jigs were assembled, cell-seeded alginate was injected with a syringe into the molds. Then, a pH-adjusted buffer solution containing 60 mM $CaCl_2$, 15 mM HEPES, and 52.5 mM NaCl was applied in the upper reservoir of the jigs. Calcium ions penetrated through the porous membrane (Nuclepore track-etched poly(carbonate) membrane, Whatman, Florham Park, NJ) to crosslink the cell-seeded alginate. The injected cell-seeded alginate was allowed to cross-link for 1 h.

Two components of microfluidic scaffold - the flat slab on the slide-tubing assembly and the microstructured slab - were assembled and sealed by mechanical pressure within a cartridge. This cartridge was formed directly from components of the molding jigs. The precision of the interlocking of the jigs ensured alignment of the tubing with the inlets of the microfluidic network. Functionality of microfluidic

34

collagen was examined by delivering fluorescein (MW 376.27 Da) via microchannels (Fig. 2.5A).

D. Live/dead assay for process viability

Cell-seeded microfluidic alginate scaffolds were used to characterize cell viability after the fabrication process. After the cross-linking step, the two layers of the scaffold were submerged in a live/dead staining solution (5 μM calcein-AM-green and 0.5 μM ethidium homodimer-1; Invitrogen) in the pH-adjusted buffer. The submerged layers were allowed to incubate for 1 h at 37 °C and 5 % CO_2. Fluorescence images were acquired using an inverted microscope (Model ECLIPSE TE 2000-S, Nikon Instruments Inc., Melville, NY) and a CCD camera (Model SPOT RT-KE, Diagnostic Instruments Inc., Sterling Heights, MI). ImageJ (http://rsbweb.nih.gov/ij/) enabled the merging of green and red fluorescence images.

E. Delivery of small molecules in cell-seeded microfluidic alginate scaffolds

Microfluidic alginate scaffolds seeded with chondrocytes (1×10^7 cell/mL) were stained with two different stains (5 μM calcein-AM-green and 2 μM calcein-AM-red in the pH-adjusted buffere solution; Invitrogen) via the embedded microchannels (Fig. 2.1D, 2.7). Microfluidic delivery of the staining solutions was carried out for ~ 160 min, and then the pH-adjusted buffer was delivered for 60 min to extract non-enzymatically cleaved (autohydrolyzed) dyes within the scaffold. The flow rate was 50 and 75 μL/min for the single-network and double-network respectively. Fluorescence images were acquired at regular intervals using a stereomicroscope (MZ FLIII, Leica), a CCD (charge-coupled device) camera (Retiga 1300, QImaging), and QCapture Pro 5.1 (QImaging).

F. OSCC-3 cell isolation and seeding

Oral squamous cell carcinoma (OSCC-3) cells (gift from Peter Polverini, University of Michigan) were cultured with DMEM, 10% [v/v] FBS, and 1% [v/v] penicillin/streptomycin (PS; 120 U/mL; Gibco, Grand Island, NY). Cells were harvested using 0.05 % trypsin / EDTA and quenched with DMEM to re-suspend the cells. Cells were fed and passed every 2-3 days.

Phenol red free DMEM was added to lyopholized Protanal LF 20/40 to yield 4 % [w/v] alginate solution. The alginate was allowed to be fully dissolved in an incubator at 37 °C for 12-24 h. The alginate solution was then applied to a OSCC-3 cell pellet. Cells were re-suspended in the alginate by slow stirring with a sterile spatula.

G. Culture of microfluidic alginate scaffolds seeded with OSCC-3s

Microfluidic alginate scaffolds seeded with OSCC-3s were fabricated as described above, using autoclaved, plasma-sterilized, and ethanol-sterilized jig parts. The scaffolds were then cultured in an incubator (37 °C, 17 % O_2, and 5 % CO_2) for desired culture periods (Fig. 2.2). Phenol red free DMEM was delivered to the tumor cell-seeded scaffold via microchannels, using a syringe pump. The media was collected in an outlet reservoir for quantitative measurements of proteins secreted by the seeded cells.
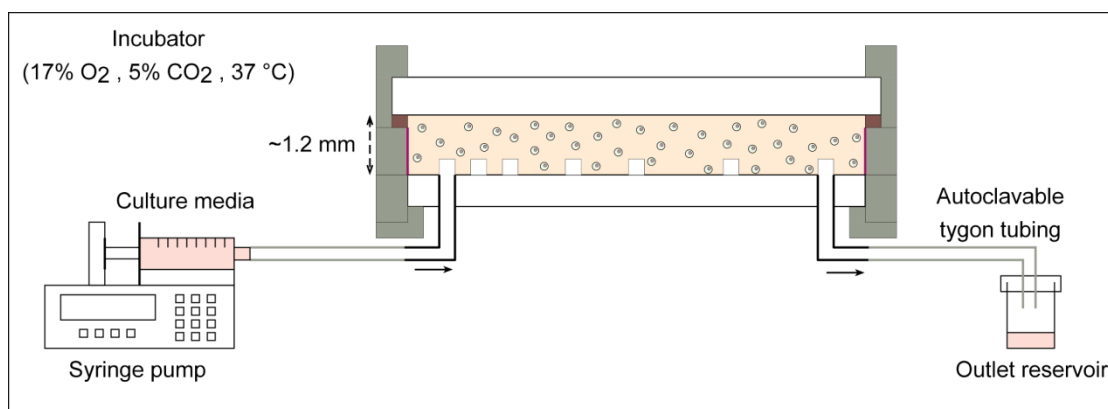
Figure 2.2 Culture of microfluidic alginate scaffolds seeded with OSCC-3s.

Dispersed cells are shown as double circles. Microchannels are shown as squares.

H. Histological analysis

Prior to harvesting, the microfluidic alginate scaffolds seeded with OSCC-3s were incubated with hypoxyprobe (HPI, Inc., Burlington, MA) for 90 min. The hypoxyprobe was delivered via microchannels. Then, the alginate scaffolds were rinsed with a buffer solution and fixed with 3.7% [w/v] formaldehyde (Polysciences, Warrington, PA). Histological cross-sections were then imaged with hematoxylin and eosin (H&E) stain to determine cellularity, and hypoxyprobe stain with mouse IgG_1 anti-pimonidazole MAb (primary antibody) and rabbit anti-mouse conjugated with Alexa Fluor® 488 (secondary antibody) to locate regions of hypoxia. Images were taken on an inverted microscope (Axio Observer; Carl Zeiss, Inc., Thornwood, NY), in bright field.

I. Analysis of angiogenic factor secretion

To quantify soluble VEGF and IL-8 in the collected media, enzyme-linked immunosorbent assay (ELISA; R&D Systems, Minneapolis, MN) was used. The alginate scaffolds were dissolved in 50 mM EDTA, released cells were rinsed, and then lysed in Caron's buffer. DNA content was measured using Quant-iT™ PicoGreen® dsDNA reagent (Invitrogen Co., Carlabad, CA), and cell number calculated using a measured value of 15.1 pg DNA/OSCC-3 cell. Calculated cell numbers were then used to normalize VEGF and IL-8 secretions.

J. Fabrication of microfluidic collagen scaffold

Prior to fabricating microfluidic collagen scaffolds, collagen (1 or 2 % [w/v]) was first prepared by mixing concentrated (2 or 3 % [w/v]) rat-tail collagen dissolved in 0.1 % [v/v] acetic acid with 1 N NaOH (~2% [v/v] of a stock volume, V_s), 10×

BioWhittaker® medium 199 (M199, Lonza, Walkersville, MD; 10 % [v/v] of a final volume, V_f), and an amount of 1× M199.

Microfluidic collagen was fabricated similarly as described above (Fig. 2.3B): 1) uncross-linked rat-tail collagen was injected into a closed mold where a micropatterned PDMS stamp was inserted, and 2) cross-linked collagen with an imprinted microfluidic network was then pressure-sealed against a 1.2 mm-thick glass slide (Ted Pella, Inc., Redding, California). Functionality of microfluidic collagen was examined by delivering green-fluorescent latex microbeads (Fluoresbrite™ Carboxylate YG 1.0 micron Microspheres; Polyscience, Inc., Warrington, Pennsylvania) suspended in phosphate-buffered silane (PBS) (Invitrogen) and rhodamine B isothiocyanate-dextran (RITC-dextran, MW 70 kDa, Sigma-Aldrich) via microchannels (Fig. 2.5B).

K. Endothelial cell isolation

Human umbilical vein endothelial cells (HUVECs) were purchased from Lonza Inc. (Walkersville, MD) and were used in passages 3-10. HUVECs were cultured in M199 (Lonza) containing 20 % [v/v] FBS, 30 µg/mL endothelial cell growth supplement (ECGS, Millipore Co., Billerica, MA), 5 U/mL heparin solution (Invitrogen), 200 mM L-glutamine, and 120 U/mL penicillin/streptomycin (PS). This growth media was changed every 2-3 days.

HUVECs at 75-95 % confluency were washed with PBS or HEPES buffered saline solution, removed from culture flasks with trypsin-EDTA, neutralized with growth media, centrifuged, and re-suspended at ~1×10^6 cell/mL.

L. Endothelialization of microfluidic collagen scaffold

Isolated HUVECs were seeded into microchannels by applying HUVEC-suspended media in the inlet reservoir (Fig. 2.3B). After confirming that endothelial cells were seeded uniformly within microchannels, the outlet reservoir was filled with growth media to balance the height difference between the in- and outlet reservoir. Endothelial cells were then allowed for attachment at 37 °C for ~30 min. Non-attached cells were rinsed away by applying growth media in the inlet reservoir.

HUVEC-attached microfluidic collagen scaffolds were cultured in an incubator (37 °C and 5 % CO_2) for up to 21 days. Growth media was used for 2-3 days and vasculogenesis media (M199 with ECGS, 20 % [v/v] FBS, 1 % [v/v] PS, 1 % [v/v] L-ascorbic acid (50 µg/mL, Acros Organics, Morris Plains, NJ), and 0.16 % [v/v] tetradecanoyl phorbol acetate (TPA, 50 ng/mL, Cell Signaling Technology Inc., Danvers, MA)) for the rest culture period. Media was changed every day.

M. Confocal imaging

Confocal microscopy (LSM 700, Carl Zeiss Inc., Thornwood, NY) was used to obtain z-stacks of endothelia formed in collagen microchannels. After fixing cells with 3.7 % [w/v] formaldehyde *in situ*, endothelial cell nuclei were stained with either YOYO®-1 iodide or 4', 6-diamidino-2-phenylindole, dilactate (DAPI, dilactate), and actin stained with Alexa Fluor® either 568 or 488 phalloidin (Invitrogen). Images were viewed and analyzed with ImageJ and LSM Image Browser (www.zeiss.com).

N. Morphometric analysis of endothelial cells

For endothelia formed on various substrates, cell density was calculated by counting cell nuclei with the cell counter plug-in embedded in ImageJ. In order to assess the extent of elongation, cell shape index ($CSI \equiv 4\pi A_{cell} / P_{cell}^2$) was calculated

by estimating cell area (A_{cell}) and perimeter (P_{cell}) in ImageJ. CSI varies from 0 (a straight line) to 1 (a perfect circle).

O. Statistical analysis

Plots represent mean±standard deviations (SD). Analysis of variance (ANOVA) with Tukey post-test was used for statistical analysis (GraphPad Prism, La Jolla, CA) and significance denoted as $*P<0.05$; $**P<0.01$; $***P<0.001$.

Results and discussion

A. Choice of biomaterials

In the formation of a microfluidic scaffold, the host material must satisfy constraints imposed by the need to form both an appropriate cellular environment and a functional microfluidic structure. Specific constraints on the material include: (1) biocompatibility, (2) mechanical stability to enable replication of microstructure and definition of discrete convective paths, (3) high diffusive permeability to small and large molecules, and (4) processability under physiological conditions (for example, pH, temperature, osmolarity and mechanical stress).

Our work[9,20,32-36] and that of others[37] point to calcium alginate hydrogels as a promising candidate material for this application. Studies of calcium alginate as a tissue scaffold have shown that it is appropriate for long-term culture and formation of functional tissue[9,34], compatible with macroscale molding to form cell-seeded structures with physiological geometries[35,38] and chemically modifiable to enable the presentation of biospecific extracellular ligands[36-37]. Our recent work demonstrated that laminated alginate hydrogels, the format used here to fabricate microfluidic structures, had shear moduli (3-25 kPa) that were similar to those reported for monolithic alginate hydrogels[39-40] and supported long-term (10 weeks) culture of

primary chondrocytes with deposition of an ECM[32]. We have also shown that calcium alginate gels are compatible with fabrication of functional, acellular microfluidic systems[20].

In addition to calcium alginate hydrogels, collagen is another good host material for the study of dynamic cellular processes due to its specificity for extracellular adhesion and remodelability by a large number of tissue cells, including endothelial cells (ECs) and tumor cells. Collagen gels are generally more difficult to handle and to form functional microfluidic structures compared with calcium alginate due to their low elastic modulus (0.04-2 kPa; 0.3-2 % [w/v]). However, we have made progress towards overcoming these challenges with processing higher mass fraction up to 2 % [w/v]. Collagen-based microfluidic scaffolds can be valuable tools for studies of vasculogenesis, angiogenesis, and organogenesis of lymph node (LN), all of which involve cellular remodeling of ECM. We can also endothelialize pre-defined microchannels in microfluidic collagen scaffolds with ECs, which is an essential step towards developing perfusable microvascular structure in parallel with tissue cells growing in the bulk of the scaffolds. In the following, we will further demonstrate that fabrication can be carried out with living cells present.

B. *Fabrication of microfluidic biomaterials*

Figure 2.3A shows a lithographic process that enables the incorporation of living cells within a microfluidic scaffold formed in 4 % [w/v] calcium alginate. The key steps in the process are (see Materials and methods section and Appendix 1 for details): (1) definition via soft lithography of a silicone stamp as a master on which to mold a hydrogel with microstructure, (2) injection and crosslinking of cell-seeded alginate within aluminum molding jigs (Fig. A1.1) and 3) sealing of hydrogel layers to form a sealed fluidic structure with application of pressure within an aluminum jig.

The aluminum jig was used to create an enclosed scaffold within which the exchange of solutes is mediated entirely by the flow of solutions through the microchannels embedded within 4 % [w/v] calcium alginate (Fig. 2.4A) , and to simplify the sealing process relative to the formation of a chemical seal, as in our previous work[20,32]. We note that chemical sealing can be also used in the current process and that the main points of this article are still valid with either method. Sealed microfluidic alginate scaffolds seeded with cells maintained functionality and sterility in an incubator for up to 1 week (data not shown).

We have also successfully fabricated single-layered microfluidic collagen in a similar way (Fig. 2.3B). The glutaraldehyde-coated plexiglass jig provided enough mechanical support such that functional fluidic networks formed with 1 % [w/v] collagen (lower limit) as shown in Fig. 2.4B and C. We note that the fabrication of microfluidic collagen with higher concentrations up to 3 % [w/v] was indeed achievable and that microfluidic 0.6 % [w/v] collagen failed sustaining pressure-driven flows ($\sim$ 1 µL/min) mainly due to the low modulus of the gel ($<$ 200 Pa) even though microstructure was successfully molded (data not shown). All other microfluidic biomaterials made with $>$ 1 % [w/v] collagen sustained pressure-driven flows (1-10 µL/min). Microfluidic collagen scaffolds can be used as templates for microvascular endothelialization to investigate remodeling dynamics of ECs such as tube formation, vasculogenesis, and (tumor) angiogenesis in a more controlled manner. As shown in Fig. 2.3B, we endothelialize the pre-defined microchannels by delivering EC-suspended media via the channels. A cell density of $\sim 1 \times 10^6$ cell/mL and gravity-driven flows by applying 100-200 µL of the cell suspension in the inlet allowed for relatively uniform initial seeding. Too high cell densities can cause clogging, and too high pressures to resolve the clogging is highly likely to burst devices and may deform collagen permanently. In addition, too large volumes of EC suspension can cause an

unnecessarily large number of cells left in external reservoirs which will eventually proliferate and deprive endothelialized cells in microchannels of nutrients.

As shown in Fig. 2.5, microfluidic biomaterials are compatible with the replication of 100-µm-scale microchannels. As shown in Fig. 2.6, we achieve high cellular viabilities with mild stirring and injection. We have observed similarly high viabilities for HepG2/C3A and L2 cell lines passed through the fabrication of microfluidic alginate scaffolds; these other cell types were used to demonstrate the versatility of this technique.

C. *Effect of shear imposed during the seeding and injection step on cell viability*

We found that the degree of viability of chondrocytes after fabrication was sensitive to the magnitude of shear imposed during the dispersal and injection of the cells in the alginate solution. After isolation, cells were pelleted in a centrifuge tube (50 mL). A 4 % [w/v] alginate solution was poured onto the pellet and the cells were mildly re-suspended using a spatula (30 rpm for ~ 1 min). The cell-seeded 4 % [w/v] alginate solution was taken into a syringe (5 mL) and injected through 3 cm of tygon tubing into the molding jigs at ~ 150 µL/min. It was observed that the standard method employed for injection molding chondrocytes in lower concentration alginate[32] led to significant loss in viability when used in 4 % [w/v] alginate solution. We believe that this difference is due to increased viscosity of 4 % [w/v] alginate solution.
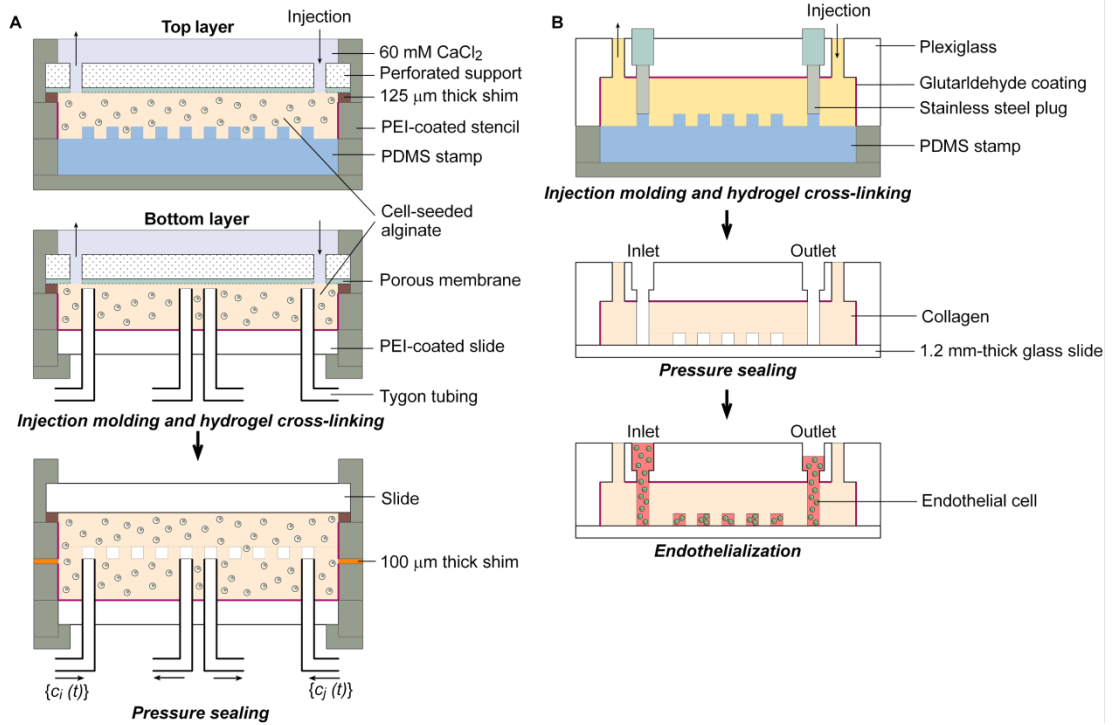
Figure 2.3 Fabrication of microfluidic biomaterials. **A.** Schematic diagram of the fabrication of microfluidic alginate scaffolds. $c_i(t)$ and $c_j(t)$ denote instantaneous concentration of solutes i and j respectively in injected solutions. The red line indicates PEI coating. **B.** Schematic diagram of the fabrication of microfluidic collagen scaffolds and endothelialization. The red line indicates glutaraldehyde coating.
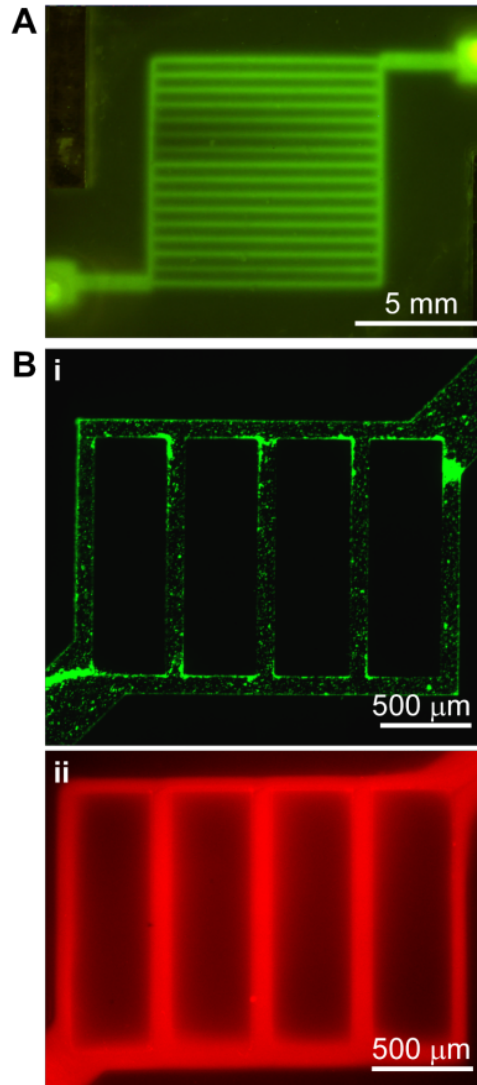
Figure 2.4 Functionality of microfluidic biomaterials. A. Fluorescence micrograph of a microfluidic alginate scaffold at an early time point during delivery of fluorescein to the scaffold via embedded microchannels. **B.** Fluorescence micrograph of microfluidic collagen scaffolds at early time points during delivery of green-fluorescent latex microbeads (i) and rhodamine B (ii) via microchannels.
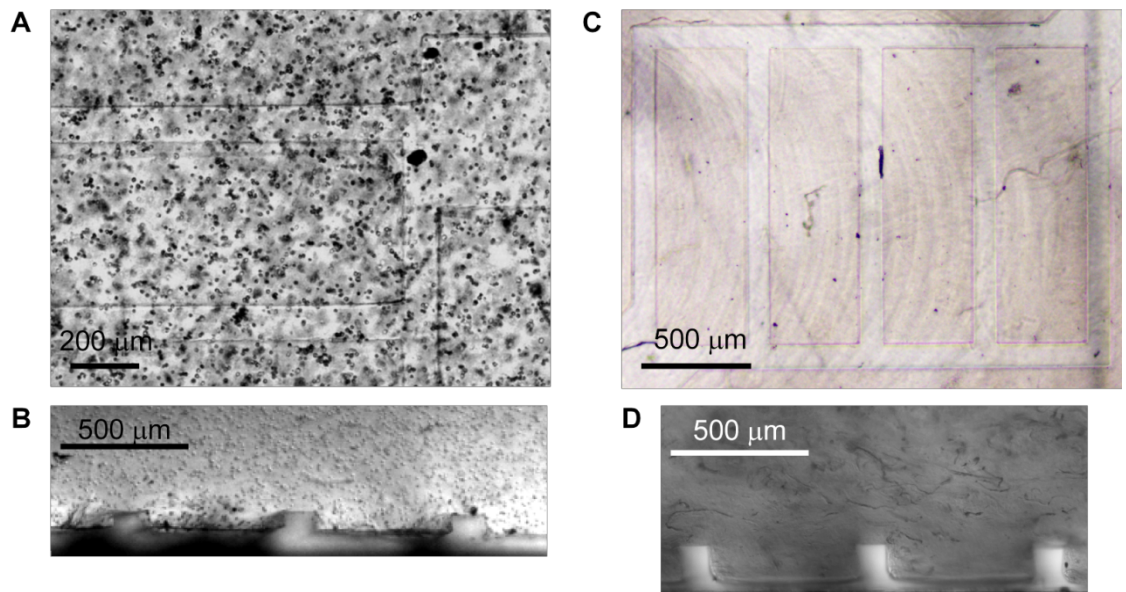
Figure 2.5 Fidelity of microstructure. A and B. Optical micrographs showing microstructure of 4 % [w/v] calcium alginate seeded with primary chondrocytes (1×10^7 cell/mL). **C and D.** Optical micrographs showing microstructure of 1 (C) and 3 (D) % [w/v] collagen.
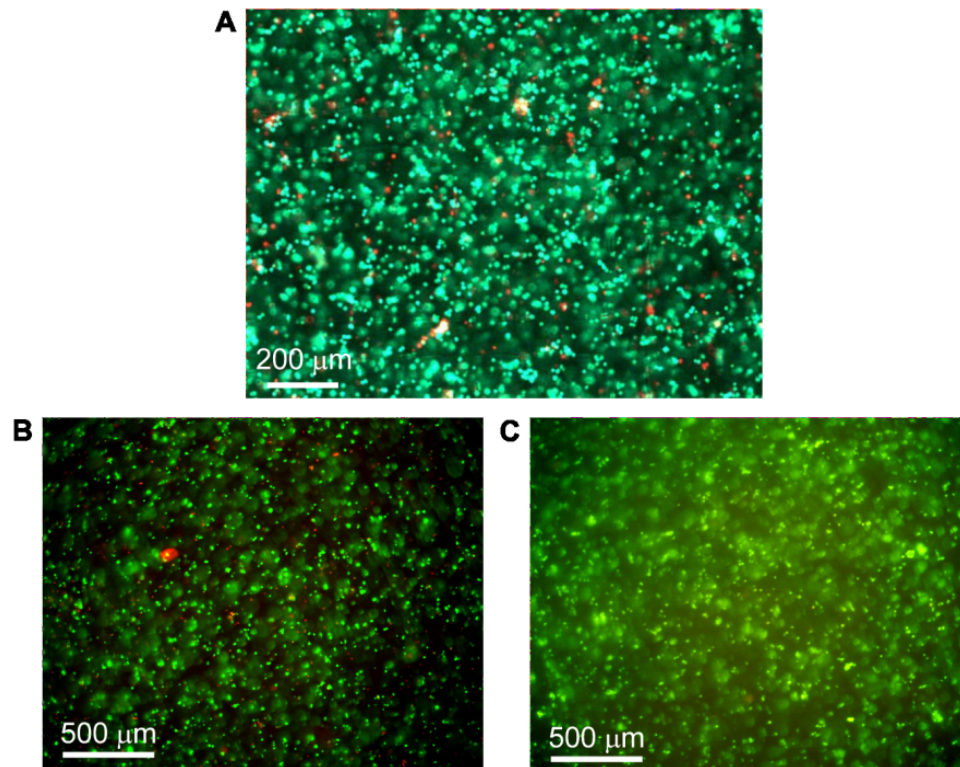
Figure 2.6 Process viability of cell-seeded microfluidic alginate scaffolds.

Fluorescence micrograph showing cells stained by 5 μM calcein-AM (green – live) and 0.5 μM ethidium homodimer-1 (red – dead). **A.** Chondrocytes (corresponding to Fig. 2.5A). **B.** HepG2 cells (2×10^6 cell/mL). **C.** L2 cells (1×10^6 cell/mL).

D. Microfluidic alginate scaffolds for tissue engineering

One of major challenges and key aspects in culturing engineered tissue constructs is to maintain a uniform metabolic environment within the bulk. Figure 2.7A qualitatively demonstrates that we can achieve this condition with appropriately chosen design parameters such as cell seeding density, interchannel distance, and scaffold thickness for a microfluidic biomaterial. More detailed discussion about metabolic activity of cells (chondrocytes in this case) seeded in microfluidic alginate scaffolds is described in the following chapter.

The incorporation of more than one independent network within a microfluidic scaffold enables the maintenance of steady-state gradients in the concentration of solutes within the matrix (Fig. 2.1B). Each network can serve as a source for certain solutes and as a sink for others such that gradients can be maintained at steady-state. Figure 2.7B shows the generation of gradients in a microfluidic scaffold with two independent networks (as in Fig. 2.1Dii) for reactive solutes. The images were captured after several hours such that transient gradients had ample time to dissipate: the observed variations are features of the steady-state distributions of the solutes. This capability to form steady-state gradients in 3-D cultures will enable the study of cellular responses to physiologically relevant spatial variations of soluble factors.
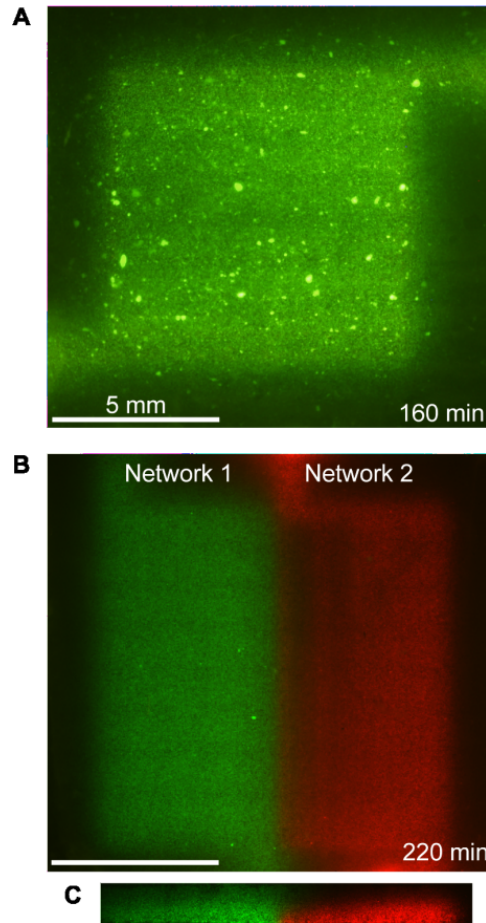
Figure 2.7 Steady-state distributions of solutes delivered to microfluidic alginate scaffolds via embedded microchannels. **A.** Fluorescence micrograph of uniformly stained primary chondrocytes (1×10^7 cell/mL) by 5 µM calcein-AM delivered via the embedded microchannels. The image in A was taken after 160 min of delivery. **B.** Fluorescence micrograph of chondrocyte-seeded (1×10^7 cell/mL) microfluidic scaffold after delivery of calcein-AM-green (5 µM; network 1) and calcein-AM-red (2 µM; network 2). **C.** Fluorescence micrograph of a cross-section of the top (micropatterned) layer (1×10^7 cell/mL) of the scaffold in C. The images in B and C were taken after 220 min of delivery in both networks.

50

E. Microfluidic alginate scaffolds for tissue-scale tumor biology

Tumors consist of spatially and functionally distinct niches which may result from spatiotemporal variation in oxygen concentration within tissues of growing tumors. Oxygen, and specifically lack thereof, or hypoxia, is a key factor regulating tumor angiogenesis[4,41]. Hypoxic tumor cells up-regulate factors that promote angiogenesis, such as vascular endothelial growth factor (VEGF)[42]. Microfluidic alginate scaffolds also enable tissue-scale biology, specifically a study of angiogenic activity of tumor cells in 3-D scaffolds, by recapitulating *in vivo*-like environments. Key steps include 1) control of cellular 3-D microenvironment, 2) capability to perform long-term cultures with maintaining sterility and functionality of a microfluidic scaffold, and 3) analytical access to soluble biochemical environment in a spatiotemporally resolved manner. This approach also accompanies histological analyses and an analysis of angiogenic factor secretion as shown in Fig. 2.8. Figure 2.8A and B shows that a single-layered microfluidic alginate scaffold seeded with tumor cells maintain cellularity and high viability over 2 days. Figure 2.8C demonstrates that there are more tumor cells exposed to hypoxia (< 1 % O_2) at regions far from microchannels. This is an example of a solid tumor *in vivo* where its periphery is well oxygenated but core oxygen-depleted, which is believed to induce tumor angiogenesis by secreting soluble factors such as VEGF and IL-8. Figure 2.8D shows that the embedded microchannels can be used not only as pathways to deliver media but also as 'taps' to access biochemical environments and quantitatively measure angiogenic activity of tumor cells seeded in the bulk. We note that we have also utilized the double-network to create two zones of distinct oxygen concentration (i.e., normoxia in network 1 and hypoxia in network 2) and cultured the scaffold for 6 days (data not shown). With these tools, more valuable future studies need to aim understanding details of angeogenic signaling of tumor cells in 3-D for example, by

integratively monitoring and controlling oxygen concentration, and measuring angiogenic activity within scaffolds in a spatiotemporally resolved manner. This motivates 1) quantitative analyses of metabolic activity (e.g., oxygen consumption rate; Chapter 3), 2) the development of an oxygen-sensing system (Chapter 4) and 3) remodelable microfluidic biomaterials towards investigating direct tumor angiogenesis in tissue-scale. In the following, we will demonstrate microfluidic collagen scaffolds as a platform for remodelable microfluidic biomaterials.
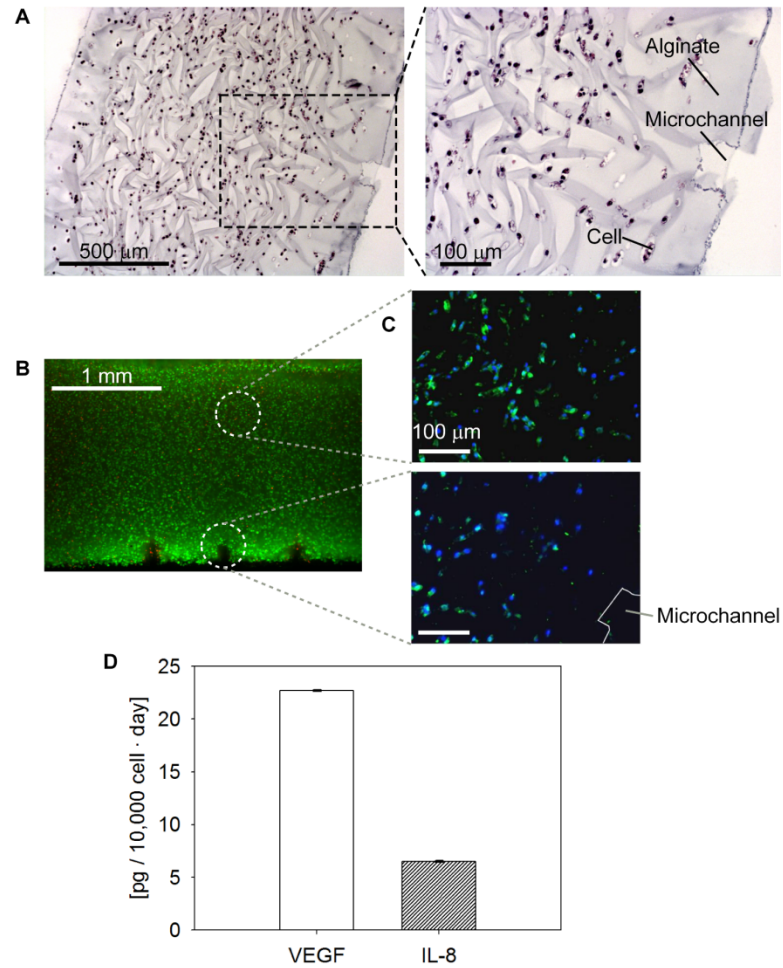
Figure 2.8 Microfluidic alginate scaffold for tissue-scale tumor biology. A.
Optical micrographs of a histological cross-section of a microfluidic alginate scaffold
seeded with OSCC-3s (2×10^7 cell/mL) stained by H&E after 2 day-microfluidic
culture. **B.** Fluorescence micrograph of a cross-section of the scaffold showing cells
stained by 5 μM calcein-AM (green – live) and 5 μM ethidium homodimer-1 (red –
dead) after the culture. **C.** Fluorescence micrographs of a histological cross-section of
the scaffold stained by DAPI (blue - cell nuclei) and hypoxyprobe (green - hypoxic
cells) after the culture. **D.** Plot of cell-secreted pro-angiogenic factors (i.e., VEGF and
IL-8) measured by ELISA after the culture.

Microfluidic 1 and 2 % [w/v] collagen scaffolds were cultured with 1) growth media for first 2-3 days to allow for cell proliferation, and 2) vasculogenesis media for the rest of culture periods to promote EC invasion into the bulk of the gels. The microfluidic collagen scaffolds were operated with gravity-driven flows by applying different volumes of media in the in- and outlet reservoirs on a daily basis. We have observed that the gravity-driven flows reached an equilibrium state (i.e., no persistent flows in microchannels) in ~ 5 hr. Therefore, it is fair to state that ECs were exposed to modulating flow rates over the culture periods. Initial flow speed within microchannels by this gravity-driven pump ranged from 1.3 ~ 4.4 mm/s corresponding to 0.78 ~2.6 µL/min with an assumption that the cross-sectional area of a microchannel was 10^4 µm^2 (100 µm × 100 µm). The flow speed was estimated by delivering fluorescent latex microbeads.

With the given flow conditions, sealed microfluidic collagen seeded with ECs in microchannels maintained functionality and sterility and allowed for the formation of complete endothelia for at least 3 weeks (Fig. 2.9 and 2.10). We found that initially seeded ECs attached and proliferated well on 2 % [w/v] collagen in 3 days (Fig. 2.9A) such that ECs spread out and formed a monolayer on three walls of collagen microchannels (Fig. 2.7B). In 23 days, ECs formed a complete endothelium along microchannels (i.e., 3 collagen sides and 1 plexiglass side). Figure 2.9C and D show lots of stained ECs on the collagen and a plexiglass side respectively. We note that the endothelium was partially ripped off for better qualities of confocal microscopy. Therefore, some regions where there are no stained cells do not imply that the microfluidic endothelium was imperfect in the specific locations. An endothelilum was formed in microchannels in 23 days, but there was no obvious EC invasion over the 21 day-culture of endothelialized microfluidic 2 % [w/v] collagen with

vasculogenesis media. However, we observed that there were many short protrusions from ECs at the interface between endothelialized microchannels and the bulk of the collagen. We believe that these protrusions may be anchors to initiate invasion. This behavior is slower than what we have observed in our vertical invasion assays (ECs on top of flat collagen) where ECs start invading into 2 % [w/v] collagen in 21 days. Although we fixed and stained ECs without disassembling the device, it was necessary to remove the plexiglass side for confocal microscopy with high magnification and to achieve detailed cellular information. We have resolved this issue by slightly modifying the jig such that the confocal microscopy can be done without the disassembly in the following case of endothelialized microfluidic 1 % [w/v] collagen (Fig. 2.10): the collagen network was sealed against a 1.2 mm-thick glass slide (Fig. 2.3B).

A complete endothelium on both collagen (Fig. 2.10Ai) and glass side (Fig. 2.10Aii) was also formed in microfluidic 1 % [w/v] collagen in 14 days (growth media for 3 days and vaculogenesis media for 11 days), yet no obvious invasion was found. It was observed that ECs started invading into flat 1 % [w/v] collagen in 14 days. The interchannel connection seen in Fig. 2.10Aii is likely due to cell migration through the collagen-glass slide interface (dashed circles in Fig. 2.10Bii). We confirmed that the device was still well-sealed by delivering fluorescent latex microbeads. In 21 days, we observed that invading ECs formed lumens into the bulk of 1 % [w/v] collagen near the inlet and that there were invasion marks in the network region (data not shown). We speculate that differences in culture conditions within endothelialized microfluidic collagen may have delayed cellular invasion dynamics, for instance, initial seeding density, growth factor and nutrient supply due to flow conditions, and geometric confinement. In the following section, we will present our effort to look for

some clues by analyzing cell density and morphology in the endothelialized microfluidic collagen.

G. *Morphometric analyses of ECs*

We have analyzed morphology of ECs on a monolayer by estimating cell density and cell shape index (CSI) on PDMS, flat 1 and 2 % [w/v] collagen, and microfluidic 1 and 2 % [w/v] collagen. Figure 2.11B shows that EC density on PDMS is significantly higher than all other cases and that cell densities on collagen are not significantly different except for the two cases between ECs on flat 2 % [w/v] collagen and those on microfluidic 2 % [w/v] collagen. We note that the latter significant difference is due to cell loss during the disassembly process for the confocal microscopy. Because PDMS is a relatively rigid material (from cells' point of view) and does not allow cellular remodeling at all, initially seeded ECs are likely to keep spreading and proliferating on PDMS. Figure 2.11A qualitatively shows that ECs on PDMS have larger cell area (red; actin) compared with cells on 1 and 2 % [w/v] collagen. This also suggests that PDMS is a very adhesive substrate on which cell adhesion and proliferation can be enhanced. We argue that one should be careful when comparing cell density because cell density on a monolayer at a certain time point is dependent on initial seeding density. Initial seeding density of ECs on PDMS might have been higher than other cases. We also note that it is technically challenging to precisely control seeding density in microfluidic collagen. Seeding ECs in microchannels with a syringe pump that would allow for more controlled and steady flows may help address this challenge.

CSI is defined as $4\pi A_{\text{cell}} / P_{\text{cell}}^2$, where A_{cell} is cell area and P_{cell} is cell perimeter. CSI varies from 0 (a perfect circle) to 1 (a straight line). The estimation of CSI is a way to assess whether cells are elongated. Figure 2.12 shows ECs in endothelialized

56

microfluidic collagen were significantly more elongated compared with cells on flat collagen as well as PDMS. We have also found that CSI values at various locations (100 µm-wide and -high microchannels, and 400 µm-wide and 100µm-high in- and outlet regions) within a microfluidic collagen scaffold were not significantly different (data not shown). This suggests that the morphology of ECs in microchannels were influenced by geometric confinement and flow conditions, or a combinatorial effect of the two. For future studies, therefore, it is necessary to culture microfluidic collagen scaffolds with a syringe pump that allows for persistent flow conditions. This will help identify significant factors affecting cell morphology and invasion. Furthermore, an additional morphometric analysis that allows assessing the alignment of ECs in microchannels along flow directions is required for further studies. These morphometric analyses of ECs suggest that invasions in the endothelialized microfluidic collagen might have been delayed due to periods of time over which morphological changes occurred.
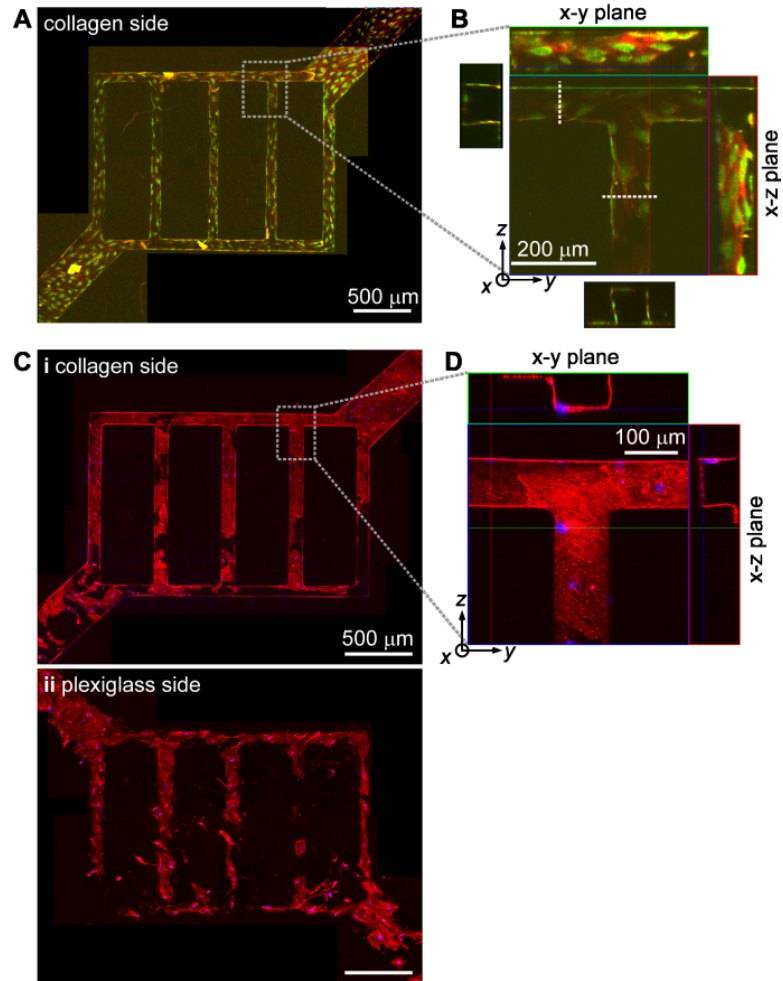
Figure 2.9 Endothelialized microfluidic 2 % [w/v] collagen. A. Confocal fluorescence micrograph showing endothelial cells on collagen side stained by YOYO (green - cell nuclei) and phalloidin (red - actin) on day 3. **B and D.** Confocal fluorescence micrograph showing endothelialized microchannel walls from *x*-stacks. **C.** Confocal fluorescence micrographs showing endothelial cells on collagen side (i) and plexiglass side (ii) stained by DAPI (blue - cell nuclei) and phalloidin (red - actin) on day 23.
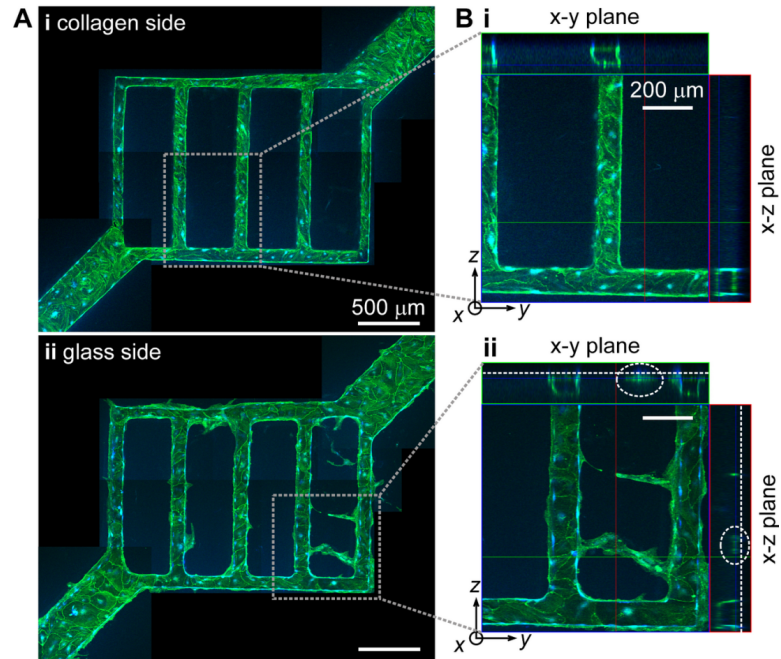
Figure 2.10 Endothelialized microfluidic 1 % [w/v] collagen. A. Confocal fluorescence micrographs showing endothelial cells on collagen side (i) and glass side (ii) stained by DAPI (blue - cell nuclei) and phalloidin (green - actin) on day 14. **B.** Confocal fluorescence micrograph showing endothelialized microchannel walls from *x*-stacks.
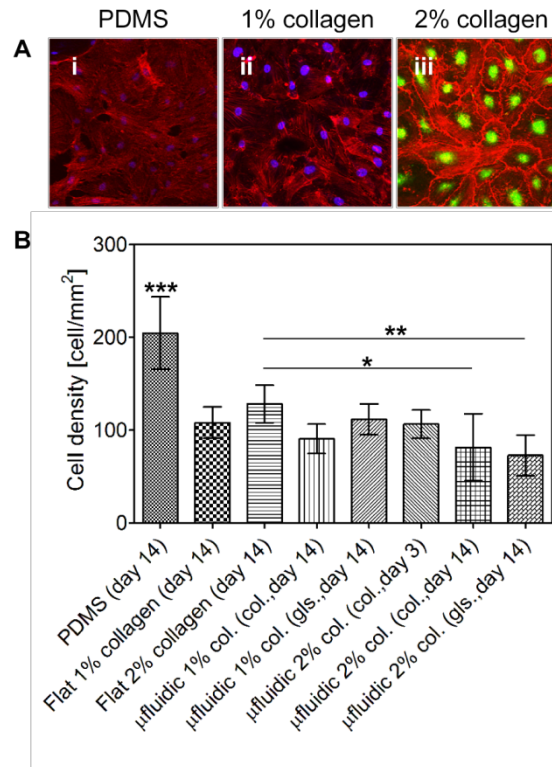
Figure 2.11 Endothelial cells on various substrates. A. Fluorescence micrographs showing endothelial cells on PDMS (i), 1 % [w/v] collagen (ii) stained by DAPI (blue - cell nuclei) and phalloidin (red - actin), and 2 % [w/v] collagen (iii) stained by YOYO (green - cell nuclei) and phalloidin (red - actin) on day 14. **B.** Plot of endothelial cell density on various substrates. (*P<0.05; **P<0.01; ***P<0.001).
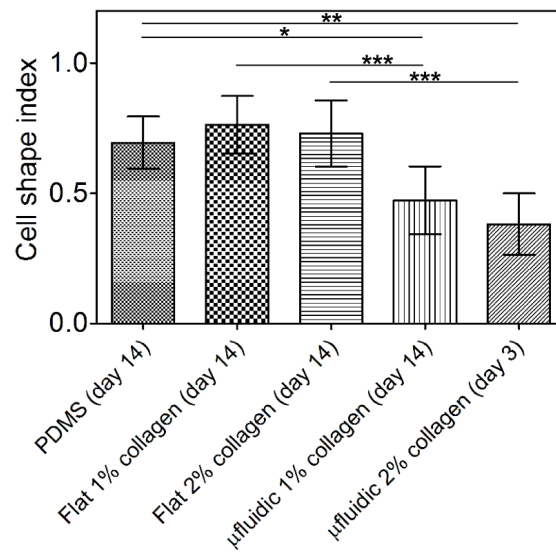
Figure 2.12 Morphometric analysis of endothelial cells. Plot of cell shape index (CSI) for endothelial cells on various substrates. (*P<0.05; **P<0.01; ***P<0.001).

Conclusions

We have demonstrated direct fabrication of a functional microfluidic structure within 3-D scaffolds of 1) calcium alginate seeded with multiple cell types and 2) collagen with ECs. Embedded microchannels in microfluidic alginate scaffolds enable the maintenance of a uniform metabolic environment within the bulk of the scaffold and the creation of distinct soluble environments experienced by cells in their 3-D environment. Microfluidic alginate scaffolds represent a new format for the design of cellular bioreactors[43], bio-artificial organs[44-45]. Important characteristics of microfluidic scaffolds as a bioreactor include: (1) dispersion of cells within biocompatible, biodegradable, and biochemically tunable ECM[9,32,46], (2) scalability to sub-millimetre dimensions, and (3) lithographic definition of fluid paths to enable precise control of distributions and fluxes of solutes. Remaining challenges for this technique include: (1) generalization of network structures to 3-D, (2) incorporation of multiple cell types in physiologically relevant geometries and (3) integration of distinct stimuli such as mechanical forces[47] and patterns of extracellular chemistry[48]. 3-D printing with cell-seeded calcium alginate[49] and writing techniques[50] could be important tools to form microfluidic scaffolds. The development of the technique presented here opens new opportunities to study the response of cells to spatial and temporal variations of soluble factors within well-defined 3-D cultures. In the context of tissue engineering, this tool may aid in growing thick sections of tissue without necrosis in the core, and in directing the development of cells, towards, for example, spatially differentiated tissues.

Pre-defined microchannels in microfluidic collagen scaffolds serve as templates for microvascular endothelialization and allow for the formation of complete endothelia. These microfluidic collagen scaffolds can be also a valuable format for studies of vasculogenesis, (tumor) angiogenesis, and organogenesis of

lymph node in 3-D not only because both chemical and mechanical microenvironment can controlled but also because cells can remodel their 3-D environment. The development of such remodelable microfluidic scaffolds could also allow finding mechanistic clues for the stabilization of microvasculature, for example, by seeding pericytes in the bulk.

REFERENCES

1.   Fischbach, C. *et al.*, Engineering tumors with 3D scaffolds. *Nature Methods* **4**, 855-860 (2007).

2.   Pampaloni, F. *et al.*, The third dimension bridges the gap between cell culture and live tissue. *Nature Rev. Mol. Cell Biol.* **8** (10), 839-845 (2007).

3.   Yamada, K.M. & Cukierman, E., Modeling tissue morphogenesis and cancer in 3D. *Cell* **130** (4), 601-610 (2007).

4.   Carmeliet, P. & Jain, R.K., Angiogenesis in cancer and other diseases. *Nature* **407** (6801), 249-257 (2000).

5.   Kamei, M. *et al.*, Endothelial tubes assemble from intracellular vacuoles *in vivo*. *Nature* **442**, 453-456 (2006).

6.   Viravaidya, K. *et al.*, Development of a microscale cell culture analog to probe naphthalene toxicity. *Biotechnol. Progr.* **20** (1), 316-323 (2004).

7.   Langer, R. & Vacanti, J.P., Tissue Engineering. *Science* **260** (5110), 920-926 (1993).

8.   Cao, Y.L. *et al.*, Transplantation of chondrocytes utilizing a polymer-cell construct to produce tissue-engineered cartilage in the shape of a human ear. *Plast. Reconstr. Surg.* **100** (2), 297-302 (1997).

9.   Chang, S.C.N. *et al.*, Tissue engineering of autologous cartilage for craniofacial reconstruction by injection molding. *Plast. Reconstr. Surg.* **112** (3), 793-799 (2003).

10.   Fittkau, M.H. *et al.*, The selective modulation of endothelial cell mobility on RGD peptide containing surfaces by YIGSR peptides. *Biomaterials* **26** (2), 167-174 (2005).

11. Urech, L. *et al.*, Mechanical properties, proteolytic degradability and biological modifications affect angiogenic process extension into native and modified fibrin matrices in vitro. *Biomaterials* **26** (12), 1369-1379 (2005).

12. Freed, L.E. *et al.*, Advanced tools for tissue engineering: Scaffolds, bioreactors, and signaling. *Tissue Eng.* **12** (12), 3285-3305 (2006).

13. Pazzano, D. *et al.*, Comparison of chondrogensis in static and perfused bioreactor culture. *Biotechnol. Progr.* **16** (5), 893-896 (2000).

14. Powers, M.J. *et al.*, A microfabricated array bioreactor for perfused 3D liver culture. *Biotechnol. Bioeng.* **78** (3), 257-269 (2002).

15. Albrecht, D.R. *et al.*, Probing the role of multicellular organization in three-dimensional microenvironments. *Nat. Methods* **3** (5), 369-375 (2006).

16. Tang, M.D. *et al.*, Fabrication of collagen gels that contain patterned, micrometer-scale cavities. *Adv. Mater.* **16** (15), 1345-1348 (2004).

17. Sivaraman, A. *et al.*, A microscale in vitro physiological model of the liver: Predictive screens for drug metabolism and enzyme induction. *Curr. Drug. Metab.* **6** (6), 569-591 (2005).

18. Chrobak, K.M. *et al.*, Formation of perfused, functional microvascular tubes in vitro. *Microvasc. Res.* **71** (3), 185-196 (2006).

19. Fidkowski, C. *et al.*, Endothelialized microvasculature based on a biodegradable elastomer. *Tissue Eng.* **11** (1-2), 302-309 (2005).

20. Cabodi, M. *et al.*, A microfluidic biomaterial. *J. Am. Chem. Soc.* **127** (40), 13788-13789 (2005).

21. Golden, A.P. & Tien, J., Fabrication of microfluidic hydrogels using molded gelatin as a sacrificial element. *Lab Chip* **7**, 720-725 (2007).

22. Ling, Y. *et al.*, A cell-laden microfluidic hydrogel. *Lab Chip* **7**, 756-762 (2007).

23.   Diao, J.P. *et al.*, A three-channel microfluidic device for generating static linear gradients and its application to the quantitative analysis of bacterial chemotaxis. *Lab Chip* **6** (3), 381-388 (2006).

24.   Rosoff, W.J. *et al.*, A new chemotaxis assay shows the extreme sensitivity of axons to molecular gradients. *Nat. Neurosci.* **7** (6), 678-682 (2004).

25.   Dertinger, S.K.W. *et al.*, Gradients of substrate-bound laminin orient axonal specification of neurons. *P. Natl. Acad. Sci. USA*. **99** (20), 12542-12547 (2002).

26.   Tuli, R. *et al.*, Human mesenchymal progenitor cell-based tissue engineering of a single-unit osteochondral construct. *Tissue Eng.* **10** (7-8), 1169-1179 (2004).

27.   Rahaman, M.N. & Mao, J.J., Stem cell-based composite tissue constructs for regenerative medicine. *Biotechnol. Bioeng.* **91** (3), 261-284 (2005).

28.   Fischbach, C. *et al.*, Engineering tumors with 3D scaffolds. *Nat. Methods* **4** (10), 855-860 (2007).

29.   Fischbach, C. *et al.*, Cancer cell angiogenic capability is regulated by 3D culture and integrin engagement. *Proc. Natl. Acad. Sci. U. S. A.* **106** (2), 399-404 (2009).

30.   Carmeliet, P., Mechanisms of angiogenesis and arteriogenesis. *Nat. Med.* **6** (4), 389-395 (2000).

31.   Bissell, M.J. & Radisky, D., Putting tumours in context. *Nat. Rev. Cancer* **1** (1), 46-54 (2001).

32.   Lee, C.S.D. *et al.*, Integration of layered chondrocyte-seeded alginate hydrogel scaffolds. *Biomaterials* **28**, 2978-2993 (2007).

33.   Gleghorn, J.P. *et al.*, Adhesive properties of laminated alginate gels for tissue engineering of layered structures. *J. Biomed. Mater. Res.* DOI: 10.1002/jbm.a.31565 (2007).

34.   Mizuno, H. *et al.*, Biomechanical and biochemical characterization of composite tissue-engineered intervertebral discs. *Biomaterials* **27** (3), 362-370 (2006).

35.   Ballyns, J.J. *et al.*, CT-guided injection molding of tissue engineered meniscus. *Tans. Orthop. Res. Soc.* **30**, 292 (2005).

36.   Genes, N.G. *et al.*, Effect of substrate mechanics on chondrocyte adhesion to modified alginate surfaces. *Arch. Biochem. Biophys.* **422** (2), 161-167 (2004).

37.   Rowley, J.A. *et al.*, Alginate hydrogels as synthetic extracellular matrix materials. *Biomaterials* **20** (1), 45-53 (1999).

38.   Chang, S.C.N. *et al.*, Injection molding of chondrocyte/alginate constructs in the shape of facial implants. *J. Biomed. Mater. Res.* **55** (4), 503-511 (2001).

39.   Lee, K.Y. *et al.*, Degradation behavior of covalently cross-linked poly(aldehyde guluronate) hydrogels. *Macromolecules* **33** (1), 97-101 (2000).

40.   LeRoux, M.A. *et al.*, Compressive and shear properties of alginate gel: Effects of sodium ions and alginate concentration. *J. Biomed. Mater. Res.* **47** (1), 46-53 (1999).

41.   Harris, A.L., Hypoxia - A key regulatory factor in tumour growth. *Nat. Rev. Cancer* **2** (1), 38-47 (2002).

42.   Kerbel, R.S., Molecular origins of cancer: Tumor angiogenesis. *N. Engl. J. Med.* **358** (19), 2039-2049 (2008).

43.   Martin, I. *et al.*, The role of bioreactors in tissue engineering. *Trends Biotechnol.* **22** (2), 80-86 (2004).

44.   Colton, C.K., Engineering challenges in cell-encapsulation technology. *Trends Biotechnol.* **14** (5), 158-162 (1996).

45.   Griffith, L.G. & Swartz, M.A., Capturing complex 3D tissue physiology in vitro. *Nat. Rev. Mol. Cell Bio.* **7** (3), 211-224 (2006).

46. Augst, A.D. *et al.*, Alginate hydrogels as biomaterials. *Macromol. Biosci.* **6** (8), 623-633 (2006).

47. Mauck, R.L. *et al.*, The role of cell seeding density and nutrient supply for articular cartilage tissue engineering with deformational loading. *Osteoarth. Cartilage* **11** (12), 879-890 (2003).

48. Hahn, M.S. *et al.*, Three-dimensional biochemical and biomechanical patterning of hydrogels for guiding cell behavior. *Adv. Mater.* **18** (20), 2679-2684 (2006).

49. Cohen, D.L. *et al.*, Direct freeform fabrication of seeded hydrogels in arbitrary geometries. *Tissue Eng.* **12** (5), 1325-1335 (2006).

50. Therriault, D. *et al.*, Chaotic mixing in three-dimensional microvascular networks fabricated by direct-write assembly. *Nat. Mater.* **2** (4), 265-271 (2003).

CHAPTER 3

MASS TRANSPORT IN MICROFLUIDIC BIOMATERIALS

I. Introduction

In the previous chapter, we demonstrated the direct fabrication of functional microfluidic biomaterials using calcium alginate and collagen. We also qualitatively showed that embedded microchannels within the microfluidic biomaterials enabled efficient exchange of solutes with the bulk of cellular 3-D microenvironment. In designing and operating microfluidic biomaterials, we must take mass transport into account because diffusion of non-reactive solutes and diffusion-reaction of reactive solutes are the main processes within the microfluidic biomaterials. Such considerations allow choosing appropriate design parameters such as interchannel distance λ_c and scaffold thickness, H in creating desired distributions of soluble chemical environment.

Figure 3.1 shows some parameters related to mass transport in microfluidic biomaterials: solutes are delivered by pressure-driven flows (flow speed, u_c [cm/s]) to the bulk of the scaffold. The exchange of solutes proceeds in two steps: interfacial convective mass transfer between the flowing solutions and the walls of the microchannels (mass transfer coefficient, k_c [cm/s]), and molecular diffusion between these walls and the bulk of the scaffold. For reactive solutes, diffusion-reaction processes define gradients of concentration at steady state. As shown schematically in Fig. 3.1A (and also qualitatively illustrated in Fig. 2.1), for a solute delivered via the channels and consumed in the bulk, variations of concentration will occur over a characteristic distance, $\lambda_K \sim \sqrt{D_{s,g} c_0 / R}$ [cm], that we will call the Krogh length[1]; here $D_{s,g}$ [cm^2/s] is the molecular diffusivity of the solute in the scaffold, R [mol/L$\cdot$s] is the consumption rate, and c_0 [mol/L] is the concentration of the solute in

the channel. For vital metabolites or toxic waste products, it is often desirable to minimize the variations in solute concentrations associated with these gradients; this condition can be achieved in a microfluidic scaffold in which the channel spacing, $\lambda_c < 2\lambda_K$. For non-reactive solutes, the steady state distribution will be uniform unless both sources and sinks are embedded in the scaffold. The scaffold thickness, H can also play a role in determining a transition length scale of the distribution of solutes between two distinct zones (created by two fluidic networks; Fig. 2.1Dii). A desirable mode of operation is achieved if the flow speed is high enough to: 1) avoid depletion of reagents along the length of the channels (achieved at high Peclêt number, $Pe = u_c h_c / D_{s,c} \gg L / h_c$) and 2) ensure that resistance to convective mass transfer is much less than resistance to purely diffusive transfer within gel (achieved at high Biot number, $Bi = k_c H / D_{s,g}$ for non-reactive solutes or $Bi = k_c \lambda_K / D_{s,g}$ for reactive solutes)[2] (Fig. 3.1C and D). Here, $D_{s,c}$ [cm^2/s] is diffusivity of a solute in the solution in the microchannels.

In this chapter, details of mass transport in microfluidic biomaterials are discussed. The details include 1) diffusion of solutes, 2) temporal and spatial control and diffusion-reaction of metabolites in microfluidic biomaterials. We will conclude with the implications of the mass transport considerations and new opportunities.
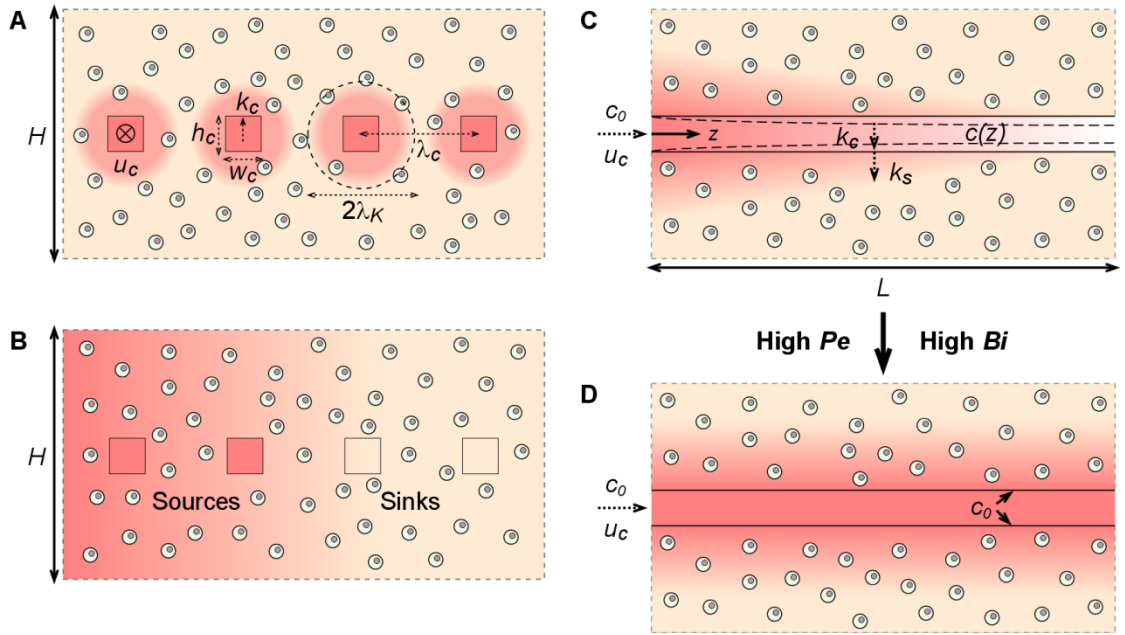
Figure 3.1 Schematic representations of mass transport in microfluidic biomaterials. A and B. Cross-sectional views of microfluidic biomaterials. Dispersed cells are shown as double circles. Microchannels are shown as squares. The pink shading represents steady-state distributions of solutes: in A, reactive solute is delivered via the channels and is consumed by cells as it diffuses into the matrix; in B, non-reactive solute is delivered via the two channels on the left and extracted by the channels on the right. Geometric parameters are defined in A and B: λ_K [cm] is the Krogh length, λ_c [cm] is the inter-channel distance, w_c [cm] is the microchannel width and h_c [cm] is the microchannel height. u_c [cm/s] is the flow speed in microchannels. k_c [cm/s] is the mass transfer coefficient of the flow in the microchannels. H [cm] is the thickness of the scaffold. **C and D.** Schematic diagrams showing convective mass transfer mediated by embedded microchannels at low (C) and high (D) flow speeds. L [cm] is the microchannel length. c_0 [mol/L] is the concentration of a solute injected from the inlet.

Materials and methods

    A. Measurement of diffusion in microfluidic biomaterials (Fluorescence

        measure After Microfluidic Illumination, FAMI)

Acellular microfluidic biomaterials were used to carry out transient diffusion experiments (Fig. 3.9 and 3.10) with 20 μM fluorescein (MW 376.27 Da ; Sigma-Aldrich) and 6 μM fluorescein isothiocyanate (FITC)-BSA (MW 66 kDa; Sigma-Aldrich) in 4 % [w/v] calcium alginate, and 10 μM FITC-dextran (MW 70 kDa; Sigma-Aldrich) in 1 % [w/v] collagen. Fluorescein and FITC-BSA were dissolved in our standard pH-adjusted buffer solution containing 10 mM $CaCl_2$, 15 mM N-(2-hydroxyethyl)-piperazine-N'-2-ethanesulfonic acid (HEPES), and 127.5 mM NaCl. FITC-dextran was dissolved in Phosphate buffered saline (PBS). The extra $CaCl_2$ maintained rigidity of the microfluidic alginate scaffold. The fluorescent solutions were delivered into the microfluidic alginate and collagen via microchannels at a flow rate of 50 and 10 μL/min respectively. As soon as the microchannels were filled, the delivery was stopped and fluorescence images were acquired at regular intervals using a stereomicroscope (MZ FLIII, Leica), a CCD (charge-coupled device) camera (Retiga 1300, QImaging), and Qcapture Pro 5.1 (Qimaging) for microfluidic alginate and an inverted microscope (IX 81, Olympus), a CCD camera (Hamamatsu Orca CCD, Hamamatsu), and SlideBook4.2 (Olympus) for microfluidic collagen. Image analyses including quantification of fluorescence intensity and fast Fourier transform were carried out in MATLAB (The MathWorks).

    B. Fabrication of 1-channel microfluidic system

1-channel microfluidic systems were fabricated similarly as described in Chapter 2 (Fig. 2.2 and 3.2): 1) a machined plexiglass mold was pre-coated sequentially with 1% [v/v] polyethylenimine (PEI) to allow adhesion of alginate, and

both 1 % [v/v] PEI and 0.1% [v/v] glutaraldehyde for collagen, with an aluminum plug inserted to block a microchannel, 2) either alginate or collagen was casted in the machined plexiglass mold, 3) Another machined plexiglass was placed to pressure-seal a device. Note that the aluminum plug was replaced with a rubber plug when sealing the device.

C. *Measurement of diffusion in 1-channel microfluidic system*

The 1-channel microfluidic system was used to estimate diffusivity of FITC-dextran (70 kDa) in 1 % [w/v] collagen. The fluorescent solution was delivered into the slab of collagen via the microchannel at a flow rate of 50 µL/min (Fig. 3.2B and C). Fluorescence images were acquired at every 5 min for 60 min using the stereomicroscope. Image analyses to estimate penetration depth, δ were carried out in MATLAB.
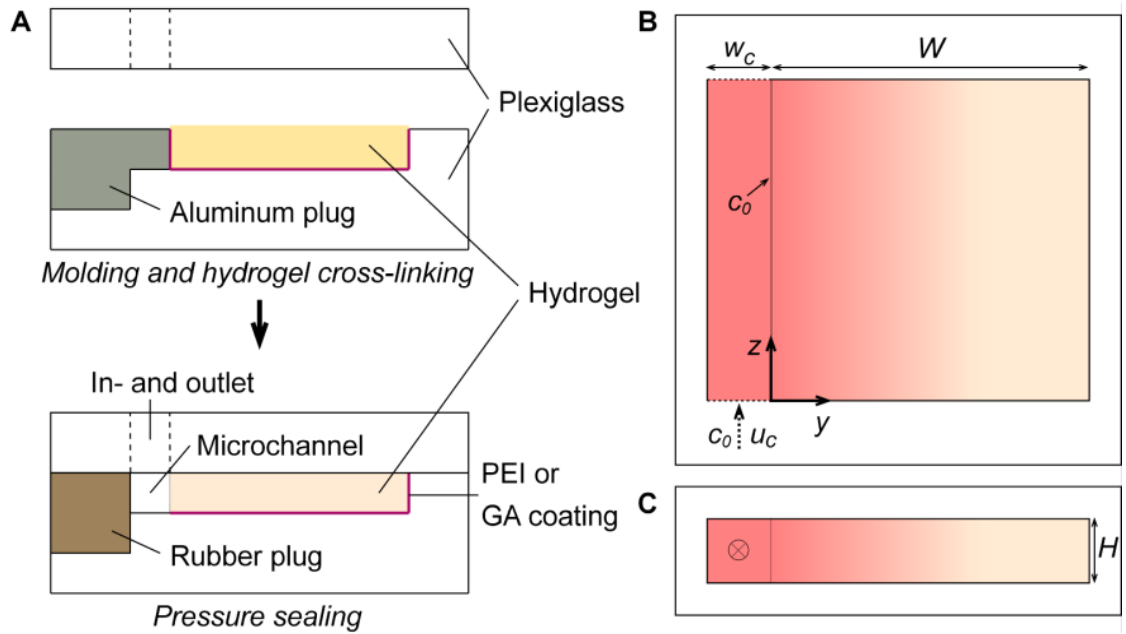
Figure 3.2 Fabrication of 1-channel microfluidic system. A. Schematic diagram of the fabrication of 1-channel microfluidic systems. The red line indicates either PEI or glutaraldehyde coating. **B and C.** Schematic illustration of the 1-channel microfluidic system: top-down view (C) and cross-sectional view (D). The pink shading represents distributions of solutes diffusing into the scaffold.

D. Temporally and spatially resolved delivery of small molecules in microfluidic alginate scaffold

An acellular microfluidic alginate scaffold was used to sequentially deliver small molecules via the embedded microchannels in the single network (Fig. 2.1Di): (1) fluorescein solution and (2) rhodamine B solution were delivered through the network at a flow rate of 50 µL/min (Fig. 3.12A).

An acellular microfluidic scaffold was used to deliver a series of small molecules via the embedded microchannels in the two independent networks (Fig. 2.1Dii): (1) the pH-adjusted buffer without fluorescent dye, (2) fluorescein solution (5 µM in buffer) and (3) rhodamine B solution (5 µM in buffer) were delivered through the networks at a flow rate of 50 µL/min (Fig. 3.13A and Ax.1).

A microfluidic scaffold seeded with chondrocytes (1×10^7 cell/mL) was stained with two different stains (Fig. 3.13C) as described in Chapter 2. Image acquisition and analyses were carried out in the same way as described above.

E. Visualization of diffusion-reaction of metabolites in microfluidic alginate scaffolds

Chondrocyte-seeded microfluidic alginate scaffolds with various seeding densities were used to visualize diffusion-reaction processes. Microfluidic delivery of 5 µmol/L calcein-AM-green, dissolved in the pH-adjusted buffer, was carried out for ~ 2.5 h. The flow rate was set to be 10 µL/min. To obtain cross-sectional view, the microfluidic scaffolds were cut into thin (1 ~ 2 mm) samples. These images were used to measure radial intensity profiles around a concentric point in a microchannel. Images were acquired in the same way as for transient diffusion. ImageJ was used to measure the radial intensity profiles (Fig. 3.1). Finite element analyses were carried out in Comsol Multiphysics (COMSOL).

F. Analysis of distribution of fluorescent product in cross-sectional images

Cross-sectional images were cropped, and a region of interest was copied in a black-backgrounded canvas; the height of the canvas was twice that of the cropped image (Fig. 3.1). A Radial distribution of calcein about a concentric point in a microchannel was then obtained using a plugin of Radial Profiles provided in ImageJ.

G. Fabrication of thin discs seeded with OSCC-3 cells

Cylindrical calcium alginate discs (200 µm thick, 4 mm in diameter) were fabricated by 1) casting the cell-seeded alginate in a machined plexiglass mold, 2) placing a porous membrane, and 3) cross-linking with 60 mM $CaCl_2$ (buffered with 15 mM HEPES; osmotically balanced with 52.5 mM NaCl; pH-adjusted) for ~15 min. Cross-linked, cell-seeded discs were removed from the mold, and transferred to well plates.
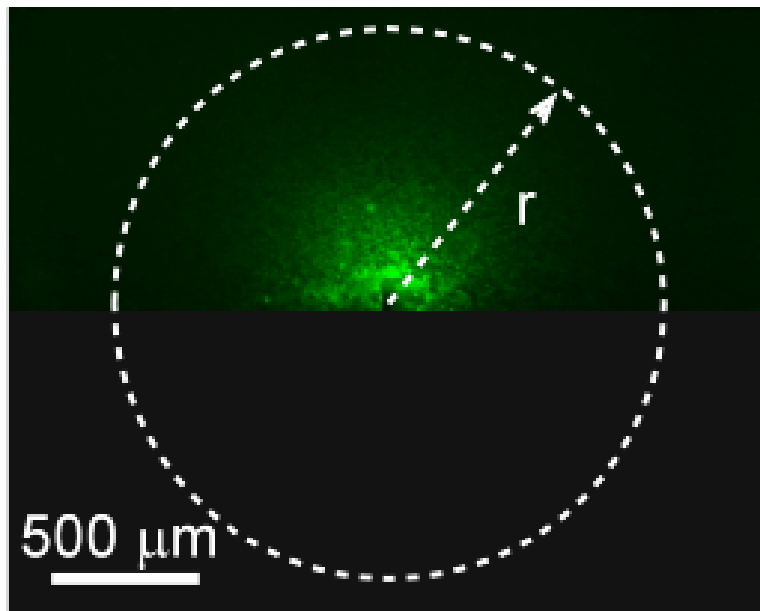
Figure 3.3 Radial distribution of calcein about a microchannel. Fluorescence micrograph of a cross-section of top (micropatterned) layer of a microfluidic alginate scaffold seeded with primary chondrocytes (7.3×10^7 cell/mL).
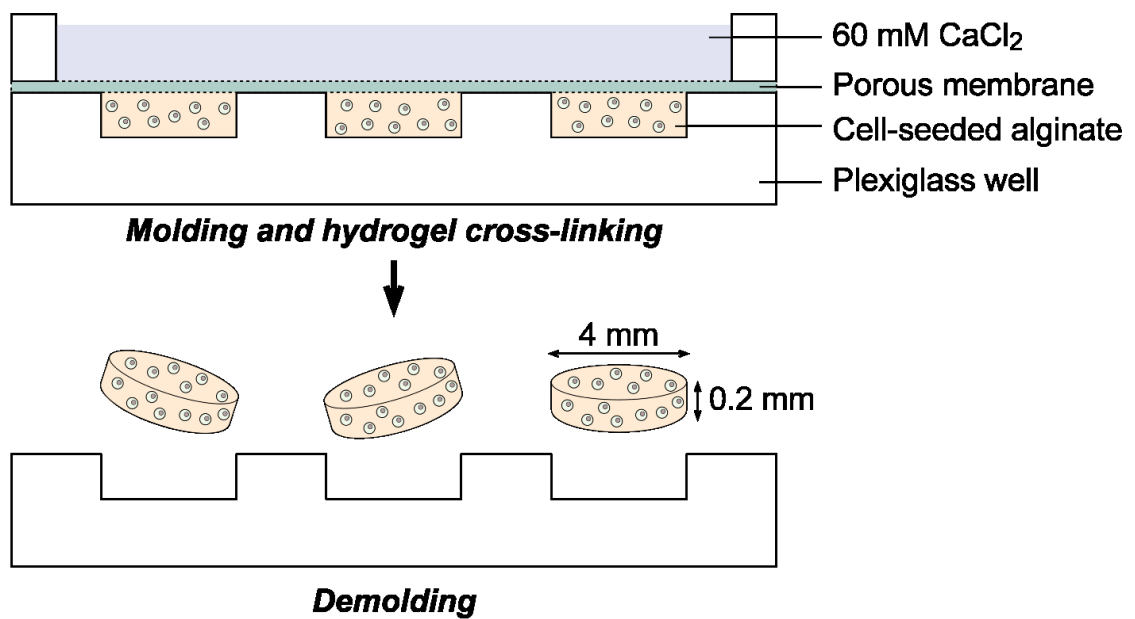
Figure 3.4 Fabrication of thin disc seeded with cells. Schematic diagram of the fabrication of 200 µm-thick 4 % [w/v] alginate discs seeded with cells.

H. Measurement of oxygen consumption rate (OCR) and finite element modeling

OSCC-3 oxygen consumption was measured for cell-seeded 200 μm thick alginate discs. Fabricated cell-seeded alginate discs were first cultured for 2-3 days at 17 % O_2 and pre-incubated overnight at 1, 5, 9, 13, and 17 % O_2.prior to measurements. Four discs were submerged in 2 mL media in a sealed glass chamber (Agilent Technologies Inc., Santa Clara, CA), and kept stirring at 37 ^{o}C. Media was initially equilibrated at the pre-incubation O_2 concentrations and 5 % CO_2, and reduction in oxygen level due to cellular consumption was measured with a dissolved oxygen meter (Innovative Instruments, Inc., Tampa, FL) as illustrated in Fig. 3.5. Measurements were taken for 30 min, at a rate of one measurement per minute. This process was repeated 4 times with fresh media used each time. Consumption rate was calculated from a linear fit to the O_2 level versus time (Fig. 3.18A). For OCR at 17 % O_2, consumption kinetics was treated as zeroth order in the range measured (from 13 to 5 % O_2) due to the linearity of the O_2 level versus time curve. Using this measured consumption rate, an assumed oxygen diffusivity (D_{O_2}) for water[3], and a cell seeding density (ρ_{cell}) of 2×10^7 cell/mL, the cross-sectional O_2 profile in 200, 500, and 1000 μm thick discs was computed by solution of the steady-state diffusion-reaction equation ($D_{O_2}\nabla^2 c_{O_2} = -\rho_{cell}R_{O_2,cell}$). The solution was obtained with finite element method (FEM), implemented with Comsol Multiphysics (Comsol, Inc., Burlington, MA), assuming a fixed boundary concentration at 17 % O_2. Delivery of O2 to the boundary surface was assumed not to be rate limiting, which was accomplished in practice by culturing discs on a shaker.
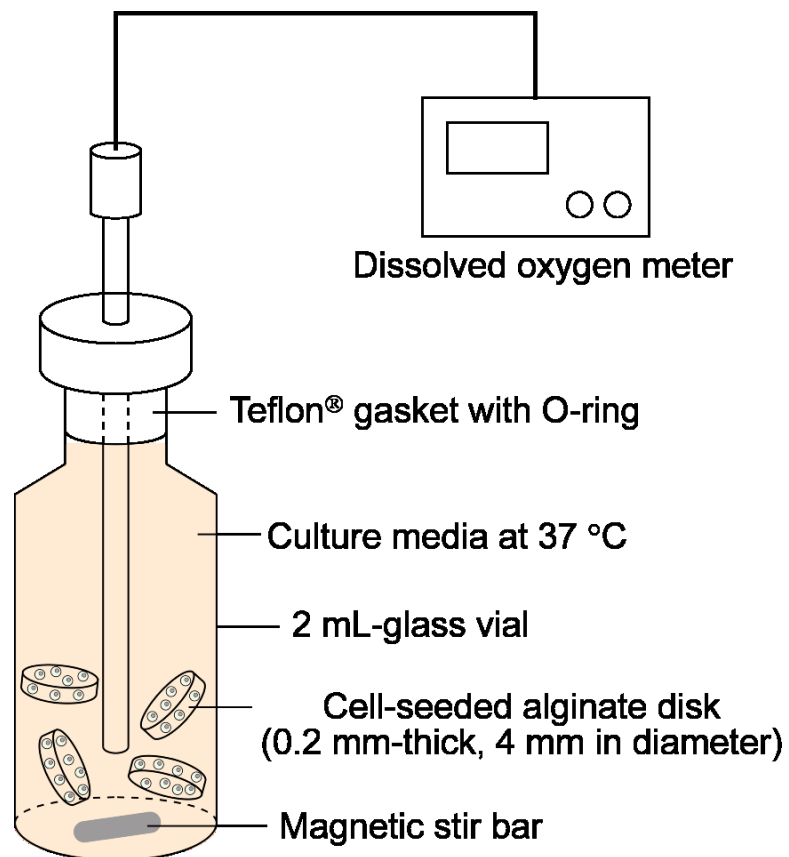
Figure 3.5 Schematic illustration of the measurement of oxygen consumption rate (OCR).

Plots represent mean±standard deviations (SD). Analysis of variance (ANOVA) with Tukey post-test was used for statistical analysis (GraphPad Prism, La Jolla, CA) and significance denoted as *P<0.05; **P<0.01; ***P<0.001.

Theoretical background

A. Measurement of diffusivity using FAMI

For simplicity, we present analysis for early times after the injection of the dye into the scaffold ($t < H^2 / D_{s,g}$) for which the diffusion occurs in a domain that is effectively infinite in extent along the *x*-axis (Fig. 3.6); the experiments presented in Fig. 3.9 and 3.10 are in this regime. Using methods of image sources, this approach (in particular, the integration over *x*) can also be shown to be appropriate for all times in a domain bounded by parallel, impermeable boundaries. At early times, the time-dependent concentration distribution due to an instantaneous source, $M(x, y)$ at $t = 0$ can be expressed in integral form as:

$$c(x, y, t) = \int_{-\infty}^{\infty} \int_{-\infty}^{\infty} \frac{M(x', y')}{4\pi D_{s,g} t} \exp\left[-\frac{(x - x')^2 + (y - y')^2}{4 D_{s,g} t} \right] dx' dy' \qquad (3.1)$$

In equation 3.1, the axes are as defined as in Fig. 3.6A, with the *x*-axis into the page, through the thickness of the scaffold. For fast injection (high *Pe* and high *Bi*), we neglect variations along *z*. We have verified that the fluorescence intensity, $I(y, t)$, in micrographs taken from above at low magnification (~10x), as in Fig. 3.9A and 3.9B, is linearly proportional to the concentration of dye and the thickness of the scaffold. Therefore, we expect the following relationship between intensity and concentration:

$$I(y,t) = \alpha \int_0^H c(x,y,t)\,dx \approx \alpha \int_{-\infty}^{\infty} \int_{-\infty}^{\infty} \int_{-\infty}^{\infty} \frac{M(x',y')}{4\pi D_{s,g} t} \exp\left[-\frac{(x-x')^2 + (y-y')^2}{4 D_{s,g} t}\right] dx'\,dy'\,dx$$

$$= \alpha \int_{-\infty}^{\infty} \frac{M_x(y')}{2\sqrt{\pi D_{s,g} t}} \exp\left[-\frac{(y-y')^2}{4 D_{s,g} t}\right] dy'$$

(3.2)

In equation 3.2, α is a constant that depends on the intensity of the illumination, quantum yield of the fluorophor, the length of the exposure, and the sensitivity of the camera, and $M_x(y')$ is the x-integrated distribution of the initial source. In the second step, we have used the assumption of early times to extend the bounds of the integral along x to $\pm\infty$. In the absence of variations along z, $I(y,t) = \bar{I}_z(y,t)$, the z-averaged intensity in Fig. 3.6B. Performing a continuous Fourier transform on this x-integrated intensity in equation 3.2 gives the following expression for the amplitude of the fundamental Fourier mode:

$$\hat{I}(k_0,t) = M_x(k_0) e^{-t/\tau}$$

(3.3)

, where the time constant for the decay, $\tau = 1/k_0^2 D_{s,g}$ and $\hat{M}_x(k)$ is the Fourier transform of $M_x(y')$, defined as

$$\hat{M}_x(k) = \frac{1}{\sqrt{2\pi}} \int_{-\infty}^{\infty} M_x(y') e^{-iky'} dy'$$

(3.4)

See Appendix 3 for detailed derivation.
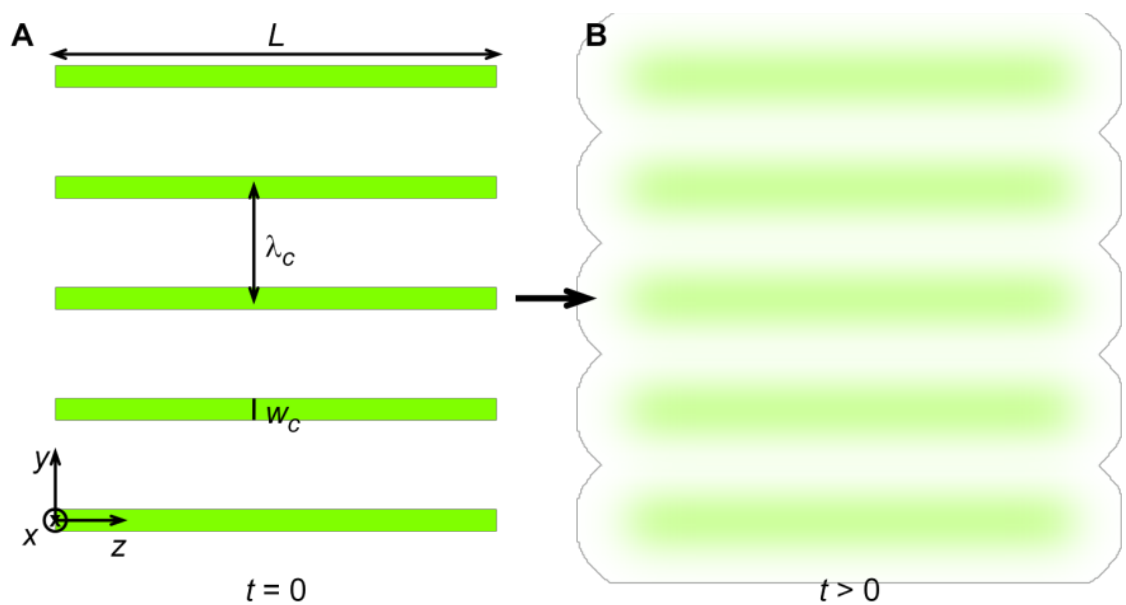
Figure 3.6 Schematic representation of Fluorescence measure After Microfluidic Illumination (FAMI). Schematic illustrations showing the initial (A) and subsequent ($t > 0$, B) distribution of a fluorescent solute delivered in a pulse into a set of uniformly spaced microchannels.

B. Measurement of diffusivity in 1-channel microfluidic system

Diffusivity of fluorescent solutes can be also estimated using 1-channel microfluidic system for early-time analysis. For fast delivery (high *Pe* and high *Bi*), we again neglect variations along *z*. At early times, we can treat the system as a semi-infinite slab. In other words, the impermeable boundary at *y* = *W* can be considered as $c(W,t) \approx c(\infty,t) = 0$. Then, an analytical solution for the trainsient diffusion of a solute in a hydrogel ($\partial c / \partial t = D_{s,g} \partial^2 c / \partial y^2$) is given by the similarity method:

$$c(y,t) = c_0 erfc(\eta) \tag{3.5}$$

where η is the similarity variable defined as

$$\eta = \frac{y}{2\sqrt{D_{s,g}t}} \tag{3.6}$$

With a similar strategy described in the previous section, it is reasonable to state that $c(y,t) \approx I(y,t) = \overline{I}_z(y,t)$. Because the theoretical concentration profile of a fluorescent solute rapidly drops to $0.1c_0$ at $\eta = 1.163$ (i.e., $erfc(1.1613) = 0.1$), we define penetration depth, δ as

$$\delta = 2.3\sqrt{D_{s,g}t} \tag{3.7}$$

For the experimentally acquired images, the penetration depth was length at which normalized fluroescence intensity was 0.1 (i.e., $I(\delta,t)/I_{max} = 0.1$).
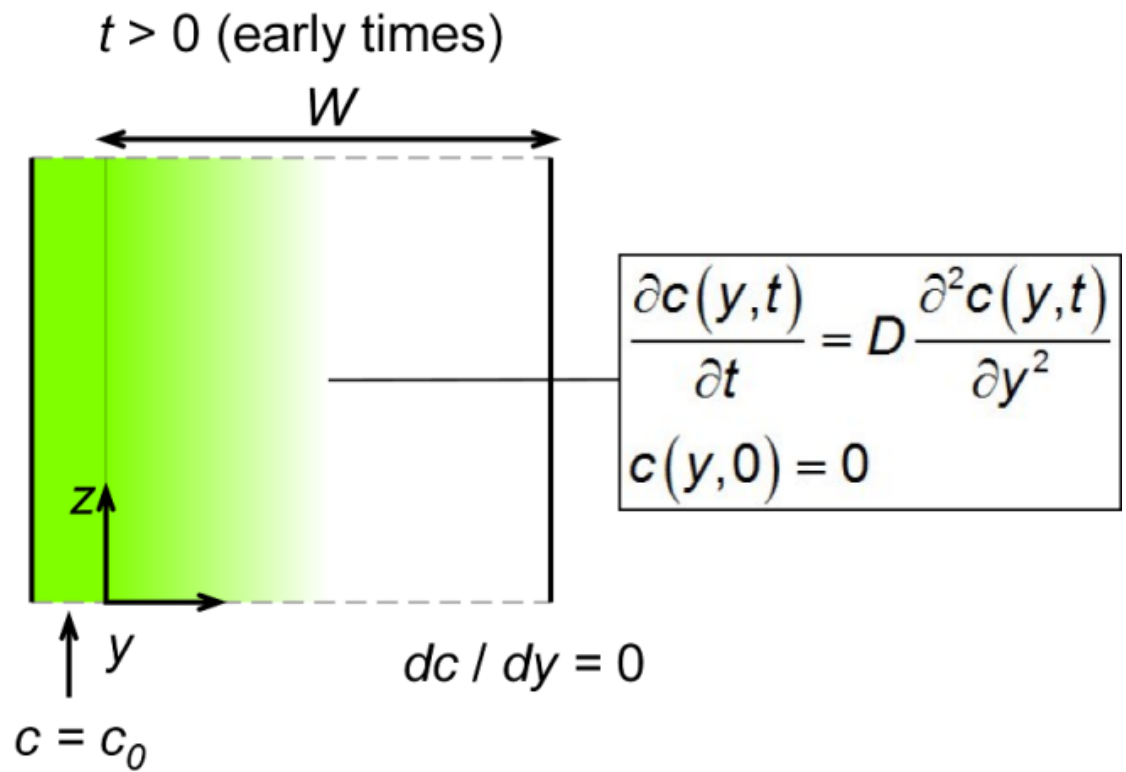
Figure 3.7 Schematic representation of diffusion of solutes to a slab of hydrogel in 1-channel microfluidic system. The green shading represents distributions of solutes diffusing into the slab of hydrogel.

C. Transient enzymatic transformation (diffusion-reaction) of calcein-AM in
   alginate

Visualization of diffusion-reaction of a model metabolite (calcein-AM) is
directly associated with enzymatic production of calcein (see Appendix 2 and Fig. 3.9).
Given that $\frac{dP}{dt} = \rho_{cell}k_{cell}S$, a distribution of calcein within microfluidic scaffolds can
be expressed as

$$P(x,y,z,t) = \int_0^t \rho_{cell}k_{cell}S(x,y,z,t)\,dt \qquad (3.8)$$

, where P [mol/L] and S [mol/L] are concentration of calcein and calcein-AM
respectively. If the distribution of calcein-AM reaches a steady state in a short time
relative to the length of the experiment, the distribution of calcein reduces to

$$P_{ss}(x,y,z,t) \approx \rho_{cell}k_{cell}tS_{ss}(x,y,z) \qquad (3.9)$$

The corresponding fluorescence intensity of calcein can be written as

$$I(x,y,z,t) = \alpha P_{ss}(x,y,z,t) = \alpha\rho_{cell}k_{cell}tS_{ss}(x,y,z) \qquad (3.10)$$

, where α is again a constant relating concentration and intensity. In addition, the
observed intensity is the integrated intensity along the *x*-axis;

$$I(y,z,t) \equiv \int_0^H I(x,y,z,t)\,dx \qquad (3.11)$$

Figure 3.5 presents the transient distributions of calcein (A) and their collapse at long
times, when normalized by the time of injection (B). This behavior verifies that the
distribution of calcein-AM reaches a steady state at long times and that measuring the

86

concentration of P via fluorescence gives a measure of the steady state distribution of reactant.

D. Measurement of OCR

In a closed batch system across which there is no mass flux of oxygen, OCR, $R_{O_2,\text{cell}}$ [mol/s$\cdot$cell] is defined as

$$R_{O_2,\text{cell}} \equiv \frac{-\dfrac{dn_{O_2}}{dt}}{N_{\text{cell}}} \tag{3.12}$$

where n_{O_2} [mol] is mole of oxygen dissolved in media and N_{cell} [cell] is total number of cells in the system. Equation 3.12 can be re-written with more practical parameters that were used in experiments:

$$R_{O_2,\text{cell}} = \frac{V_{\text{vial}}}{N_{\text{cell}}}\left(-\frac{dc_{O_2}}{dt}\right) = \frac{V_{\text{vial}}}{\left(V_{\text{disc}}\rho_{\text{cell}}\right)N_{\text{disc}}}\left(-\frac{dc_{O_2}}{dt}\right) \tag{3.13}$$

where V_{vial} [m^3] is volume of the glass vial (the closed system), V_{disc} [m^3] is volume of an alginate disc, ρ_{cell} [cell/m^3] is cell seeding density in the alginate disc, N_{disc} is number of discs submerged in the vial during the measurement of OCR.
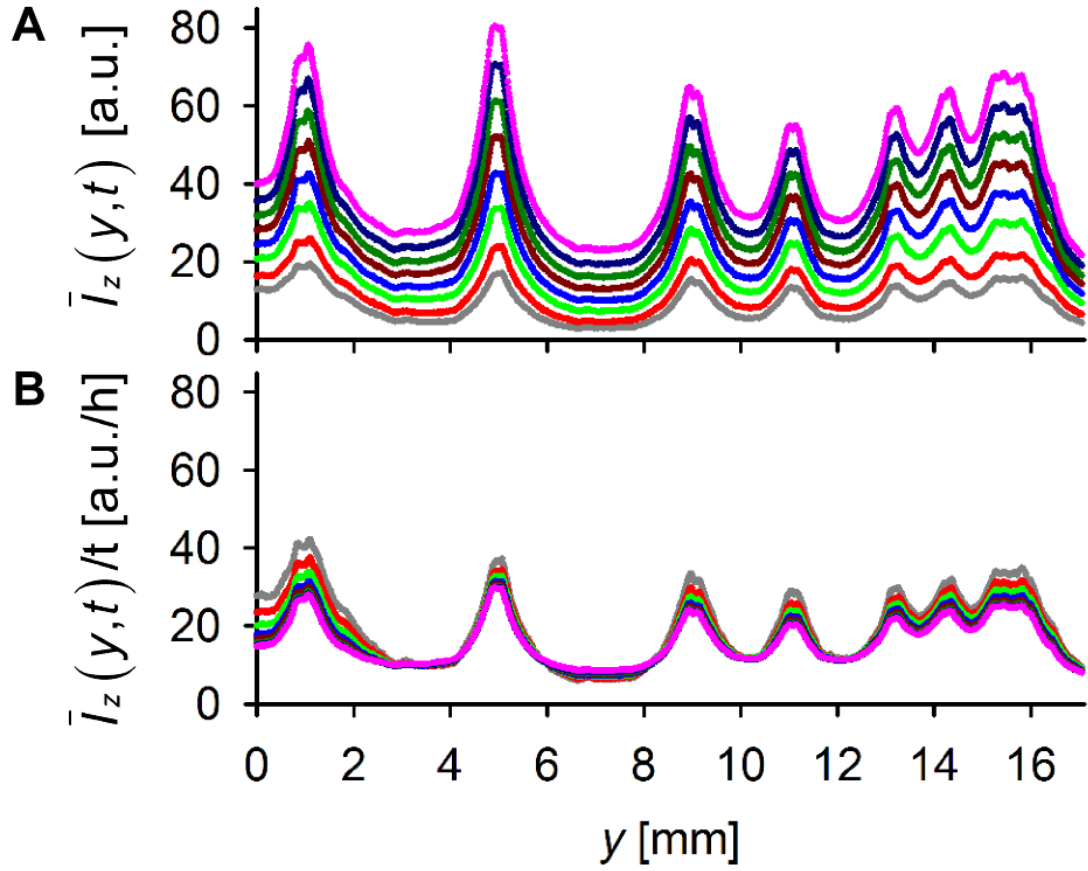
Figure 3.8 Transient distributions of calcein and their collapse at long times. A.
Plot of z-averaged intensity, $\bar{I}_z(y,t)$ measured in Fig. 3.15A at times (20 min (dark
grey), 40 min (red), 60 min (green), 80 min (blue), 100 min (dark red), 120 min (dark
green), 140 (dark blue), 160 min (pink)). **B.** Plot of z-averaged intensity divided by
time [h], $\bar{I}_z(y,t)/t$.

Results and discussion

A. Measurement of diffusivity in 4 % [w/v] alginate using FAMI

Permeability to diffusion of both small (e.g., biochemical factors) and large

(e.g., secreted extracellular matrix (ECM) components) molecules is essential for any

matrix for 3D cell culture, and for the function of a microfluidic scaffold in particular

(Fig. 3.1). We have developed a systematic method to measure diffusivity (also see

Theoretical background) of fluorescent molecules within the 3D volume of the matrix

that defines the microfluidic scaffold; this method is analogous to fluorescence

recovery after photobleaching[4]. A heterogeneous initial distribution of fluorescent dye

is created by injection of a pulse of fluorescent solution into the channels of a

microfluidic scaffold (network as in Fig. 2.1Di); after injection, the distribution of

solute is allowed to evolve by pure diffusion towards a uniform state in the bulk of the

microfluidic gel (Fig. 3.6 and 3.9A); the progression of this diffusive broadening is

monitored in the amplitude of the fundamental Fourier mode of the z-averaged

distribution, $\hat{\bar{I}}_z\left(k_0,t\right)$, where the wavenumber $k_0 = 2\pi / \lambda_c$. Figure 3c shows the

temporal evolution of $\ln\left[\hat{\bar{I}}_z\left(k_0,t\right)\right]$ for fluorescein (MW 376.27 Da) and fluorescein

isothiocyanate-bovine serum albumin (FITC-BSA, MW 66 kDa). The observed single

exponential decay indicates that both solutes follow Fickian diffusion (that is, constant

macroscopic diffusivity) within the gel. Given this behavior, the time constant for the

decay (the negative of the slope) is $\tau = 1/k_0^2 D_{s,g}$ (also see Theoretical background) [2].

From fits of this decay, we find $D_{fluor,g} = 3.6\times10^{-6}\,\mathrm{cm^2/s} = 0.60 D_{fluor,w}$ and $D_{BSA,g}$

$=1.5\times10^{-7}\,\mathrm{cm^2/s} = 0.52 D_{BSA,w}$ for fluorescein and FITC-BSA respectively, where,

$D_{s,w}$ is the diffusivity of the solute in water[4-5]. Taken together these observations

indicate that the diffusive motion of both small and macromolecules is unhindered

within the pores of the matrix, and we conclude that the pore size of 4 % [w/v]

calcium alginate is large relative to BSA (radius of gyration, $R_G = 3.6$ nm[6]). This

same technique should be useful to measure diffusivities in the matrix after remodeling and production of ECM has occurred within a microfluidic scaffold.

B. *Measurement of diffusivity in 1 % [w/v] collagen using FAMI*

Diffusivity of a macromolecule in 1 % [w/v] collagen was measured in the same way as described in the previous section. Figure 3.10B shows the temporal evolution of $\ln\left[\hat{\bar{I}}_z\left(k_0,t\right)\right]$ for FITC-dextran (MW 70 kDa) where we find $D_{dextran,g}$ $= 3.5 \times 10^{-7} \, \text{cm}^2/\text{s}$. This measured value is comparable with the diffusivity of FITC-dextran (MW 70 kDa) in water, $D_{dextran,w} = 2.3 \times 10^{-7} \, \text{cm}^2/\text{s}$ [7]. Using Stokes-Einstein relation ($D_{s,w} = k_B T / 6\pi\eta_w R_s$), where k_B is Boltzmann constant, T is temperature, η_w is viscosity of water, and R_s is radius of a solute ($R_{dextran(70kDa)} \approx 7.1 \, \text{nm}$), theoretically calculated diffusivity of dextran (70 kDa) in water is $3.9 \times 10^{-7} \, \text{cm}^2/\text{s}$ [8]. We note that one should be careful not to have residual convective flows while allowing a fluorescent solute to evolve into the bulk of a gel by pure diffusion (i.e., at $t > 0$). In the presence of convective flow at $t > 0$, the FAMI analysis underestimates diffusivity because the continous (in time) source (fluorescence) in microchannels at $t > 0$ causes intensity to decay more slowly. We have verified this hypothesis by carrying out FAMI experiments in the presence of persistent convective flows (0.1, 1, and 10 µL/min; data not shown). We also note that dextran is a linear chain polymer and that its diffusion in hydrogels can be more complicated due to interactions between dextran and a hydrogl matrix[9]. For future measurements in collagen, non-adhesive globular proteins that are conjugated with a fluorophore would be preferrable.
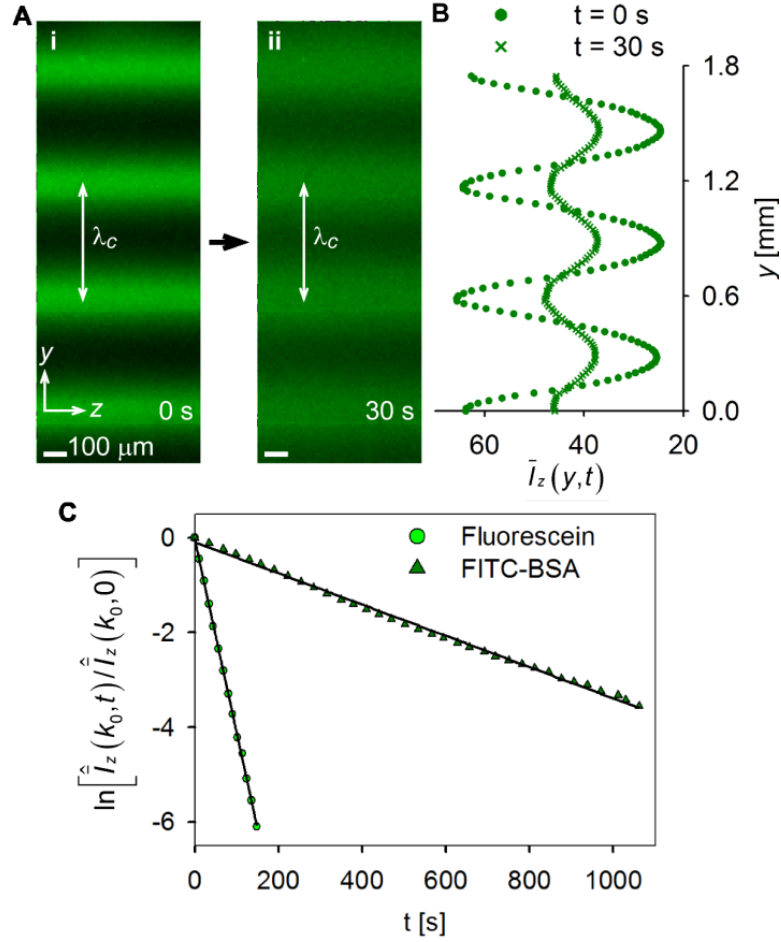
Figure 3.9 Measurement of diffusivity in 4 % [w/v] alginate using FAMI. A.
Fluorescence micrographs showing the initial (i) and subsequent ($t = 30$ s, ii)
distribution of fluorescein delivered in a pulse into a set of uniformly spaced
microchannels. **B.** Plot of the z-averaged fluorescence intensity, $\bar{I}_z(y,t)$, measured in
the images in A. The plot was obtained from a single sample. The results were
consistent sample to sample. The experimental data points are mean values of the
fluorescence intensity (234 pixels in the z direction) in the images. Standard
deviations were smaller than the symbols. **C.** Log-linear plot of time evolution of the
fundamental Fourier mode ($k_0 = 2\pi / \lambda_c$) of intensity profiles such as those in B for
fluorescein (circles) and FITC-BSA (triangles).
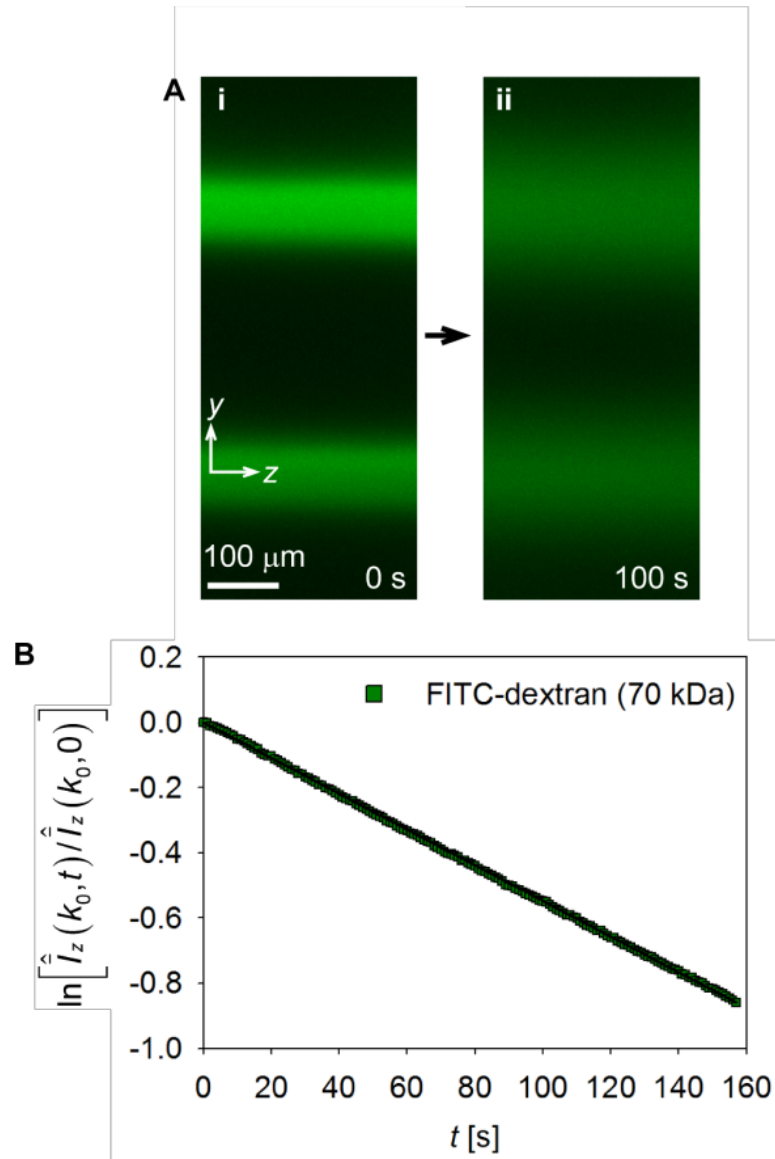
Figure 3.10 Measurement of diffusivity in 1 % [w/v] collagen using FAMI. A.
Fluorescence micrographs showing the initial (i) and subsequent ($t = 100$ s, ii)
distribution of FITC-dextran (70 kDa) delivered in a pulse into a set of uniformly
spaced microchannels. **B.** Log-linear plot of time evolution of the fundamental
Fourier mode ($k_0 = 2\pi / \lambda_c$) of intensity profiles for FITC-dextran.

C. Measurement of diffusivity in 1-channel microfluidic system

We have also measured diffusivity of the FITC-dextran in 1 % [w/v] collagen by designing a simpler 1-channel microfluidic system (Fig.3.2) based on a classical mass transport topic (i.e., diffusion in a semi-infinite slab; also see Theoretical background). Because a solute can be evolve only through one side wall of a gel (Fig. 3.2), we can treat the system as 1-D. As a fluorescent solute is continuosly delivered via the single channel, the solute is allowed to laterally diffuse into a gel. At early times ($t \ll \tau_d = W^2 / D_{s,g}$), penetration depth, δ is proportional to $\sqrt{D_{s,g}t}$. The penetration depths were estimated by analyzing acquired fluorescence images at times (Fig. 3.11A and B; also see Materials and methods and Theoretical background). We found $D_{dextran,g} = 4.3 \times 10^{-7} \, \text{cm}^2/\text{s}$ which was also similar to the measured diffusivity from the FAMI and $D_{dextran,w}$. This measurement served as an additional way to verify the FAMI analyses as described above and allowed eliminating experimental ambiguousness regarding the residual convective flows in the microchannel during the FAMI in case a microfluidic biomaterial is sensitive to small disturbance, causing unexpected convective flows during the FAMI. We note that too fast flow rates in the microchannel (therefore, too high pressures) may cause lateral convection into especially soft gels, resulting in overestimating diffusivity. The fluorescence micrograph shown in Fig. 3.11Ai does not represent the case. The imperfect diffusion broadening appeared because the interface between the microchannel and the gel was not sharp and slightly deformed by an air bubble that was accidentally induced prior to the measurement. The slightly large value of diffusivity could have been due to the imperfectness of the gel.
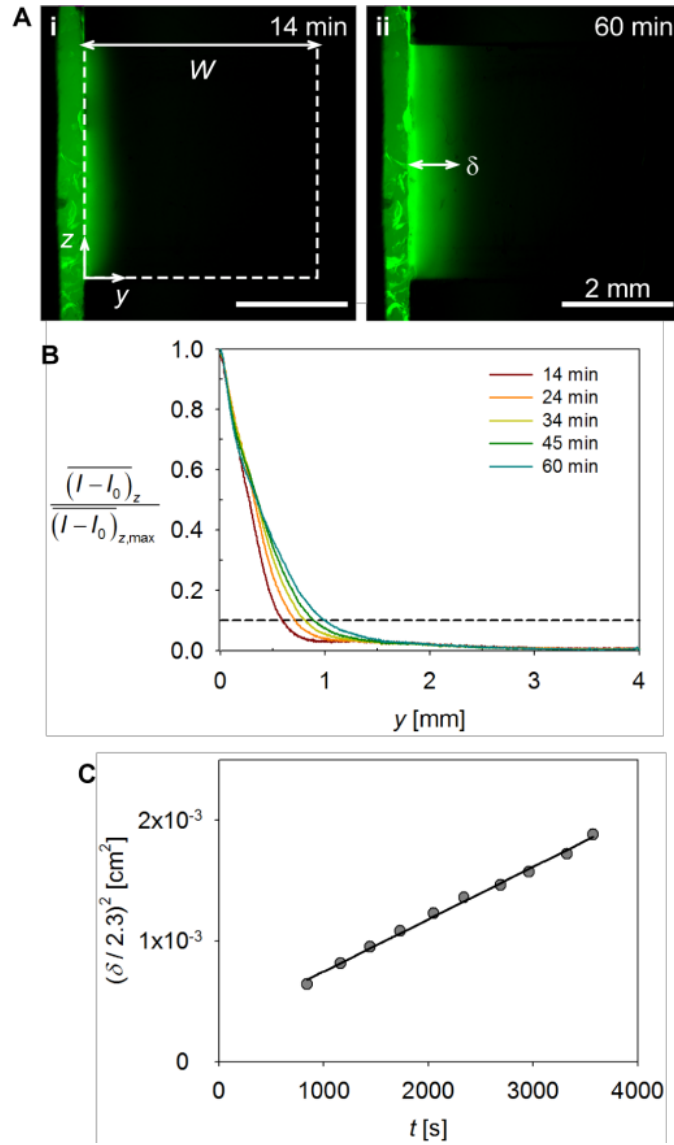
Figure 3.11 Measurement of diffusivity in 1 % [w/v] collagen using 1-channel microfluidic system. A. Fluorescence micrographs showing an early (t = 14 min, i) and later (t = 60 min, ii) distribution of FITC-dextran (70 kDa) delivered in 1-channel microfluidic system. δ [mm] is the penetration depth of a fluorescent solute. **B.** Plot of background-subtracted, z-averaged fluorescence intensity, measured in the images in A. **C.** Plot of time evolution of the penetration depth, δ of FITC-dextran estimated from the images in A and the plot in B.

D. Effective diffusion in a porous material

   To clarify our interpretation of the dynamics of fluorescein and FITC-BSA as "unhindered" pore diffusion (Fig. 3.9), we introduce the basic concepts of pore diffusion: for any solute that can move freely within and between the pores of a porous material, the effective macroscopic diffusivity will be related to its free diffusivity by a single coefficient, $C_{pore} < 1$, that is related to the geometry of the pores:

$$D_g = C_{pore}D_w = \left(\frac{l}{l_{eff}}\right)\left(\frac{A_{eff}}{A}\right)D_w \tag{3.14}$$

where l [m] is a macroscopic length over which diffusion occurs within the porous material, l_{eff} [m] is an effective length of the path of the solute through pores, A [m^2] is a macroscopic cross-sectional area of the porous material through which the solute motion, A_{eff} [m^2] is a reduced area available for flow of the solute, and D_w [cm^2/s] is the diffusivity of the solute in water[10]. Our experiments with fluorescein and FITC-BSA indicate that $C_{pore} \sim 0.5$ for 4 % [w/v] calcium alginate.

   We also highlight the observations that indicate conclusively that mass transfer within the gel is diffusive (not convective): 1) the quantitative agreement between purely diffusive model and transient profiles (Fig. 3.9); note that Darcy convection of the solute would lead to a sharp solute front and non-diffusive temporal scaling[11] and 2) the measured coefficients of pore diffusion scale in the expected way with molecular weight and free diffusivity; if a convective mechanism were at play, there should be no dependence of the rate of broadening on molecular weight.

E. Temporal control

We use pressure-driven flow of solutions through the microfluidic biomaterials to maintain hydration and mediate convective mass transfer to the bulk of the gels. As stated above in Introduction section, high Peclêt number ($Pe = u_c h_c / D_{s,c} \gg L/h_c$) and high Biot number ($Bi \gg 1$; $Bi = k_c H / D_{s,g}$ for non-reactive solutes or $Bi = k_c \lambda_K / D_{s,g}$ for reactive solutes) are required to avoid depletion of reagents along the length of the channels. When these conditions are not met (low *Pe* and *Bi*), gradients will develop both axially and transversely in both the fluid and the gel, as shown in Fig. 3.1C. When these conditions are met (high *Pe* and *Bi*), the concentration of solute at the inlet is delivered directly to the internal surfaces along the microchannels, as shown in Fig. 3.1D. In this regime, the mass transfer process is controlled by pure diffusion-reaction within the bulk of the scaffold with concentration boundary conditions defined by the inlet concentrations. The desirable mode of operation is required to achieve temporal control. Figure 3.12A shows snapshots of a microfluidic scaffold during delivery of fluorescein (frames 1 and 2) and simultaneous delivery of rhodamine B and extraction of fluorescein (frames 3 and 4) at high *Pe* and *Bi* ($u_c = 8$ cm/s, $Pe_{fluor} = 1.3 \times 10^4$, $Pe_{rhod} = 2.5 \times 10^4 \gg L/h_c$, $Bi_{fluor} = 300$ and $Bi_{rhod} = 370$). These images show that (1) the solutes within the scaffold can be changed over time via convective mass transfer and (2) at sufficiently high flow speeds, this temporal modulation occurs in a spatially uniform manner across the entire of the network (Fig. 3.12B). This temporal control will enable culture conditions to be tuned rapidly and uniformly to study dynamic response and to direct development of tissues.
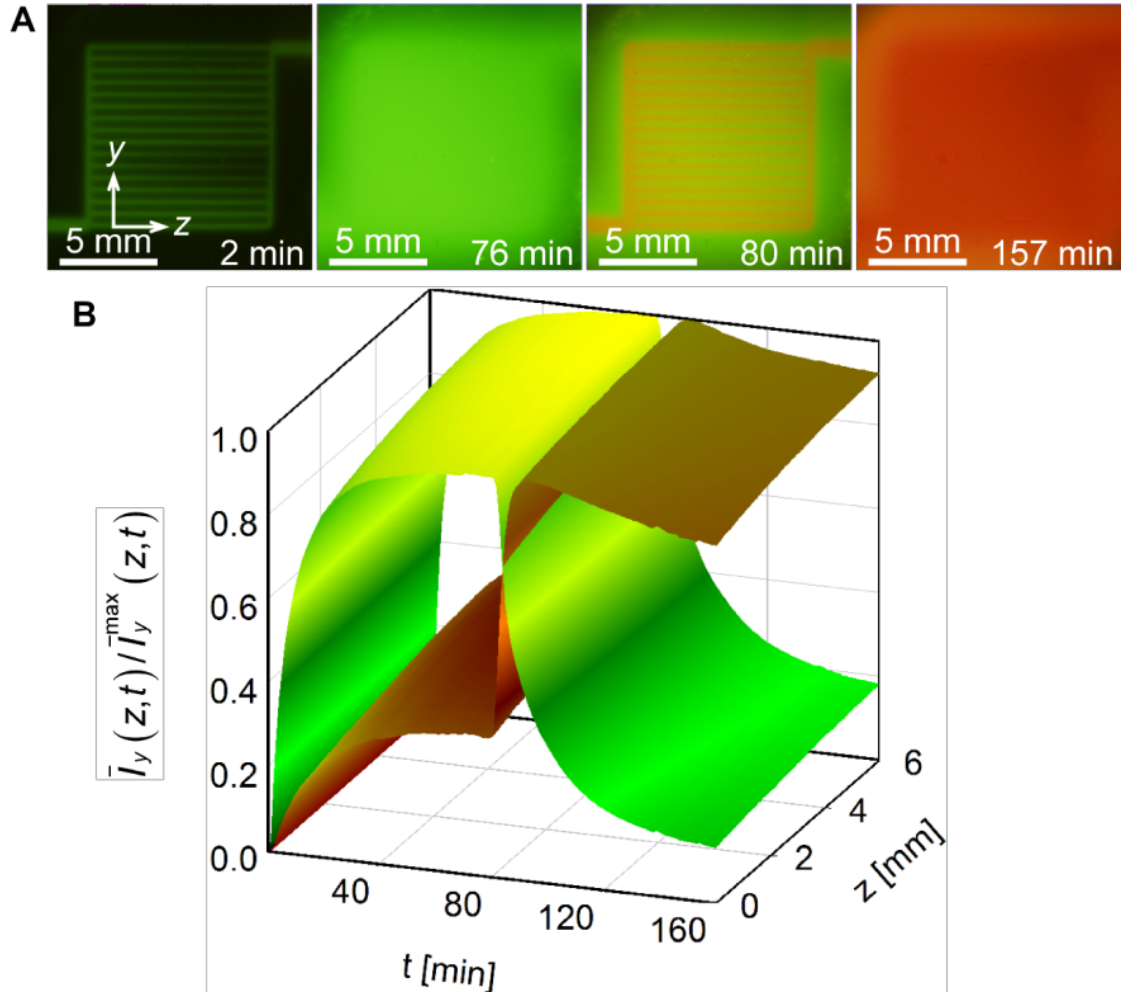
Figure 3.12 Temporal control in microfluidic biomaterials. **A.** Fluorescence micrographs of the microfluidic scaffold at time points during sequential delivery of solutes (fluorescein (green) and rhodamine B (red)) to the scaffold via embedded microchannels. **B.** Plot of normalized y-averaged intensity, $\bar{I}_y(z,t)$, of fluorescein (green) and rhodamine B (red) in a sequence of images as in A. The plot was obtained from a single sample. The results were consistent sample to sample. The experimental data points are mean values of fluorescence intensity (291 pixels in the y-direction) in the images. Standard deviations are smaller than the symbols.

F. Spatial control

As qualitatively described in the previous chapter (Fig. 2.6B and C), the double-network (as in Fig. 2.1Dii) allows maintaining gradients of solutes at steady state for both non-reactive and reactive solutes. The steady-state distribution of a non-reactive solute is uniform in the absence of sinks (Fig. 3.12A and B). Figure 3.13 shows the generation of gradients in microfluidic alginate scaffolds with two independent networks for non-reactive solutes (Fig. 3.13A and B; also see Fig. A4.1) and reactive solutes (Fig. 3.13C-E). The non-uniformity seen in the red zone in Fig. 3.13C is due to slight imperfections in the network that led to lower *Pe* in several channels. For the non-reactive low-molecular-weight solutes, the linear extent of the transition zones between regions of distinct chemistry is ~1 mm, as seen in the intensity profiles in Fig. 3.13B. Finite element models of this system indicate that this distance is controlled by the thickness of the scaffold ($H = 2$ mm) for this geometry. Sharper gradients can be attained in this system by reducing the total thickness of the scaffold; for $H < \lambda_c$ we predict that the gradient will be defined by λ_c. Figure 3.14 presents computational calculations of the distributions of non-reactive solutes in scaffolds of two different thicknesses. These calculations illustrate that the avaerage sharpness of the gradient achieved varies with the thickness in these cases for which the thickness is large compared to the interchannel spacing, λ_c. For reactive species, the extent of the transition between regions is ~0.5 mm for both solutes, as seen in the profiles in Fig. 3.13E. The fact that this distance is similar to the extent of the decay of intensity at the outside edges of the networks indicates that consumption of the reactive dyes is controlling the gradients in this case. In the following, we will further present the quantitative analysis of cellular consumption of one of the reactive dyes (i.e., calcein-AM-green) in microfluidic alginate scaffolds.

Figure 3.13 Spatial control in microfluidic biomaterials. A. Fluorescence

micrograph of acellular microfluidic scaffold after delivery of solutions of fluorescein

(5 μM; network 1) and rhodamine B (5 μM; network 2) at 50 μL/min

($Pe_{fluor} = 1.3 \times 10^4$ and $Pe_{rhod} = 2.5 \times 10^4$). The image was taken after 240 min;

fluorescein had been delivered for 120 min and rhodamine B for 240 min (also see Fig.

A4.1). **B.** Normalized intensity of fluorescein and rhodamine B along the *y* axis from

the image in A. The plot was obtained from a single sample. The results were

consistent sample to sample. **C.** Fluorescence micrograph of chondrocyte-seeded

(1×10^7 cell/mL) microfluidic scaffold after delivery of calcein-AM-green (5 μM;

network 1) and calcein-AM-red (2 μM; network 2) at 75 μL/min ($Pe_{calc-g} = 2.7 \times 10^4$

and $Pe_{calc-r} = 2.5 \times 10^4$). **D.** Fluorescence micrograph of a cross-section of the top

(micropatterned) layer (1×10^7 cell/mL) of the scaffold in C. The images in C and D

were taken after 220 min of delivery in both networks. **E.** Normalized intensity of

calcein-AM-green and calcein-AM-red along the *y* axis in the image in C. The plot

was obtained from a single sample. The results were consistent sample to sample.

A Network 1 120 min Network 2 240 min

y

5 mm

B

- ● Fluorescein
- ▲ Rhodamine

Normalized intensity

1.2
1.0
0.8
0.6
0.4
0.2
0.0

y [mm]

0 2 4 6 8 10 12 14

C Network 1 Network 2

y

5 mm

220 min

D

E

- ● Calcein-AM, green
- ▲ Calcein-AM, red-orange

Normalized intensity

1.2
1.0
0.8
0.6
0.4
0.2
0.0

y [mm]

0 2 4 6 8 10 12 14

100
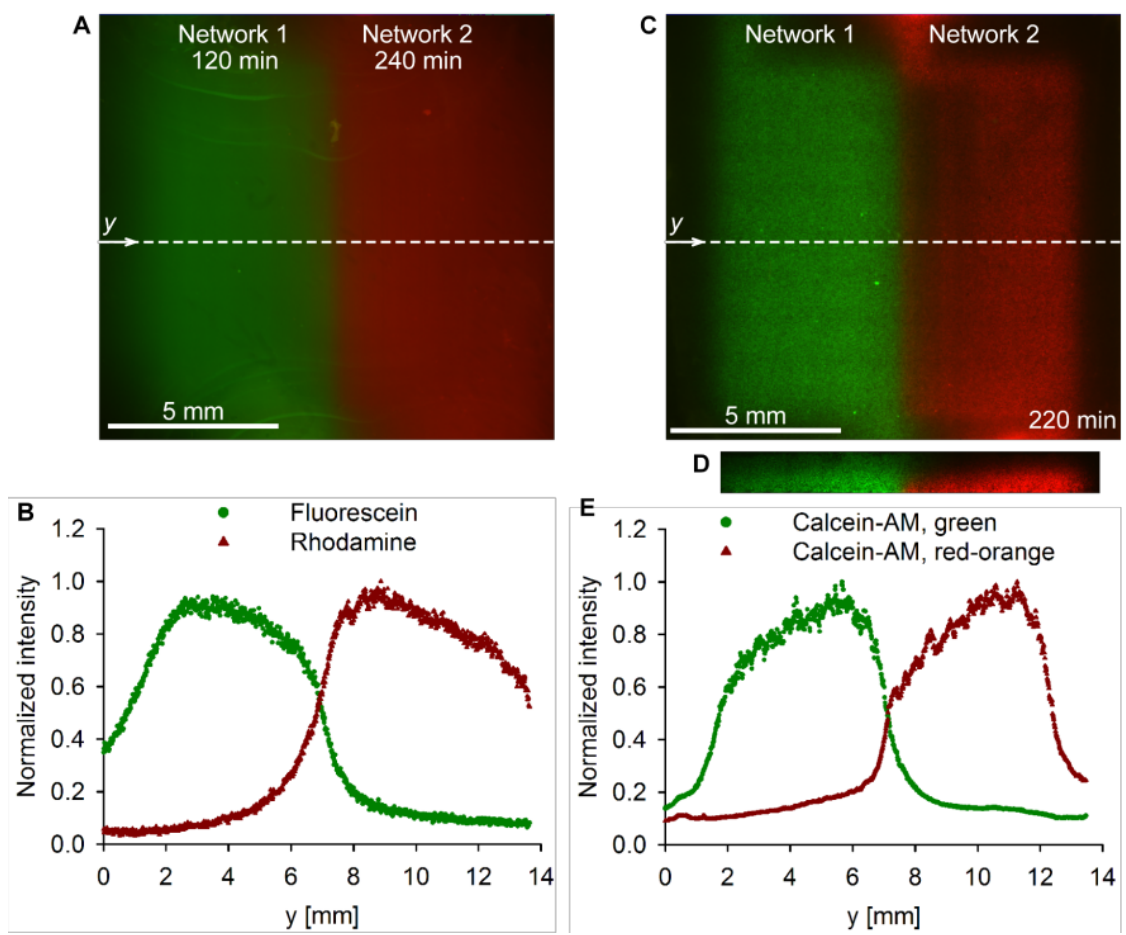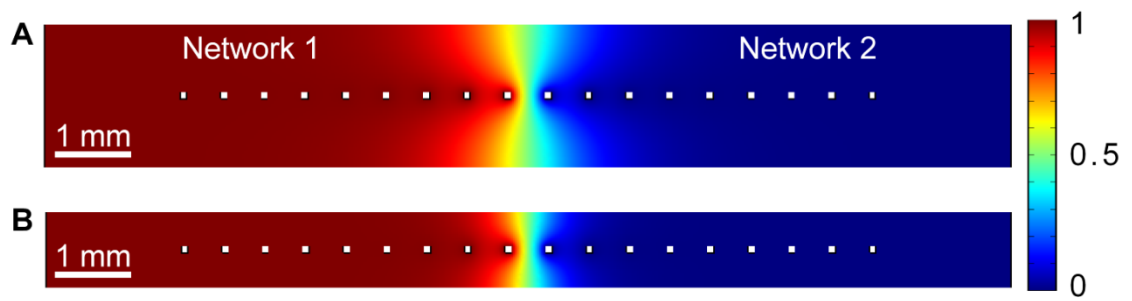
Figure 3.14 Steady-state distribution of a non-reactive solute delivered via the embedded microchannels in network 1 and extracted via those in network 2. Computationally calculated concentration profiles within a microfluidic scaffold with the thickness of 2 mm (A) and 1 mm (B). Concentration boundary conditions were maintained at the channel wall ($c_{wall} = 1$ in network 1; $c_{wall} = 0$ in network 2), and no-flux conditions were maintained at the top and bottom boundaries.

G. Quantitative analysis of metabolic diffusion-reaction processes in 3-D

With complete analysis of the distribution of fluorescent product in cross-sectional images as in Fig. 3.15B (also see Fig. 3.3), we can quantify metabolic diffusion-reaction processes within the 3D scaffold. Figure 3.15C shows the radial profile of fluorescence around microchannels in scaffolds seeded with cells at three different number densities: $\rho_{cell} = 1\times10^7$, 2.5×10^7, and 7.3×10^7 cell/mL. As expected, the zone of metabolic activity decays over a shorter distance at higher densities of cells. Furthermore, the observed profiles are in good agreement with computations. The computations were made with an effective first-order rate constant, $k_{eff} = \rho_{cell}k_{cell}$ $[\text{s}^{-1}]$, with a single value for the cellular rate constant, $k_{cell} = 1\times10^{-11}$ mL/cell·s (Fig. 3.16). These observations indicate that a continuum treatment of transport within a matrix seeded with discrete cells is appropriate and that k_{cell} is constant with respect to both the position and the density of the cells. The rate constant we infer from the comparison of experimental and computational profiles in Fig. 3.15C is six times lower than that measured for cells in suspension culture: $k_{cell}^{scaff} / k_{cell}^{susp} = 1/6$. This difference could be due to specific responses of the cells to the different culture environments; such differences between suspension or monolayer culture and 3-D culture have been noted before[12-17] and understanding their causes will require the type of quantitative tools for controlling and monitoring culture conditions in 3-D that we present here.

Figure 3.15 Delivery of metabolites via microfluidic network. A. Fluorescence micrographs of a chondrocyte-seeded (2.5×10^7 cell/mL) microfluidic scaffold after delivery of 5 μM calcein-AM-green through microfluidic network for 2 h. **B.** Fluorescence micrograph of a cross-section of the top (micropatterned) layer (2.5×10^7 cell/mL) of the scaffold in A. **C.** Radial profiles of experimentally measured calcein intensity ($I_{\text{Exp.}} / I_{\text{Exp.}}^{\max}$; symbols) and computationally calculated calcein-AM concentration ($c_{\text{FEM}} / c_{\text{FEM}}^{\max}$; solid lines) at various seeding densities (1×10^7 (red), 2.5×10^7 (green), and 7.3×10^7 (blue) cell/mL). The experimental data points are mean values of the normalized intensity of the calcein around the microchannels (three channels for 1×10^7 cell/mL, four channels for 2.5×10^7 cell/mL, and five channels for 7.3×10^7 cell/mL) in images such as in B. Each plot presenting experimental data was obtained from a single sample. The error bars indicate standard deviations. R^2 of 0.97, 0.97, and 0.98; RMSE of 0.030, 0.056, and 0.035 for 1×10^7, 2.5×10^7, and 7.3×10^7 cell/mL, respectively (also see Appendix 5).

A

4.1 mm   2.1 mm 1.1 mm 0.6 mm

z

y

5 mm

120 min

B

C

$\dfrac{I_{Exp.}}{I_{Exp.}^{max}}$ and $\dfrac{C_{FEM}}{C_{FEM}^{max}}$

1.0

0.8

0.6

0.4

0.2

0.0

0.0   0.2   0.4   0.6   0.8

Radial distance [mm]
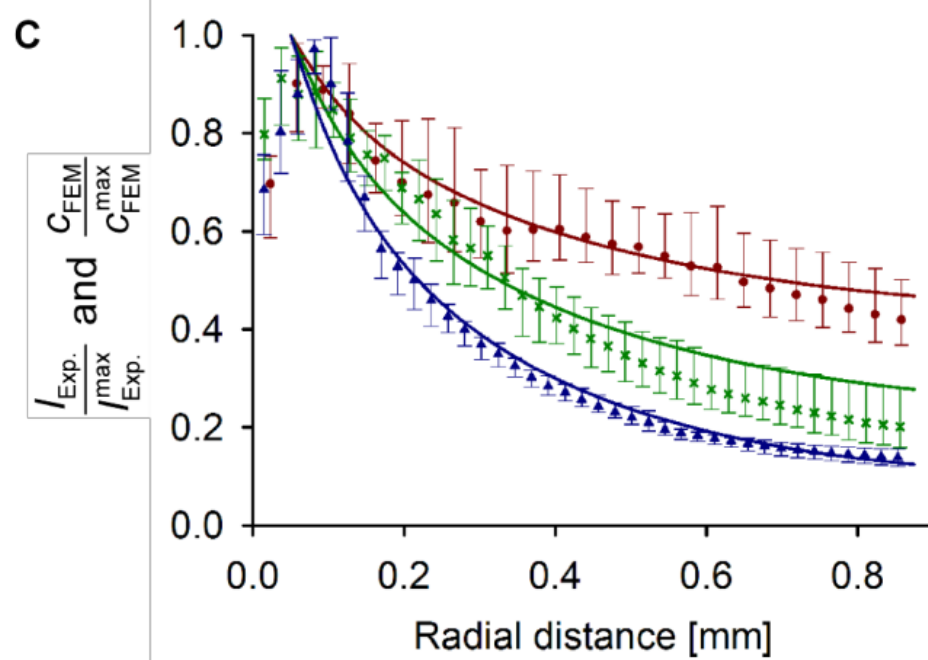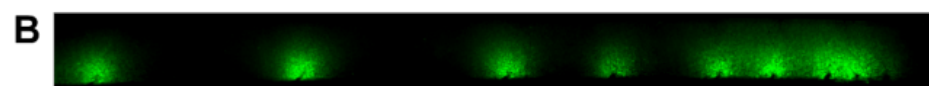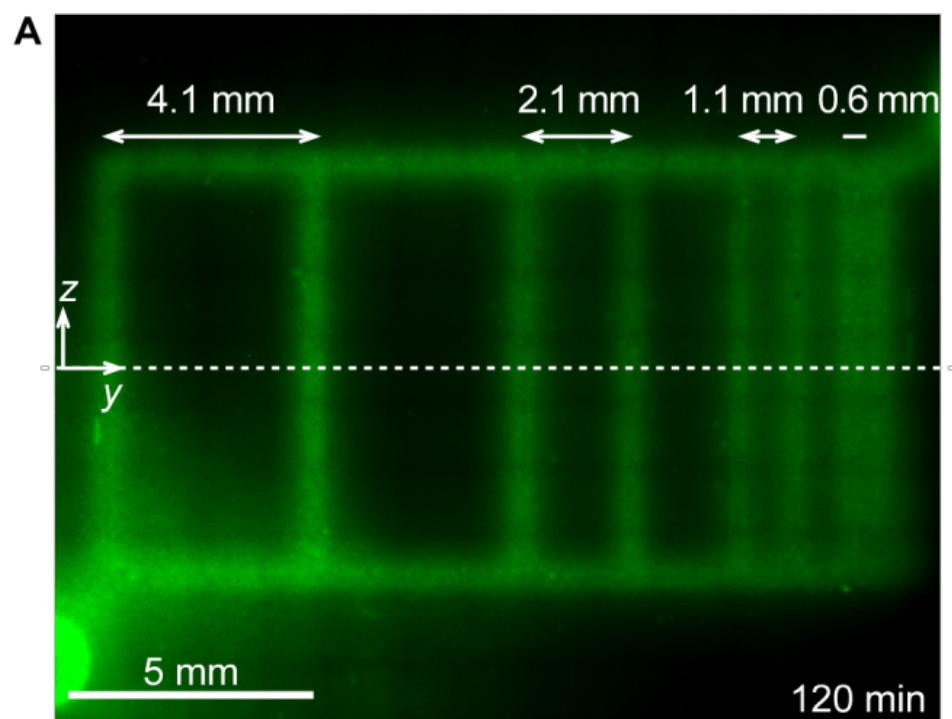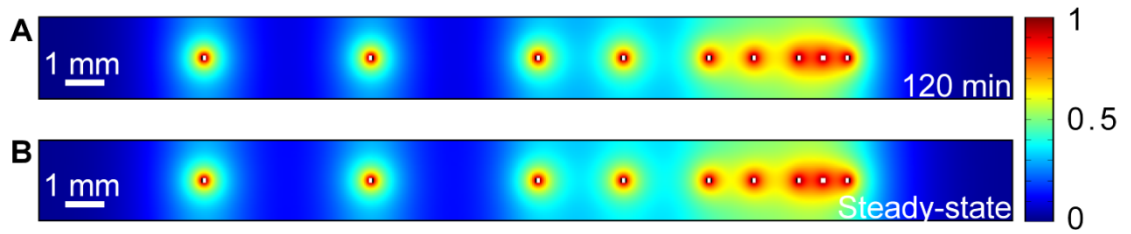
Figure 3.16 Distribution of a reactive solute delivered via the embedded microchannels within a microfluidic scaffold with variably spaced microchannels. Concentration of calcein-AM calculated by finite element method with an assumption of first order kinetics with $D_{calc-g,g} = 2.4 \times 10^{-6}$ cm^2/s, $k_{cell} = 1 \times 10^{-11}$ mL/cell·s, and $\rho_{cell} = 2.5 \times 10^{7}$ cell/mL. Concentration boundary conditions were maintained at the channel walls ($c_{wall} = 1$), and no-flux conditions were maintained at the top and bottom boundaries. The distributions are shown for $t = 120$ min (A) and steady state (B).

H. Diffusion-reaction of a metabolite (oxygen) in alginate

Quantitative measurement of metabolic activity (i.e., oxygen consumption rate, OCR) of cells in 3-D allows estimating oxygen depletion length or Krogh lengh, λ_K. As briefly stated in the previous chapter and also demonstrated above, such estimation is essential in designing microfluidic biomaterials (i.e., scaffold thickness, H and interchannel distance, λ_c). As shown in Fig. 2.8C, it is clear that there was a mixed distribution of normoxic (near microchannels) and hypoxic cells (far from microchannels) within a single scaffold due to significant gradients of oxygen concentration created by cellular consumption. The measurement of OCR allows appropriately choosing the design parameters such that we can 1) avoid creating necrotic regions within tissue constructs in the context of tissue engineering, and 2) elucidate oxygen-dependent cellular activity in the context of tissue-scale biology. We have adapted this principle to study oxygen-dependent angiogenic activity of tumor cells in 3-D by culturing 200 µm-thick alginate discs seeded with OSCC-3s. We have chosen 200 µm to achieve uniform distributions of oxygen concentration. Figure 3.17 shows histological sections of the tumor cell-seeded alginate discs stained with H&E and hypoxyprobe on day 6. Similarly as shown Fig. 2.8, cellularity was maintained through the both cultures at 1 and 17 % O_2, and hypoxic cells (brown) were uniformly stained only in the disc cultured at 1 % O_2 (Fig. 3.17). This confirms that we have successfully separated hypoxic and normoxic regions. These regions represent hypoxic core and normoxic periphery in a solid tumor.
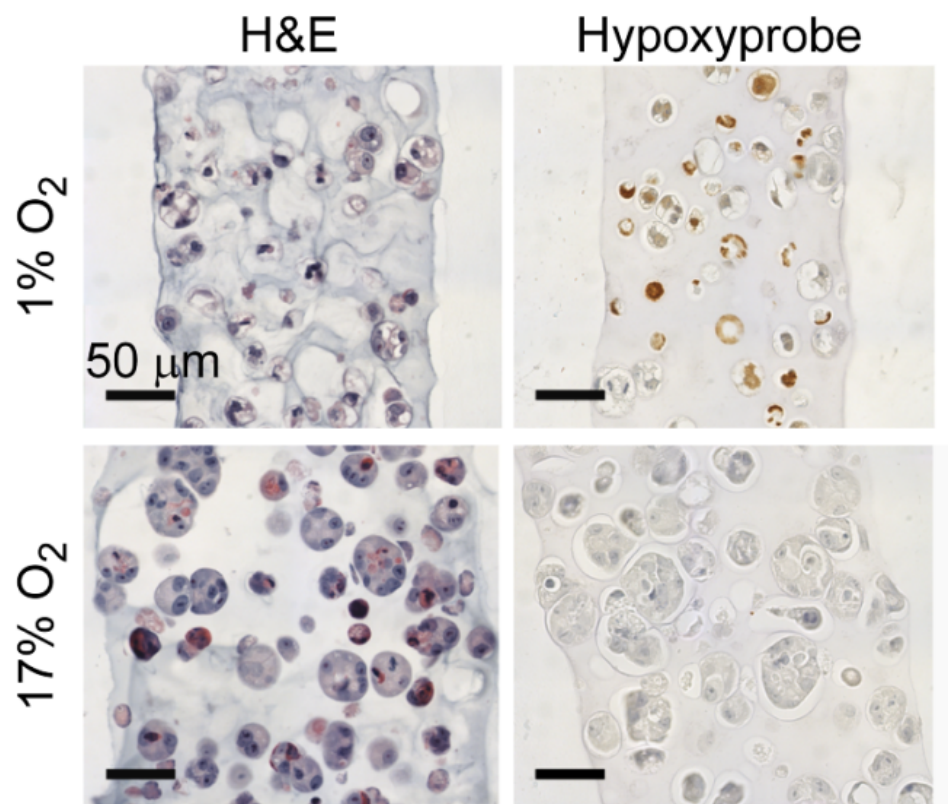
Figure 3.17 Histological images of alginate discs seeded with OSCC-3s. Optical micrographs showing histological cross-sections of 4 % [w/v] alginate seeded with OSCC-3s (2×10^7 cell/mL), cultured at 1 (top) and 17 (bottom) % O_2 for 6 days, stained with H&E (left) and hypoxyprobe (right) after the culture. Brown circles are hypoxic cells.

Cellular O_2 consumption was similar between OSCC-3s cultured in alginate ($R_{O_2,cell}^{scaff} = 5.4 \pm 0.2 \times 10^{-17}$ mol/s·cell), and those measured in suspension ($R_{O_2,cell}^{susp} = 4.8 \pm 0.5 \times 10^{-17}$ mol/s·cell), indicating that encapsulation within alginate did not significantly affect the metabolic activity of these cells. Furthermore, these rates were similar to the O_2 consumption rate reported for other tumor cells[18-19]. Finite element modeling of the steady-state O_2 distribution within the engineered tumors (cell seeding density, measured O_2 consumption and a reported O_2 diffusivity were used as inputs) indicated uniformity of oxygen concentration within 200 μm-thick tumor models (central and peripheral c_{O_2} differed by < 2 % for the initial seeding density); whereas significant non-uniformity was predicted for tumor models ≥ 500 μm in thickness (> 25 % difference between central and peripheral c_{O_2} values at the initial seeding density for a 1 mm thick scaffold) (Fig. 3.19). Theoretically calculated $\lambda_K = \sqrt{c_0 D_{O_2} / \rho_{cell} R_{O_2,cell}}$ with the assumption of zeroth order kinetics is 668 μm which confirms that 200 μm was indeed thin enough to achieve uniform oxygen concentration within the tumor cell-seeded alginate discs.

We have also measured OCR of OSCC-3s cultured at different oxygen concentrations. Figure 3.18B shows that 1) OCR at 17 % O_2 is significantly larger than that at other pre-incubation oxygen concentrations, and 2) the measured OCRs of OSCC-3s pre-incubated at 1, 5, 9, and 13 % O_2 are similar (except for the case between 1 and 9 % O_2). Generally, it is reasonable to state that oxygen consumption kinetics generally follows Michaelis-Menten kinetics:

$$R_{O_2,cell} = \frac{v_{m,cell} c_{O_2}}{K_M + c_{O_2}} \tag{3.15}$$

, where $v_{m,cell}$ [mol/s·cell] is maximum consumption rate, and K_M [mol/m^3] is Michaelis-Menten constant. The consumption kinetics falls to zeroth order

($R_{O_2} \approx \rho_{cell} v_{m,cell}$) when $c_{O_2} \gg K_M$ and first order ($R_{O_2} \approx \left(\rho_{cell} v_{m,cell} / K_M \right) c_{O_2}$) when $c_{O_2} \ll K_M$. Figure 3.18B seemingly implies that oxygen consumption kinetics of OSCC-3s seeded in alginate is neither zeroth nor first order. However, we have observed that the linearity of c_{O_2} decrease was maintained consistently throughout the four measurements at every pre-incubation c_{O_2}. We note that oxygen concentration within the 2 mL-glass chamber decreased by a factor of ~3 for OCR at 17 % O_2 (Fig. 3.18A). In addition, reported K_M values range from 10^{-5} to 7×10^{-3} mol/m^3 [20]; 17 % O_2 corresponds to ~1.7 mol/m^3. This indicates that it is valid to assume that the kinetics is zeroth order. The discrepancy between our observations could result from the following two reasons: 1) $v_{m,cell}$ may be a function of pre-incubation c_{O_2} such that cells have adapted to become metabolically low over the pre-incubation period (no such pre-incubation period for 17 % O_2), and 2) measured OCR values of the cells pre-incubated at lower oxygen concentrations do not represent actual OCR at the lower concentrations due to technical difficulty of the measurement at low c_{O_2}. For example, oxygen concentration of media pre-incubated at 1 % O_2 rapidly increased up to ~ 6 % when an actual measurement was initiated. This is because the ambient oxygen was rapidly diffusing into the glass chamber filled with the pre-incubated media while four discs were transferred to the chamber. This technical difficulty could be resolved by pre-incubating open chambers where four discs have been already submerged in media. We expect that this approach eliminates at least the ambiguity caused by the disc-transfer process. For future experiments, it is also required to allow the measurements to last until the linearity breaks down to find out cellular response time scales to change their metabolic activity.
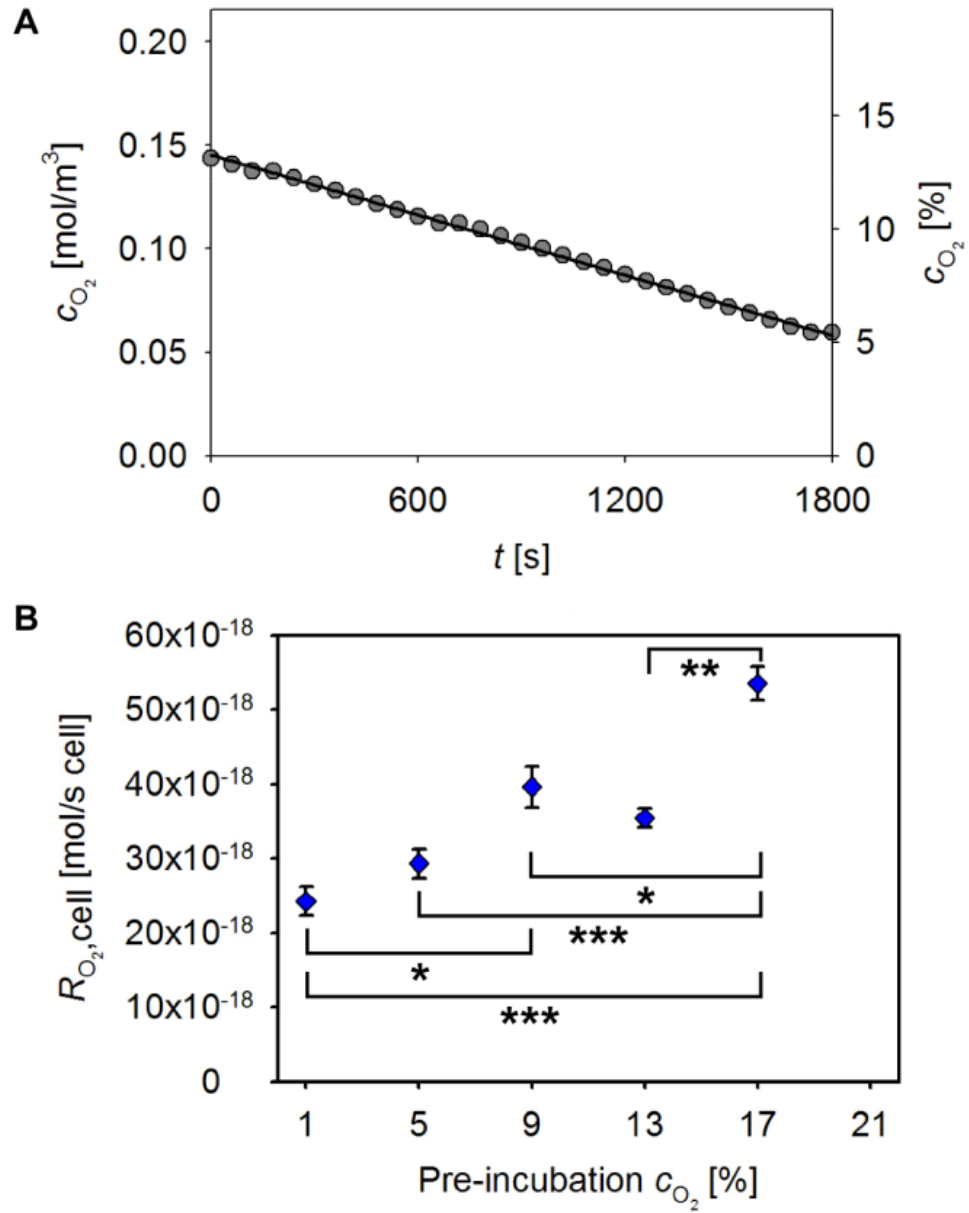
Figure 3.18 Oxygen consumption of OSCC-3s seeded in alginate discs. A. Plot of time evolution of oxygen concentration in disc-suspended media within a sealed glass chamber. **B.** Plot of oxygen consumption rate of OSCC-3 pre-incubated at various oxygen concentrations.
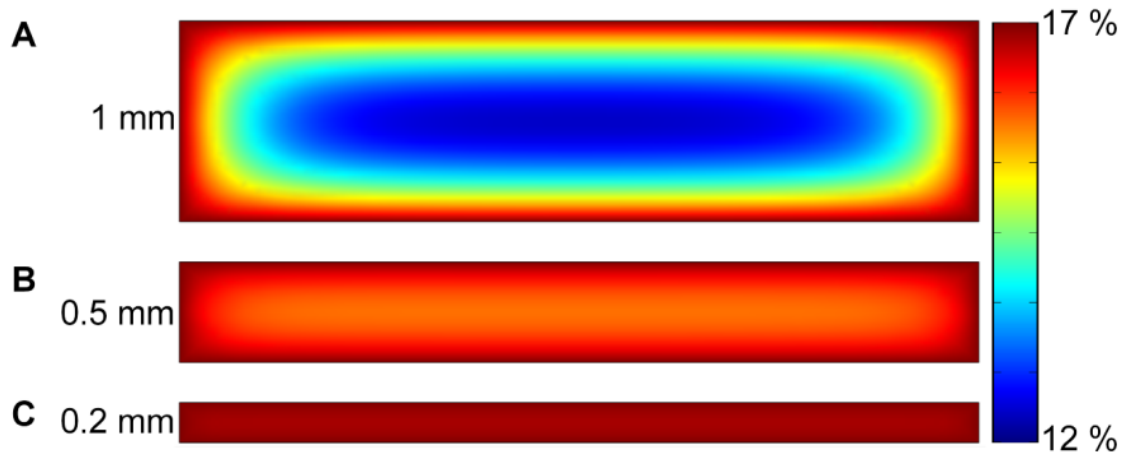
Figure 3.19 Steady-state distributions of oxygen within tumor cell-seeded alginate discs. A-C. Concentration of oxygen calculated by finite element method with an assumption of zeroth order kinetics with $D_{O_2} = 2.76 \times 10^{-5}$ cm^2/s, $c_0 = 0.17$ mol/m^3, $R_{O_2,\text{cell}} = 5.4 \times 10^{-17}$ mol/s$\cdot$cell, $\rho_{\text{cell}} = 2 \times 10^7$ cell/mL, $H = 1$ (A), 0.5 (B), and 0.2 (C) mm. Concentration boundary conditions were maintained at all surfaces of the discs ($c = c_0$).

Conclusions

In this chapter, we have presented detailed mass transport considerations in microfluidic biomaterials where diffusion and diffusion-reaction processes controlled by convective delivery of solutes via microchannels are essential. These microfluidic channels enable quantitative control of the soluble environment experienced by the cells in their 3D environment. The FAMI technique allows measuring diffusivity of small and macromolecules within microfluidic biomaterials, and should be also useful to measure diffusivity of solutes after remodeling and deposition of ECM components has occurred within microfluidic scaffolds. In addition to the diffusivity measurements, the quantitative analyses of metabolic diffusion-reaction processes within microfluidic biomaterials allow determining important design parameters for tissue engineering and tissue-scale biology. More specifically, oxygen transport is the key not only in maintaining metabolic activity of cells within growing engineered tissue constructs but also in elucidating roles of oxygen in various physiological and pathological processes in tissue-scale (e.g., differentiation and phenotypic behavior of stem cells, angiogenic activity of tumor cells, tumor angiogenesis in 3-D scaffolds). A remaining challenge is to run multiple replicates of microfluidic biomaterials for long periods of time (weeks) without significantly loosing functionality. There is still a lack of microscopy techniques and equipments that allow monitoring systems of interest in real time. Customizable and relatively small-sized microscopy technique[21] that can be operated in incubators may aid to study dynamic biological processes. Combining with other useful tools to monitor oxygen distribution in a spatiotemporal manner will also open new opportunities.

REFERENCES

1.   Fournier, R.L., *Basic transport phenomena in biomedical engineering*, 1st ed. (Taylor & Francis, London, 1999).

2.   Bird, R.B. *et al.*, *Transport Phenomena*, 2nd ed. (John Wiley & Sons, Inc., Hoboken, 2002).

3.   Spaeth, E.E. & Friedlan.Sk, Diffusion of oxygen, carbon dioxide, and inert gas in flowing blood. *Biophys. J.* **7** (6), 827-851 (1967).

4.   Gribbon, P. & Hardingham, T.E., Macromolecular diffusion of biological polymers measured by confocal fluorescence recovery after photobleaching. *Biophys. J.* **75** (2), 1032-1039 (1998).

5.   Moore, A.W. & Jorgenson, J.W., Study of zone broadening in optically gated high-speed capillary electrophoresis. *Anal. Chem.* **65** (24), 3550-3560 (1993).

6.   Schwuchow, J.M. *et al.*, Tip-growing cells of the moss Ceratodon purpureus are gravitropic in high-density media. *Plant Physiol.* **130** (4), 2095-2100 (2002).

7.   Periasamy, N. & Verkman, A.S., Analysis of fluorophore diffusion by continuous distributions of diffusion coefficients: Application to photobleaching measurements of multicomponent and anomalous diffusion. *Biophys. J.* **75** (1), 557-567 (1998).

8.   Bohrer, M.P. *et al.*, Influence of molecular configuration on the passage of macromolecules across the glomerular capillary wall. *J. Gen. Physiol.* **74** (5), 583-593 (1979).

9.   Williams, J.C. *et al.*, Partition and permeation of dextran in polyacrylamide gel. *Biophys. J.* **75** (1), 493-502 (1998).

10.   Scheidegger, A.E., *The physics of flow through porous media*. (University of Toronto, Toronto, 1960).

11.   Neeves, K.B. *et al.*, Fabrication and characterization of microfluidic probes for convection enhanced drug delivery. *J. Control. Release* **111** (3), 252-262 (2006).

12.   Benya, P.D. & Shaffer, J.D., Dedifferntiated chodrocytes reexpress the differentiated collagen phenotype when cultured in agarose gels. *Cell* **30** (1), 215-224 (1982).

13.   Liu, H. *et al.*, Re-expression of differentiated proteoglycan phenotype by dedifferentiated human chondrocytes during culture in alginate beads. *Biochim. Biophys. Acta.* **1425** (3), 505-515 (1998).

14.   Coward, S.M. *et al.*, Proliferation rates of HepG2 cells encapsulated in alginate are increased in a microgravity environment compared with static cultures. *Artif. Organs* **29** (2), 152-158 (2005).

15.   Sivaraman, A. *et al.*, A microscale in vitro physiological model of the liver: Predictive screens for drug metabolism and enzyme induction. *Curr. Drug. Metab.* **6** (6), 569-591 (2005).

16.   El-Ali, J. *et al.*, Cells on chips. *Nature* **442** (7101), 403-411 (2006).

17.   Matsumoto, T. *et al.*, Mechanical strain regulates endothelial cell patterning in vitro. *Tissue Eng.* **13** (1), 207-217 (2007).

18.   Muellerklieser, W. *et al.*, A new photometric method for oxygen consumption measurements in cell suspensions. *J. Appl. Physiol.* **61** (2), 449-455 (1986).

19.   Spaeth, E.E. & Friedlan.Sk, Diffusion of oxygen, carbon dioxide, and inert gas in flowing blood. *Biophys. J.* **7** (6), 827-& (1967).

20.   Lovett, M. *et al.*, Vascularization Strategies for Tissue Engineering. *Tissue Eng. Part B-Rev.* **15** (3), 353-370 (2009).

21.   Sung, J.H., Choi, J. Y., Kim, D, Shuler, M. L., Fluorescence optical detection in situ for real-time monitoring of cytochrome P450 enzymatic activity of liver cells in multiple microfluidic devices. *Biotechnol. Bioeng.* **104** (3), 516-525 (2009).

CHAPTER 4

DISPERSIBLE OXYGEN-SENSING PARTICLES FOR APPLICATIONS *IN VITRO*

AND *IN VIVO*

I. Introduction

In the previous chapter, we demonstrated quantitative analyses of metabolic activity of cells within microfluidic biomaterials. We also measured the oxygen consumption rate of cells and showed that it was a necessary piece of information in designing microfluidic biomaterials. In this chapter, we present the development of a powerful tool for oxygen-sensing, which can also be combined with microfluidic biomaterials. There has been remarkably increased interest in sensing oxygen levels in biomedical fields for the preceding few years[1-3]. Strategies for measurement of oxygen levels include commercially available oxygen electrodes[4] and oxygen-sensing luminophores[1,5]. However, the oxygen electrodes are difficult to adapt to the small size scales relevant to oxygen diffusion limits within tissue. In addition, the electrodes, based on electrochemical reduction of oxygen, cause oxygen consumption and have relatively long response times[6]. In the context of dispersed luminophores, either an optical sensing matrix or biology is confined in a certain place, which does not allow fully mapping the distribution of oxygen levels within cell-seeded tissue scaffolds. To overcome these difficulties, we propose to develop oxygen-sensing particles that are stably dispersible in aqueous environments and biocompatible. Figure 4.1 shows our strategy: 1) the synthesis of the oxygen-sensing micro- and nanoparticles using oxygen-sensitive phosphors and monomers, 2) characterization of the particles, 3) calibration of the particles with the measurement of phosphorescence lifetimes, and 4) demonstrations for visualization and measurement of oxygen-depletion lengths in

tumor cell-seeded alginate, *in vitro* and oxygen imaging in blood vessels *in vivo*. We will then conclude with some remaining challenges and future directions.

Materials and methods

    A. Synthesis of oxygen-sensing microparticles

    Oxygen-sensing polymeric microparticles were synthesized via dispersion polymerization[7] using Pt(II) meso-Tetra(pentafluorophenyl)porphine (PtTFPP; MW 1168.62 Da; Frontier Scientific Inc., Logan, UT) as an oxygen-sensitive phosphor[8] and poly(styrene) (PS; Sigma-Aldrich, St. Louis, MO) as an encapsulating polymer[9]. A reaction medium was prepared with 4.45 % [w/w] poly(vinyl pyrrolidone) (PVP; Sigma-Aldrich, St. Louis, MO) dissolved in 90 % [v/v] ethanol. A monomer medium was prepared with 10 % [w/w] styrene (monomer), 0.5 % [w/w] 2,2'-azobisisobutyronitrile (AIBN; initiator; Sigma-Aldrich, St. Louis, MO), and 1 % [w/w] PtTFPP. After allowing each medium to be well-mixed for 1.5 hr, the monomer medium was transferred into the reaction medium. Dispersion polymerization was then allowed for 24 hr with mild stirring in a 70 ºC silicone oil bath. Synthesized oxygen-sensing microparticles were washed several times with 10 % [v/v] ethanol and kept dispersed in water at room temperature prior to usage (also see Appendix 6).
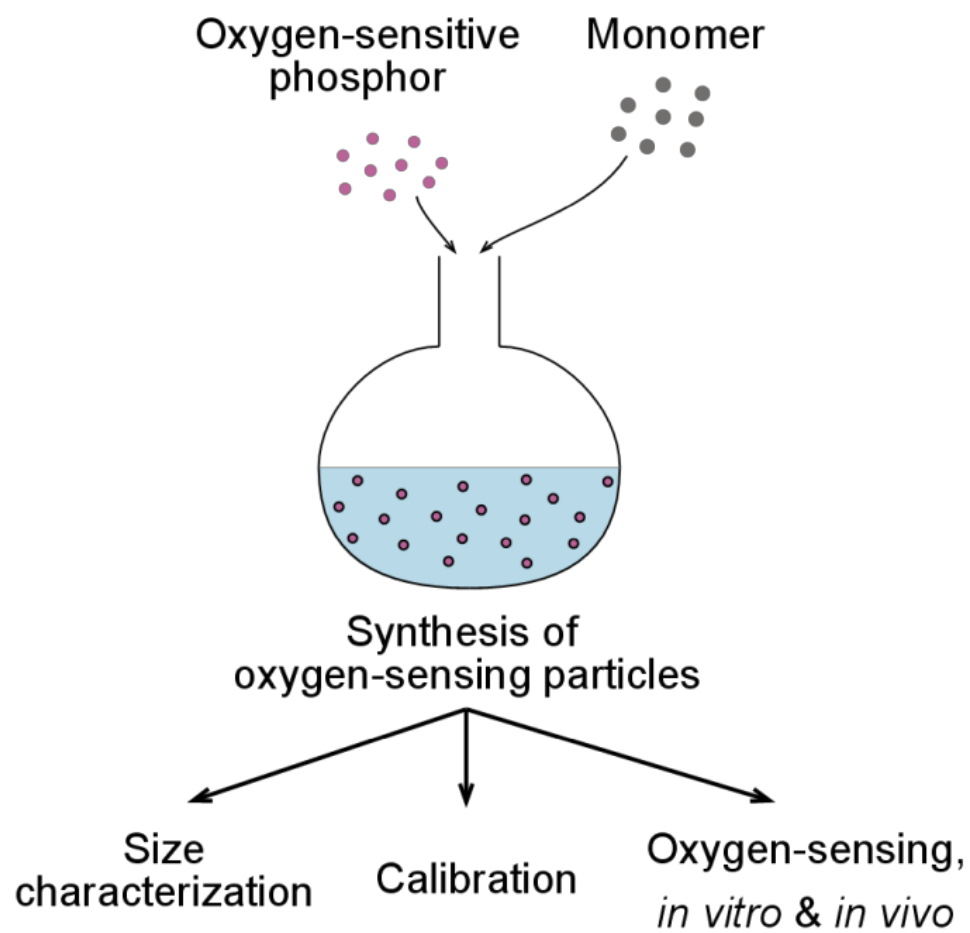
Figure 4.1 Schematic illustration of experimental approach for oxygen-sensing.
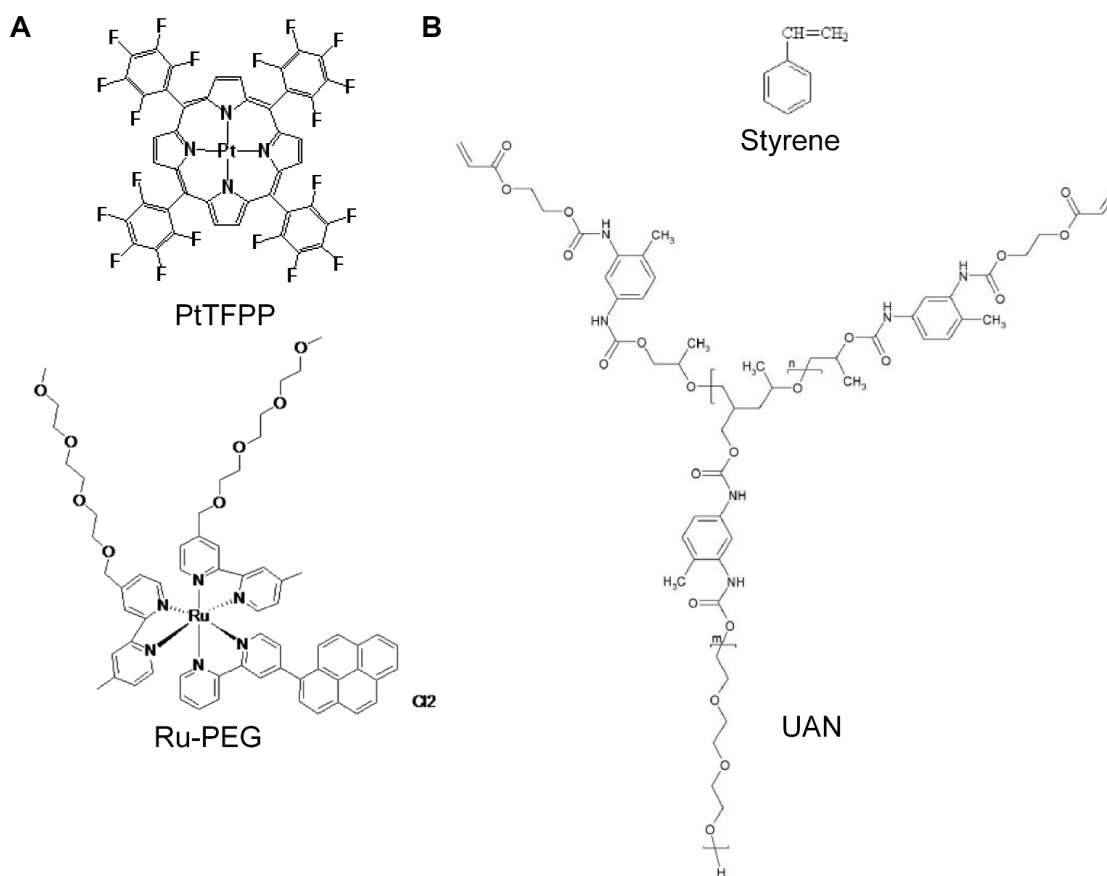
Figure 4.2 Chemical structure of oxygen-sensitive phosphors and monomers used in this study. **A.** Oxygen-sensitive phosphors. PtTFPP, Ru-PEG stand for Pt(II) meso-Tetra(pentafluorophenyl)porphine and $[Ru(dmb-PEG)_2(pyr-bpy)]Cl_2$ respectively. **B.** Monomers used for synthesizing polymeric particles. UAN stands for urethane acrylate nonionomer.

B. Synthesis of oxygen-sensing nanoparticles

Oxygen-sensing polymeric nanoparticles were synthesized via emulsion polymerization using either PtTFPP or [Ru(dmb-PEG)$_2$(pyr-bpy)]Cl$_2$ (Ru-PEG; provided by Schmehl group at Tulane University, New Orleans, LA) as oxygen-sensitive phosphors and poly(urethane acrylate nonionomer) (PUAN; provided by Kim group at Kangwon National University, Samcheok, Korea) as an encapsulating polymer. First, a phosphor was pre-partitioned in amphiphilic precursor, urethane acrylate nonionomer (UAN): 1) ~ 4 µmol of a phosphor was dissolved in 3 ~ 4 mL of methylene chloride (MC), 2) 1 g of UAN was dissolved in the phosphor-dissolved MC, and 3) MC was allowed to evaporate in a fume hood for ~ 8 h. After the phosphor-partitioned UAN was fully re-dissolved in 9 g of potassium persulfate (KPS; thermal initiator)-dissolved deionized (DI) water (2 mg/mL), emulsion polymerization was then allowed with strong agitation in a 65 ℃ silicone oil bath for 5 h. Nitrogen gas was applied into the reaction medium for first 2 h. Oxygen-sensing nanoparticle suspensions were dialyzed with a molecular weight cutoff of 50,000 for 2 days and stored at room temperature prior to usage (also see Appendices 7 and 8).

C. Measurement of the size distribution of micro- and nanoparticles using Dynamic Light Scattering (DLS)

The size distribution of oxygen-sensing micro- and nanoparticles suspended in water was measured using Zetasizer Nano-ZS (Malvern Instruments Ltd., Worcestershire, UK). 400 µL of each suspension at a concentration of < 1 % [w/v] (microparticles) or 10 % [w/v] (nanoparticles) was used for a measurement and analyzed with 4 mW He-Ne laser (633 nm) to avoid unnecessary excitation from the phosphors that might affect DLS measurements. Each measurement consisted of 40 ~

50 repeated sub-measurements and size distributions were computed automatically in Zetasizer Software (www.malvern.com).

D. Transmission Electron Microscopy (TEM)

Nanoparticles were suspended in water at a concentration of approximately 1 % [w/v] solid content. A 5 μL droplet of this solution was applied to a freshly glow-discharged 300 mesh, carbon-coated formvar grid (Ted Pella Inc., Redding, CA). After a 2 min-incubation, the nanoparticle suspension was removed from the grid by wicking with filter paper, the grid was washed with distilled water, and a 5 μL droplet of 1% [w/v] uranyl acetate (UA) staining solution was applied to the grid for 1 min. After the staining solution was removed, the grid was allowed to air dry at room temperature. The grids were imaged at a magnification of x180,000 using a G^2 Spirit Tecnai (120 kV) transmission electron microscope (FEI, Hilsboro, OR).

E. Calibration of oxygen-sensing particles by the measurement of phosphorescence lifetime

Oxygen-sensing nanoparticles suspended in aqueous dispersants (i.e., water, ethanol, and alginate) were calibrated to obtain Stern-Volmer plots (phosphorescence lifetime vs. oxygen concentration) by measuring phosphorescence lifetime at various oxygen concentrations between 0 and 40 % O_2. Oxygen levels were controlled using an OxyDial gas mixer (Starr Life Sciences Co., Oakmont, PA).

Lifetime measurements were made on a two photon microscope consisting of a Ti:Sapphire laser (Millennia Xs/Tsunami combination, Spectra Physics, Mountain View, CA) directed into a modified BioRad MRC 600 laser scanner interfaced with a modified (fixed-stage) upright microscope (Olympus AX-70, Center Valley, PA). A 350-80 BKLA Pockel's Cell (Conoptics, Danbury, CT) with custom-made electronics

provided beam intensity modulation and blanking during scanner flyback. 880nm light (~440 nm excitation) was focused into the specimen with a large-barrel Olympus 20x/0.95 NA water immersion dipping objective. Emission was separated with a 750 nm long-pass dichroic, filtered with a HQ650/100M emission filter (both from Chroma Technology, Rockingham, VT) and detected with a GAsP PMT (H7422P-40, Hamamatsu, Hamamatsu City, Japan), amplified, and directed into the external ports of the BioRad acquisition electronics.

The Pockel's Cell was used to deliver repeated pulses followed by monitoring periods with no laser power (< 3 % corresponding to < 0.1 % excitation). Phosphorescence curves were acquired using a SR430 multichannel scaler (Stanford Research Systems, Sunnyvale,CA) and the electronics were synchronized for repeated 5 µs-pulse patterns using a DG535 digital delay/pulse generator (Stanford Research Systems). The decay curves were fit to single exponentials using SigmaPlot (Systat Software Inc., San Jose, CA). More detailed information about the multi-photon microscopy can be found from work done by Williams, *et al.*[10].

F. 2-D culture of tumor cells with oxygen-sensing particles

Oral squamous cell carcinoma (OSCC-3; provided by Fischbach group at Cornell University) cells were cultured in BD Falcon[TM] 12-well plates (BD Biosciences, San Jose, CA), at 37 ºC, 5 % CO_2, for 1 week, either without or with oxygen-sensing particles. OSCC-3s were initially plated at a density of 10,000 cell/well, and fed with Dulbecco's Modified Eagle Medium (DMEM; Invitrogen Co., Carlabad, CA) with 10 % [v/v] fetal bovine serum (FBS; Lonza Inc., Walkersville, MD) and 1 % [v/v] penicillin/streptomycin (PS; 120 U/mL; Gibco, Grand Island, NY). Various doses of oxygen-sensing particles (0.02, 0.05, 0.1, 1, and 10 % [w/v] for Ru-PEG-PUAN nanoparticles, and 5×10^7 bead/mL for PtTFPP-PS microparticles) were

prepared by re-suspending sterile particles in culture media. Microparticles were sterilized by suspending in 70 % [v/v] ethanol for several hours and nanoparticles by syringe-filtering through a 200 nm-pore membrane. At the end of the culture, cells were trypsinized and counted for comparison between cases.

G. *3-D culture of tumor cells seeded in oxygen-sensing particle-dispersed alginate discs*

Sterile oxygen-sensing particles were first dispersed in phenol red-free DMEM (Invitrogen): 1 % [w/v] for nanoparticles. 4 % [w/v] oxygen-sensing particle-dispersed alginate was prepared by dissolving lyopholized alginate (Protanal LF; FMC Biopolymer, Philadelphia, PA) in the media. Then, trypsinized OSCC-3s were gently suspended in the alginate and calcium alginate discs (200 µm thick, 4 mm in diameter) were fabricated as described in Chapter 3 (Fig. 3.x). Alginate discs seeded with both OSCC-3s and oxygen-sensing particles were cultured in 24-well plates at 37 ℃, 5% CO_2 for 7 days.

H. *Live/dead assay*

Viability of OSCC-3s seeded in oxygen-sensing particle-dispersed alginate discs was qualitatively estimated on day 0 and 7. Alginate discs were submerged in a live/dead staining solution (5 µM calcein-AM-green and 5 µM ethidium homodimer-1; Invitrogen) in a pH-adjusted buffer solution. The submerged discs were incubated for 1 h prior to fluorescence microscopy. Images were taken on an inverted microscope (Axio Observer; Carl Zeiss Inc., Thornwood, NY). ImageJ enabled the merging of green and red fluorescence images.

I. DNA assay

Alginate discs were dissolved using ethylenediaminetetraacetic acid (EDTA, EMD Chemicals, Gibbstown, NJ), released cells were rinsed, and then lysed in Caron's buffer. DNA content was measured using Quant-iT™ PicoGreen® dsDNA reagent (Invitrogen), and cell number calculated using a measured value of 15.1 pg DNA/OSCC-3 cell on day 0 and 7.

J. Direct imaging of phosphorescence

PtTFPP was excited at 392 nm and corresponding phosphorescence images were acquired at 650 nm using a stereomicroscope (Model MZ FLIII, Leica, Allendale, NJ), a CCD camera (Model Retiga 1300, QImaging, Surrey, Canada), and QCapture Pro 5.1 (QImaging, Surrey, Canada). Acquired images were then analyzed and color-mapped using Matlab (The Mathworks Inc., Natick, MA).

K. In vivo oxygen imaging

Female FVB mice (4-6 week old) were anesthetized with 1-2 % isoflurane gas, adjusted to maintain a breathing rate of 100 breaths/min. Each mouse was positioned in dorsal recumbency on one side of the stage on top of a heating pad with a rectal feedback probe (FHC Inc.) set to maintain core temperature at 36.5 ºC. Its left limb was extended into a separate chamber for perfusion with saline, and a minor incision through the skin was made to expose the saphenous vessels, leaving the fascia intact. Once positioned under the microscope, the extended hindlimb was perfused with warm saline, and the breath rate and core temperature were continuously monitored for assuring animal health. Several minutes before imaging the mouse received an intracardiac injection with the Ru-PEG-PUAN particles (3 µL/g mouse weight).

The vasculature was imaged with a custom-built multiphoton microscope described previously[11] and above. Excitation light was focused into the vasculature using an Olympus 20X/0.95NA water-immersion objective that provided a large field of view and several mm of necessary working distance. The illumination wavelength was tuned to 780 nm and nonlinear emissions were collected in epifluorescence mode and separated from the excitation beam using a 750DCXRU long-pass dichroic filter (Chroma Technology, Rockingham, VT). The resulting nonlinear emissions were spectrally split by a 560DCXRU into blue- (BGG22, Chroma) and red- (650DF100MP, Chroma) pseudocolored channels. The blue emission (autofluorescence and collagen SHG) was detected with a bi-alkali PMT (HC125-02, Hamamatsu) and the Ru-PEG emission was detected using a red-sensitive GaAsP photocathode PMT (H7422P-40, Hamamatsu) with custom-designed amplifier circuitry.

L. Statistical analysis

Plots represent mean±standard deviations (SD). Analysis of variance (ANOVA) with Tukey post-test was used for statistical analysis (GraphPad Prism, La Jolla, CA) and significance denoted as *P<0.05; **P<0.01; ***P<0.001; ****P<0.0001.

Results and discussion

A. Oxygen-sensing by use of phosphors

Oxygen-sensitive phosphors, typically metal-ligand complexes, emit phosphorescence as they fall down to singlet ground state where all electrons are spin-paired from triplet excited state where one set of electron spins is unpaired. However, energy transfer between oxygen molecules that diffuse and collide with oxygen-sensitive phosphors at their triplet excited state (energy donor) can occur such that the

phosphors fall into their ground state without emitting phosphorescence. This process is called collisional quenching and can be applied to oxygen-sensing systems; higher concentration of oxygen (quencher) decreases phosphorescence. Not only phosphorescence but also phosphorescence lifetime of an oxygen-sensitive phosphor follows the same principle. Stern and Volmer first proposed that the ratio between luminescence lifetime in the absence of quenching molecules and that in the presence of those is linearly proportional to the concentration of the quenching molecule:

$$\frac{\tau_0}{\tau} = 1 + K_{SV}Q \qquad (4.1)$$

, where τ [s] is phosphorescence lifetime, K_{SV} is Stern-Volmer constant $[\text{m}^3/\text{mol}]$, and Q $[\text{mol}/\text{m}^3]$ is concentration of quenching molecule. Subscript 0 denotes the absence of oxygen. For ideal collisional quenching of the triplet excited state by molecular oxygen, the phosphorescence intensity should vary in the same ratio as the lifetime[12]:

$$\frac{I_0}{I} = \frac{\tau_0}{\tau} = 1 + K_{SV}c_{O_2} \qquad (4.2)$$

, where I is phosphorescence intensity. Therefore, we can quantify oxygen concentration from the measurement of phosphorescence or lifetime in principle. In the following, we will characterize oxygen-sensitive phosphor-incorporated micro- and nanoparticles that we have synthesized.

B. Synthesis and characterization of oxygen-sensing micro- and nanoparticles

We have successfully incorporated two oxygen-sensitive phosphors, PtTFPP and Ru-PEG, into polymeric micro- and nanoparticles by polymerization of phosphor-

126

monomer mixture. These oxygen-sensing particles are dispersible in water such that

they can be used in biological environments *in vitro* and *in vivo* such as cell-seeded

biomaterials and animal models. We have first chosen PS as an encapsulating

polymer because 1) it is one of the most well known polymeric materials with which

synthesis of microparticles is relatively simple, and 2) it has been also used for

luminescence sensing[13-14]. The concentration of a radical initiator, AIBN was chosen

to control the average size of PS microparticles. Measured average size of PtTFPP-PS

by dynamic light scattering was ~ 2 µm in diameter (Fig. 4.3A and Table 4.1). Water-

dispersibility of PtTFPP-PS microparticles could result from a possibility that PVP

(stabilizer) has been incorporated in PS matrix to some extent. Residual PVP in the

dispersion polymerization medium was removed by washing synthesized

microparticles several times with 10 % [v/v] ethanol.

We have also tried PDMS and poly(methyl methacrylate) (PMMA) to

synthesize microparticles incorporated with PtTFPP. However, it was practically very

difficult to control a size distribution of PDMS microparticles in emulsion, and water

appeared to decrease oxygen sensitivity of PtTFPP significantly when it is

incorporated in PMMA microparticles. We note that synthesis of Ru-PEG-PS

microparticles was not feasible because water-soluble Ru-PEG appeared to remain in

the reaction medium (90% [v/v] ethanol) instead of being incorporated in hydrophobic

PS during emulsion polymerization.

UAN is an amphiphilic precursor that is mainly composed of hydrophobic

poly(propylene oxide)-based segment (PPO segment; MW 700 Da for the synthesis

presented here) and hydrophilic poly(ethylene oxide) segment (PEO segment; MW

1,500 Da for the synthesis presented here). Because the UAN precursors are water-

dispersible by forming micelles (inner layer: PPO, outer layer: PEO), no stabilizer or

surfactant was required during emulsion polymerization. Synthesis of PUAN

nanoparticles is effectively polymerizing the micelles and cross-linking acrylate chains in UAN by a radical initiator, KPS in water as a reaction medium. The size of PPO and PEO segments determines the thickness of hydrophobic and hydrophilic layers respectively. The combination of the two main segments determines the size of nanoparticles. Average diameters of PtTFPP-PUAN and Ru-PEG-PUAN are 42 and 55 nm respectively (Fig. 4.3B and Table 4.1). We believe that thickness of hydrophilic layer in these nanoparticles is 3-4 nm. The size difference between PtTFPP-PUAN and Ru-PEG-PUAN is likely due to experimental conditions that may have varied randomly during polymerization. Figure 4.3B shows that PUAN nanoparticles in the TEM image appear to be deformed spheres. This is likely due to TEM processes where water was removed. PUAN is a relatively soft polymer, and PUAN nanoparticles are very stable in water owing to steric stabilization of PEO chains onto their surface. However, removal of water could cause aggregation and deformation of the nanoparticles. Synthesized oxygen-sensing nanoparticles were dialyzed with a molecular cutoff of 50 kDa to ensure to filter free phosphor molecules that were possibly not incorporated in PUAN. This process is especially required with Ru-PEG-PUAN because Ru-PEG is also amphiphilic and water-soluble. Because PtTFPP is water-insoluble, we highly doubt that unincorporated PtTFPP will be left in the reaction medium. We have not observed any noticeable PtTFPP aggregates after the emulsion polymerization in water. We have also verified that no Ru-PEG micelles larger than the 50 kDa MW cutoff formed by attempting to measure the size of nanoscale micelles with Ru-PEG dissolved in water. If the phosphor did form micelles (above critical micelle concentration (CMC)), light induced reactions would be affected by variations in the concentration of luminophore (which we have not seen). Furthermore, possibly formed Ru-PEG micelles in water are more likely to be dialyzed in the presence of 6-7 L of water (effectively going below CMC).

Oxygen-sensitive phosphors can be also incorporated in PUAN by a two-step process: 1) synthesis of PUAN nanoparticles and 2) incorporation of the phosphors into PUAN. We found that incorporation efficiency was greatly enhanced by the single-step process as stated above.

C. *Calibration of oxygen-sensing particles with measurement of phosphorescence lifetime*

We have calibrated oxygen-sensing particles suspended in water with lifetime measurements that allow for quantitative and consistent analyses in monitoring oxygen concentrations. The lifetime measurements are also known to be independent of optical artifacts (e.g., scattering within a matrix) and the concentration of a phosphor[15]. With the complete calibration over a range of oxygen concentration, we can obtain information about sensitivity of the oxygen-sensing particles. In addition, the calibration allows for back-calculation of actual oxygen concentration at regions of interest (e.g., cell-seeded scaffolds, vasculature in animals). Figures 4.4 and 4.5 show Stern-Volmer plots - the linear relationship between oxygen concentration and τ_0 / τ as shown in the Stern-Volmer equation (Eq. 4.2) - from which Stern-Volmer constant, K_{SV} (sensitivity of a phosphor) can be estimated. As expected, τ_0 / τ linearly increases as c_{O_2} increases for the all oxygen-sensing particles (Fig. 4.4). We find that oxygen-sensitivities of PtTFPP-PS, PtTFPP-PUAN, and Ru-PEG-PUAN are similar (Table 4.1) although a lifetime response to 40 % O_2 of PtTFPP-PS microparticles is slightly smaller compared with PUAN nanoparticles. We note that the response of oxygen-sensing particles in alginate is similar to that in aqueous suspension (Fig. 4.5A and B). Therefore, it is valid to use the calibration performed in water for other aqueous environments. Figure 4.5C shows that oxygen sensitivity of PtTFPP dissolved in ethanol is very similar to that of PtTFPP-incorporated oxygen-sensing particles up to

21 % O_2 (also see Table 4.1 and 4.2) and that PtTFPP-PUAN nanoparticles appears to perform better at 40 % O_2. This observation indicates that no significant interaction between PtTFPP and polymeric matrices is involved in affecting oxygen sensitivity within a biologically relevant range of oxygen concentration (i.e., 0-21 % O_2). However, oxygen sensitivity of Ru-PEG dissolved in water appears to be higher than that of Ru-PEG-PUAN (Fig. 4.5D). This seemingly suggests that it is better to use solely Ru-PEG for oxygen-sensing. However, we have observed that Ru-PEG dissolved a buffer solution caused animal death (data not shown), which implies that the phosphor itself is toxic to cells.

This calibration should be also done with direct phosphorescence imaging which one can perform in a laboratory without sophisticated optical equipments used for the lifetime measurement. A cross-comparison between the calibration with the lifetime measurement and direct phosphorescence imaging would allow choosing an optimal combination of an oxygen-sensitive phosphor, encapsulating polymeric material. Our observations reveal that micron-sized luminescent particles (possibly, any particles bigger than excitation/emission wavelength) may cause optical artifacts, for example, scattering. By the fact that the PUAN nanoparticle suspensions are remarkably optically clear, it would be preferable to use PUAN-based oxygen-sensing particles for our applications that will be introduced later in this chapter. Overall, we believe that Ru-PEG-PUAN nanoparticles would perform better for oxygen-sensing. In the following, we will further discuss about biocompatibility of the oxygen-sensing particles.
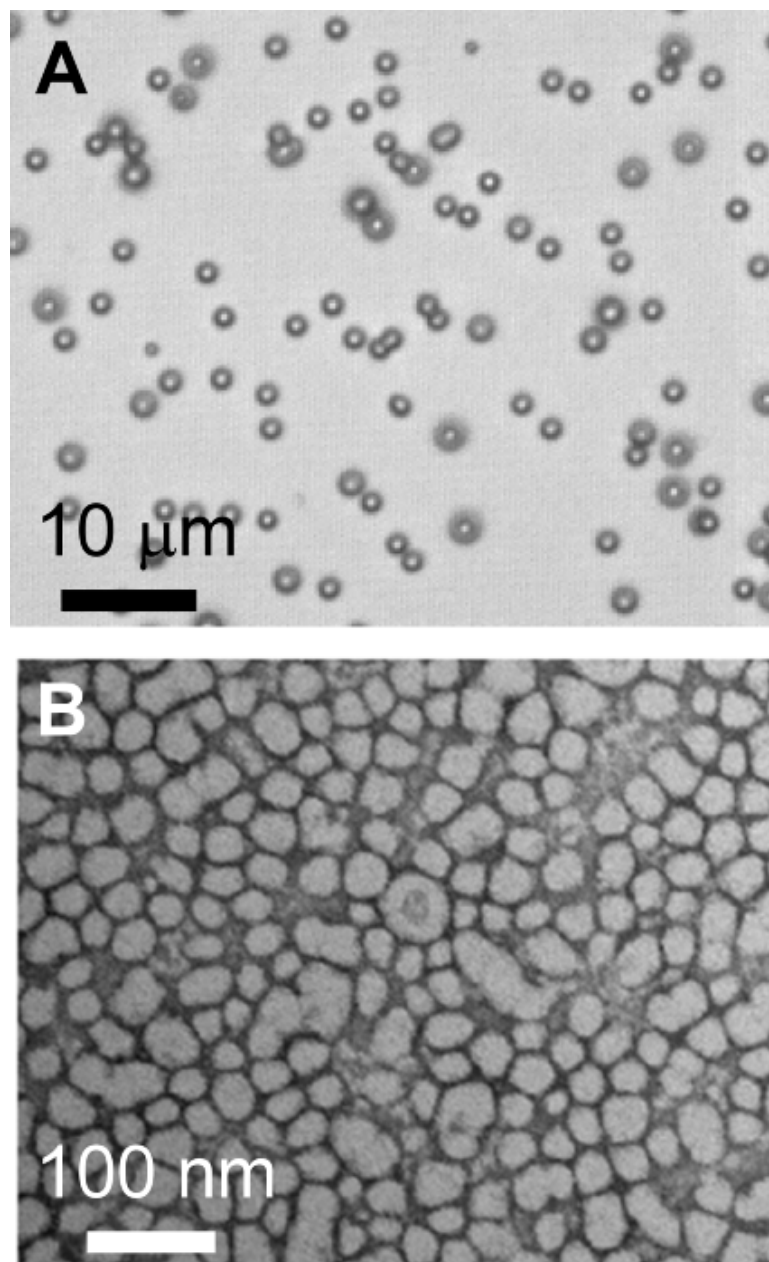
Figure. 4.3 Microscope images of oxygen-sensing micro- and nanoparticles. A.
Bright field image of PtTFPP-PS microparticles. **B.** Transmission electron
microscopy (TEM) image of Ru-PEG-PUAN nanoparticles.
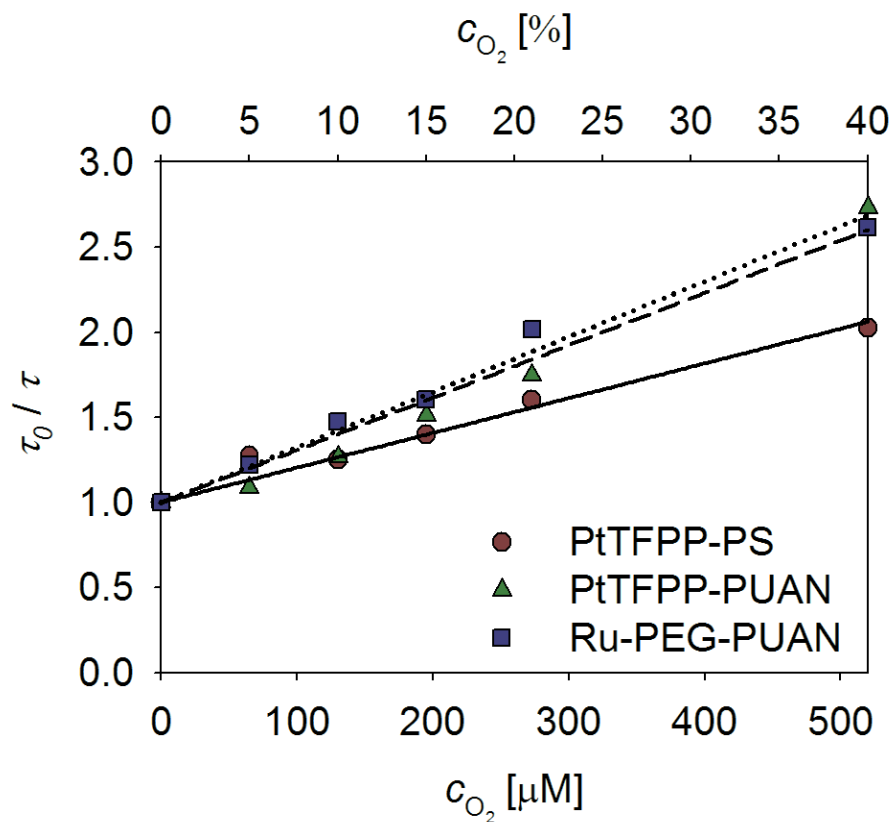
Figure 4.4 Stern-Volmer plots for oxygen-sensing particles suspended in water. PtTFPP-PS (red circle), PtTFPP-PUAN (green triangle), and Ru-PEG-PUAN (blue square). Fitted lines are linear regression plots based on Eq. 4.2 ($\tau_0 / \tau = 1 + K_{SV} c_{O_2}$): solid line for PtTFPP-PS, dash line for PtTFPP-PUAN, and dotted line for Ru-PEG-PUAN.
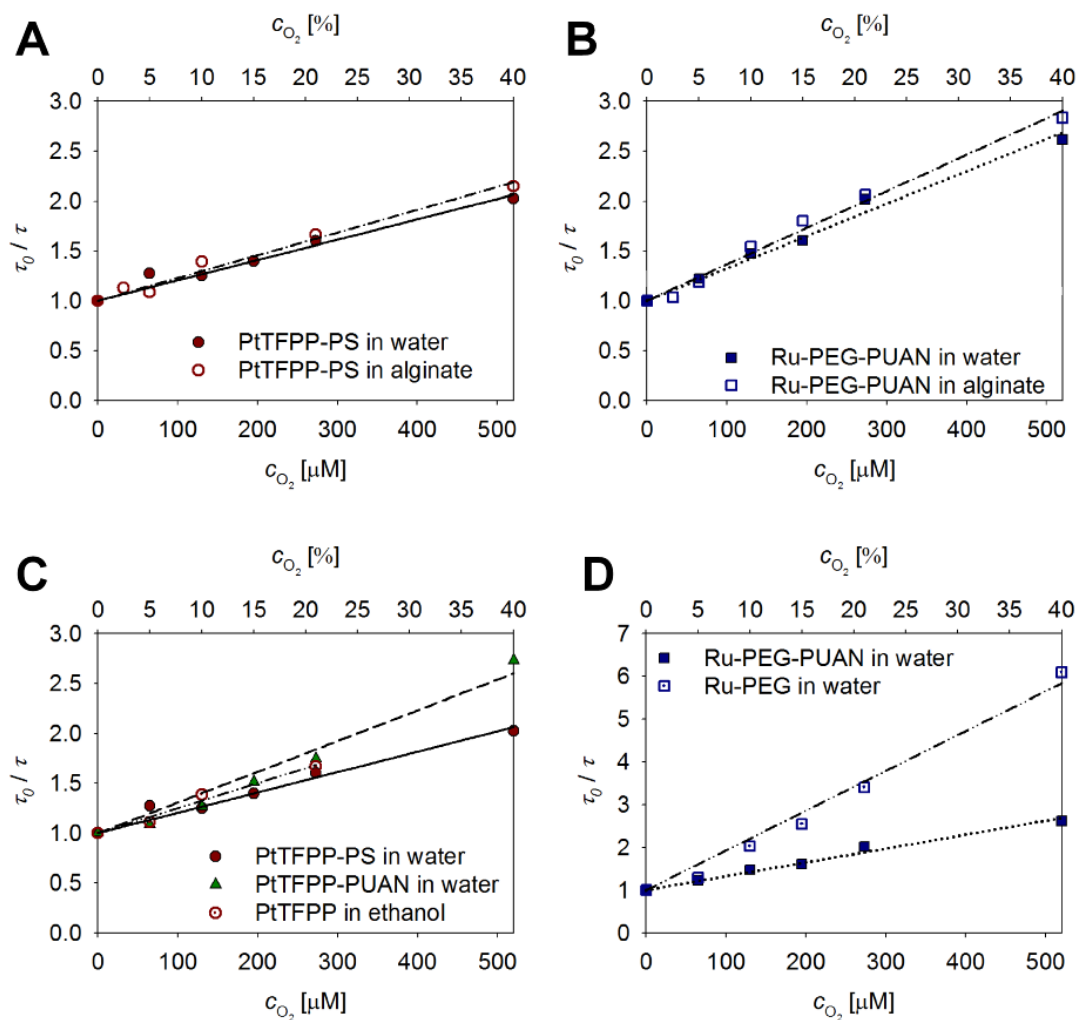
Figure 4.5 Stern-Volmer plots for oxygen-sensing particles dispersed in alginate, and for oxygen-sensitive phosphors. A. PtTFPP-PS in water (filled red circle and solid line) and alginate (empty red circle and dash-dotted line). **B.** Ru-PEG-PUAN in water (filled blue square and dotted line) and alginate (empty blue square and dash-dotted line). **C.** PtTFPP-PS in water (filled red circle and solid line), PtTFPP-PUAN in water (green triangle and dash line), and PtTFPP in ethanol (dotted red circle and dash-double dotted line). **D.** Ru-PEG-PUAN in water (filled blue square and dotted line) and Ru-PEG in water (dotted blue square and dash-double dotted line).

Table 4.1 Average diameter, polydispersity index, and oxygen sensitivity (Stern-Volmer constant) of oxygen-sensing particles

	Average diameter [nm]	Polydispersity index	O_2 sensitivity in water [m^3/mol]
PtTFPP-PS	2034 ± 69.72	0.201 ± 0.033	2.04
PtTFPP-PUAN	42.28 ± 0.6280	0.211 ± 0.006	3.08
Ru-PEG-PUAN	54.90 ± 0.5823	0.196 ± 0.005	3.2

Table 4.2 Oxygen sensitivity of oxygen-sensing particles dispersed in alginate, and oxygen-sensitive phosphors

	PtTFPP-PS in alginate	PtTFPP in ethanol	Ru-PEG-PUAN in alginate	Ru-PEG in water
O_2 sensitivity [m^3/mol]	2.3	2.5	3.7	9.3

D. Biocompatibility oxygen-sensing micro- and nanoparticles

As briefly mentioned in the previous section, an oxygen-sensitive phosphor (or any heavy metal complex) could cause cell death possibly due to direct contact between the phosphor and cells. We have examined cytotoxicity of our oxygen-sensing micro- and nanoparticles by both 2-D and 3-D cultures of tumor cells in the presence of the particles. For the 2-D culture, oxygen-sensing particles were suspended in culture media. For the 3-D culture, the particles were dispersed in 200 µm-thick alginate discs.

We have found that ≤ 0.1 % [v/v] Ru-PEG-PUAN nanoparticles suspended in media did not affect viability of OSCC-3s growing on well plates in 7 days (Fig. 4.6A) and that PtTFPP-PS microparticles (5×10^7 bead/mL) and higher volume fractions (1 and 10 % [v/v]) of Ru-PEG-PUAN nanoparticles resulted in less proliferation compared with control (no particles) in 6 days (Fig. 4.6B). OSCC-3s were initially seeded at 10^4 cell/well. We note that PtTFPP-PS microparticles that were suspended relatively well in water started settling down on the bottom of wells in a day and significantly covered cell monolayers and areas on which the cells could have proliferated for the rest of the culture period (data not shown). OSCC-3s with PtTFPP-PS still proliferated at least by a factor of ~ 10 in 6 days. Figure 4.7 shows that OSCC-3s in alginate dispersed with both oxygen-sensing micro- and nanoparticles remained viable for 7 days (Fig. 4.7A) and proliferated by a factor of ~3 over the culture period (Fig. 4.7B). In addition, there was no significant difference between the two cases on each day. We note that both the extent of proliferation and estimated cell number from DNA assay observed here are within a typical range in 1 week-cultures of OSCC-3s in 200 µm-thick alginate discs without oxygen-sensing particles. From the both 2-D and 3-D cultures, we conclude that the oxygen-sensitive phosphors encapsulated in PS micro- and PUAN nanoparticles do not cause significant

cell death from direct contact. Note that the oxygen-sensitive phosphors are still likely to be present on the surface of the polymeric matrices after the synthesis. However, it is still questionable whether the oxygen-sensing particles may cause phototoxicity to cells after the exposure to excitation light (i.e., 392 nm for direct phosphorescence imaging and ~800 nm for lifetime measurements with multiphoton microscopy). Future studies should address this question if reactive oxygen species (i.e., singlet excited oxygen molecules generated by the collisional quenching) affect cell viability because the main reason for dispersing the particles is for oxygen imaging and quantification of oxygen concentration from the lifetime measurements. Furthermore, biocompatibility of the oxygen-sensing particles, *in vivo* should be examined. Our preliminary observation shows that PtTFPP-PS (< 1 % [w/v]), PtTFPP-PUAN (1 % [w/v]; 3.4 μmol of PtTFPP incorporated in PUAN), and Ru-PEG-PUAN (1 % [w/v]; 4.5 μmol of Ru-PEG incorporated in PUAN) injected into the vasculature of mice did not cause acute death for > 7 days (data not shown).
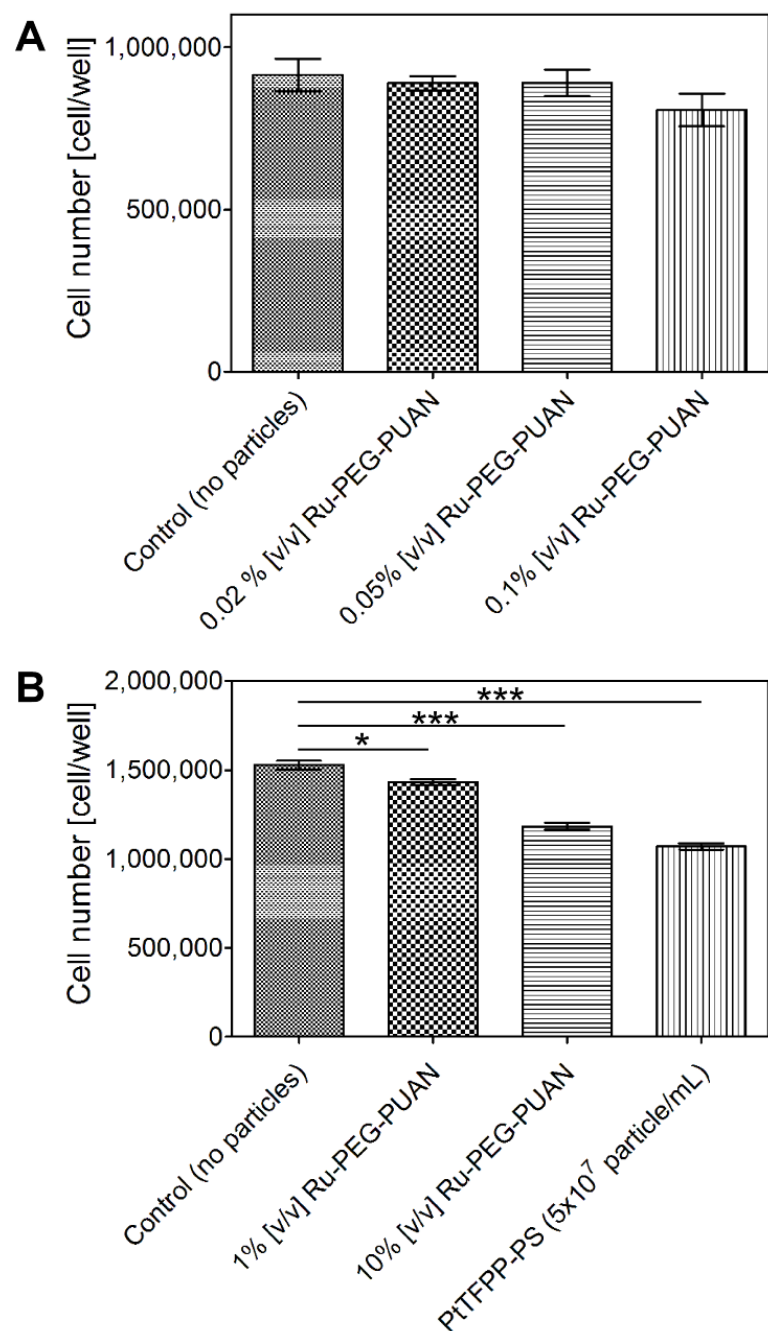
Figure 4.6 Plots of cell number after 2-D culture of OSCC-3s with oxygen-sensing particles. **A.** Counted cells after 6 day-culture. **B.** Counted cells after 7 day-culture. Error bars are standard error of the mean (SEM). (*P<0.05 and ***P<0.001).
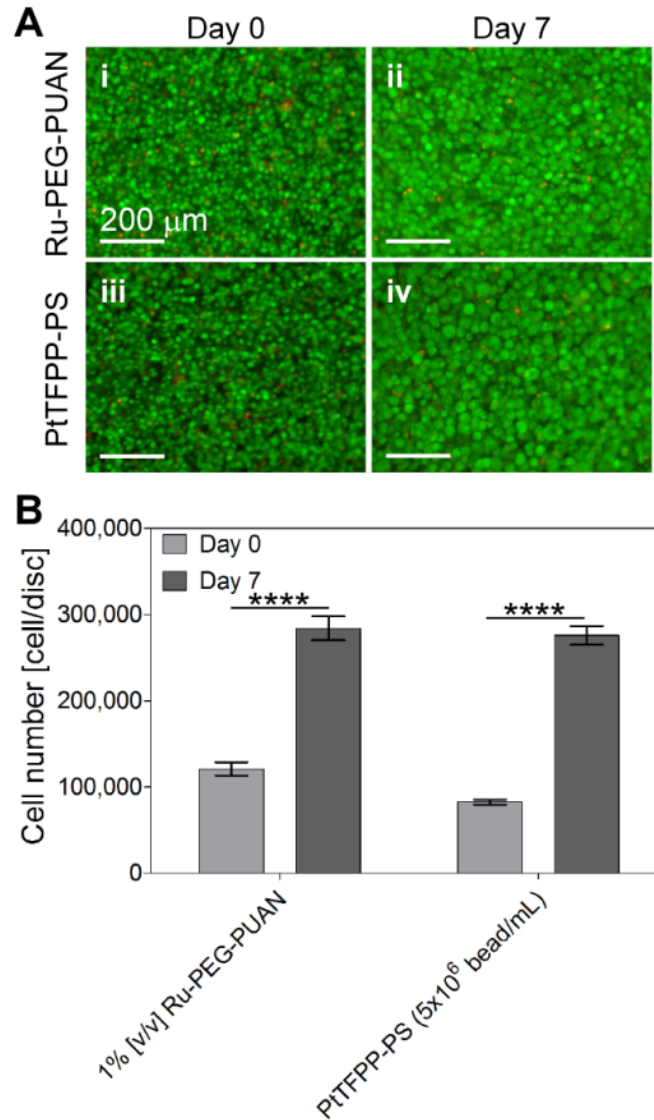
Figure 4.7 Live/dead and DNA assay after 3-D culture of OSCC-3s in oxygen-sensing particle-dispersed 4 % [w/v] alginate. **A.** Fluorescence micrographs showing cells stained by 5 μM calcein-AM (green – live) and 5 μM ethidium homodimer-1 (red – dead). Cells with Ru-PEG-PUAN on day 0 (i) and 7 (ii). Cells with PtTFPP-PS on day 0 (iii) and 7 (iv). **B.** Plot of cell number calculated from DNA assay. Error bars are standard error of the mean (SEM). (****P<0.0001).

E. Demonstration of temporal and spatial control of oxygen concentration within microfluidic alginate scaffolds dispersed with oxygen-sensing microparticles

As demonstrated in the previous chapters, microfluidic biomaterials are useful tools to control soluble 3-D microenvironment. Using oxygen-sensing particles dispersed within microfluidic biomaterials, oxygen concentration can be not only controlled but also monitored. Figure 4.8A shows colormapped phosphorescence micrographs of a microfluidic alginate scaffold seeded with PtTFPP-PS microparticles (5×10^7 particle/mL) over the sequential delivery of a deoxygenated buffer solution (~0 % of saturation, "hypoxic"; frames i-iii) and an oxygenated buffer solution (21 % of saturation concentration of oxygen, "normoxic"; frames iv-vi) (also see Fig. 4.8B). Oxygen quenches PtTFPP such that the observed phosphorescence intensity decreases in well-oxygenated regions. The incorporation of two independent networks, one hypoxic and one normoxic, within a monolithic scaffold (inset in Fig. 4.8C) allows for the maintenance of steady-state gradients. Each network can serve as a source and a sink for oxygen (Fig. 4.8C and D). These results confirm that 1) the oxygen-sensitive phosphor encapsulated in polymeric microparticles is functional, 2) the oxygen-quenching mechanism is reversible, and 3) oxygen concentration within scaffolds can be not only controlled but also monitored in a spatiotemporal manner. This capability would allow elucidating roles of oxygen in angiogenic signaling of tumor cells in 3-D scaffolds.
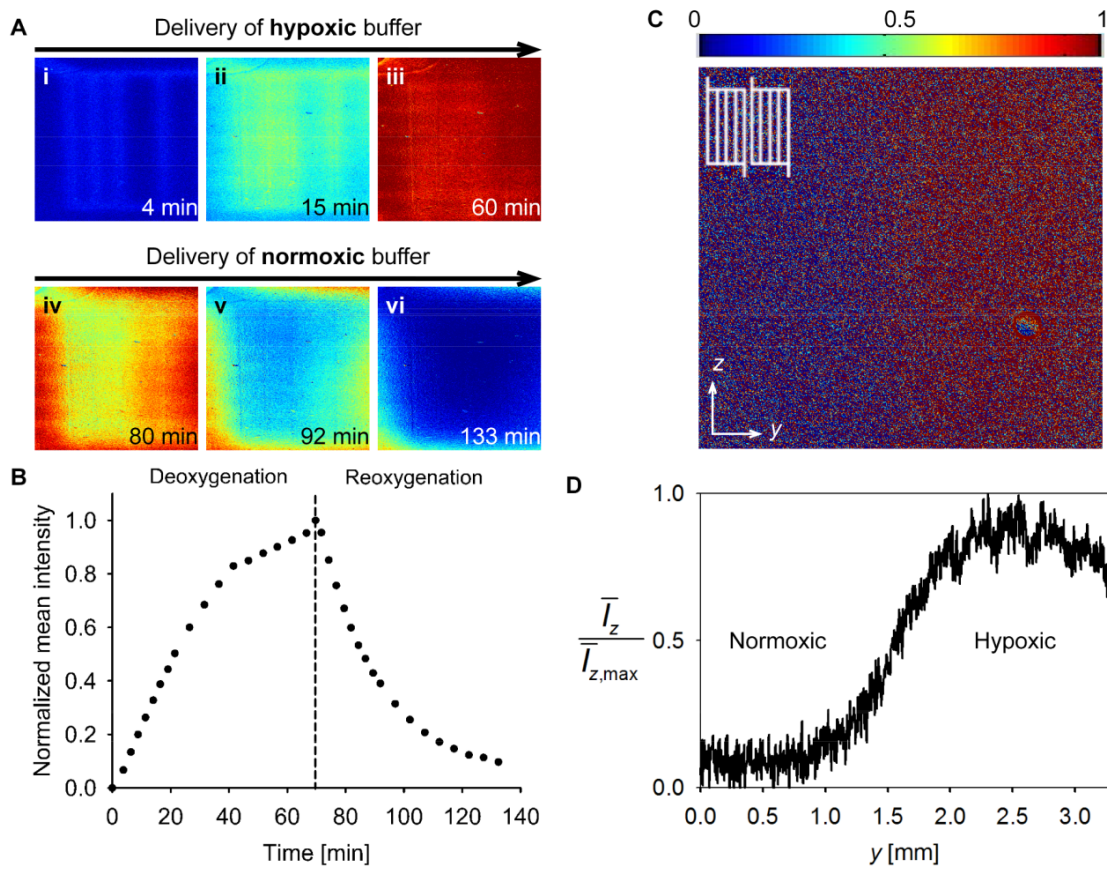
Figure 4.8 Demonstration of temporal and spatial control of oxygen concentration within oxygen-sensing microfluidic scaffolds. **A.** Phosphorescence micrographs of an oxygen-sensing alginate scaffold at time points during the sequential delivery of a hypoxic buffer solution (i-iii) and a normoxic buffer solution (iv-vi) via embedded microchannels. **B.** Normalized, mean phosphorescence intensity from the images in A. **C.** Normalized phosphorescence micrograph from an oxygen-sensing alginate scaffold operated with a normoxic buffer solution in the left network and a hypoxic solution in the right. Inset shows structure of network. The scaffold was 500 μm thick with inter-channel distance of 200 μm. **D.** Normalized, z-averaged phosphorescence intensity from the image in C.

F. Visualization and optical measurement of oxygen-depletion lengths in a simple microfluidic tumor model, in vitro

As discussed in Chapter 3, the quantitative analysis of metabolic activity of cells in microfluidic biomaterials is essential and valuable in designing microfluidic tissue scaffolds for tissue-scale biology as well as tissue engineering. In addition to the measurement of OCR, we can also visualize and optically measure oxygen-depletion lengths (Krogh lenghs) using the oxyen-sensing particles. The Krogh length[16], λ_K is inversely proportional to the square root of cell seeding density, ρ_{cell}, assuming that oxygen consumption rate is zeroth order:

$$\lambda_K \approx \sqrt{\frac{c_0 D_{O_2}}{\rho_{cell} R_{O_2,cell}}} \qquad (4.3)$$

Prior to experimentally testing this hypothesis, we have demonstrated this approach as another example in a simple microfluidic tumor model (i.e., a microfluidic alginate scaffold seed with OSCC-3 cells). We used the 1-channel microfluidic system for this demonstration (Fig. 4.9). Phosphorescence micrographs in Fig. 4.10A and C present oxygen distribution within the tumor cell-seeded scaffold before and after the delivery of normoxic culture media (DMEM with 10 % [v/v] FBS). Gradients of oxygen were created by diffusion and cellular consumption, and approached a steady-state within 20 min. The average profiles of phosphorescence along the *z*-direction (Fig 4.10B and D) show that the oxygen gradient length scale increases as cell seeding density is decreased by a factor of 5. Furthermore, the normalized profile of background-subtracted phosphorescence for the two cell seeding densities indicates that an effective Krogh length, defined as a length scale at which the normalized phosphorescence is 0.2, for 1×10^6 and 5×10^6 cell/mL is 2.2 and 1.3 mm respectively (Fig. 4.10E). Estimated oxygen consumption rates, $R_{O_2,cell}$ using the equation above

are 1.1×10^{-16} and 6.1×10^{-17} mol/s cell for 1×10^6 and 5×10^6 cell/mL respectively. These estimated rates are comparable to what we have measured from the measurement of OCR presented in the previous chapter (5.4×10^{-17} mol/s cell at 17 % O_2) and the oxygen consumption rate in rabbit corneal stroma[17] although optically measured values appears to be overestimated in the case of 1×10^6 cell/mL. The difference may be due to optical artifacts or culture conditions (e.g., temperature, ambient oxygen concentration). Future experiments should include 1) the same analysis with the oxygen-sensing nanoparticles, 2) lifetime measurement in quantifying Krogh lengths, and 3) more careful considerations in providing appropriate culture environment during the operation. Our preliminary measurement of spatially resolved oxygen concentration in the microfluidic tumor model, using the lifetime measurement and the calibration, shows that oxygen concentration decreases from 21 % (microchannel side) to ~10 % (bulk of tumor cell-seeded alginate; 5×10^6 cell/mL) over 3.5 mm (data not shown). This indicates that $R_{O_2,cell}$ might have been reduced due to lower temperature (~ 22 °C) at which the measurement was carried out, compared with temperature inside an incubator (37 °C). In addition, cell seeding density needs to be chosen relevantly such that oxygen-depletion length scales are compatible with optical resolutions. Figure 4.11A and B show finite element models for oxygen consumption at steady-state ($D_{O_2}\nabla^2 c_{O_2} = -\rho_{cell}R_{O_2,cell}$) by cells in the microfluidic tumor model, where important input parameters are $c_0 = 0.17$ mol/m^3 (17 % O_2) and $R_{O_2,cell} = 5.4\times10^{-17}$ mol/s·cell. We have confirmed transient solutions indicate that the distributions have already approached to state-state within 60 min as observed in the experiments (data not shown). However, oxygen-depletion length scales do not agree with the experimental observations. Specifically, oxygen concentration does not appear to be depleted over the width of the scaffold, $W = 4$ mm at 1×10^6 cell/mL whereas oxygen is completely depleted at ~ 500 μm at 5×10^6 cell/mL

(Fig. 4.11 A and B). Moreover, the theoretical estimation of the Krogh length does

not appear to agree with finite element models as cell seeding density increases (>

1×10^6 cell/mL). Fig. 4.11C is a log-log plot of λ_K^2 versus ρ_{cell}. The slope value for

the finite element models is -1.35, indicating λ_K is proportional to $\left(\rho_{cell}\right)^{-1.35}$. This

suggests that the simple argument in estimating oxygen-depletion length scale may

have to be revised, but experimental validation should be carried out first.

G. In vivo O₂ imaging with oxygen-sensing nanoparticles

Because synthesized oxygen-sensing particles can be dispersed well in aqueous

environments and show biocompatibility, they can be also used for oxygen imaging, *in

vivo*. We have demonstrated that one of our oxygen-sensing nanoparticles (Ru-PEG-

PUAN) is useful to monitor oxygen levels in blood streams by injecting the particles

into the vasculature (saphenous vessels) of mice and measuring lifetimes (Fig. 4.12).

Figure 4.12C shows that oxygen concentration in vein is clearly lower than that in

artery. This preliminary demonstration confirms that the dispersible oxygen-sensing

particles are valuable tools for oxygen-sensing *in vivo* as well as *in vitro* applications.
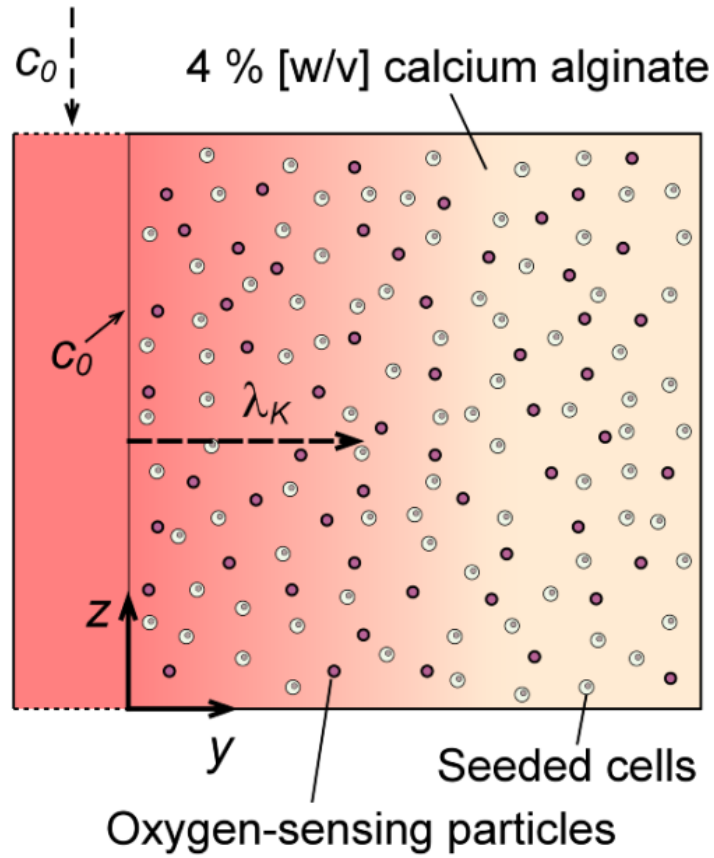
Figure 4.9 Schematic representation of oxygen-sensing microfluidic scaffold seeded with cells (top-down view). Dispersed cells are depicted as double circles and oxygen-sensing particles as red circles. The pink shading represents steady-state distribution of oxygen within cell-seeded scaffold. The Krogh length, λ_K, is the characteristic distance over which oxygen diffuses into the scaffold from the microchannel. c_0 is oxygen concentration at the scaffold-microchannel interface.

Figure 4.10 Visualization and optical measurement of Krogh lengths in a simple microfluidic tumor model. **A** and **C.** Phosphorescence micrographs of oxygen-sensing microfluidic scaffolds seeded with OSCC-3s (A: 5×10^6 cell/mL, C: 1×10^6 cell/mL) at time points. **B** and **D.** *Z*-averaged phosphorescence intensity from the images in A and C. **E.** Background-subtracted, *z*-averaged, and normalized phosphorescence intensity from the images at 120 min in A and C.
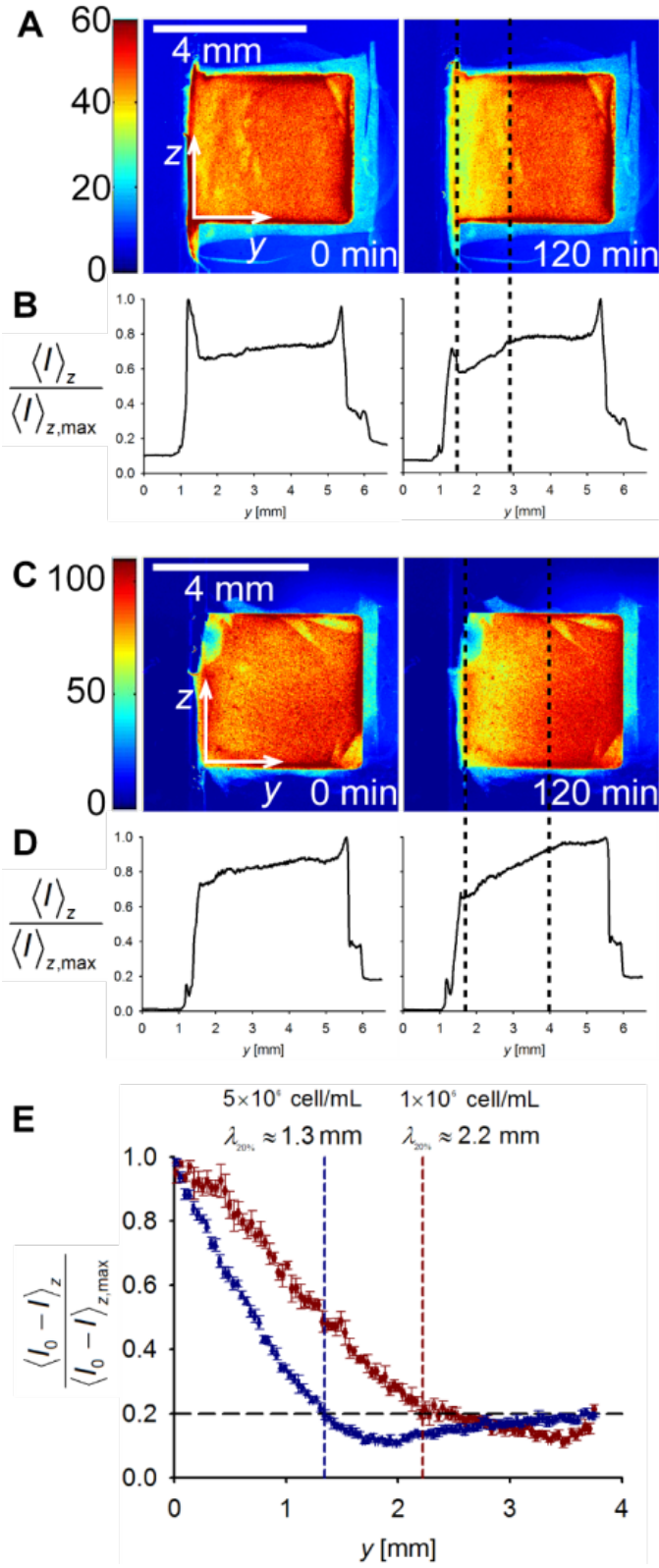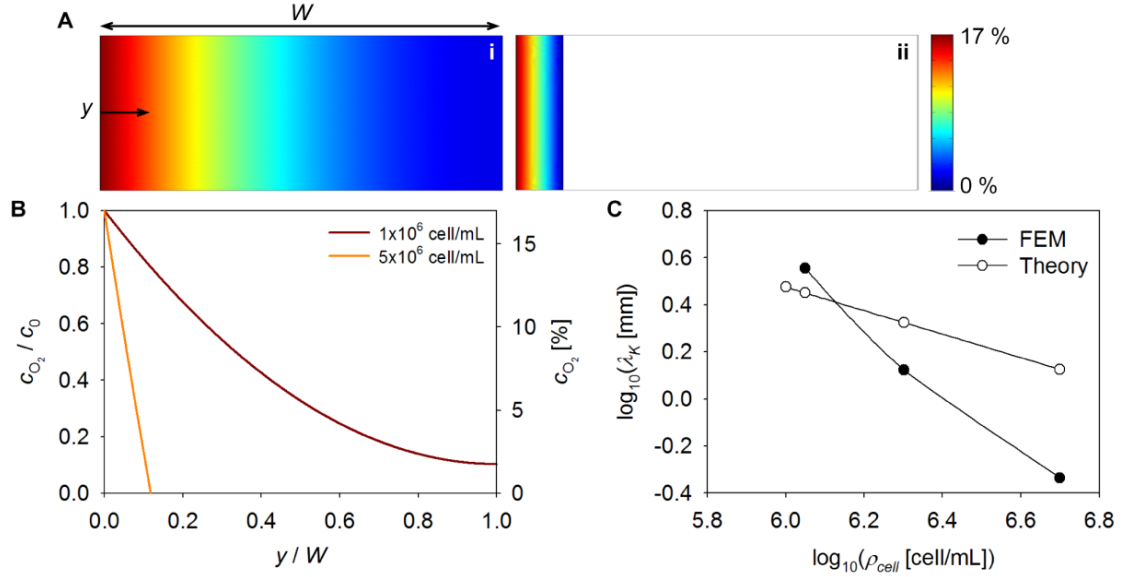
Figure 4.11 Computational model for oxygen consumption in simple microfluidic tumor model. **A.** Steady-state distribution of oxygen concentration calculated by finite element method with an assumption of zeroth order kinetics with $W = 4$ mm $D_{O_2} = 2.76 \times 10^{-5}$ cm^2/s, $c_0 = 0.17$ mol/m^3, $R_{O_2,\text{cell}} = 5.4 \times 10^{-17}$ mol/s$\cdot$cell, $\rho_{\text{cell}} = 1 \times 10^6$ (i) and 5×10^6 (ii) cell/mL. Concentration boundary conditions were maintained at the channel walls ($c_{y=0} = c_0$), and no-flux conditions were maintained at other boundaries. **B.** Plot of normalized concentration (c_{O_2} / c_0; solid lines) along y-direction, calculated in A, at cell seeding densities of 1×10^6 (red) and 5×10^6 (orange) cell/mL. **C.** Log-log plot of Krogh lengths, λ_K estimated from the finite element method (black) and Eq. 4.3 (white) at various seeding densities (1×10^6, 1.12×10^6, 2×10^6, and 5×10^6 cell/mL).

148
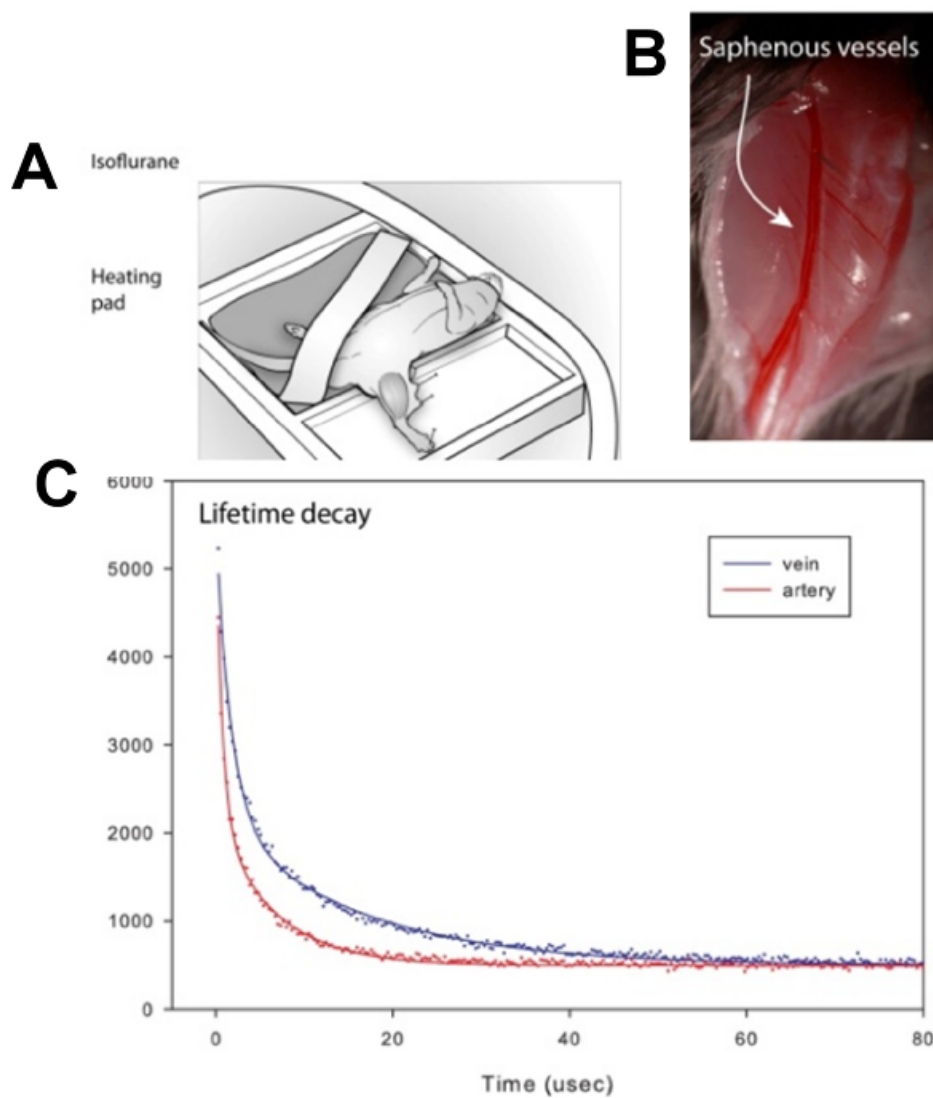
Figure 4.12 *In vivo* **oxygen imaging. A.** Schematic illustration of experimental setup.
B. Image showing saphenous vessels of a mouse as in A. **C.** Plot of phosphorescence
lifetime decay of Ru-PEG-PUAN nanoparticles in vein (blue) and artery (red).

Conclusions

We have synthesized oxygen-sensing particles in both micro- and nanoscale that are stably dispersible, biocompatible in aqueous environments, by encapsulating oxygen-sensitive phosphors in polymeric matrices. Calibration of these particles allows estimating oxygen-sensitivity and quantifying oxygen concentration with optical measurements. Both direct phosphorescence imaging and phosphorescence lifetime measurement with multi-photon microscopy can be used in monitoring oxygen levels. Combining this tool with microfluidic biomaterials, we can not only control but also monitor oxygen concentration in a spatiotemporal manner. This opens a great opportunity for *in vitro* biological applications. For example, the measurement of spatially resolved distributions of oxygen concentration allows estimating oxygen-depletion length scales within 3-D scaffolds seeded with cells. This serves as one of key parameters in designing microfluidic tissue scaffolds. In addition, spatiotemporally resolved oxygen-sensing allows elucidating oxygen-dependent physiological processes (e.g., phenotypic behavior of stem cells, cellular function in liver) and pathological processes (e.g., angiogenic activity of tumor cells, tumor angiogenesis) in tissue-scale. The oxygen-sensing particles are also powerful for quantifying oxygen levels in blood streams without causing animal death, and even smaller particles may be potentially useful to monitor oxygen concentration in animal tissues. Remaining challenges are to 1) develop techniques in maintaining long-term cultures with real time imaging in a non-invasive way and 2) synthesize a few nanometer scale particles that can freely diffuse between vasculature and tissue without causing destruction of cell membrane. Overall, the dispersible oxygen-sensing particles can be powerful tools for applications both *in vitro* and *in vivo*.

REFERENCES

1.	Sud, D. *et al.*, Optical imaging in microfluidic bioreactors enables oxygen monitoring for continuous cell culture. *J. Biomed. Opt.* **11** (5), 3 (2006).

2.	Mehta, G. *et al.*, Quantitative measurement and control of oxygen levels in microfluidic poly(dimethylsiloxane) bioreactors during cell culture. *Biomed. Microdevices* **9** (2), 123-134 (2007).

3.	Acosta, M.A. *et al.*, Fluorescent microparticles for sensing cell microenvironment oxygen levels within 3D scaffolds. *Biomaterials* **30** (17), 3068-3074 (2009).

4.	Braun, R.D. *et al.*, Comparison of tumor and normal tissue oxygen tension measurements using OxyLite or microelectrodes in rodents. *Am. J. Physiol. Heart Circ. Physiol.* **280** (6), H2533-H2544 (2001).

5.	Kellner, K. *et al.*, Determination of oxygen gradients in engineered tissue using a fluorescent sensor. *Biotechnol. Bioeng.* **80** (1), 73-83 (2002).

6.	Fernandez-Sanchez, J.F. *et al.*, Novel oxygen sensitive complexes for optical oxygen sensing. *Talanta* **71** (1), 242-250 (2007).

7.	Kimura, F. *et al.*, Dual luminophore polystryrene microspheres for pressure-sensitive luminescent imaging. *Meas. Sci. Technol.* **17**, 1254-1260 (2006).

8.	Bedlek-Anslow, J.M. *et al.*, Micro-heterogeneous oxygen response in luminescence sensor films. *Langmuir* **16** (24), 9137-9141 (2000).

9.	Amao, Y. *et al.*, Oxygen sensing based on lifetime of photoexcited triplet state of platinum porphyrin-polystyrene film using time-resolved spectroscopy. *J. Porphyr. Phthalocya.* **4** (3), 292-299 (2000).

10.	Williams, R.M. *et al.*, Solute transport in growth plate cartilage: In vitro and in vivo. *Biophys. J.* **93** (3), 1039-1050 (2007).

11. Williams, R.M. *et al.*, Solute transport in growth plate cartilage: In vitro and in vivo. *Biophys. J.* **93** (3), 1039-1050 (2007).

12. Lakowicz, J.R., *Principles of Fluorescence Spectroscopy*, 2nd ed. (Kluwer Academic/Plenum, New York, 1999).

13. Im, S.H. *et al.*, Synthesis of polystyrene beads loaded with dual luminophors for self-referenced oxygen sensing. *Talanta* **67** (3), 492-497 (2005).

14. Kimura, F. *et al.*, Dual luminophore polystyrene microspheres for pressure-sensitive luminescent imaging. *Meas. Sci. Technol.* **17**, 1254-1260 (2005).

15. Rodriguez, J.C.C. *et al.*, Measurement of low oxygen concentrations by phosphorescence lifetime using optical fibers. *IEEE Trans. Instrum. Meas.* **48** (5), 949-955 (1999).

16. Fournier, R.L., *Basic transport phenomena in biomedical engineering*, 2nd ed. (Taylor & Francis, London, 2006).

17. Takahash, G.H. *et al.*, Oxygen consumption rate of tissue measured by a micropolarographic method. *J. Gen. Physiol.* **50** (2), 317-335 (1966).

CHAPTER 5

CONCLUSIONS AND FUTURE DIRECTIONS

After a broad introduction to regenerative medicine, tissue engineering, and tissue-scale biology as well as the state of the art of the fields in Chapter 1, we presented the development of microfluidic biomaterials that could be used as enabling tools for tissue engineering and tissue-scale biology, *in vitro* in Chapter 2. Successful fabrication of functional microfluidic networks within both calcium alginate and collagen requires important characteristics: 1) dispersion of cells within scaffold biomaterials,2) biocompatibility of the fabrication, 3) scalability to sub-millimeter dimensions, and 4) lithographic definition of fluid paths to enable precise control of distributions and fluxes of solutes. Embedded microchannels in microfluidic biomaterials enable maintaining a uniform metabolic environment within the bulk of the scaffold, creating distinct soluble environments experienced by cells in their 3-D environment, and accessing to biochemical environment created by cells. We also demonstrated that pre-defined microchannels in microfluidic collagen scaffolds served as templates for microvascular endothelialization. Microfluidic collagen scaffolds are a potentially more valuable platform for studies of vasculogenesis, (tumor) angiogenesis, and organogenesis of lymph node in 3-D not only because both chemical and mechanical microenvironment can controlled but also because cells can remodel their 3-D environment. The development of such remodelable microfluidic scaffolds could also aid to find mechanistic clues in the stabilization of microvasculature, for example, by seeding pericytes, fibroblasts, and smooth muscle cells in the bulk. In the context of tissue engineering, this tool may aid in growing thick sections of tissue without necrosis in the core, and in directing the development

of cells towards spatially differentiated tissues; for example, an integrated cartilage-bone composite tissue by seeding mesenchymal stem cells (MSCs).

In Chapter 3, we presented mass transport considerations in microfluidic biomaterials. Such considerations include quantitative measurements of diffusion and diffusion-reaction of solutes, which should be also used in designing and operating microfluidic biomaterials. Appropriately chosen design parameters allow both spatiotemporal control of the soluble environment experienced by cell in 3-D, by efficient exchange of solutes via embedded microchannels. Specifically,as stated in Chapter 1, oxygen transport is the key not only in maintaining metabolic activity of cells within growing engineered tissue constructs but also in elucidating roles of oxygen in various physiological and pathological processes in tissue scale. Systematic control of oxygen within microfluidic biomaterials, combined with the quantitative measurement of metabolic activity, would promote investigating differentiation and phenotypic behavior of stem cells, angiogenic signaling of tumor cells, tumor angiogenesis in 3-D scaffolds. A remaining challenge is to run multiple replicates of microfluidic biomaterials for long periods of time (weeks) without significantly loosing functionality. There is still a lack of microscopy techniques and equipments that allow monitoring systems of interest in real time. Development of customizable and maybe portable in some sense microscopes that can be operated in incubators may aid to study dynamic biological processes.

In Chapter 4, we described the development of an additional tool for oxygen-sensing. We showed the synthesis of oxygen-sensing micro- and nanoparticles in which oxygen-sensitive phosphors were incorporated. Unlike conventional yet still generally useful techniques to probe oxygen levels (e.g., dissolved oxygen meters with electrodes), the oxygen-sensing particles allow monitoring oxygen concentration in a spatiotemporally resolved manner when they are combined with microfluidic

biomaterials. We have demonstrated that the particles are stably dispersible in aqueous environment and biocompatible as well. We have also demonstrated the direct visualization and optical measurement of oxygen-depletion lengths within cell-seeded 3-D scaffolds *in vitro*. The use of oxygen-sensing particles can be extended in quantifying oxygen levels in blood streams without causing animal death. Even smaller particles may be potentially useful to monitor oxygen concentration in animal tissues to capture real-time *in vivo* physiology. Remaining challenges are to 1) develop techniques in maintaining long-term cultures with real-time imaging in a continuously non-invasive way and 2) synthesize a few nanometer scale particles that can freely diffuse between vasculature and tissue without causing destruction of cell membrane. With greatly increasing interest in oxygen-sensing for biological applications, this technology could open new opportunities and lead to vast impact in the field of tissue-scale biology as well as tissue engineering.

Specific future directions related to tissue-scale tumor biology include further investigation of 1) angiogenic activity and signaling of tumor cells in 3-D scaffolds, and 2) direct angiogenesis. Microfluidic alginate can serve as a structurally inert scaffold in terms of remodeling that allows examining angiogenic activity of tumor cells prior to the initiation of angiogenesis. An underlying hypothesis is that paracrine signaling from hypoxic cells up-regulates the expression of angiogenic factors in normoxic region (Fig. 5.1E and F). Embedded microchannels within a double-network scaffold (Fig. 5.1A) enable not only creating a steady-state gradient of oxygen to recapitulate hypoxic core and normoxic periphery in solid tumor (Fig. 5.1E and F) but also locally sampling angiogenic factors secreted by cells in the bulk (Fig. 5.1B). For systematic comparisons, exogenous angiogenic factors could be delivered via microchannels in the hypoxic zone as mimic of tumor cell secretion (Fig. 5.1C). In addition, angiogenic factor-blocking antibodies or cell-based techniques such as

siRNA could be used to inactivate effects of the hypoxic core (Fig. 5.1D). Furthermore, dynamic angiogenic responses of tumor cells could be examined by temporally modulating oxygen concentration. Quantitative measurement of distributions of angiogenic factors may allow developing a model to predict tumor progression.

Remodelable microfluidic collagen could aid in finding mechanistic clues in direct angiogenesis. For example, to test a hypothesis that there may be the threshold of oxygen level and that of secretion level of angiogenic factors to drive tumor angiogenesis, an endothelialized microfluidic network within a tumor cell-seeded scaffold could be allowed to undergo direct angiogenesis; controlled oxygen concentration as an input stimulus and secreted angiogenic factors as an output indication (Fig. 5.2A). Recent studies have found evidence that chemoattracting factors stimulate to release bone marrow derived (BMD) endothelial cells (ECs) from bone marrow (stimulated by mobilizing factors such as tissue ischemia), and to recruit them to angiogenesis sites[1-6]. These suggest that the recruited BMD ECs may become newly assembling ECs or at least facilitate angiogenesis. Therefore, it may be feasible to enhance the extent of angiogenesis by delivering BMD ECs (Fig. 5.2B) and additionally delivering angiogenic factors (Fig. 5.2C) via endothelialized microchannels. Furthermore, we could test whether angiogenic factors secreted by tumor cells recruit BMD ECs via vascular vessels, by connecting two microfluidic endothelialized collagen scaffolds; one for tumor part and the other for bone marrow part (Fig. 5.2D). Fluorescently labeled bone marrow cells (BMCs) would allow tracking recruited cells. Improved understandings of tumor angiogenesis in tissue scale may aid in developing anti-angiogenic treatment, and could also be extended to tissue engineering applications towards angiogenesis and vascularization within engineered 3-D tissues.
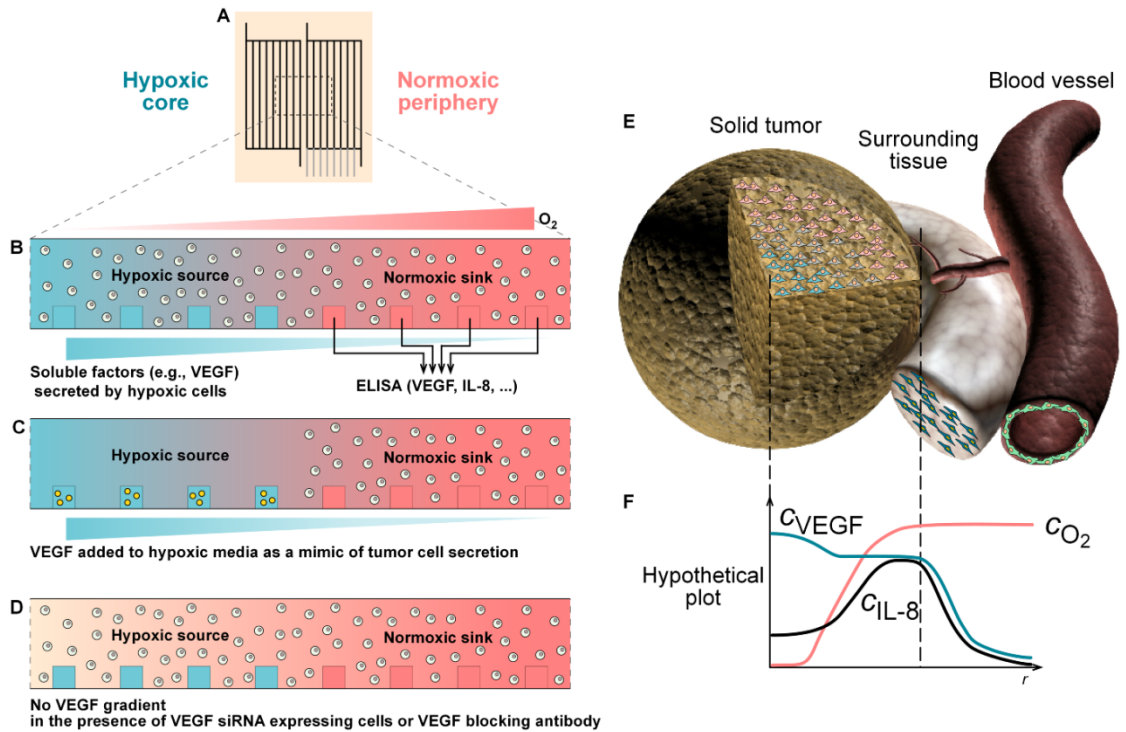
Figure 5.1 Microfluidic tumor model in calcium alginate. **A.** Schematic top-down view of microfluidic tumor with two independent networks. The left side mimics the hypoxic conditions of the core of the tumor; the right side mimics the peripheral zone and surrounding tissue. Black lines represent embedded microchannels. Grey lines represent channels used as chemical "taps" to monitor local concentrations of soluble factors. **B-D.** Schematic cross-sectional views of model tumor, each representing a different experiment: in B, microchannels impose gradients in the concentration of oxygen and tumor cells respond to create distributions of angiogenic factors. In C, hypoxia and exogenous VEGF are delivered to model tumor zone, without cells. In D, VEGF activity is blocked. Red shading indicates oxygen concentration. Blue shading indicates VEGF concentration. **E.** Schematic representation of solid tumor (tan), host tissue (pink), and vascular structure (brown). **F.** Hypothetical plots of the concentrations of oxygen, VEGF, and IL-8, in the tumor and surrounding tissue.

157
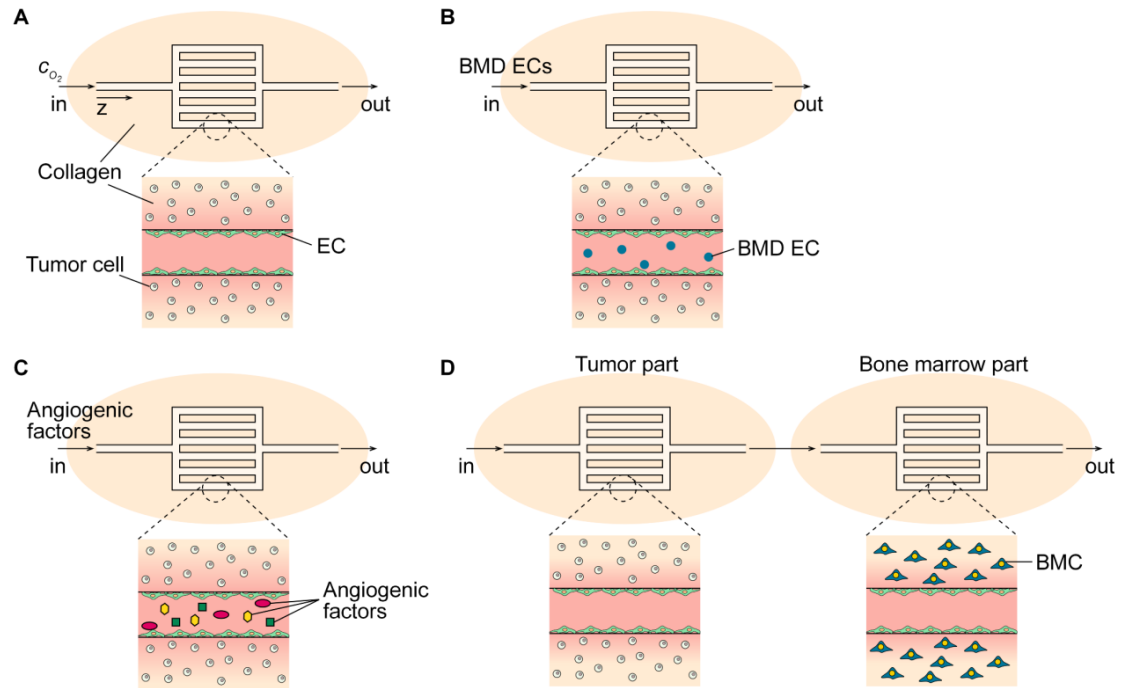
Figure 5.2 Collagen-based microfluidic tumor models for direct angiogenesis study. **A-C.** Single-network design. c_{O_2} [mol] is inlet concentration of oxygen. **D.** Interconnected network design.

REFERENCES

1. Schatteman, G.C. *et al.*, Biology of bone marrow-derived endothelial cell precursors. *Am. J. Physiol.-Heart C.* **292** (1), H1-H18 (2007).

2. Mathews, V. *et al.*, Recruitment of bone marrow-derived endothelial cells to sites of pancreatic beta-cell injury. *Diabetes* **53** (1), 91-98 (2004).

3. Golledge, J. *et al.*, Bone marrow - derived cells and arterial disease. *J. Vasc. Surg.* **46** (3), 590-600 (2007).

4. Lyden, D. *et al.*, Impaired recruitment of bone-marrow-derived endothelial and hematopoietic precursor cells blocks tumor angiogenesis and growth. *Nature Med.* **7** (11), 1194-1201 (2001).

5. Peters, B.A. *et al.*, Contribution of bone marrow-derived endothelial cells to human tumor vasculature. *Nature Med.* **11** (3), 261-262 (2005).

6. Young, P.P. *et al.*, VEGF increases engraftment of bone marrow-derived endothelial progenitor cells (EPCs) into vasculature of newborn murine recipients. *P. Natl. Acad. Sci. USA.* **99** (18), 11951-11956 (2002).

SUPPLEMENTARY METHOD: FABRICATION OF MICROFLUIDIC ALGINATE

SCAFFOLDS

I. Jig components

Figure A1.1 shows a photo with all of the parts used in the jigs for molding

and operating microfluidic scaffolds:

O-rings (Fig. A1i): an O-ring (McMaster-Carr®, Robbinsville, New Jersey)

was inserted in a 2-mm recess on the bottom of an aluminum part (Figure A1.1ii).

Inserted O-rings served as gaskets to prevent $CaCl_2$ solution from leaking during the

cross-linking step.

Aluminum parts (Fig. A1.1ii, v, vi, vii, and ix): machined aluminum parts

served as rigid frames to provide thermal stability and mechanical strength when

autoclaved, and precision when assembled to form a sealed microfluidic scaffold.

Perforated aluminum support (Fig. A1.1iii): perforated aluminum sheets (812

μm thick, 838 μm in diameter round perforations; Small Parts, Inc., Miami Lakes,

Florida) were cut, and screw holes and injection ports were created. Tygon tubing (1

mm in inner diameter; Small Parts, Inc., Miami Lakes, Florida) was glued on one of

the ports using cyanoacrylate adhesive (Super Glue Corp., Rancho Cucamonga,

California).

Plastic sheets: Plastic sheem sheets (AccuTrex Products, Inc., Canonsburg,

Pennsylvania) were cut, and screw holes and windows were created with a scalpel.

Poly(dimethylsiloxane) (PDMS) stamp (Fig. A1.1viii): a mold was pre-

assembled with a lithographically defined SU-8 master (see Materials and methods in

Chapter 2) and jig parts for top layer of the microfluidic scaffold (Fig. A1.1ii, vi, and

vii). PDMS (Sylgard 184, Dow Corning, Midland, Michigan) was poured as a pre-

polymer into the mold and cured in two steps: 24 h at room temperature and followed by 1 h at 65 °C. This two-step process was necessary to avoid deformation of the stamp due to thermal expansion during the initial cross-linking of the pre-polymer.

Assembly of molds for calcium alginate

Coating with poly(ethylenimine): a solution of poly(ethylenimine) (PEI) (MW 750,000; branched.; Sigma-Aldrich, St. Louis, Missouri) was made at 0.1 % [v/v] in water. Components v and xi were oxidized for 1 min in a plasma cleaner/sterilizer (Model PDC-001, Harrick Plasma, Ithaca, New York) at the highest RF power. Immediately following oxidation, ~ 28 µL/cm^2 (corresponding to a total of 250 µL)of the solution of PEI was applied onto the surfaces of each part. These parts were allowed to dry in a sterile hood overnight.

Mold for top layer of calcium alginate: the PDMS stamp was oxidized for 1 min in the plasma cleaner/sterilizer. This oxygen plasma treatment was performed immediately before each fabrication run in order to increase wettability of the PDMS stamp by uncross-linked alginate during the injection step. A mold for the top layer of the scaffold was formed by stacking the following parts: i, ii, iii, iv, v, vi, viii, and vii.

Mold for bottom layer of calcium alginate: a mold for the bottom layer of the scaffold was formed by stacking the following parts: i, ii, iii, iv, v, vi, xi, and ix.

Assembly of cartrigde for operation of microfluidic scaffold

Once cross-linked with CaCl$_2$ solution, the top and bottom layers of calcium alginate were assembled into the functional microfluidic scaffold. The complete cartridge is formed as a stack of the following parts (Fig. A1.1): ii, x, xii, v with the top layer of calcium alginate inside the window, xiii, v with the bottom layer of alginate inside the window, xi, vi, and ix.
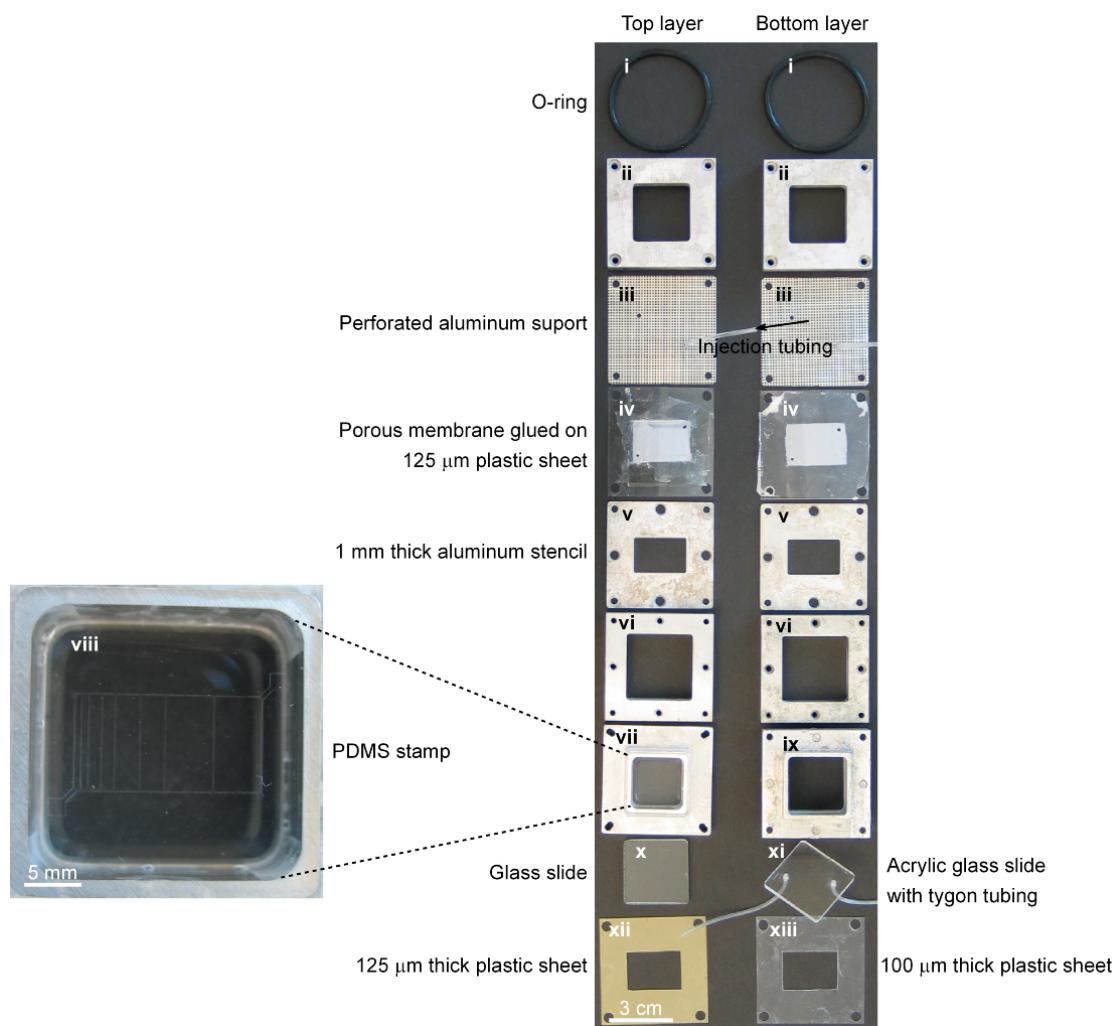
Figure A1.1 Assembling jig parts used to fabricate microfluidic scaffold

APPENDIX 2

ENZYMATIC CONSUMPTION OF CALCEIN-AM

Experiments with cells in suspension were performed to study the enzymatic consumption of calcein-AM by primary chondrocytes in suspension. Isolated chondrocytes and solutions of calcein-AM with various concentrations (i.e., 1.25, 2.5, 5, 10, 20 μM) were dispensed into wells of a 96-well plate. In addition, cells without calcein-AM, calcein-AM without the cells, and completely pre-cleaved calcein (Carlo, D. D., Aghdam, N. & Lee, L. P. Single-cell enzyme concentrations, kinetics, and inhibition analysis using high-density hydrodynamic cell isolation arrays. *Anal. Chem.* **78** (14), 4925-4930 (2006)) without the cells were dispensed for estimating background, autohydrolization, and intracellular concentrations of calcein respectively. Fluorescence was measured in a microplate reader (Model Synerge$^{\text{TM}}$ HT, BioTek, Winooski, VA) every minute for 1 h. The intensity of both the background and autohydrolization were subtracted from the raw fluorescence intensity of calcein. After converting the corrected intensity to concentration of calcein (product concentration, P [mol/L]) production rate at early times (i.e., 5 ~ 15 min when P linearly increased over time) was obtained. It was found that the enzymatic kinetics was first order with respect to the concentration of calcein-AM (substrate concentration, S [mol/L]) with a rate constant, $k_{eff} = \rho_{cell} k_{cell}^{susp}$, where the cellular rate constant, $k_{cell}^{susp} = 5.9 \times 10^{-11}$ mL/cell·s.
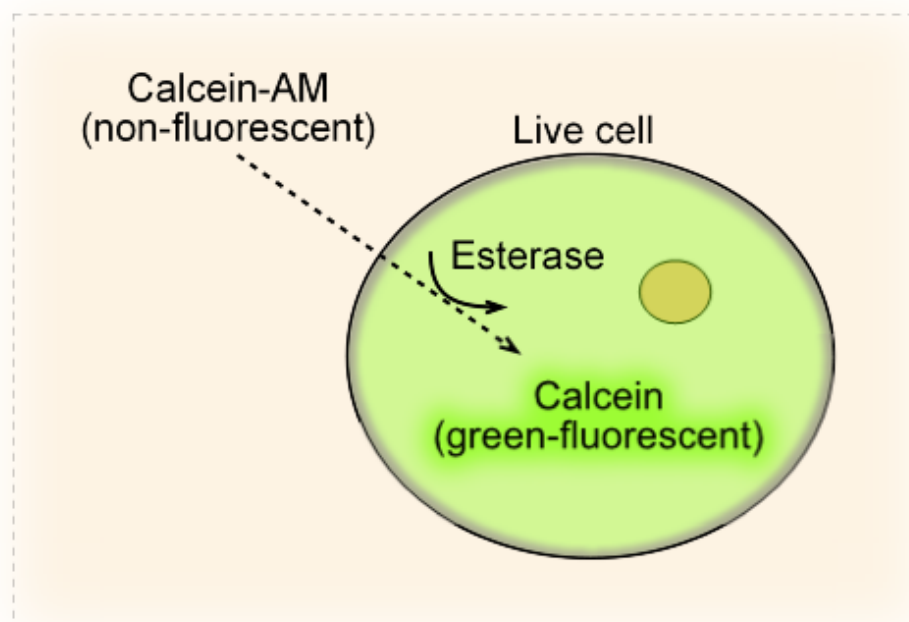
Figure A2.1 Schematic illustration of diffusion-reaction process for calcein-AM

APPENDIX 3

DETAILED DERIVATION OF THE ANALYSIS OF FLUORESCENCE

MEASURE AFTER MICROFLUIDIC ILLUMINATION (FAMI)

Suppose that instantaneous microfluidic illumination of a fluorescent dye occurs at $t = 0$ (Fig. 3.6A). Then, we can allow for only diffusion of the dye into the bulk of hydrogels, experimentally by stopping the delivery of the dye via microchannels. Concentration of the dye in the gel is a function of position (x, y, z) and time (t); that is, $c = c(x, y, z, t)$. Diffusion of the dye in the gel is governed by

$$\frac{\partial c}{\partial t} = D\nabla^2 c, \qquad (A3.1)$$

where D [m^2/s] is diffusivity. We assume that concentration of the dye is linearly proportional to fluorescence intensity; it is necessary to confirm the linearity prior to FAMI. We also assume that observed fluorescence intensity (I) for each image is integrated intensity along x-direction which is the thickness of a microfluidic gel. In other words, $I = I(y, z, t)$.

The observed fluorescence intensity is averaged along z-axis assuming that there is no variation of concentration of the dye in z-direction. This requires the operation of microfluidic gels with Peclet number as stated in Chapter 3. z-averaged fluorescence intensity can be defined as

$$\bar{I}(y,t) \equiv \frac{1}{L}\int_0^L I(y, z, t)\,dz. \qquad (A3.2)$$

From the governing equation (Eq. A3.1) and assumptions above,

$$\frac{\partial \overline{I}}{\partial t} = D \frac{\partial^2 \overline{I}}{\partial y^2}, \tag{A3.3}$$

with an instantaneous point source (as illustrated in Fig. 3.6A),

$$S(y) = \begin{cases} \overline{I}_0(y) & (t = 0) \\ 0 & (t > 0) \end{cases} \tag{A3.4}$$

An analytical solution to Eq. A3.3 is the transient 1-D Green's function:

$$G(y,t) = \frac{1}{2\sqrt{\pi Dt}} \exp\left[-\frac{y^2}{4Dt}\right] \tag{A3.5}$$

To find a real solution with a spatially continuous source, method of convolution can be used:

$$\overline{I}(y,t;y') = \int_{-\infty}^{\infty} G(y-y',t) S(y') dy'$$
$$= \int_{-\infty}^{\infty} \frac{1}{2\sqrt{\pi Dt}} \exp\left[-\frac{(y-y')^2}{4Dt}\right] S(y') dy' \tag{A3.6}$$

Then, perform continuous Fourier transform to convert $\overline{I}(y,t)$ to $\hat{\overline{I}}(k,t)$ where k is spatial frequency:

$$\hat{\overline{I}}(k,t) = \frac{1}{\sqrt{2\pi}} \int_{-\infty}^{\infty} \overline{I}(y,t) e^{-iky} dy$$
$$= \frac{1}{\sqrt{2\pi}} \int_{-\infty}^{\infty} \frac{S(y')}{2\sqrt{\pi Dt}} \int_{-\infty}^{\infty} e^{-iky} e^{-\frac{(y-y')^2}{4Dt}} dy \, dy'$$
$$= \frac{1}{\sqrt{2\pi}} \int_{-\infty}^{\infty} \frac{S(y')}{2\sqrt{\pi Dt}} \int_{-\infty}^{\infty} \exp\left[-\frac{1}{4Dt}\left\{(y-y')^2 + (4ikDt) y\right\}\right] dy \, dy'$$
$$= \frac{1}{\sqrt{2\pi}} \int_{-\infty}^{\infty} \frac{S(y')}{2\sqrt{\pi Dt}} I_1 \, dy' \tag{A3.7}$$

where I_1 is defined as

$$I_1 \equiv \int_{-\infty}^{\infty} \exp\left[-\frac{1}{4Dt}\left\{(y-y')^2 + (4ikDt)\,y\right\}\right] dy$$

$$= \int_{-\infty}^{\infty} \exp\left[-\frac{1}{4Dt}\left\{y^2 - 2y'y + y'^2 + (4ikDt)\,y\right\}\right] dy$$

$$= \int_{-\infty}^{\infty} \exp\left[-\frac{1}{4Dt}\left\{\begin{array}{l} y^2 + (4ikDt - 2y')\,y + y'^2 \\ + \left(\dfrac{4ikDt - 2y'}{2}\right)^2 - \left(\dfrac{4ikDt - 2y'}{2}\right)^2 \end{array}\right\}\right] dy \qquad \text{(A3.8)}$$

$$= \int_{-\infty}^{\infty} \exp\left[-\frac{1}{4Dt}\left\{\left(y + (2ikDt - y')\right)^2 + \left(y'^2 - (2ikDt - y')^2\right)\right\}\right] dy$$

$$= \exp\left[-\frac{1}{4Dt}\left(y'^2 - (2ikDt - y')^2\right)\right] \int_{-\infty}^{\infty} \exp\left[-\frac{1}{4Dt}\left(y + (2ikDt - y')\right)^2\right] dy$$

By letting $y'' \equiv y + (2ikDt - y')$ and $dy = dy''$,

$$I_1 = \exp\left[-\frac{1}{4Dt}\left(y'^2 - (2ikDt - y')^2\right)\right] \int_{-\infty}^{\infty} \exp\left[-\frac{y''^2}{4Dt}\right] dy''$$

$$= \exp\left[-\frac{1}{4Dt}\left(y'^2 - (2ikDt - y')^2\right)\right] \left(2\sqrt{\pi Dt}\right) \qquad \text{(A3.9)}$$

where

$$\int_{-\infty}^{\infty} e^{-ax^2} dx = \sqrt{\frac{\pi}{a}} \qquad \text{(A3.10)}$$

Then, the transformed intensity, $\hat{\bar{I}}(k,t)$ becomes

$$\hat{\bar{I}}(k,t) = \frac{1}{\sqrt{2\pi}} \int_{-\infty}^{\infty} \frac{S(y')}{2\sqrt{\pi Dt}} \exp\left[-\frac{1}{4Dt}\left(y'^2 - (2ikDt - y')^2\right)\right] \left(2\sqrt{\pi Dt}\right) dy'$$

$$= \frac{1}{\sqrt{2\pi}} \int_{-\infty}^{\infty} S(y') \exp\left[-\frac{1}{4Dt}\left(y'^2 - (2ikDt - y')^2\right)\right] dy' \qquad \text{(A3.11)}$$

$$= \frac{1}{\sqrt{2\pi}} \int_{-\infty}^{\infty} S(y') A(y',t) dy'$$

where $A(y',t)$ is

$$A(y',t) \equiv \exp\left[-\frac{1}{4Dt}\left(y'^2 - (2ikDt - y')^2\right)\right]$$

$$= \exp\left[-\frac{1}{4Dt}\left(y'^2 + 4k^2D^2t^2 + (4ikDt)y' - y'^2\right)\right]$$

$$= \exp\left[-\frac{1}{4Dt}\left(4k^2D^2t^2 + (4ikDt)y'\right)\right] \qquad \text{(A3.12)}$$

$$= \exp\left[-k^2Dt - iky'\right]$$

$$= e^{-k^2Dt}e^{-iky'}$$

Therefore, the transformed intensity, $\hat{\bar{I}}(k,t)$ is

$$\hat{\bar{I}}(k,t) = \frac{1}{\sqrt{2\pi}} \int_{-\infty}^{\infty} S(y')\left(e^{-k^2Dt}e^{-iky'}\right) dy'$$

$$= \left[\frac{1}{\sqrt{2\pi}} \int_{-\infty}^{\infty} S(y')e^{-iky'}dy'\right] e^{-k^2Dt} \qquad \text{(A3.13)}$$

$$= \hat{S}(k)e^{-k^2Dt}$$

The transformed intensity at a characteristic spatial frequency, $k_0 \equiv 2\pi / \lambda_c$,

$$\hat{\bar{I}}(k_0,t) = \hat{S}(k_0)e^{-k_0^2Dt} \qquad \text{(A3.14)}$$

Fourier transformed values are often complex numbers. Typically, absolute values can be used:

$$Abs\left[\hat{\bar{I}}(k_0,t)\right] = Abs\left[\hat{S}(k_0)e^{-k_0^2 Dt}\right] = Abs\left[\hat{S}(k_0)\right]e^{-k_0^2 Dt}$$

$$= \sqrt{\left(\mathrm{Re}\left[\hat{S}(k_0)\right]\right)^2 + \left(\mathrm{Im}\left[\hat{S}(k_0)\right]\right)^2}\, e^{-k_0^2 Dt} \qquad \text{(A3.15)}$$

By taking natural log in Eq. A3.15,

$$\ln\left[Abs\left[\hat{\bar{I}}(k_0,t)\right]\right] = \ln\left[\sqrt{\left(\mathrm{Re}\left[\hat{S}(k_0)\right]\right)^2 + \left(\mathrm{Im}\left[\hat{S}(k_0)\right]\right)^2}\right] - k_0^2 Dt \quad \text{(A3.16)}$$

Therefore, diffusivity, D can be estimated from a plot of time vs. magnitude of Fourier transformed peak at the characteristic spatial frequency:

$$D = \frac{|slope|}{k_0^2} = |slope|\frac{\lambda_c^2}{4\pi^2} \qquad \text{(A3.17)}$$

APPENDIX 4

SPATIALLY RESOLVED DELIVERY OF NON-REACTIVE SOLUTES VIA

EMBEDDED MICROFLUIDIC NETWORKS

An acellular microfluidic scaffold was used to deliver a series of small molecules via the embedded microchannels in the two independent networks (Fig. 2.1Dii): 1) the pH-adjusted buffer without fluorescent dye, 2) fluorescein solution (5 μM in buffer), and 3) rhodamine B solution (5 μM in buffer) were delivered through the networks at a flow rate of 50 μL/min.
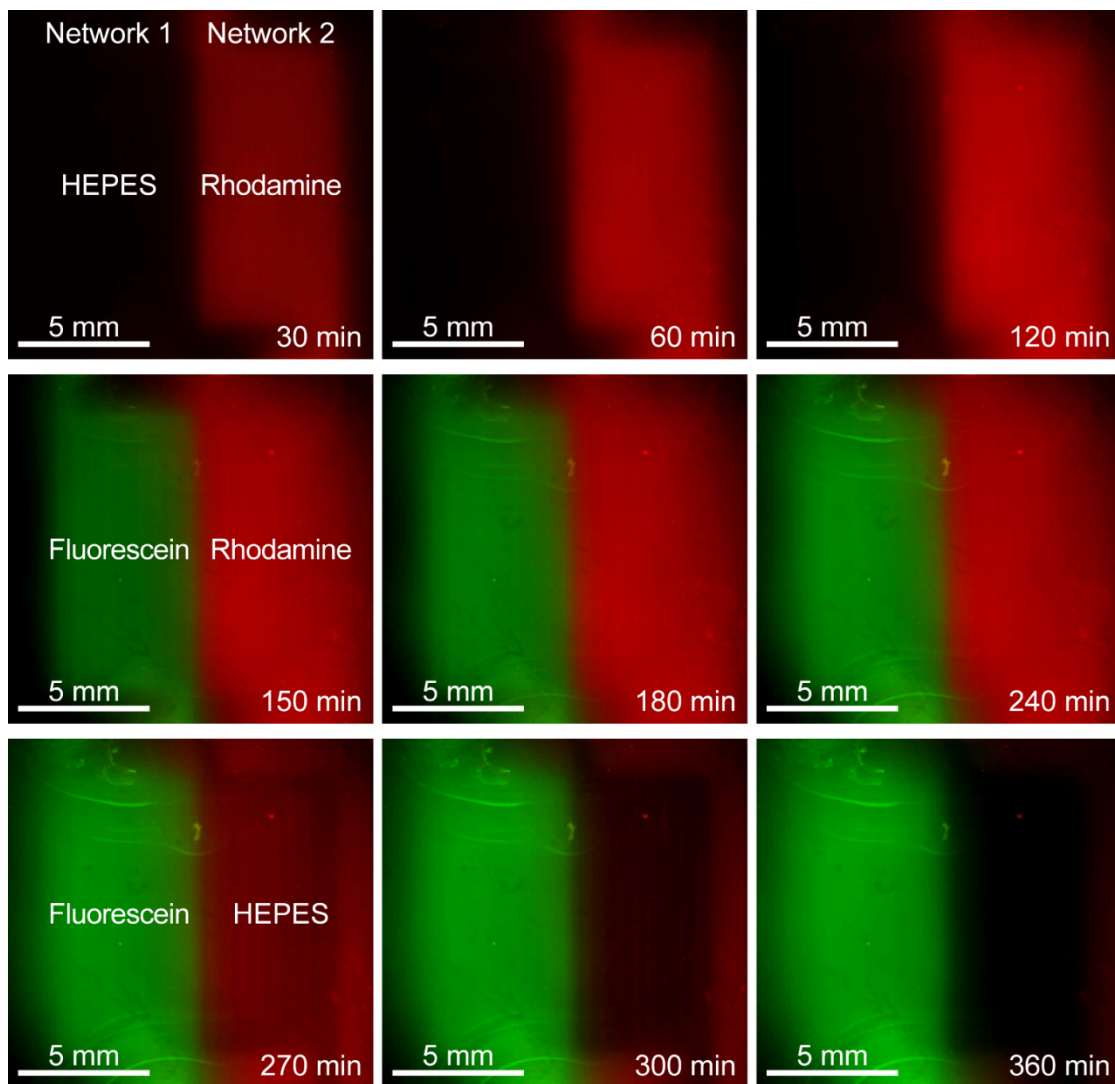
Figure A4.1 Spatially resolved delivery of non-reactive solutes via embedded microfluidic networks. Fluorescence micrographs of two-network microfluidic scaffold (acellular) after **A.** 2 hr-delivery of the pH-adjusted buffer through network 1 and 5 μM rhodamine B, dissolved in the pH-adjusted buffer, through network 2. **B.** 2 hr-delivery of 5 μM fluorescein, dissolved in the pH adjusted buffer, through network 1 and rhodamine B through network 2. **C.** 2 hr-delivery of fluorescein through network 1 and the pH-adjusted buffer through network 2.

APPENDIX 5

QUANTITATIVE COMPARISON BETWEEN EXPERIMENTAL AND COMPUTATIONAL RESULTS PRESENTED IN FIG. 3.15C

To quantitatively compare how well the computational curves fit with the experimental results, square correlation coefficient (R^2) and root mean square error (RMSE) are calculated at each cell seeding density:

$$R^2 = \left[\frac{N\sum_{i=1}^{N}\left(\bar{X}_{i,\text{experiment}} X_{i,\text{computation}}\right) - \sum_{i=1}^{N}\bar{X}_{i,\text{experiment}} \sum_{i=1}^{N}X_{i,\text{computation}}}{\sqrt{N\sum_{i=1}^{N}\bar{X}_{i,\text{experiment}}^{2} - \left(\sum_{i=1}^{N}\bar{X}_{i,\text{experiment}}\right)^{2}} \sqrt{N\sum_{i=1}^{N}X_{i,\text{computation}}^{2} - \left(\sum_{i=1}^{N}X_{i,\text{computation}}\right)^{2}}} \right]^{2} \quad \text{(A5.1)}$$

$$\text{RMSE} = \sqrt{\frac{1}{N}\sum_{i=1}^{N}\left(\bar{X}_{i,\text{experiment}} - X_{i,\text{computation}}\right)^{2}} \quad \text{(A5.2)}$$

where N is a number of data points at a cell seeding density. We note that computational data points, corresponding to experimental ones, were selected at each cell seeding density so that $N_{\text{experiment}}$ is equal to $N_{\text{computation}}$.

SUPPLEMENTARY METHOD: SYNTHESIS OF PTTFPP-PS MICROPARTICLES

This appendix describes a protocol for the synthesis of PtTFPP-PS microparticles via dispersion polymerization (also refer to Chapter 4 and Fig. 4.3A). Suppose that we would like to make 10 g of 10 % [w/w] microparticle suspension,

- Monomer: styrene = 10 % [w/w] = 1 g

- Initiator: 2,2'-azobisisobutyronitrile (AIBN) = 0.5 % [w/w] = 0.05 g

- Stabilizer: poly(vinyl pyrrolidone) (PVP) = 4.45 % [w/w] = 0.445 g

- Solvent: 90 % [v/v] ethanol = 10 g - styrene - AIBN - PVP = 8.505 g

    o Ethanol = $8.505 \times 0.9 = 7.6545$ g

    o DI water = $8.505 \times 0.1 = 0.8505$ g

- Oxygen-sensitive phosphor: Platinum(II)-5,10,15,20-tetrakis-(2,3,4,5,6-pentafluorphenyl)-porphyrin (PtTFPP) = 1 % [w/w] = 0.1 g

Dispersion polymerization

1. Prepare two separate mixtures in two 20 mL-glass vials

    - Mixture 1 (vial 1): EtOH, DI water, and PVP

    - Mixture 2 (vial 2): Styrene, AIBN, and PtTFPP

2. Stir the mixtures for 1.5 hr

3. In the mean time, heat a silicone oil bath to 70 °C

4. Pour the mixture 2 into the mixture 1

5. (Optional) Apply N_2 (g) to the reaction vial to allow for the exchange of the gas atmosphere for N_2 (g)

    - Radicals from oxygen can potentially initiate the polymerization

- We want only AIBN to initiate the polymerization because the concentration of AIBN controls the size of microparticles
- Ideally, bubble N_2 (g) directly into the reaction vial (also see Appendices 7 and 8)

6. Seal the vial with parafilm
7. Clamp the vial to a ring stand so as to suspend it in the oil bath
8. Stir the oil bath at 60 rpm
9. Allow the dispersion polymerization for 24 hr at 70 °C

Post-processes after the synthesis

1. Remove the vial from the oil bath and allow it to cool down to room temperature
2. While cooling, prepare 10 % [v/v] ethanol
3. After cooling, centrifuge the polymerization product for 3 min at 3000 rpm
4. Remove the supernatant
5. Add approximately 20 mL of 10 % [v/v] ethanol to the pellet
6. Re-suspend the pellet in 10 % [v/v] ethanol
7. Centrifuge the suspension for 3 min at 3000 rpm
8. Repeat steps 4-7 until the supernatant is clear (~ 4 times)
9. (Optional) Remove the final supernatant
10. (Optional) Allow the pellet (PtTFPP-PS microparticles) to dry overnight

Refer to more references that describe aspects of this synthesis[1-4].

REFERENCES

1.   Amao, Y. *et al.*, Oxygen sensing based on lifetime of photoexcited triplet state of platinum porphyrin-polystyrene film using time-resolved spectroscopy. *J. Porphyr. Phthalocyanines* **4** (3), 292-299 (2000).

2.   Im, S.H. *et al.*, Synthesis of polystyrene beads loaded with dual luminophors for self-referenced oxygen sensing. *Talanta* **67** (3), 492-497 (2005).

3.   Kimura, F. *et al.*, Dual luminophore polystyrene microspheres for pressure-sensitive luminescent imaging. *Meas. Sci. Technol.* **17**, 1254-1260 (2005).

4.   Lee, S.K. & Okura, I., Photostable optical oxygen sensing material: Platinum tetrakis(pentafluorophenyl)porphyrin immobilized in polystyrene. *Anal. Commun.* **34** (6), 185-188 (1997).

APPENDIX 7

SUPPLEMENTARY METHOD: SYNTHESIS OF RU-PEG-PUAN

NANOPARTICLES

This appendix describes a protocol for the synthesis of Ru-PEG-PUAN nanoparticles via emulsion polymerization (also refer to Chapter 4 and Fig. 4.3B). Suppose that we would like to make 10 g of 10 % [w/w] nanoparticle suspension,

- Monomer: urethane acrylate nonionomer (UAN)[1-2] = 10 % [w/w] = 1 g

- Initiator: potassium persulfate (KPS) = 0.2 % [w/w] = 0.02 g

- Solvent: DI water = 9 g

- Oxygen-sensitive phosphor: $[Ru(dmb-PEG)_2(pyr-bpy)]Cl_2$ (Ru-PEG; MW 1150.3301) = 0.052 % [w/w] = 5.2 mg (4.5 µmol)

Emulsion polymerization

1. Mix 1 g of UAN with ~3 mL of 1.5 mM Ru-PEG dissolved in methylene chloride (MC)

2. Vortex several times to make sure that both Ru-PEG and UAN are homogeneously dissolved

3. Allow MC to evaporate

4. Dissolve the solid mixture of Ru-PEG and UAN in 9 mL of KPS-dissolved in DI water (2 mg/mL) (Fig. A7.1A)
   - Strongly agitated for ~30 min
   - Magnetic stir bar

5. Transfer Ru-PEG-UAN-KPS-dissolved in DI water to a 50 mL flask with the magnetic stir bar (Fig. A7.1B)
   - Submerge the flask in a silicone oil bath

176

       i. Make sure to submerge just the reaction volume

- Bubble N_2 (g) directly into the solution

6. Agitate the flask at 650 rpm

7. Increase temperature to 65 ℃

8. Stop applying N_2 (g) after ~2 hr-purging

9. Allow emulsion polymerization for another 3 hr

10. Stop polymerization by turning off the hot plate

11. Transfer UAN nanoparticle-suspended water to a 30 mL-conical tube (Fig. A7.1C)

12. Store the tube at room temperature in the dark

Refer to more references that describe aspects of this synthesis[1-2].
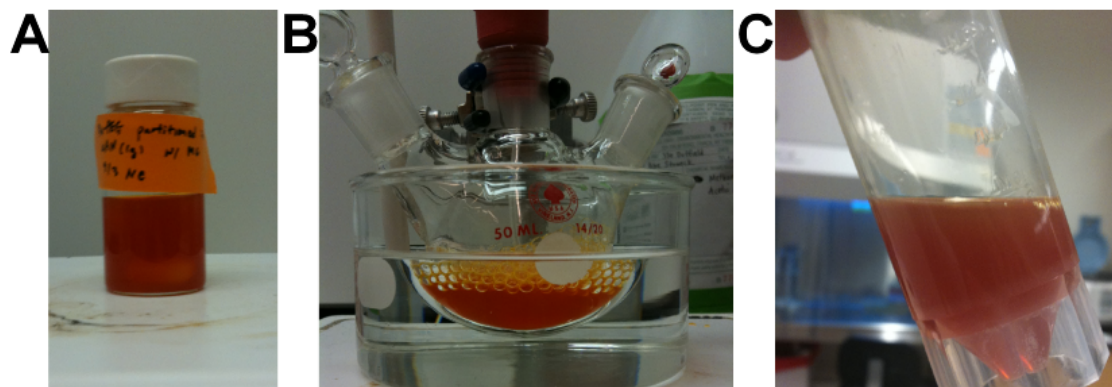
Figure A7.1 Synthesis of Ru-PEG-PUAN nanoparticles. **A.** Ru-PEG-partitioned
UAN in 9 mL of KPS-dissolved in DI water. **B.** The reaction flask with bubbling N_2
(g). **C.** Synthesized Ru-PEG-PUAN nanoparticles suspended in water.

REFERENCES

1.   Kim, J.Y. *et al.*, Comparison of amphiphilic polyurethane nanoparticles to nonionic surfactants for flushing phenanthrene from soil. *J. Hazard. Mater.* **116** (3), 205-212 (2004).

2.   Kim, J.Y. *et al.*, Use of polymer nanoparticles as functional nano-absorbents for low-molecular weight hydrophobic pollutants. *J. Nanosci. Nanotechnol.* **7**, 4000-4004 (2007).

APPENDIX 8

SUPPLEMENTARY METHOD: SYNTHESIS OF PtTFPP-PUAN

NANOPARTICLES

This appendix describes a protocol for the synthesis of PtTFPP-PUAN nanoparticles via emulsion polymerization (also refer to Chapter 4). Suppose that we would like to make 9 g of 10 % [w/w] nanoparticle suspension,

- Monomer: urethane acrylate nonionomer (UAN) = 10 % [w/w] = 0.9 g
- Initiator: potassium persulfate (KPS) = 0.2 % [w/w] = 0.018 g
- Solvent: DI water = 8.1 g
- Oxygen-sensitive phosphor: Platinum(II)-5,10,15,20-tetrakis-(2,3,4,5,6-pentafluorphenyl)-porphyrin (PtTFPP; MW 1168.62) = 0.044 % [w/w] = 4 mg (3.4 µmol)

Emulsion polymerization

1. Dissolve 0.9 g of UAN in ~4 mL of methylene chloride (MC)
2. Add ~80 µL of ~43 mM PtTFPP in MC
3. Vortex several times to make sure that both PtTFPP and UAN are homogeneously dissolved (Fig. A8.1A)
4. Allow MC to evaporate for ~2 days (Fig. A8.1B)
5. Dissolve the solid mixture of PtTFPP and UAN in 8.1 mL of KPS-dissolved in DI water (2 mg/mL)
   - Strongly agitated for ~30 min
   - Magnetic stir bar
6. Transfer PtTFPP-UAN-KPS-dissolved in DI water to a 50 mL flask with the magnetic stir bar (Fig. A8.1C)

- Submerge the flask in a silicone oil bath

    i. Make sure to submerge just the reaction volume

- Bubble N_2 (g) directly into the solution

7. Agitate the flask at 650 rpm

8. Increase temperature to 65 °C

9. Stop applying N_2 (g) after ~2 hr-purging (Fig. A8.1D)

10. Allow emulsion polymerization for another 3 hr

11. Stop polymerization by turning off the hot plate

12. Transfer UAN nanoparticle-suspended water to a 30 mL-conical tube (Fig. A8.1E)

13. Store the tube at room temperature in the dark

Refer to the references listed in Appendix 7.
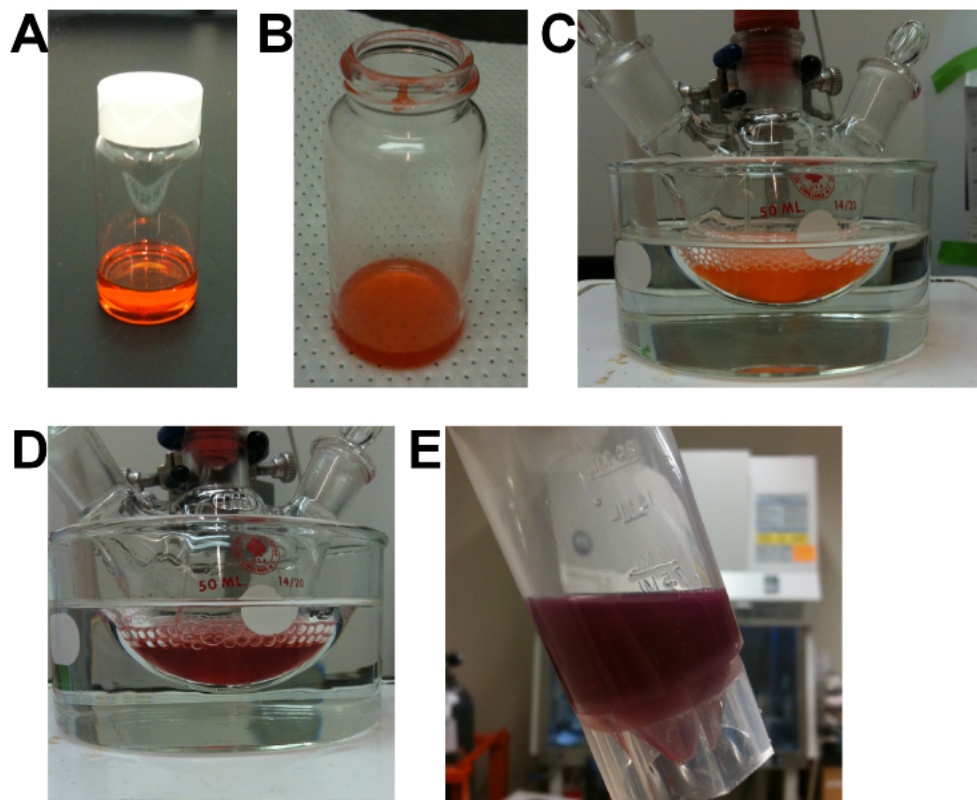
Figure A8.1 Synthesis of PtTFPP-PUAN nanoparticles. A. PtTFPP and UAN

dissolved in MC. **B.** Ru-PEG-partitioned UAN. **C.** The reaction flask with bubbling

N$_2$ (g). **D.** The reation flask immediately after stopping N$_2$-bubbling during the

polymerization. **E.** Synthesized PtTFPP-PUAN nanoparticles suspended in water.

APPENDIX 9

COMPUTATIONAL AND ANALYTICAL APPROACHES TO MODEL

BIOMINERALIZATION IN HYDROGELS

I. Introduction

Calcium phosphate (CP) is a major component of bone and teeth[1-2] and exists as a biogenic crystalline phase, hydroxyapatite (HA; $Ca_{10}(PO_4)_6OH_2$)[2-3] *in vivo*. The formation of HA, via a process of biomineralization, is biologically regulated, leading to the creation of organic-inorganic composites (e.g., bone-cartilage interface; Fig. A9.1); a transition from compliant cartilage to biomineralized bone is made through an intermediate continuous region called calcified cartilage. This transition region is known as the tidemark between bone and cartilage. The osteochondral interface typically occurs over a sub-milimeter scale and has mechanical properties that bridge those of the two dissimilar tissues. It has been proposed that *in vivo* concentration gradients of inhibitors and promoters are involved in regulating the formation of the bone mineral, HA[4-7]. Such gradients of biomacromolecules may establish the location of the tidemark and contribute to the successful integration of cartilage with bone. For example, ariticular chondrocytes are known to synthesize pyrophosphate (PPi), which is a soluble and potent inhibitor of the HA formation[7-9]. If the balance of interactions between the biomacromolecules and tissue matrices is broken under certain pathological conditions, abnormal biomineralization can occur and cause detrimental effects in tissues and organs[6-7]. Therefore, it is important to study the biomineralization to identify matrix molecules involved and elucidate their roles. Improved understandings would also lead to success in designing new organic-inorganic composite materials that could be used for tissue engineering and therapeutic purposes.
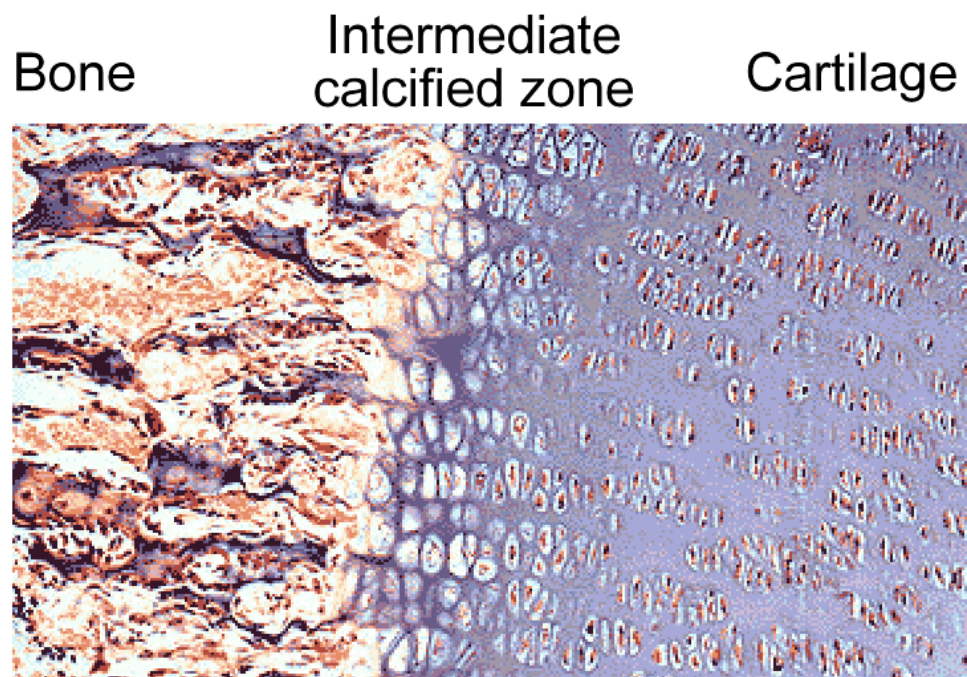
Figure A9.1 Histological section of bone-cartilage interface. Image was obtained from http://faculty.une.edu/com/abell/histo/histolab3.htm.

In understanding the mineralization process of HA, *in vitro* hydrogel precipitation methods, used for the past decades for the growth of large crystals[10], have been applied to elucidate the roles of biomacromolecules[11]. Such *in vitro* hydrogel precipitation methods in the absence of cells aid to characterize the chemical process in a more controlled manner, compared with *in vivo* studies. In addition, the hydrogel precipitation methods have advantages that solution precipitation methods do not provide: 1) small amounts of biomolecules are required to reduce the volume of precipitation, and 2) diffusion-reaction of molecules and ions in gels allows the recapitulation of physiological environment. Silverman and Boskey introduced the double-diffusion system (DDS), where calcium ions are delivered from one end and phosphate ions from the other, for the purposes described above[11] (also see Fig. A9.2).
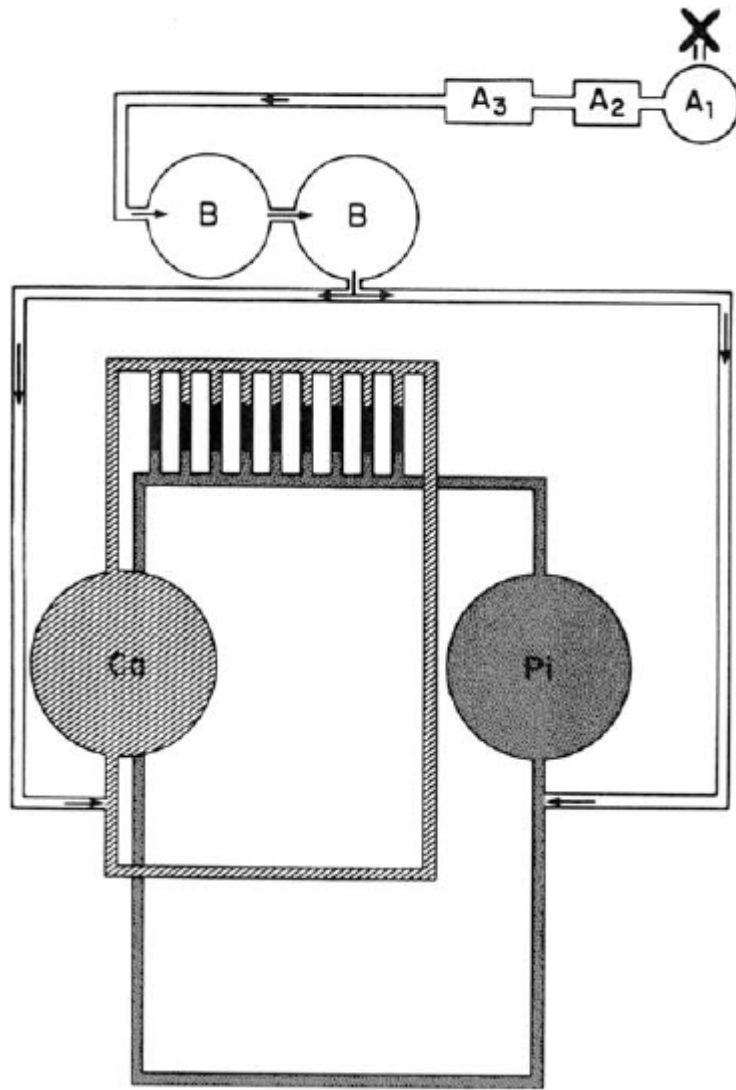
Figure A9.2 Schematic diagram of the dynamic hydroxyapatite formation system (the double-diffusion system (DDS)). Image was obtained from Silverman, L. & Boskey, A.L., Diffusion systems for evaluation of biomineralization. *Calcif. Tissue Int.* **75** (6), 494-501 (2004).

Along with experimental observations, it would be also valuable to model the formation of HA (i.e., precipitation of calcium phosphate) in the DDS because models can be applied in a predictive role. Using the models as our guide, we could predict: 1) when a precipitation event will occur, 2) where it will be within a hydrogel, and 3) the expected composition of the mineralized band. However, the formation of HA is believed to be mediated by the formation of intermediate CP precursors such as amorphous calcium phosphate (ACP), dicalcium phosphate dihydrate (DCPD), and octacalcium phosphate (OCP)[2-3,12]. In addition, it is a complex multi-step process with seemingly high order kinetics (i.e., 9th order with respect to calcium, phosphate, and hydroxyl ions) where supersaturation, nucleation, and crystal growth are involved[12-14]. The global reaction for the crystallization of HA in aqueous environment is given by

$$5Ca^{2+} + 3PO_4^{3-} + OH^- \longrightarrow Ca_5(PO_4)_3(OH) \qquad (A9.1)$$
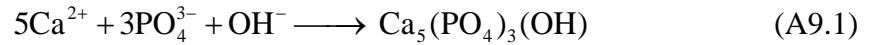
Despite a large number of both experimental and theoretical studies aimed to decipher details about the mechanisms and kinetics of the formation of HA[12-17], most studies are based on the solution precipitation methods. From the perspective of mass transport, these studies have a fundamental difference; in the solution precipitation methods, reacting ions are convectively well-stirred whereas, the DDS is a continuously fed unstirred reactor (CFUR) that results in the creation of spatially distinct regions (i.e., regions for the free diffusion of the ions and a region for the fast crystal formation). This complicated nature of the formation of HA and the lack of necessary information (e.g., interfacial tension between HA and a gel matrix) make it difficult to model the system. Furthermore, although a supersaturation threshold can be identified experimentally (i.e., critical concentrations of calcium and phosphate ions at a given position and time) and has been widely used to predict the formation of

HA for decades[18], it has not led to the identification of a specific reaction mechanism in the DDS.

In order to generate predictions of the dynamics and mass transport of the system, our attempt to use continuum equations to simulate the concentration profiles confronted divergence limitations due to the complex nature of the high order kinetics of the formation of HA embedded in supersaturation (S); the continuum model is extremely unstable due to the high local variability of supersaturation, which is the driving force for crystal growth. This model is based on the assumption that the rate-limiting step follows the global stoichiometry that is high-ordered (Eq. A9.1). We note that orders higher than three for an elementary reaction are extremely rare in homogeneous chemical reactions because the kinetic order of reactions is directly dependent on the probability of physical contact between the reacting species; the probability for quadrimolecular collisions to occur in a single step is negligibly small. Such high orders may become probable in heterogeneous reactions such as adsorption or crystal growth where multimolecular aggregates and multistep processes are involved. A different approach that can be considered is to simulate all the dynamics (chemical and physical) by the implementation of Kinetic Monte Carlo (KMC) method. Along with Molecular Dynamics (MD), this approach has been widely used to understand crystal growth phenomena on a molecular level, by treating the growth process as a stochastic and probabilistic description[19-20].

In this appendix, we report a computational model that presents an alternative solution to the limitations. A multiscale computational modeling approach, by hybridizing KMC with finite difference (FD), offers the advantage of separating the diffusion time scale (treating it as a bulk property of the system) from the reaction time scales of nucleation and growth. In addition, the discretization of the reaction tube in the DDS (also see Fig. A9.5A) enables the evaluation of local dynamics. This

technique allows modeling the formation of HA under the assumption of stoichiometric mechanisms of the crystallization. Then, we present an analytical approach to model a general diffusion-limited $m\text{A} + n\text{B} \rightarrow \text{C}$ (inert) type reaction in the DDS. Such diffusion-limited reactions include many physical, chemical, and biochemical reactions, including precipitation and crystal formation. We focus on finding the location of a confined reaction layer (i.e., the depletion sink) and its characteristics. We also present our effort to model the inhibition of the HA formation (i.e., the formation of calcium pyrophosphate (CPP)) in the DDS (also see Fig. A9.3B), using the finite element method (FEM). It is also a relatively simple diffusion-limited reaction compared with the formation of HA, and serves as a basis not only to validate our analytical model but also to extract detailed kinetic information for further investigation of the crystal formation (e.g., the width of crystal bands). We will then conclude with our current assessment of the computational models as predictive tools and future directions towards exploiting the biomineralization processes.
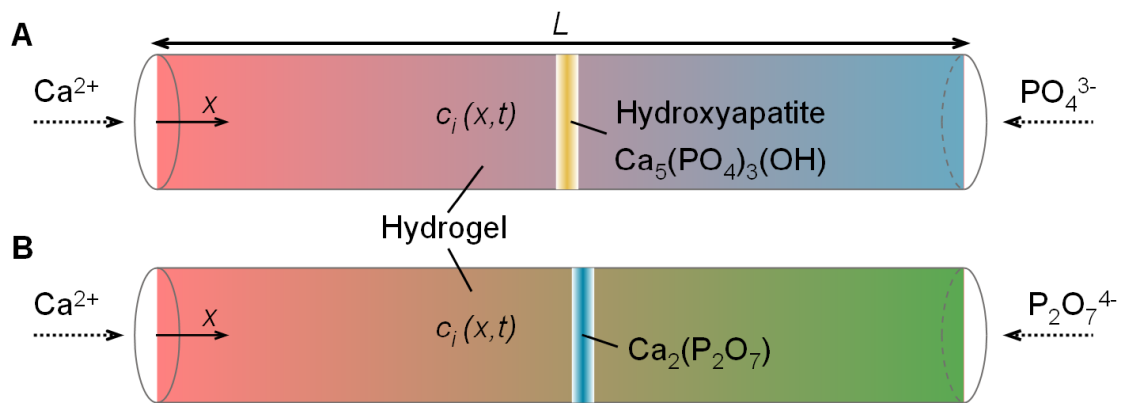
Figure A9.3 Schematic representation of double-diffusion system. A. The formation of hydroxyapatite (HA). **B.** The formation of calcium pyrophosphate (CPP). The pink shadings represent the concentration of calcium ions. The blue shading represents the concentration of phosphate ions. The green shading represents the concentration of pyrophosphate ions.

Formation of HA

The global reaction for the crystallization of HA in aqueous environment is given by

$$5Ca^{2+} + 3PO_4^{3-} + OH^- \longrightarrow Ca_5(PO_4)_3(OH) \qquad (A9.2)$$
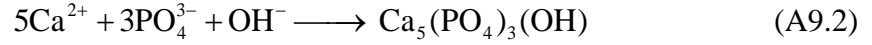
However, the crystallization process is known to occur by two distinct steps: nucleation and growth (Fig. A9.4).

A. Nucleation

The model for nucleation rate considered is based on the classical heterogeneous nucleation:

$$R_n = (K'P)\exp\left[-\frac{\beta\gamma_I^3 v^2 f(\theta)}{k_B^3 T^3 \ln(S)^2}\right] \qquad (A9.3)$$

β is a geometrical factor and in our model it has a value of $16\pi/3$ representing a spherical nucleus. γ_I is the interfacial tension between the calcium phosphate and the solution and has a value of 104 mJ/m^2. v is the molecular volume of a HA unit determined by its crystal structure and has a value of 263.24 Å^3. $f(\theta)$ is the contact angle function given by the classical theory of heterogeneous nucleation[21], and it has values from 0 to 1. The contact angle function can be estimated based on the shape of HA on a substrate surface (e.g., gelatin or agarose). An angle of 0° corresponds to a value of the contact angle function of 0, while and angle of 180° corresponds to a value of 1 and represents homogeneous nucleation. We have chosen the contact angle function to have a value of 1/2 since its variation does not affect significantly the nucleation rate. k_B is Boltzmann's constant and T is the solution temperature (taken as ambient). K' is a constant that was determined from experiments and has a value of

$1.364 \times 10^{28} \, L^{-1}s^{-1}$. The parameters described above are based on a theoretical study of calcium phosphate precipitation in simulated body fluid, a solution with calcium and phosphate ions, and a physiological pH value (i.e. pH 7.4)[13]. Supersaturation of HA, S_{HA} is defined as

$$S_{HA} = \frac{a_{Ca^{2+}}^5 \, a_{PO_4^{3-}}^3 \, a_{OH^-}}{K_{sp,HA}} \qquad (A9.4)$$

where a represents activity of each ion and K_{sp} (2.35×10^{-59}) is the solubility product for HA crystal. The activities are defined as the product of the molar fraction and the activity coefficient for each ion. The activity coefficients (γ) for each ion can be obtained from the modified Debye-Hückel equation:

$$\log \gamma_i = -Az_i^2 \left(\frac{I^{1/2}}{1 + I^{1/2}} - 0.3I \right) \qquad (A9.5)$$

where A is the Debye-Hückel constant dependent on temperature ($A = 0.5211$ at 37°), z_i is the charge number of the ion and I is the total ionic strength of the solution and is defined as

$$I = \frac{1}{2} \sum c_i z_i^2 \qquad (A9.6)$$

where c_i is the molar concentration of each ion unit. OH⁻ concentration is always fixed by unchanging pH. The nucleation rate is also proportional to the probability that the appropriate ion units of calcium phosphate meet to compose a nucleus in solution. This probability is defined as

192

$$P = \frac{9![Ca^{2+}]^5[PO_4^{3-}]^3[OH^-]}{5!3!([Ca^{2+}]+[PO_4^{3-}]+[OH^-])^9}$$ (A9.7)

B. Crystal growth

The model for crystal growth rate is proportional to the relative solution supersaturation, σ, with respect to HA, defined as

$$R_{cg} = k_{cg}\sigma^n$$ (A9.8)

where n is the apparent order of the crystallization process and k_{cg} is the rate constant. Both if these values are determined by fitting experimental data of crystal growth ($n = 1.87$ and $k_{cg} = 2.59201 \times 10^{22}$ m^{-2}s^{-1})[14]. The relative supersaturation is defined as

$$\sigma = S^{1/9} - 1$$ (A9.9)

where S is the supersaturation as in Eq. A9.3.
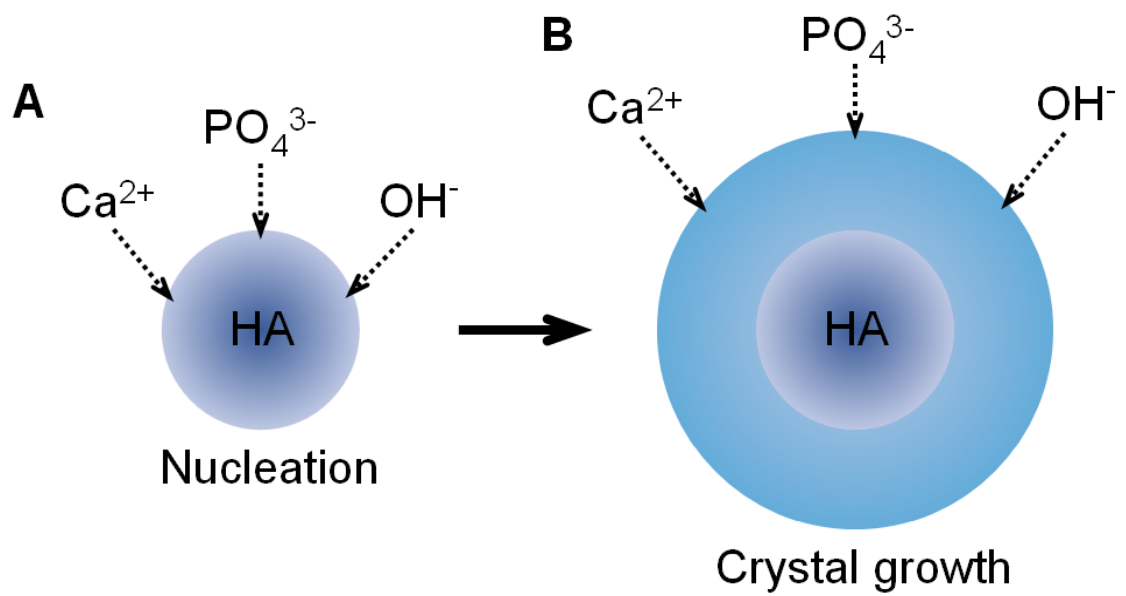
Figure A9.4 Schematic illustration of the formation of HA. A. Nucleation. **B.**

Crystal growth.

C. Implementation of multiscale computational modeling: finite difference (FD)-Kinetic Monte Carlo (KMC)

Multiscale computational modeling approaches can be used for 1) metal electrodepositing on a surface[22] or 2) a fluid phase in bulk and catalytic surface reactions within catalytic flow reactors[23], where macroscopic modeling at a continuum level does not fully capture near-surface chemistry and detailed reaction mechanisms. Such multiscale modeling approaches are carried out by coupling continuum-level modeling with molecular level simulations.

In order to describe both the diffusion of calcium and phosphate ions in the bulk of the DDS, and the crystallization process of HA, we have developed similar multiscale modeling by coupling finite difference (FD) and Kinetic Monte Carlo (KMC). Then, the diffusion of the ions is modeled on a macro-scale while the nucleation and crystal growth are modeled on a micro-scale. The diffusion equation

$$\frac{\partial c_i}{\partial t} = D_i \frac{\partial^2 c_i}{\partial x^2} \tag{A9.10}$$

has been solved for each ion in the system using the Crank-Nicholson implicit method, dividing the double-diffusion system in several volume elements of length Δx (Fig. A9.5). The transient 1-D diffusion equation becomes

$$D_i \left\{ \frac{c_{m+1,i} - 2c_{m,i} + c_{m-1,i}}{(\Delta x)^2} \right\} + R_{m,i} = \frac{\Delta c_{m,i}}{\Delta t} \tag{A9.11}$$

where m is the element and i is the ion species. Since there is no reaction (due to decoupling), the R term is zero for all positions except for the first and last elements where R corresponds to the boundary conditions (constant boundary concentrations). Since equation A9.10 is dependent on the concentrations at the m element, m-1

element, and $m+1$ element, we obtain a system of linear equations that can be solved using matrices:

$$\begin{bmatrix} \dfrac{-2D_i}{(\Delta x)^2} & \dfrac{D_i}{(\Delta x)^2} & & \\ \dfrac{D_i}{(\Delta x)^2} & \dfrac{-2D_i}{(\Delta x)^2} & \dfrac{D_i}{(\Delta x)^2} & \\ & \vdots & \vdots & \\ & \dots & \dfrac{D_i}{(\Delta x)^2} & \dfrac{-2D_i}{(\Delta x)^2} \end{bmatrix} \times \begin{bmatrix} C_{1,i} \\ C_{2,i} \\ \vdots \\ C_{m,i} \end{bmatrix} + \begin{bmatrix} \dfrac{D_i}{(\Delta x)^2} C_{0,i} \\ 0 \\ \vdots \\ \dfrac{D_i}{(\Delta x)^2} C_{m+1,i} \end{bmatrix} = \begin{bmatrix} \dfrac{\Delta C_{1,i}}{\Delta t} \\ \dfrac{\Delta C_{2,i}}{\Delta t} \\ \vdots \\ \dfrac{\Delta C_{m,i}}{\Delta t} \end{bmatrix} \quad \text{(A9.12)}$$

The result is a matrix of the variation of concentration with respect to time for each single element, so we can predict the concentration profile of the microchannel after a time Δt.

Macroscopic scale: Finite Difference (FD)

Ca^{2+} L PO_4^{3-}

x

Δx

Microscopic scale: Kinetic Monte Carlo (KMC)

Δx

dV (500 ions)

$\tau \sim (\Delta x)^2 / D_i$
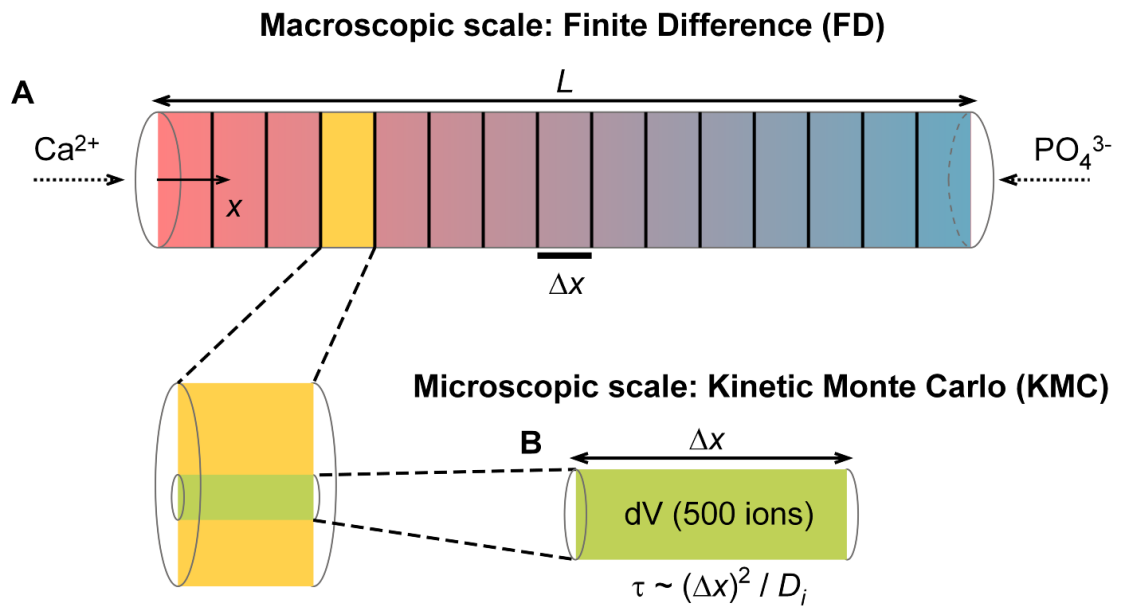
Figure A9.5 Schematic representation of the multiscale modeling, FD-KMC, showing macro to micro-scale transition. A. FD in macroscale. **B.** KMC in microscale.

Figure A9.5 depicts how a single volume element is considered as a perfect Stirred

Tank Reactor (STR), yet this element is still too large to perform KMC. Therefore, it

is divided into many sub-volumes of the same length (Δx); their radus is small

enough that a concentration of 0.1 mol/L (reference concentration) corresponds to

only 500 ions. This additional step is not preferable but necessary to lower

computational load. Ideally, KMC could capture stochastic concentration fluctuations

of ions within the entire single volume element, leading to increase of sampling

species. In addition, radial symmetry is assumed within each element; the radial flux

of any ion is the same towards and out of a sub-volume, such that only axial diffusion

should be considered. The characteristic time of such diffusion (for any single ion)

has been calculated from Einstein's result for Brownian motion. Then, we can

consider 6 pseudo-reactions for the KMC approach:

$$\left(Ca^{2+} \right)_{in} \xrightarrow{\quad k_{Ca^{2+}} \quad} \left(Ca^{2+} \right)_{out} \tag{A9.13}$$

$$\left(PO_4^{3-} \right)_{in} \xrightarrow{\quad k_{PO_4^{3-}} \quad} \left(PO_4^{3-} \right)_{out} \tag{A9.14}$$

$$\left(Cl^- \right)_{in} \xrightarrow{\quad k_{Cl^-} \quad} \left(Cl^- \right)_{out} \tag{A9.15}$$

$$\left(NH_4^+ \right)_{in} \xrightarrow{\quad k_{NH_4^+} \quad} \left(NH_4^+ \right)_{out} \tag{A9.16}$$

$$n Ca^{2+} + m PO_4^{3-} + q OH^- \xrightarrow{\quad k_n \quad} N^* \tag{A9.17}$$

$$n' Ca^{2+} + m' PO_4^{3-} + q' OH^- \xrightarrow{\quad k_{cg} \quad} HA \tag{A9.18}$$
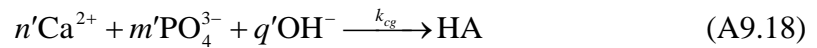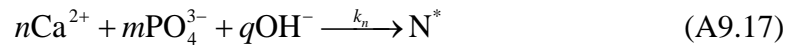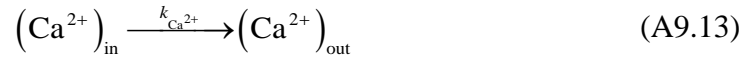
If we consider, for example, the double-diffusion system divided in 15 elements, there

are a total of 60 pseudo-reactions competing on the KMC and one is chosen randomly,

based on their propensity functions (Guillespie's method). A reaction time is sampled

using KMC criteria. Because HA cannot precipitate until Ca^{+2} and PO_4^{-3} encounter

each other, the algorithm only takes diffusion into account until Ca^{+2} and PO_4^{-3} concentrations, at any single point, reach a value that makes nucleation feasible. Once they encounter, the algorithm makes a scale change in order to evaluate the probability of nucleation or growth following the KMC criteria.

Even though KMC is useful to deal with nucleation and growth pseudo-reactions, it is not practical to model diffusion using KMC, because of the size of the double-diffusion system. Therefore, we have linked KMC with FD when a diffusion pseudo-reaction is chosen based on randomly fluctuating probabilities; in other words, 1) no nucleation or growth occurs during the KMC sampled time that also randomly fluctuates, and 2) all the ions diffuse during the time interval based on the macroscopic diffusion with the Crank-Nicholson implicit method. On the other hand, if a nucleation or growth pseudo-reaction is chosen as a single event, no ion diffuses while the pseudo-reaction occurs.

The complexity of the model can be increased by adding a nucleation inhibitor to the system, which would occur if cells (chondrocytes) are seeded at a specific position of the double-diffusion system and start producing inhibitors such as pyrophosphate. As an example, our algorithm incorporates an inhibition factor (I^*) as a calcium ion sink:

$$I^* + Ca^{2+} \longrightarrow CaI^* \qquad (A9.19)$$

The MATLAB code for the FD-KMC is appended in Appendix 10.

D. Results and discussion

With input parameters summarized in Table A9.1, we have simulated the formation of HA, using the FD-KMC. Calcium and phosphate ions were allowed to diffuse from the two ends of the DDS and to form HA. The location of the first crystal

that is formed determines a "sink" for both, calcium and phosphate ions. However, we note that this does not imply that crystallization does not take place in neighboring locations. Figure A9.6C and D shows that HA forms at slightly away from the center towards the phosphate side and that the size of HA crystal is ~ 1.2 nm. The crystal radius was estimated with

$$r_{HA} = \left(n_{HA} v \frac{3}{4\pi} \right)^{1/3} \qquad\qquad (A9.20)$$

where n_{HA} is number of HA crystal. Although we have not directly compared the crystal size estimated from the FD-KMC with experimental measurements, the plots allow for the qualitative comparison of the location of HA. The computational result shows reasonable agreement with experimental observations (Fig. A9A and B). Note that the simulation was run with experimentally measured diffusivity of calcium (i.e., 6×10^{-10} m^2/s) and phosphate (i.e., 3.9×10^{-10} m^2/s) ions within gelatin. Yet, HA forms at about the center of gelatin (Fig. A9.6A). Interestingly, in both experiment and simulation, the formation of HA is slightly shifted towards the phosphate side in agarose (Fig. A9.6B). These experimental observations suggest that crystal-matrix interactions may be involved in the formation of HA. In addition, the disagreement between the computational result and the experimental observation in gelatin is likely due to a possibility that input parameters such as interfacial surface tension, rates of nucleation and crystal growth could be different in gel matrices. The quoted values are reported ones that have been measured or estimated in solution.

In an effort to predict the effect of an inhibitor, we have placed a steady source of a calcium chelator at element 6 and allowed it to diffuse along the DDS. As expected, the presence of an inhibitor displaces the "sink" location, for both calcium and phosphate ions (Fig. A9.6E). The location of the inhibitor determines where the

first and largest crystal forms. This can be explained by the fact that nucleation rates are orders of magnitude smaller than growth rates. The outcome of this situation is that once a nucleus is formed, crystal growth takes place very rapidly and drives the consumption of reacting ions. Figure A9.6D and F indicate that the size of HA crystal formed in the presence with an inhibitor is smaller than that without the inhibitor. This is because the crystallization reaction requires more phosphate ions than calcium for it to begin while the inhibitor continuously chelates calcium ions. We have observed that locating the inhibitor (i.e. calcium chelator) at the phosphate side hardly affected the formation of HA (data not shown). These computational results suggest that once specific roles of inhibitors are identified, we could control the formation of HA in a spatially resolved manner.

Table A9.1 Input parameters used in the FD-KMC

Calcium boundary concentration	$c_{0,Ca^{2+}}$	0.1 mol/L
Phosphate boundary condition	$c_{0,PO_4^{3-}}$	0.1 mol/L
Hydroxyl ion concentration	c_{OH^-}	2.5×10^{-7} mol/L
Diffusivity of calcium ion	$D_{Ca^{2+}}$	6×10^{-10} m^2/s
Diffusivity of phosphate ion	$D_{PO_4^{3-}}$	3.9×10^{-10} m^2/s
Diffusivity of chloride ion[24]	D_{Cl^-}	2×10^{-9} m^2/s
Diffusivity of almonium ion[24]	$D_{NH_4^+}$	1.9×10^{-9} m^2/s
Diffusivity of inhibitor	D_I	2×10^{-10} m^2/s
Rate of inhibitor production	R_I	5×10^{-7} mol/L$\cdot$s
Rate constant for nucleation[13]	K'	1.36×10^{-28} 1/L$\cdot$s
Interfacial surface tension between HA and water[13]	γ_I	0.104 J/m^2
Molecular volume of HA[13]	v	2.63×10^{-28} m^3/mol
Contact angle function[13]	f	0.5
Solubility product of HA[13]	$K_{sp,HA}$	2.35×10^{-59}
Rate constant for crystal growth[14]	k_{cg}	2.59×10^{22} 1/m$^2\cdot$s
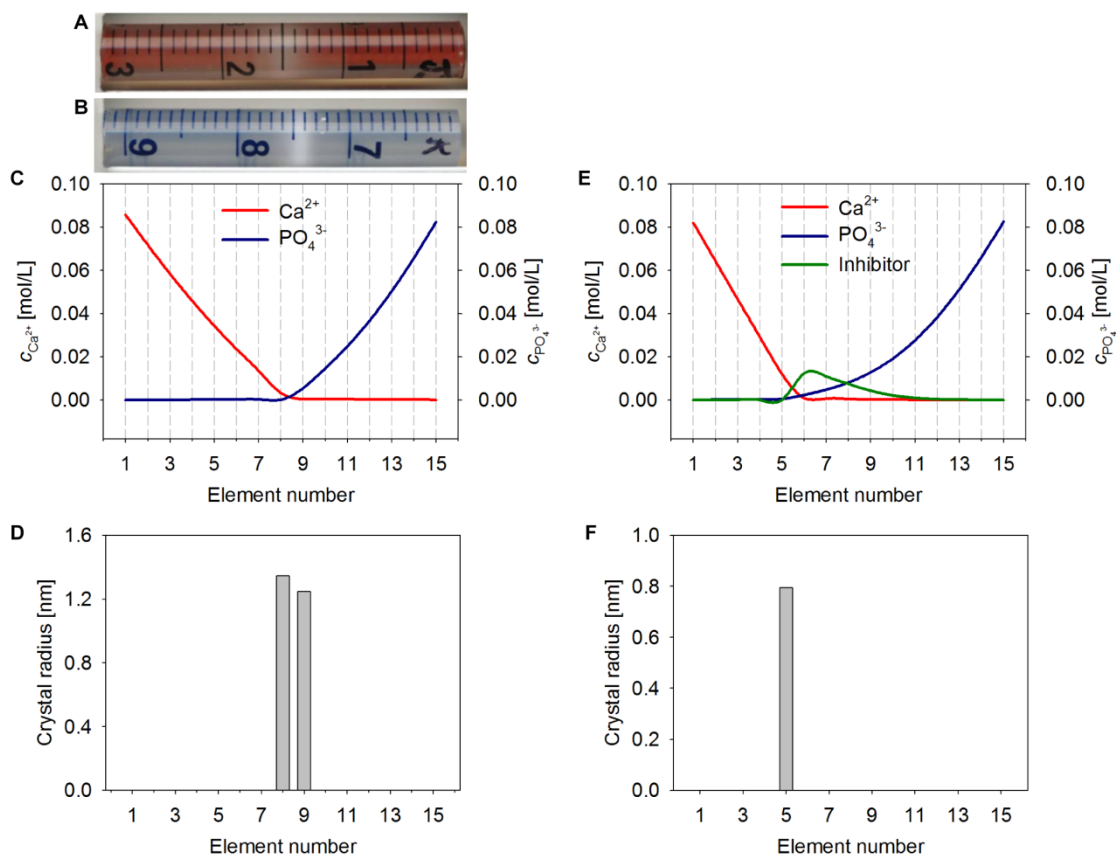
Figure A9.6 Formation of HA in the DDS: experimental observations and FD-KMC results. A and B. Optical micrographs showing the formation of HA within gelatin (A) and agarose (B) on day 5. **C.** Spatial distribution of ions in the absence of an inhibitor on day 5. **D.** Spatial distribution of HA and its crystal size without the inhibitor. **E.** Spatial distribution of ions in the presence of an inhibitor (a Ca^{2+} chelator produced at element 6) on day 5. **F.** Spatial distribution of HA and its crystal size with the inhibitor.

Formation of CPP

Articular chondrocytes synthesize inorganic pyrophosphate to prevent cartilage from being mineralized. However, excess production of pyrophosphate can also cause pathological chondrocalcinosis, the deposition of too much CPP in cartilage[6,25]. Compared with HA, little is known about the mechanisms of CPP[26-27]. The global reaction for the formation of CPP in aqueous environment is given by

$$2Ca^{2+} + P_2O_7^{4-} \xrightarrow{\quad k_{CPP} \quad} Ca_2(P_2O_7)$$ (A9.21)

Figure A9.7 shows the formation of CPP in gelatin, observed on day 7, by allowing for the diffusion of calcium and pyrophosphate ions in the DDS. The variation of calcium boundary conditions (i.e., $c_{0,Ca^{2+}}$ = 50, 100, and 400 mM), results in the formation of CPP at different locations: ~0.54L (Fig. A9.7A), ~0.5L (Fig. A9.7B), and 0.65L (Fig. A9.7C). Although the formation of CPP is accompanied by nucleation and crystal growth just as the formation of HA is, we focus on modeling the phenomenological precipitation event as shown in Eq. A9.21 mainly because similar complexity arises from the lack of kinetic information about the formation of CPP crystal and other forms of CPP such as amorphous or hydrated forms.

The ions and CPP within the DDS are governed by a series of diffusion-reactions:

$$\frac{\partial c_i}{\partial t} = D_i \frac{\partial^2 c_i}{\partial x^2} - \nu_i R$$ (A9.22)

$$\frac{\partial c_{CPP}}{\partial t} = R$$ (A9.23)

where c_i is concentration of calcium or pyrophosphate ion, D_i is diffusivity of the ions, ν_i is stoichiometric coefficient of the ions, and R is the macroscopic reaction rate

that is unknown but could be hypothetically expressed as the product of the concentration of calcium and pyrophosphate ions with effective reaction orders. We assume that produced CPP is immobile within a hydrogel. In the following sections, we present a simple analytical analysis and computational models using the finite element method (FEM) to predict primarily the location of CPP formed in the DDS.
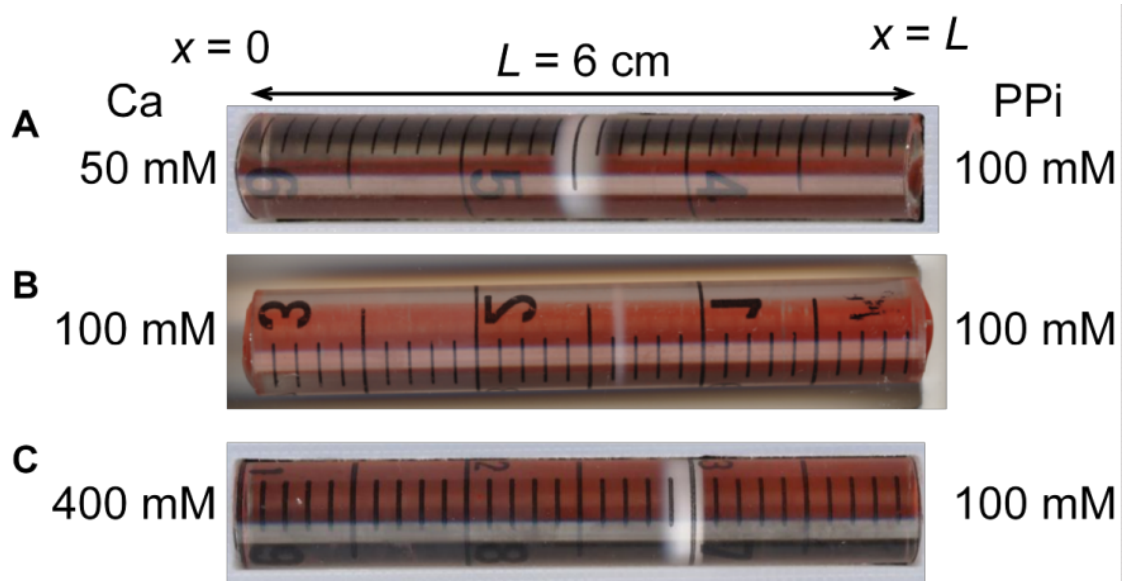
Figure A9.7 Formation of CPP in the DDS: experimental observations. A-C.
Optical micrographs showing the formation of CPP within gelatin on day 7. The DDS
(6 cm long) was fed with 100 mM of pyrophosphate (PPi; right) and various
concentrations of calcium (Ca): 50 (A), 100 (B), and 400 (C) mM.

A. Analyti4cal approach to model diffusion-limited reaction

The very small solubility product of HA (2.35×10^{-59})[13] and CPP (4.47×10^{-19})[28] reveals that the crystal formation occurs instantaneously when ions encounter (i.e., extremely fast reaction). Unlike solution-based systems, where reacting ions are convectively well-stirred, the DDS (Fig. A9.2 and A9.3) is a continuously fed unstirred reactor (CFUR) that allows for a reaction between the two counter-diffusing ions within hydrogels. If Damköhler number (Da), the ratio of reaction rate to diffusion rate ($Da \equiv kc_0L^2 / D$ for a 2nd order reaction), is large enough in the system, such rapid reaction (e.g., crystal formation) is not be reaction-limited but "diffusion-limited"; diffusing species initially separated in space irreversibly form an inert product (e.g., solid phase crystal) on contact, leading to the creation of a depletion zone or sink. Diffusion-limited reactions are readily found in many physical, chemical, and biochemical reactions such as catalysis[29-31], diffusion-limited aggregation[32], chemical vapor deposition[33], gasification[34], Liesgang pattern formation[10,35], and Turning pattern formation[36-37], including precipitation[38] and crystal growth presented in this appendix. In 1988, Gálfi and Rácz established a simplified analytical model of a diffusion-limited A + B → C type reaction in a geometry where initially separated reactants A and B counter-diffuse and form a product C, to investigate the long time behavior of the reaction zone (i.e., the distribution of the product C)[39]; their main results are 1) the center of the reaction zone scales with $t^{1/2}$, and 2) the width of the reaction zone is proportional to $t^{1/6}$. Since then, many other studies have used analytical, computational, and experimental approaches to elucidate diffusion-limited reactions[40-45]. Note that Koza reported a thorough study, providing generalizable analytical treatments in 1996[44]. This section describes a similar analytical approach, primarily focusing on finding the location of a confined reaction layer (i.e., the

depletion sink; at position, x_R) and its characteristics for a general diffusion-limited $m\text{A} + n\text{B} \rightarrow \text{C}$ (inert) type reaction in the DDS.

For simplicity, we consider a steady-state case where the concentration of both reactants A and B linearly decreases to zero as schematically illustrated in Fig. A9.8 (solid lines). In addition, we assume that the reactants are not accumulated at $x = x_R$ due to the infinitely rapid reaction (Fig. A9.8). This quasi-steady-state assumption leads to

$$D_A \frac{d^2 c_A}{dx^2} - mR = 0 \tag{A9.24}$$

$$D_B \frac{d^2 c_B}{dx^2} - nR = 0 \tag{A9.25}$$

with conditions below:

$$\begin{aligned}
c_A(0) &= c_{A0} \\
c_B(L) &= c_{B0} \\
c_A(x_R) &= c_B(x_R) = 0
\end{aligned} \tag{A9.26}$$

where R is reaction rate that is unknown but may be expressed with an assumption that the reaction occurs with both reactants A and B involved in a single step:

$$R = k c_A^m c_B^n \tag{A9.27}$$

where k is rate constant and m and n are reaction orders (positive integers) with respect to A and B respectively. We note that this rate law is a possible hypothesis. We also note that we will not consider any details about the rate constant in finding x_R. The flux of the reactants should satisfy the following condition:

$$J = \frac{J_A}{m} = \frac{J_B}{n}$$

$$J = \frac{1}{m}\left[D_A \frac{c_{A0}}{x_R} \right] = \frac{1}{n}\left[D_B \frac{c_{B0}}{(L - x_R)} \right]$$

(A9.28)

where J_A and J_B are fluxes of the reactants A and B respectively. c_{A0} and c_{B0} are the boundary concentration of the reactants. By rearranging Eq. A9.28, an equation for the location of the depletion sink, x_R is obtained as

$$x_R = \left[\frac{c_{A0}/c_{B0}}{c_{A0}/c_{B0} + (m/n)(D_B/D_A)} \right] L$$

(A9.29)

Eq. A9.29 indicates that the location of the depletion sink, x_R at steady-state is independent of the rate constant, k. In addition, it can be used to control the reaction location by changing the feeding concentration of the reactants A and B (solid lines in Fig. A9.9). This information could be potentially very useful in designing experimental systems. Figure A9.9 also shows that x_R varies with the ratio of the stoichiometric coefficients, m/n at a given set of boundary conditions. Because the location of the depletion sink is where the product C is generated, experimentally measured x_R (e.g., the location of formed CPP at steady-state) could aid to predict the ratio of the effective reaction orders with the assumption of $R = kc_A^m c_B^n$. Note that this feasibility can be valid only if a reaction occurs in a single step. We also note that the green line in Fig. A9.9 (i.e., $m/n = 2$) corresponds to the analytical prediction of the sink location at steady-state for the formation of CPP; the reactants A and B represent calcium and pyrophosphate respectively and the product C represents CPP.
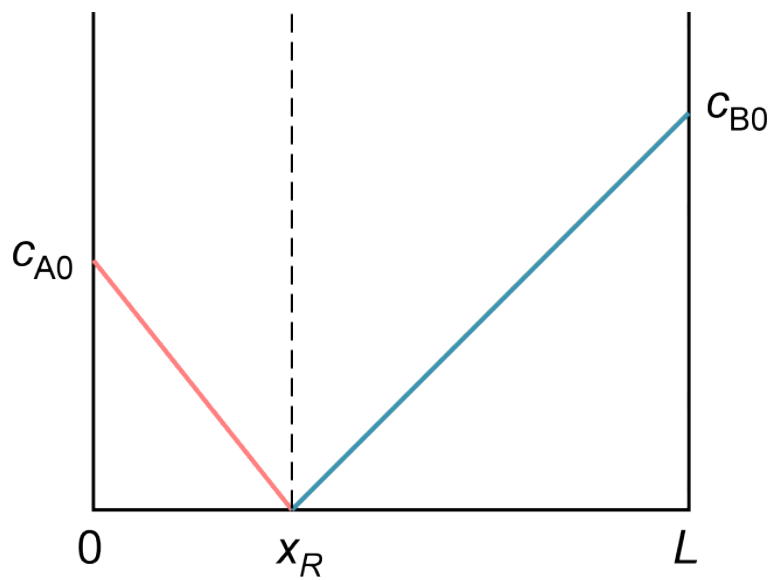
Figure A9.8 Schematic diagram of steady-state distributions of reactants A and B for diffusion-limited reaction in the DDS. Solid lines (pink for A and blue for B) are the linearly decreasing concentration from the sources (boundaries at $x = 0$ and L) to the fast reaction zone at $x = x_R$.
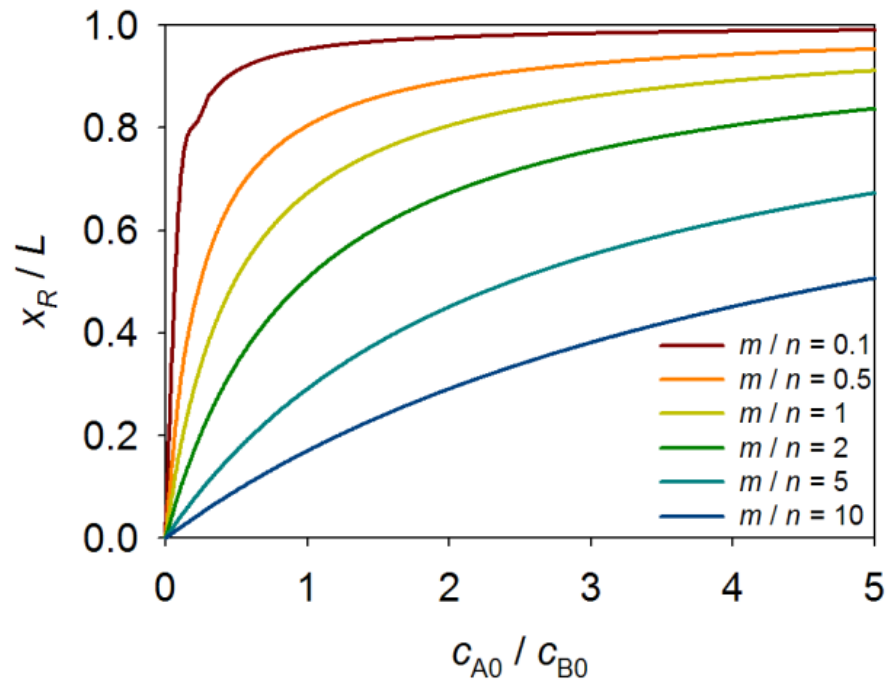
Figure A9.9 Non-dimensionalized location of the sink, x_R/L at steady-state: analytical model. The analytical model, Eq. A9.29 is plotted as a function of c_{A0}/c_{B0} with various m/n's. $D_A = 6.5 \times 10^{-6}$ cm^2/s and $D_B = 3.16 \times 10^{-6}$ cm^2/s.

B. *Finite element models of the CPP formation*

We have also developed finite element models assess the effects of multiple variables in the DDS on the final outcome (e.g., steepness of the gradient, width of the precipitation band, etc.). Then, we have compared and contrasted the validity of modeling the formation of CPP as a computationally simpler 2nd order system versus a 3rd order system. Much faster reaction rate compared with diffusion rate (i.e., high Da) allows for the implementation of the 2nd order while at the same time achieving the same mathematical end result and reducing the computational power required for the model. A series of experiments as shown in Fig. A9.7 has been used to verify the effectiveness of the model to predict the results of systematically varying the reaction conditions. We have also compared the computational models with the analytical model presented in the previous section. Comparison between the calculations and the experiments also allows for the prediction of the rate constant, k_{CPP}.

As stated above, the reaction rate for the formation of CPP, R (also see Eqs. A9.22 and A9.23) can be hypothetically expressed with 2nd or 3rd order reaction term defined as

$$R = -\frac{1}{2}\frac{dc_{Ca}}{dt} = -\frac{dc_{PPi}}{dt} = \frac{dc_{CPP}}{dt} \equiv k_{CPP}c_{Ca}c_{PPi} \tag{A9.30}$$

$$R = -\frac{1}{2}\frac{dc_{Ca}}{dt} = -\frac{dc_{PPi}}{dt} = \frac{dc_{CPP}}{dt} \equiv k_{CPP}c_{Ca}^2 c_{PPi} \tag{A9.31}$$

Finite element models were computed using COMSOL Multiphysics (Comsol, Inc., Burlington, MA; also see Appendix 11).

Transient finite element models, run with Eqs. A9.22-23, A9.30-31, and input parameters summarized in Table A9.2, indicate that the reaction order (i.e., 2nd or 3rd order) does not result in differences in the location of produced CPP (red solid and dash lines, and green solid and dash lines in Fig. A9.10). This lack of dependence

arises from the fact that both cases correspond to high Da ($10^4 \sim 10^5$), defined as $k_{CPP}c_0L^2/D_i$ for the 2nd order reaction and $k_{CPP}c_0^2L^2/D_i$ for the 3rd order reaction. Therefore, we can treat the formation of CPP as a diffusion-limited (still transient) process. In addition, 2nd order is the simplest model that is compatible with the experiments (red circles in Fig. A9.10). We note that a single value of $k_{CPP} = 3 \times 10^{-5}$ m^3/mol·s resulted in good agreement with the experimentally observed location of CPP; experimentally observed band positions are ~0.54L, ~0.5L, and 0.65L and computationally estimated band positions are 0.55L, 0.49L, and 0.67L for $c_{Ca0}/c_{PPi0} = 0.5$, 1, and 4 respectively (also see Fig. A9.7 and A9.10).

Compared with the analytical model obtained for steady-state (black solid line in Fig. A9.10), the transient finite element models indicate that the location of the sink, x_R clearly varies over times. At steady-state, x_R is stationary, but inequality of fluxes of the counter-diffusing reactants at early times results in the temporal shift of x_R. Specifically, a larger flux of one of the reactants causes the motion of the sink towards a smaller flux. Then, the sink location will eventually reach an asymptotically stationary state as the fluxes become same; for the computational models of the formation of CPP, the system reaches an asymptotic state after 10 days. We note that increase of Da (i.e., increase of the rate constant k_{CPP}), leads to decrease of time over which the sink location, x_R reaches an asymptotic state (data not shown). We also note that x_R increases over times when $c_{Ca0}/c_{PPi0} > \sim1.4$ (Fig. A9.10 and A9.11A) and the opposite is true when $c_{Ca0}/c_{PPi0} < \sim1.4$ (Fig. A9.10 and A9.11B). In addition x_R is almost immobile when $c_{A0}/c_{B0} \sim1.4$ (Fig. A9.10 and Fig. A9.11C).

Table A9.2 Input parameters used in the FEM

Calcium boundary concentration	c_{Ca0}	0.05, 0.1, or 0.4 mol/L
Phosphate boundary condition	c_{PPi0}	0.1 mol/L
Diffusivity of calcium ion	D_{Ca}	6.5×10^{-10} m^2/s
Diffusivity of phosphate ion	D_{PPi}	3.16×10^{-10} m^2/s
Rate constant for 2nd order kinetics	$k_{\mathrm{CPP}}^{\mathrm{2nd}}$	3×10^{-5} m^3/mol·s
Rate constant for 3rd order kinetics	$k_{\mathrm{CPP}}^{\mathrm{3rd}}$	3×10^{-5} m^6/mol^2·s
Length of the DDS	L	6 cm
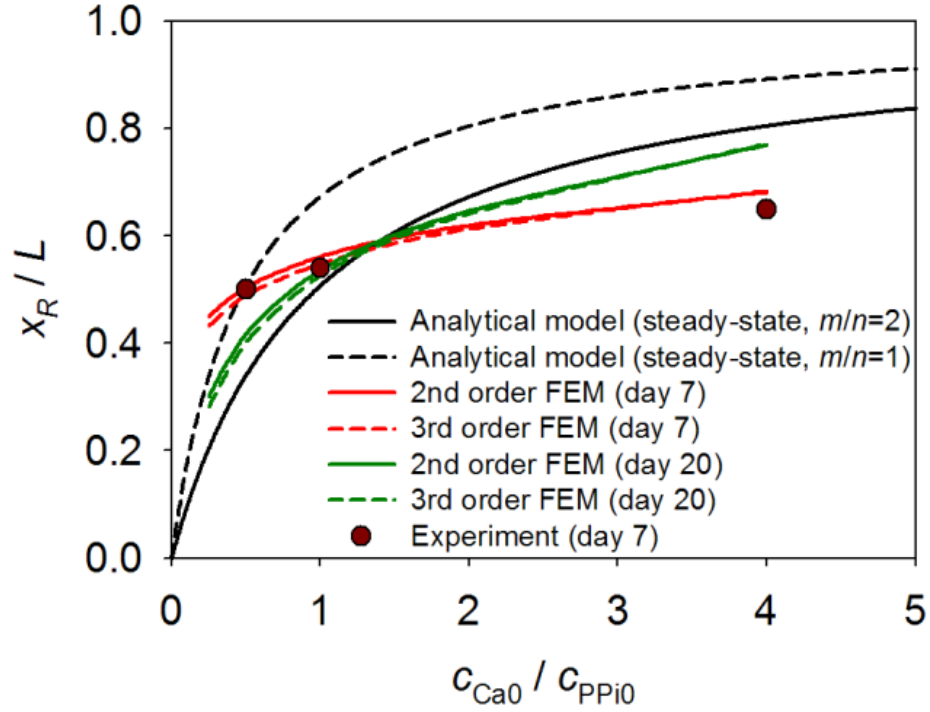
Figure A9.10 Non-dimensionalized location of the sink, x_R/L: analytical model, finite element models, and experimental observations for the formation of CPP.
Black lines represent the analytical model (Eq. A9.29) with $m/n = 2$ (solid) and 1 (dash). Red and green solid lines represent 2nd order finite element models with $k_{CPP}^{2nd} = 3 \times 10^{-5}$ m^3/mol·s . Red and green dash lines represent 3rd order finite element models with $k_{CPP}^{3rd} = 3 \times 10^{-5}$ m^6/mol^2·s . Red circles represent experimental observations as shown in Fig. A9.7.
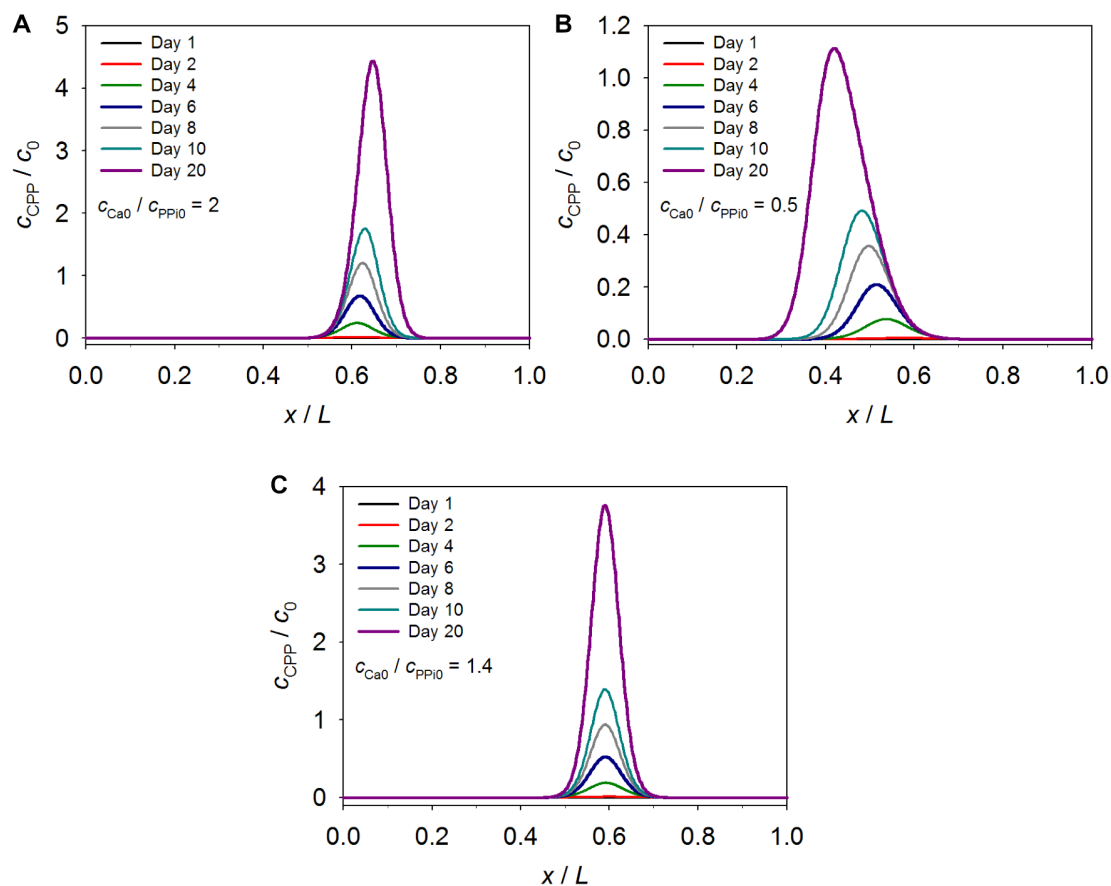
Figure A9.11 Temporal evolution of the concentration of CPP calculated from transient finite element models. A-C. Plots of the non-dimensionalized concentration of the product C at various time points for the 2nd order kinetics ($R = kc_A c_B$, $k = 3 \times 10^{-5}$ m³/mol·s): $c_{Ca0}/c_{PPi0} = 2$ (A), 0.5 (B), and 1.4 (C).

Figure A9.12 shows the total concentration of calcium (Fig. A9.12A) and pyrophosphate ions (Fig. A9.12B) calculated as follows

$$c_{Ca,total} = c_{Ca} + 2c_{CPP}$$
$$c_{PPi,total} = c_{PPi} + c_{CPP}$$

(A9.32)

The zones denoted by 1, 2, and 3 in Fig. A9.12 represent sections that were used to experimentally measure the concentration of the ions. Comparison of the average concentration in the sections 1, 2, and 3 between the experiment and the 2nd order finite element model (Table A9.3), indicates that the computational model still has weakness in predicting actual distributions of the concentration of the ions in the section 3 compared with those in the sections 1 and 2. This relatively poor agreement could result from two possibilities: 1) the width of the reaction layer (i.e., the production of CPP) in the experiment is significantly thinner than that calculated in the finite element model, and 2) the spatial resolution of the experimentally dissected sections is not high enough by the fact that the formation of CPP occurs at the interface between the section 2 and 3. Future work would have to include the measurement of 1) diffusivity of pyrophosphate in gelatin gels and 2) the ion composition of CPP at various time points such that we can correlate the optical density of CPP with the concentration of the ions. Testing of finite element models against experimental results for the formation of HA, has shown that the complex nature of the 9th order reaction is not yet achievable using a simplified 2nd order computation. For the creation of this model we determine the rate constant as a fitting parameter, without any consideration to the true order of this reaction. In an effort to find this value experimentally we could reduce the scale of the system (e.g., using microfluidics) to determine not only the rate constant but also the true reaction order of the system.
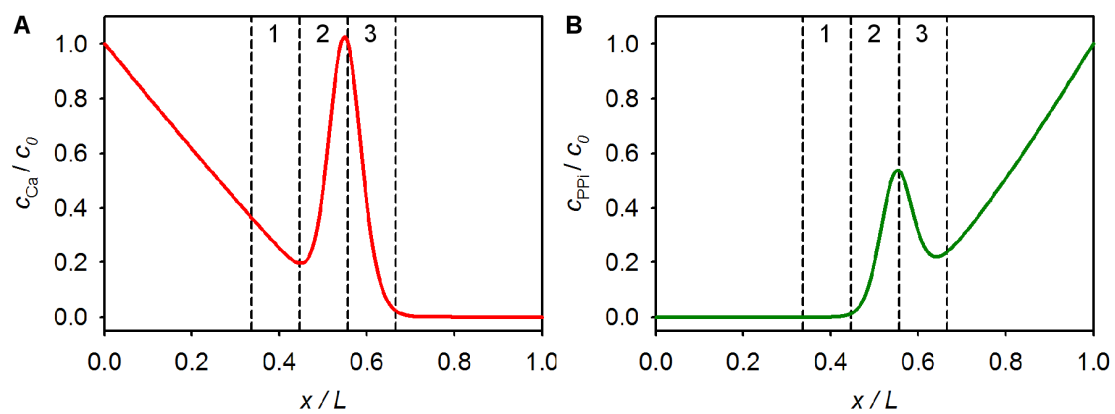
Figure A9.12 Total concentration of calcium and pyrophosphate ions in the DDS.
A. Plot of non-dimensionalized calcium ions. **B.** Non-dimensionalized pyrophosphate ions. $c_0 = 100$ mM. "1", "2", and "3" denote section numbers.

Table A9.3 Comparison of average concentration of calcium and phosphate ions in sections 1, 2, and 3 between experiment and finite element model

Section	Experiment		FEM	
	Ca [mM]	PPi [mM]	Ca [mM]	PPi [mM]
1	23.92	1.23	27.5	0.17
2	54.97	28.5	55.9	29.4
3	1.03	16.85	36.4	31.4

Figure A9.13 shows the steady-state distribution of calcium for the 2nd order reaction. At high Da ($> 10^3$), the concentration of calcium linearly decreases to zero towards the sink ($x \sim 3$ cm). This trend is typical for diffusion-limited fast reactions. However, as Da decreases, the slow kinetics are reflected in the concentration profile; the concentration is not completely depleted at the sink location. We note that when Da $< 10^3$, the non-zero values beyond the reaction zone of calcium invalidate the assumptions of the analytical model; in other words, calcium encounters pyrophosphate beyond x_R. In those cases, the diffusion-reaction process is not diffusion-limited. For Da $\sim 10^0$, the reaction is very slow and the concentration profile at steady-state is linear, as expected for simple diffusion from a source to a sink.
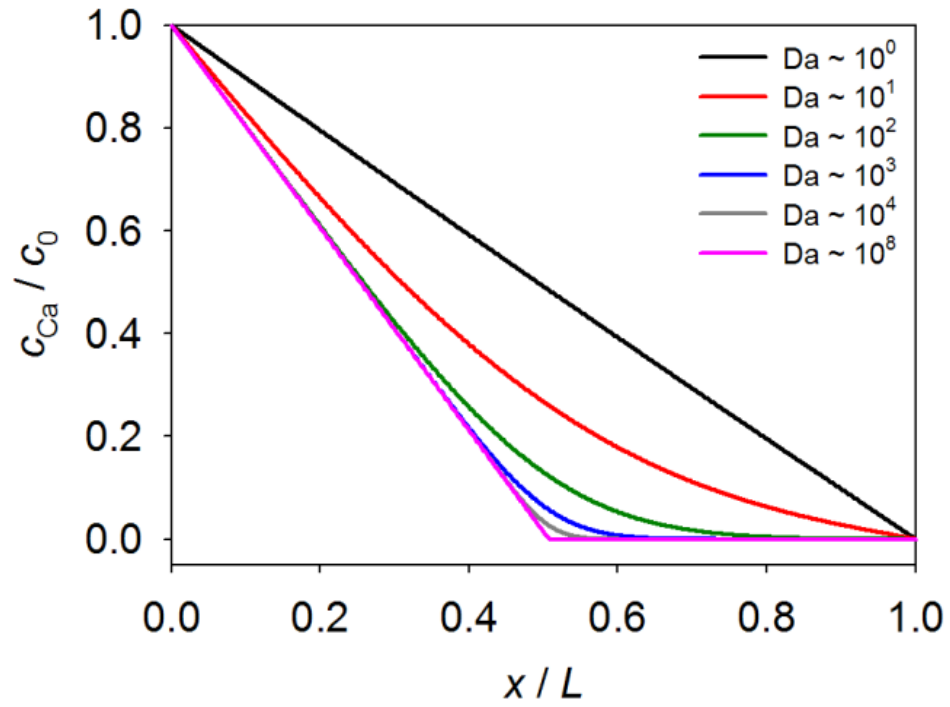
Figure A9.13 Computationally calculated steady-state distributions of calcium in the DDS. Plot of the non-dimensionalized concentration of clacium for the 2nd order kinetics ($R = kc_A c_B$, $k = 3 \times 10^{-5}$ m^3/mol·s) with various Da, defined as $Da = kL^2 c_{Ca0} / D_{Ca}$. $D_{Ca} = 6.5 \times 10^{-6}$ cm^2/s and $D_{PPi} = 3.16 \times 10^{-6}$ cm^2/s.

For diffusion-limited fast reactions, the justifiable quasi-steady-state approximation allows for the analytical estimation of the sink location with the reaction rate unknown. Transient finite element analyses reveal that the sink location reaches an asymptotically stationary state over ~10 days for the case of Da ~ 10^4. A seemingly missing aspect in this section is discussion about the width of the reaction layer. Koza reported a generalized expression of the half width, w for diffusion-limited mA + nB → C type reactions based on the scaling ansatz[39-40,44]:

$$w^{m+n+1} \equiv D_A^m D_B^n k^{-1} J^{1-m-n} \qquad (A9.33)$$

The scaling ansatz, first proposed by Gálfi and Rácz, is a method to describe the long time behavior of diffusion-limited reactions within the reaction layer; it is based on an assumption that the half width of the reaction layer, w grows with time as t^α with $\alpha <$ $1/2$[39,44]. Note that this length scale is smaller than diffusion length scale for the reactants (i.e., $\lambda_D \sim \sqrt{D_i t}$). Eq. A9.33 implies that the width of the reaction layer depends on detailed information about the reaction rate such as the rate constant, k. Therefore, future work towards investing the transient nature of w, for example, by experimentally measuring the width of the reaction layer, may allow us to extract kinetic information of biomineralization processes.

Conclusions and future work

We have successfully initiated a computational model for the formation of hydroxyapatite in the double-diffusion system. Our multiscale FD-KMC model demonstrated the potential to model the high order crystallization process. This technique could serve as a useful method to validate and predict experimental observations. In addition, our algorithm is flexible enough to make modifications for the addition of an inhibitor or a promoter, and pre-existing nuclei sites. Yet, the FD-

KMC is seemingly less powerful largely due to its application to the formation of HA in the DDS that has not been fully understood; for example, input parameters have not measured specifically in our gel matrices. We note that such measurement still remains a challenge. Exploration of parameter space with this FD-KMC could aid the investigation of kinetic information of biomineralization processes.

We have presented an analytical approach to model a general diffusion-limited reaction in the DDS. By identifying spatially distinct regions, we have derived an analytical expression to find the location of the reaction layer even without any information of the reaction rate. Our analytical model shows that the location of the depletion zone is independent of the rate constant and a function of diffusivity, feeding concentration of reactants, and the order of the reaction in each species. The analytical model also has the potential in designing future experiments because it can be used to control the location of the reaction. We have utilized steady-state and transient finite element models to test the analytical model. The finite element models reveal that the location of the reaction layer, in fact, shifts over time. To further investigate the width of the reaction layer as well as its transient nature, detailed kinetic information such as the rate constant should be experimentally measured or computationally estimated. Our analytical model could serve as a useful basis to elucidate biomineralization processes in the DDS.

We have also developed finite element models to assess the effective order of biomineralization processes in the DDS. The location, width, and concentration profile of the precipitation bands are useful outcome parameters that can be also validated with experimental observations and measurements. For this FEM, we used the formation of calcium pyrophosphate, a stoichiometrically 3rd order reaction, as a basis for creating a FEM that may be adapted to model the formation of the more complex hydroxyapatite, a 9th order reaction; however, we note that the formation of

hydroxyapatite is believed to be a multistep process including nucleation and crystal growth, elucidating the rate limiting step is an outstanding challenge. We have compared and contrasted the accuracy of modeling the formation of CPP as a computationally simpler 2nd order system versus a 3rd order system. The diffusion-limited fast reaction allows for the implementation of simpler kinetic orders while reducing the computational power required for the model. The predictions are quantitatively similar to experimental observations. In the current FEM model we designed, only the band position has been experimentally confirmed and the rate constant has been estimated. Though the trends for band location, band width, and maximum concentration appear to be very similar for both 2nd and 3rd order reactions, the absolute values for both reactions show poor agreement with those observed experimentally. Future work would have to include the measurement of 1) diffusivity of pyrophosphate in gelatin gels and 2) the ion composition of CPP at various time points such that we can correlate the optical density of CPP with the concentration of the ions. Comparison of our current finite element models to experimental results for the formation of HA, have shown that the complex nature of the 9th order reaction is not yet achievable using a simplified 2nd order computation. Current experimental double-diffusion system is limited in finding such kinetic information because it is inherently difficult to capture kinetics in the diffusion-limited reaction. In an effort towards developing better predictive models, it would be worth developing an experimental system that allows the reduction of the system scale to determine not only the rate constant but also the true reaction order of the system. For example, a millimeter-scale hydrogel enclosed between two microfluidic channels (i.e., microfluidic double-diffusion system; Fig. A9.13), could allow such investigation because steady-state is achievable in a short period of time with controlled input concentrations. Specifically, significantly lower Da ($Da = kL^2 c_{i0} / D_i$ for 2nd order

kinetics) could be achieved by reducing the length of the DDS, L such that the formation of HA or CPP is not diffusion-limited anymore; in the case of CPP, $L = 2$ mm and c_{i0} = 25 mM lead to Da ~ 10^0, and the microfluidic DDS would reach steady-state in 2 ~ 3 hr. It would be also relatively simple to run multiple devices at a time on bench-top. Furthermore, the microfluidic DDS might aid to elucidate the dynamic growth of crystals *in situ* with microscopy techniques. From the theoretical perspective, it would be worthwhile to continue to study the Gálfi and Rácz problem that could lead to more both theoretically and experimentally strategic approaches to decipher the biomineralization processes.
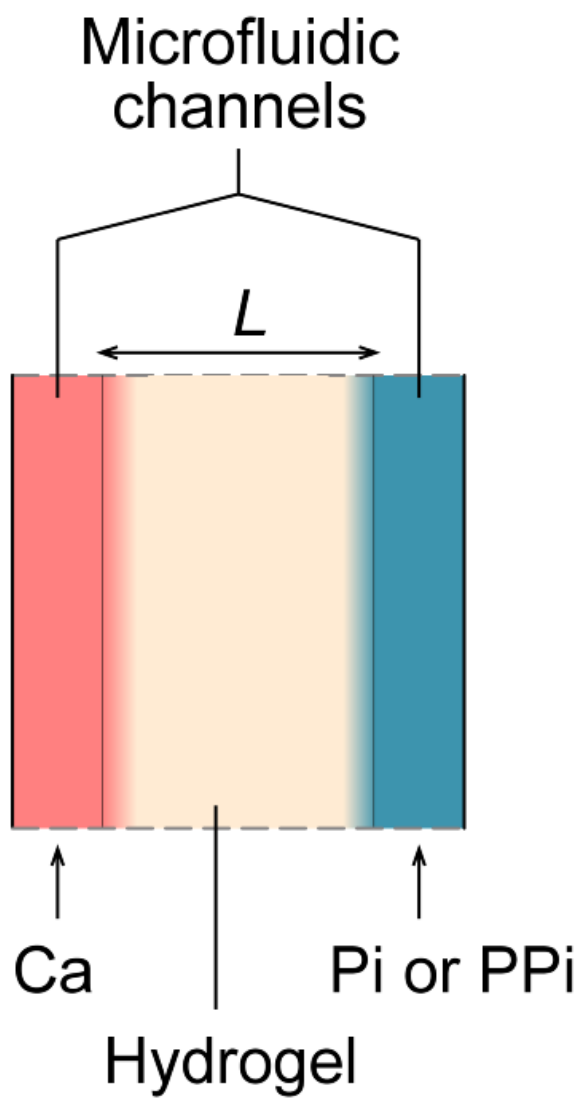
Figure A9.14 Schematic illustration of microfluidic double-diffusion system.

REFERENCES

1.   Estroff, L.A., Introduction: Biomineralization. *Chem. Rev.* **108** (11), 4329-4331 (2008).

2.   Wang, L.J. & Nancollas, G.H., Pathways to biomineralization and biodemineralization of calcium phosphates: the thermodynamic and kinetic controls. *Dalton Trans.* (15), 2665-2672 (2009).

3.   Mahamid, J. *et al.*, Amorphous calcium phosphate is a major component of the forming fin bones of zebrafish: Indications for an amorphous precursor phase. *Proc. Natl. Acad. Sci. U. S. A.* **105** (35), 12748-12753 (2008).

4.   Boskey, A.L., Matrix proteins and mineralization: An overview. *Connect. Tissue Res.* **35**, 357-363 (1996).

5.   Furedimilhofer, H. *et al.*, Interactions of matrix proteins from mineralized tissues with octacalcium phosphate. *Connect. Tissue Res.* **30** (4), 251-264 (1994).

6.   Steitz, S.A. *et al.*, Osteopontin inhibits mineral deposition and promotes regression of ectopic calcification. *Am. J. Pathol.* **161** (6), 2035-2046 (2002).

7.   Thouverey, C. *et al.*, Inorganic pyrophosphate as a regulator of hydroxyapatite or calcium pyrophosphate dihydrate mineral deposition by matrix vesicles. *Osteoarthritis Cartilage* **17** (1), 64-72 (2009).

8.   Kalya, S. & Rosenthal, A.K., Extracellular matrix changes regulate calcium crystal formation in articular cartilage. *Curr. Opin. Rheumatol.* **17** (3), 325-329 (2005).

9.   Terkeltaub, R.A., Inorganic pyrophosphate generation and disposition in pathophysiology. *Am. J. Physiol.-Cell Physiol.* **281** (1), C1-C11 (2001).

10.   Henisch, H.K., *Crystals in gels and liesegang rings: in vitro veritas*. (Cambridge University Press, Cambridge, 1988).

11.   Silverman, L. & Boskey, A.L., Diffusion systems for evaluation of biomineralization. *Calcif. Tissue Int.* **75** (6), 494-501 (2004).

12.   Ball, V. *et al.*, Nucleation kinetics of calcium phosphates on polyelectrolyte multilayers displaying internal secondary structure. *Cryst. Growth Des.* **6** (1), 327-334 (2006).

13.   Lu, X. & Leng, Y., Theoretical analysis of calcium phosphate precipitation in simulated body fluid. *Biomaterials* **26** (10), 1097-1108 (2005).

14.   Dalas, E. *et al.*, The effect of Leucine on the crystal growth of calcium phosphate. *J. Mater. Sci.-Mater. Med.* **19** (1), 277-282 (2008).

15.   Onuma, K. *et al.*, Precipitation kinetics of hydroxyapatite revealed by the continuous-angle laser light-scattering technique. *J. Phys. Chem. B* **104** (45), 10563-10568 (2000).

16.   Cao, X. *et al.*, Inhibition of calcium phosphate precipitation under environmentally-relevant conditions. *Sci. Total Environ.* **383** (1-3), 205-215 (2007).

17.   Spanos, N. *et al.*, Precipitation of calcium phosphate from simulated milk ultrafiltrate solutions. *Cryst. Growth Des.* **7** (1), 25-29 (2007).

18.   Pucar, Z. *et al.*, Precipitation in gels under conditions of double diffusion - critical concentrations of precipitating components. *Anal. Chem.* **46** (3), 403-409 (1974).

19.   Kotrla, M., Numerical simulations in the theory of crystal growth. *Comput. Phys. Commun.* **97**, 82-100 (1996).

20.   Levi, A.C. & Kotrla, M., Theory and simulation of crystal growth. *J. Phys.-Condes. Matter* **9** (2), 299-344 (1997).

21. Mullin, J.W., *Crystallization*, 4th ed. (Butterworth-Heinemann, Oxford, 2001).

22. Pricer, T.J. *et al.*, Monte Carlo simulation of the electrodeposition of copper - I. Additive-free acidic sulfate solution. *J. Electrochem. Soc.* **149** (8), C396-C405 (2002).

23. Majumder, D. & Broadbelt, L.J., A multiscale scheme for modeling catalytic flow reactors. *Aiche J.* **52** (12), 4214-4228 (2006).

24. CRC Handbook of Chemistry and Physics, edited by D. R. Lide.

25. Christoffersen, M.R. & Christoffersen, J., Effects of a bisphosphonate (EHDP) on growth, formation, and dissolution of calcium pyrophosphate crystals. *Cryst. Growth Des.* **3** (1), 79-82 (2003).

26. Christoffersen, M.R. *et al.*, Kinetics of dissolution of triclinic calcium pyrophosphate dihydrate crystals. *J. Cryst. Growth* **203** (1-2), 234-243 (1999).

27. Christoffersen, M.R. *et al.*, Kinetics and mechanisms of dissolution and growth of acicular triclinic calcium pyrophosphate dihydrate crystals. *Cryst. Growth Des.* **2** (6), 567-571 (2002).

28. Christoffersen, M.R. *et al.*, Kinetics of growth of columnar triclinic calcium pyrophosphate dihydrate crystals. *Cryst. Growth Des.* **1** (6), 463-466 (2001).

29. Ziff, R.M. & Fichthorn, K., Fractal clustering of reactants on a catalyst surface. *Phys. Rev. B* **34** (3), 2038-2040 (1986).

30. Dang, L.C. *et al.*, Kinetic and mechanistic studies on the hydrolysis of ubiquitin C-terminal 7-amido-4-methylcoumarin by deubiquitinating enzymes. *Biochemistry* **37** (7), 1868-1879 (1998).

31. Jordan, L.R. *et al.*, Diffusion layer parameters influencing optimal fuel cell performance. *J. Power Sources* **86**, 250-254 (2000).

32. Witten, T.A. & Sander, L.M., Diffusion-limited aggregation. *Phys. Rev. B* **27** (9), 5686-5697 (1983).

33. Kimoto, T. *et al.*, Growth mechanism of 6H-SIC in step controlled epitaxy. *J. Appl. Phys.* **73** (2), 726-732 (1993).

34. Wen, C.Y., Noncatalytic heterogeneous solid fluid reaction models. *Industrial and Engineering Chemistry* **60** (9), 34-& (1968).

35. Samseth, J. *et al.*, Liesegang pattern formation by gas diffusion in silica aerogels. *J. Non-Cryst. Solids* **225**, 298-302 (1998).

36. Ouyang, Q. *et al.*, Sustained patterns in chlorite iodide reactions in a one-dimensional reactor. *J. Chem. Phys.* **95** (1), 351-360 (1991).

37. Horvath, D. & Toth, A., Turing patterns in a single-step autocatalytic reaction. *J. Chem. Soc.-Faraday Trans.* **93** (24), 4301-4303 (1997).

38. Ham, F.S., Theory of diffusion-limited precipitation. *J. Phys. Chem. Solids* **6** (4), 335-351 (1958).

39. Galfi, L. & Racz, Z., Properties of the reaction front in an A+B -> type reaction-diffusion process. *Phys. Rev. A* **38** (6), 3151-3154 (1988).

40. Cornell, S. *et al.*, Role of fluctuations for inhomogeneous reaction-diffusion phenomena. *Phys. Rev. A* **44** (8), 4826-4832 (1991).

41. Koo, Y.E.L. & Kopelman, R., Space-resolved and time-resolved diffusion-limited binary reaction kinetics in capillaries - experimental observation of segregation, anomalous exponents, and depletion zone. *J. Stat. Phys.* **65**, 893-918 (1991).

42. Cornell, S. & Droz, M., Steady-state reaction-diffusion front scaling for mA+nB -> inert. *Phys. Rev. Lett.* **70** (24), 3824-3827 (1993).

43. Cornell, S. *et al.*, Dynamic multiscaling of the reaction-diffusion front for mA+nB -> 0. *Phys. Rev. E* **52** (4), 3500-3505 (1995).

44.   Koza, Z., The long-time behavior of initially separated A+B->0 reaction-diffusion systems with arbitrary diffusion constants. *J. Stat. Phys.* **85** (1-2), 179-191 (1996).

45.   Koza, Z. & Taitelbaum, H., Motion of the reaction front in the A+B->C reaction-diffusion system. *Phys. Rev. E* **54** (2), R1040-R1043 (1996).

MATLAB CODE FOR FD-KMC

Below is the MATLAB code for the FD-KMC presented in Appendix 9.

```matlab
clear
clc
% Initial Conditions
Ca_feed_conc=0.1;
PO4_feed_conc=0.1;
Cl_feed_conc=2*Ca_feed_conc;
NH4_feed_conc=3*PO4_feed_conc;
Total_length=0.06;
Ca_feed_molecules=500;       %Determines the size of DV in micro-scale
PO4_feed_molecules=round(Ca_feed_molecules*PO4_feed_conc/Ca_feed_conc);
Temp=310;
OH_conc=10^(-6.6);
I_prod=5e-7;       % Inhibitor production (mol/(L s)) -- 1e-6
% Difusivities (from CRC)
DCa=6e-10; %[m^2/s]
DPO4=3.9e-10; %[m^2/s]
DCl=20.32e-10;
DNH4=19.57e-10;
DI=2e-10;          % Inhibitor diffusivity
% Steps
Dx=0.004;
Dt=10;
Number_xsteps=Total_length/Dx;
I_source=round(0.025/Total_length*Number_xsteps);   % Point of Inhibitor production
% Diffusion & homogeneous reaction Matrices
Ca_conc=zeros(Number_xsteps,1);
PO4_conc=zeros(Number_xsteps,1);
Cl_conc=zeros(Number_xsteps,1);
NH4_conc=zeros(Number_xsteps,1);
I_conc=zeros(Number_xsteps,1);
Ca_square_matrix=zeros(Number_xsteps,Number_xsteps);
PO4_square_matrix=zeros(Number_xsteps,Number_xsteps);
Cl_square_matrix=zeros(Number_xsteps,Number_xsteps);
NH4_square_matrix=zeros(Number_xsteps,Number_xsteps);
I_square_matrix=zeros(Number_xsteps,Number_xsteps);
Ca_boundary_matrix=zeros(Number_xsteps,1);
PO4_boundary_matrix=zeros(Number_xsteps,1);
Cl_boundary_matrix=zeros(Number_xsteps,1);
NH4_boundary_matrix=zeros(Number_xsteps,1);
I_boundary_matrix=zeros(Number_xsteps,1);
DCa_Dt=zeros(Number_xsteps,1);
DPO4_Dt=zeros(Number_xsteps,1);
DCl_Dt=zeros(Number_xsteps,1);
DNH4_Dt=zeros(Number_xsteps,1);
DI_Dt=zeros(Number_xsteps,1);
```

```matlab
%Rate Constants
c_Ca=0;
c_PO4=0;
c_Cl=0;
c_NH4=0;
ki=1;          % Rate: Ca + I ===> I-CA  (mol/(L s))
% HA Constants
K=1.364e28;    %  1/L*s   (Nucleation rate constant) 1.364e28
gamma=0.105;   %  J/m2    (Surface tension water-HA)
v=2.6324e-28;  %  m3      (HA molecular volume)
f=0.5;         %          (Contact angle function)
Ksp=2.35e-59;  %          (Solubity Product)
Ks=2.59201e22; %  1/(m2 s) (Crystal growth rate constant) 2.59201e22
t_max=(60*60*24)*5; %[s]
% Other Variables
i=0;
j=0;
t=0;
Break_time=0;
DV=Ca_feed_molecules/(Ca_feed_conc*6.02e23); %litters
P=zeros(Number_xsteps,1);    %Nucleation Probability
I=zeros(Number_xsteps,1);    %Ionic strenght
Gamma_Ca=zeros(Number_xsteps,1);   % Activity coefficients
Gamma_PO4=zeros(Number_xsteps,1);
Gamma_OH=zeros(Number_xsteps,1);
a_Ca=zeros(Number_xsteps,1);   % Activity
a_PO4=zeros(Number_xsteps,1);
a_OH=zeros(Number_xsteps,1);
S=zeros(Number_xsteps,1);               %  Supersaturation
c_nucleation=zeros(Number_xsteps,1);    %  Nucleation Rate
c_growth=zeros(Number_xsteps,1);        % Crystal growth rate
n=zeros(Number_xsteps,1);   % Critical nucleus size (ion number)
n_Ca=zeros(Number_xsteps,1);    % # Ca ions in critical nucleus
n_PO4=zeros(Number_xsteps,1);   % # PO4 ions in critical nucleus
n_HA=zeros(Number_xsteps,1);    % # HA molec in critical nucleus
n_Ca_total=zeros(Number_xsteps,1);      % Total # of Ca ions/step
n_PO4_total=zeros(Number_xsteps,1);     % Total # of PO4 ions/step
n_possible_nucleus=zeros(Number_xsteps,1); % Total possible nucleus/step
n_size_HA_nuclei=zeros(Number_xsteps,1);   % Matrix of nuclei size (# HA molec)
crystal_radii=zeros(Number_xsteps,1);      % Matrix of crystal radii
Ca_ions=zeros(Number_xsteps,1);        % Total # Ca ions/step
PO4_ions=zeros(Number_xsteps,1);       % Total # PO4 ions/step
Cl_ions=zeros(Number_xsteps,1);        % Total # Cl ions/step
NH4_ions=zeros(Number_xsteps,1);       % Total # NH4 ions/step
HA_nuclei=zeros(Number_xsteps,1);      % Total # HA nuclei/step
a_Ca_diff=zeros(Number_xsteps,1);      % Propensity Functions:
a_PO4_diff=zeros(Number_xsteps,1);
a_Cl_diff=zeros(Number_xsteps,1);
a_NH4_diff=zeros(Number_xsteps,1);
a_nucleation=zeros(Number_xsteps,1);
a_growth=zeros(Number_xsteps,1);
Sum_a=0;
n_random=0;
cumulative_p=0;        % Probabilities:
diffusion_p=0;
```

```matlab
nucleation_p=0;
growth_p=0;
%========================================================
% Macro Scale
tdraw=0;
drawstep=3000;
%Insert a seed specifying size and position (when a seed is considered)
%HA_nuclei(12)=1;
%crystal_radii(12)=0.000000001;
%n_size_HA_nuclei(12)=floor((4*pi*crystal_radii(12)^3/3)/v);
% Crank-Nicholson method
% Diffusion matrix (starting values)
for i=[1:Number_xsteps]

    if i==1
        Ca_square_matrix(i,i)=-2*DCa/Dx^2;
        PO4_square_matrix(i,i)=-2*DPO4/Dx^2;
        Cl_square_matrix(i,i)=-2*DCl/Dx^2;
        NH4_square_matrix(i,i)=-2*DNH4/Dx^2;
        I_square_matrix(i,i)=-2*DI/Dx^2;
        Ca_square_matrix(i,i+1)=DCa/Dx^2;
        PO4_square_matrix(i,i+1)=DPO4/Dx^2;
        Cl_square_matrix(i,i+1)=DCl/Dx^2;
        NH4_square_matrix(i,i+1)=DNH4/Dx^2;
        I_square_matrix(i,i+1)=DI/Dx^2;
    end
    if i>1 && i<Number_xsteps
        Ca_square_matrix(i,i-1)=DCa/Dx^2;
        PO4_square_matrix(i,i-1)=DPO4/Dx^2;
        Cl_square_matrix(i,i-1)=DCl/Dx^2;
        NH4_square_matrix(i,i-1)=DNH4/Dx^2;
        I_square_matrix(i,i-1)=DI/Dx^2;
        Ca_square_matrix(i,i)=-2*DCa/Dx^2;
        PO4_square_matrix(i,i)=-2*DPO4/Dx^2;
        Cl_square_matrix(i,i)=-2*DCl/Dx^2;
        NH4_square_matrix(i,i)=-2*DNH4/Dx^2;
        I_square_matrix(i,i)=-2*DI/Dx^2;
        Ca_square_matrix(i,i+1)=DCa/Dx^2;
        PO4_square_matrix(i,i+1)=DPO4/Dx^2;
        Cl_square_matrix(i,i+1)=DCl/Dx^2;
        NH4_square_matrix(i,i+1)=DNH4/Dx^2;
        I_square_matrix(i,i+1)=DI/Dx^2;
    end
    if i==Number_xsteps
        Ca_square_matrix(i,i-1)=DCa/Dx^2;
        PO4_square_matrix(i,i-1)=DPO4/Dx^2;
        Cl_square_matrix(i,i-1)=DCl/Dx^2;
        NH4_square_matrix(i,i-1)=DNH4/Dx^2;
        I_square_matrix(i,i-1)=DI/Dx^2;
        Ca_square_matrix(i,i)=-2*DCa/Dx^2;
        PO4_square_matrix(i,i)=-2*DPO4/Dx^2;
        Cl_square_matrix(i,i)=-2*DCl/Dx^2;
        NH4_square_matrix(i,i)=-2*DNH4/Dx^2;
        I_square_matrix(i,i)=-2*DI/Dx^2;
    end
```

```matlab
    end
Ca_boundary_matrix(1)=(DCa/Dx^2)*Ca_feed_conc;
PO4_boundary_matrix(Number_xsteps)=(DPO4/Dx^2)*PO4_feed_conc;
Cl_boundary_matrix(1)=(DCl/Dx^2)*Cl_feed_conc;
NH4_boundary_matrix(Number_xsteps)=(DNH4/Dx^2)*NH4_feed_conc;
% Macroscopic Diffusion
% Main loop
while t>-1
    for i=[1:Number_xsteps]
        if i==1
            Ca_boundary_matrix(i)=(DCa/Dx^2)*Ca_feed_conc-ki*Ca_conc(i)*I_conc(i);
            I_boundary_matrix(i)=-ki*Ca_conc(i)*I_conc(i);
        end
        if i>1
            Ca_boundary_matrix(i)=-ki*Ca_conc(i)*I_conc(i);
            I_boundary_matrix(i)=-ki*Ca_conc(i)*I_conc(i);
        end
        if i==I_source
            Ca_boundary_matrix(i)=-ki*Ca_conc(i)*I_conc(i);
            I_boundary_matrix(i)=-ki*Ca_conc(i)*I_conc(i)+I_prod;
        end
    end
    DCa_Dt=Ca_square_matrix*Ca_conc+Ca_boundary_matrix;
    DPO4_Dt=PO4_square_matrix*PO4_conc+PO4_boundary_matrix;
    DCl_Dt=Cl_square_matrix*Cl_conc+Cl_boundary_matrix;
    DNH4_Dt=NH4_square_matrix*NH4_conc+NH4_boundary_matrix;
    DI_Dt=I_square_matrix*I_conc+I_boundary_matrix;
    Ca_conc=Ca_conc+DCa_Dt*Dt;
    PO4_conc=PO4_conc+DPO4_Dt*Dt;
    Cl_conc=Cl_conc+DCl_Dt*Dt;
    NH4_conc=NH4_conc+DNH4_Dt*Dt;
    I_conc=I_conc+DI_Dt*Dt;
    t=t+Dt;
    if min(round(Ca_conc*DV*6.02e23)+round(PO4_conc*DV*6.02e23))>3
        break
    end
    if t>tdraw      % This shows the free diffusion before change of scale
        x_position=[1:1:Number_xsteps];
plot(x_position,Ca_conc,x_position,PO4_conc,x_position,Cl_conc,x_position,NH4_conc,x_position,I_conc)
        xlim([1 Number_xsteps]);
        ylim([0 Ca_feed_conc]);
        refreshdata
        drawnow
        tdraw=tdraw+drawstep;
    end
end
%=====================================================
% Micro Scale
Break_time=t;   % Stores the time of first scale change.
taccum=0;
deltat=5000;
c_Ca=2*DCa/Dx^2;        % Brownian inside length step
c_PO4=2*DPO4/Dx^2;
c_Cl=2*DCl/Dx^2;
```

235

```matlab
c_NH4=2*DNH4/Dx^2;
while t<t_max
    % calculation of rates
    for i=[1:Number_xsteps]
        % Nucleation Rate
P(i)=(504*Ca_conc(i)^5*PO4_conc(i)^3*OH_conc)/(Ca_conc(i)+PO4_conc(i)+OH_conc)^9;
        I(i)=0.5*(4*Ca_conc(i)+Cl_conc(i)+9*PO4_conc(i)+NH4_conc(i));
        Gamma_Ca(i)=10^-(0.5211*4*(I(i)^0.5/(1+I(i)^0.5)-(0.3*I(i))));
        Gamma_PO4(i)=10^-(0.5211*9*(I(i)^0.5/(1+I(i)^0.5)-(0.3*I(i))));
        Gamma_OH(i)=10^-(0.5211*(I(i)^0.5/(1+I(i)^0.5)-(0.3*I(i))));
a_Ca(i)=Gamma_Ca(i)*(Ca_conc(i)/(55.55+OH_conc+Ca_conc(i)+PO4_conc(i)+Cl_conc(i)+NH4_co
nc(i)));

a_PO4(i)=Gamma_PO4(i)*(PO4_conc(i)/(55.55+OH_conc+Ca_conc(i)+PO4_conc(i)+Cl_conc(i)+NH
4_conc(i)));
a_OH(i)=Gamma_OH(i)*(OH_conc/(55.55+OH_conc+Ca_conc(i)+PO4_conc(i)+Cl_conc(i)+NH4_co
nc(i)));
        S(i)=a_Ca(i)^5*a_PO4(i)^3*a_OH(i)/Ksp;
        if S(i)>0
            c_nucleation(i)=DV*K*P(i)*exp(-(16*pi*v^2*gamma^3*f)/(3*(1.38e-
23)^3*Temp^3*log(S(i))^2));
        else
            c_nucleation(i)=0;
        end
        % Critical nucleus size (ion number)
        if S(i)>0
            n(i)=round(32*pi*gamma^3*v^2/(3*(1.38e-23)^3*Temp^3*log(S(i))^3));
        else
            n(i)=0;
        end
        % Ions number per nucleus
        n_Ca(i)=ceil(n(i)/9)*5;
        n_PO4(i)=ceil(n(i)/9)*3;
        Ca_ions(i)=round(Ca_conc(i)*DV*6.02e23);
        PO4_ions(i)=round(PO4_conc(i)*DV*6.02e23);
        Cl_ions(i)=round(Cl_conc(i)*DV*6.02e23);
        NH4_ions(i)=round(NH4_conc(i)*DV*6.02e23);
        if n_PO4(i)>0 && n_Ca(i)>0
            n_possible_nucleus(i)=min([floor(Ca_ions(i)/n_Ca(i)) floor(PO4_ions(i)/n_PO4(i))]);
            n_HA(i)=ceil(n(i)/9);
        else
            n_possible_nucleus(i)=0;
            n_HA(i)=0;
        end
        % Crystal growth rate
        if Ca_ions(i)>4 && PO4_ions(i)>2 && HA_nuclei(i)>0
            for j=[1:HA_nuclei(i)]
                c_growth(i,j)=Ks*4*pi*(crystal_radii(i,j))^2*(S(i)^(1/9)-1)^1.87;
            end
        else
            c_growth(i,:)=0;
        end
        a_Ca_diffusion(i)=c_Ca*Ca_ions(i);
        a_PO4_diffusion(i)=c_PO4*PO4_ions(i);
        a_Cl_diffusion(i)=c_Cl*Cl_ions(i);
```

```matlab
        a_NH4_diffusion(i)=c_NH4*NH4_ions(i);
        a_nucleation(i)=c_nucleation(i)*n_possible_nucleus(i);
        a_growth=c_growth;
Sum_a=sum(a_Ca_diffusion)+sum(a_PO4_diffusion)+sum(a_Cl_diffusion)+sum(a_NH4_diffusion)+sum(a_nucleation)+sum(sum(a_growth));
    end
  Dt=-1/Sum_a*log(rand);      % Random time sampling
  % Reaction selection
        n_random=rand;
        cumulative_p=0;
diffusion_p=(sum(a_Ca_diffusion)+sum(a_PO4_diffusion)+sum(a_Cl_diffusion)+sum(a_NH4_diffusion))/Sum_a;
        nucleation_p=sum(a_nucleation)/Sum_a;
        growth_p=sum(sum(a_growth))/Sum_a;
  %Diffusion
    if n_random>cumulative_p && n_random<(cumulative_p+diffusion_p)
        DCa_Dt=Ca_square_matrix*Ca_conc+Ca_boundary_matrix;
        DPO4_Dt=PO4_square_matrix*PO4_conc+PO4_boundary_matrix;
        DCl_Dt=Cl_square_matrix*Cl_conc+Cl_boundary_matrix;
        DNH4_Dt=NH4_square_matrix*NH4_conc+NH4_boundary_matrix;
        Ca_conc=Ca_conc+DCa_Dt*Dt;
        PO4_conc=PO4_conc+DPO4_Dt*Dt;
        Cl_conc=Cl_conc+DCl_Dt*Dt;
        NH4_conc=NH4_conc+DNH4_Dt*Dt;
        t=t+Dt;
    end
    cumulative_p=cumulative_p+diffusion_p;
  % Nucleation
    if n_random>cumulative_p && n_random<(cumulative_p+nucleation_p)
        [A,I]=max(a_nucleation);
        HA_nuclei(I)=HA_nuclei(I)+1;
        Ca_ions(I)=Ca_ions(I)-n_Ca(I);
        PO4_ions(I)=PO4_ions(I)-n_PO4(I);
        Ca_conc(I)=Ca_ions(I)/(6.02e23*DV);
        PO4_conc(I)=PO4_ions(I)/(6.02e23*DV);
        n_size_HA_nuclei(I,HA_nuclei(I))=n_HA(I);
        crystal_radii(I,HA_nuclei(I))=((n_HA(I)*v)*3/(4*pi))^(1/3);
        c_growth(I,HA_nuclei(I))=0;
        t=t+Dt;
    end
    cumulative_p=cumulative_p+nucleation_p;
  % Growth
    if n_random>cumulative_p && n_random<(cumulative_p+growth_p)
        cumulative_p=0;
        Sum_a=sum(sum(a_growth));
        n_random=rand;
        for j=[1:Number_xsteps]
          for m=[1:HA_nuclei(j)]
            if a_growth(j,m)>0
              if n_random>cumulative_p && n_random<(cumulative_p+a_growth(j,m)/Sum_a)
                n_size_HA_nuclei(j,m)=n_size_HA_nuclei(j,m)+1;
                crystal_radii(j,m)=((n_size_HA_nuclei(j,m)*v)*3/(4*pi))^(1/3);
                Ca_ions(j)=Ca_ions(j)-n_Ca(j);
                PO4_ions(j)=PO4_ions(j)-n_PO4(j);
                Ca_conc(j)=Ca_ions(j)/(6.02e23*DV);
```

```matlab
                    PO4_conc(j)=PO4_ions(j)/(6.02e23*DV);
                    cumulative_p=cumulative_p+a_growth(j,m)/Sum_a;
                end
            end
        end
    end
    t=t+Dt;
    end
    if t>taccum     % Shows partial times while code is running
        t
        taccum=taccum+deltat;
    end
end
% Shows some final results
n_HA
n_size_HA_nuclei
crystal_radii
x_position=[1:1:Number_xsteps];
plot(x_position,Ca_conc,x_position,PO4_conc,x_position,Cl_conc,x_position,NH4_conc,x_position,I_
conc)
xlim([1 Number_xsteps]);
ylim([0 Ca_feed_conc]);
t
beep
```

APPENDIX 11

FINITE ELEMENT MODELS OF MASS TRANSPORT USING COMSOL

MULTIPHYSICS

We have used the finite element method (FEM) to model mass transport within biomaterials; specifically, 1) the diffusion of a non-reactive solute (Fig. 3.14), and 2) the diffusion-reaction of reactive solutes (i.e., calcein-AM (Fig. 3.16) and oxygen (Figs. 3.19 and 4.11)). This appendix briefly describes details of the use of COMSOL Multiphysics (Comsol, Inc., Burlington, MA) for the diffusion and diffusion-reaction processes.

Two-dimensional (2-D) finite element models used in this dissertation represent cross-sectional areas of three-dimensional (3-D) scaffolds (Figs. 3.14, 3.16, 3.19, and 4.11). We presume that there is no convection in the domains of interest. Another important assumption is that individual cells seeded in scaffolds do not serve as discrete sinks causing significant concentration gradients of reactive solutes. We have verified this aspect with a 3-D finite element model indicating that the gradient of oxygen concentration is negligible across single cells (data not shown). Therefore, an continuum approach using macroscopic parameters would be valid for the diffusion-reaction processes; for example, the global consumption rate of oxygen, $R_{O_2} = \rho_{cell} R_{O_2,cell}$, can be applied to the domains with an assumption that cells are uniformly distributed.

General steps to run finite element models in COMSOL are as follows:

1. Non-dimensionalize governing equation(s) and boundary conditions with characteristic lengths (e.g., microchannel width)

2. Open an appropriate module in COMSOL (e.g., transient 2-D diffusion; Fig. A11.1A)

3. Draw domain(s) (Fig. A11.1B)

4. Pre-define constants that will be used in a model (e.g., diffusivity, consumption rate; Fig. A11.1C)

5. Set up the domain based on the governing equation(s) (Fig. A11.1D)

6. Set up the boundary conditions (Fig. A11.1E)

Steps 1 and 4 are not mandatory, but the steps make it convenient to test a model with varying parameters. If we specify commonly used units of constants when pre-defining them, COMSOL will automatically convert the constants into the SI unit.

As an example, we describe procedure for the transient diffusion-reaction of a reactive solute within a microfluidic scaffold. Figure 3.16A shows the distribution of calcein-AM delivered via the embedded microchannels and enzymatically consumed by cells in the bulk. The transient diffusion-reaction of the solute in the 2-D domain (i.e., a cross-sectional area of the microfluidic scaffold) is governed by

$$\frac{\partial c_{calc-g,g}}{\partial t} = D_{calc-g,g} \nabla^2 c_{calc-g,g} - \left(k_{cell} \rho_{cell} \right) c_{calc-g,g} \tag{A11.1}$$

with boundary conditions:

$$c_{calc-g,g} \left(\text{microchannel walls} \right) = c_0$$
$$\nabla c_{calc-g,g} \left(\text{outer boundaries of the scaffold} \right) = 0 \tag{A11.2}$$

Non-dimensionalized variables can be defined as

$$\tilde{c}_{calc-g,g} \equiv \frac{c_{calc-g,g}}{c_0}$$
$$\tilde{\nabla} \equiv w_c \nabla \tag{A11.3}$$
$$\tilde{t} \equiv \frac{t}{w_c^2 / D_{calc-g,g}}$$

Then, the governing equation and boundary conditions become

$$\frac{\partial \tilde{c}_{calc-g,g}}{\partial \tilde{t}} = \tilde{\nabla}^2 \tilde{c}_{calc-g,g} - \tilde{k}_{calc-g,g} \tilde{c}_{calc-g,g} \quad \text{(A11.4)}$$

$$\tilde{c}_{calc-g,g} \left(\text{microchannel walls} \right) = 1$$
$$\tilde{\nabla} \tilde{c}_{calc-g,g} \left(\text{outer boundaries of the scaffold} \right) = 0 \quad \text{(A11.5)}$$

where non-dimensionalized rate constant, $\tilde{k}_{calc-g,g}$ is

$$\tilde{k}_{calc-g,g} = \frac{k_{cell} \rho_{cell} w_c^2}{D_{calc-g,g}} \quad \text{(A11.6)}$$

After pre-defining constants as summarized in Table A11.1, Eqs. A11.4 and 5 are applied to the domain. Figure 3.16A is a transient solution to Eq. A11.4 at 120 min. Other finite element models presented in this dissertation were fomularized in the same way.

Table A11.1 Pre-defined input parameters for the 2-D finite element model of the enzymatic consumption of calcein-AM

Diffusivity of calcein-AM	$D_{calc-g,g}$	2.4×10^{-6} cm^2/s
Microchannel width	w_c	100 µm
Cell seeding density	ρ_{cell}	2.5×10^{7} cell/mL
Rate constant for the enzymatic consumption	k_{cell}	1×10^{-11} mL/cell·s
Time	t	120 min
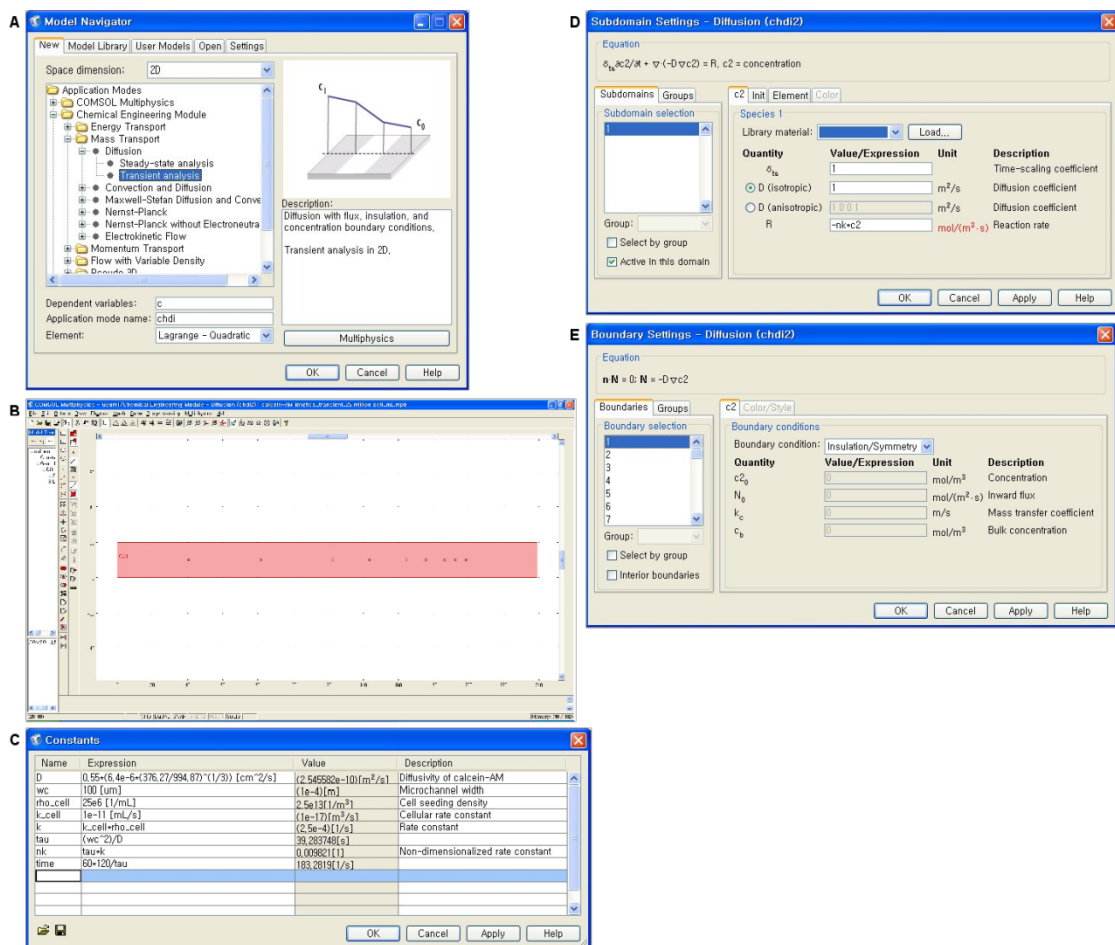
Figure A11.1 General steps to run finite element models in COMSOL Multiphysics. A. Module choice. **B.** Draw mode. **C.** Pre-definition of input parameters. **D.** Subdomain settings. **E.** Boundary settings.